Numerical simulation of buoyancy-induced flow in a sealed rotating cavity

Lewis, Tanat

Award date:
1999

Awarding institution:
University of Bath

NUMERICAL SIMULATION OF BUOYANCY–INDUCED FLOW IN A SEALED ROTATING CAVITY

Submitted by Tanat Lewis

for the degree of

Doctor of Philosophy

of the University of Bath

1999

ProQuest LLC
789 East Eisenhower Parkway
P.O. Box 1346
Ann Arbor, MI 48106-1346

Contents

Acknowledgements

I would like to express my deepest gratitude to all my colleagues, friends and family who assisted me during the course of my research.

In particular, I wish to thank my supervisor Dr. D.A.S. Rees for his continued encouragement, guidance and support. I am greatly indebted to him for all the help that I received and the experience that I have gained.

Many thanks must also go to Dr. M. Wilson for his very valuable assistance during various stages of this work. I would also like to thank Professor J.M. Owen for his advice and very helpful comments.

I gratefully acknowledge the receipt of a bursary award from Bath University, without whose financial support this research would not have been possible.

Special thanks also go to my family for all their support and encouragement during my years at Bath University.

Summary

This thesis describes a fundamental numerical investigation into the buoyancy–induced flow and heat transfer characteristics of a sealed rotating cavity. The outer cylindrical shroud is assumed to be uniformly hot and the inner cylindrical hub uniformly cold. The disk side walls are assumed to be adiabatic and all the surfaces rotate at a uniform angular speed with gravitational buoyancy effects neglected in order to simulate more fully the flow in turbomachinery disk–spaces. Also considered is an isothermal, sealed rotating cavity configuration with a stationary outer cylindrical surface. Here a forced convection flow is investigated.

Initially, a radial/axial axisymmetric buoyancy–induced flow is considered. A streamfunction–vorticity formulation is applied with coupling with the temperature equation achieved through the assumption that the density varies linearly with temperature. The Reynolds number multiplies the Coriolis force which is found to oppose the destabilising effect of the buoyancy force. A Linear Stability Theory (LST) analysis is used to solve the linearised perturbation equations in order to obtain the neutral stability characteristics of the flow.

The second two–dimensional flow investigated is in the radial/tangential plane with zero axial velocity assumed. The Coriolis force scales out of the governing equations with the introduction of a streamfunction–vorticity formulation, but the Reynolds number is nevertheless retained in the buoyancy correction terms. Convection is in the form of cyclonic/anti–cyclonic pairs where the cyclones rotate in the same sense as the cavity and the anti–cyclones in the opposite sense of rotation. LST suggests that numerous discrete wavenumber solutions are stable for given defining parameters, with the buoyancy correction only having a localised effect on the neutral stability at small Reynolds numbers. Non–linear numerical investigation confirms that various wavenumber solutions may be obtained for a given cavity, with the cyclonic/anti–cyclonic pairs having increasingly isothermal cores and becoming time dependent with an increase in the Rayleigh number. The rolls are also observed to precess relative to the rotating surfaces and this is attributed exclusively to the magnitude of the buoyancy correction.

To investigate the influence of the disks on the two–dimensional flow described above, a three–dimensional vorticity–velocity formulation is applied. The velocity field is described by three Poisson equations which are solved at each time level using a Multigrid acceleration technique to enhance the performance of the relaxation procedure. The three–dimensional flow bears a strong similarity to the two–dimensional radial/tangential flow and is again characterised by regions of cyclonic/anti–cyclonic activity. Non–unique solutions are obtained with various wavenumber solutions stable for a given set of parameters. The effect of the disks on the flow is relatively localised with axial velocity away from the disks in regions of cyclonic activity and toward the disks in regions of anti–cyclonic activity. The rate of precession of the rolls is additionally dependent on the proximity of the disks, with an increase in the precession rate with a decrease in the separation. It is noted however that for some of the cases presented the results may only be regarded as being qualitatively correct as the fluid can take negative densities in part of the computational domain.

Finally, the sealed cavity with a stationary shroud problem is investigated using suitably modified versions of the code developed for the axisymmetric flow. The primary flow is in the radial–tangential plane, however, a time–dependent secondary flow in the radial–axial plane is computed. Comparisons with experimental results show reasonable agreement.

Nomenclature

N.B. The following is a guide. For example, v is a generic term for tangential velocity; the precise notation in the text distinguishes between dimensionless / dimensional / rotational forms.

A, B, C	three–dimensional vorticity components
a	dimensional inner radius of cylindrical hub
d	dimensional distance between differentially heated surfaces
E	Eckman number $(= \frac{\nu}{\Omega R^2})$
Gr	Grashof number $(= \frac{Ra}{Pr})$
g	acceleration due to gravity
I_c	Fourier cosine coefficient
I_s	Fourier sine coefficient
J	Jacobian operator
j	imaginary number $(\sqrt{-1})$
K	thermal conductivity
k	wavenumber
Nu	local Nusselt number
Nu_0	total Nusselt number
n	discrete wavenumber
P	static Pressure
Pe	Peclet number
Pr	Prandtl number $(= \frac{\nu}{\kappa})$

$\dot{q}$	rate of heat transfer
$\dot{q}_\lambda$	rate of heat transfer due to conduction alone
R	dimensional outer radius of cylindrical shroud
Ra	rotational Rayleigh number ($= \frac{R\Omega^2\beta\Delta T R^3}{\nu\kappa}$)
Ra_b	gravitational Rayleigh number ($= \frac{g\beta\Delta T d^3}{\nu\kappa}$)
Ra_{gap}	gap based rotational Rayleigh number ($= \frac{R\Omega^2\beta\Delta T(R-a)^3}{\nu\kappa}$)
Re	rotational Reynolds number ($= \frac{R^2\Omega}{\nu}$)
r	radial coordinate
r_m	arithmetical mean radial coordinate ($= \frac{1}{2}(R-a)$)
r_0	radius ratio ($= \frac{a}{R}$)
S	standard deviation
s	dimensional axial dimension of cavity
T	temperature
T_c	dimensional cold surface temperature
T_h	dimensional hot surface temperature
T_m	arithmetical mean temperature ($= \frac{1}{2}\Delta T$)
t	time
U	dimensional radial velocity
u	radial velocity
V	dimensional, stationary frame tangential velocity
v	tangential velocity
W	bulk average velocity
w	axial velocity
z	axial coordinate

Greek characters

β	volumetric expansion coefficient
ΔT	dimensional temperature difference between cold and hot surfaces
δr	radial interval
δt	timestep
δz	axial interval
$\delta\theta$	tangential interval
κ	thermal diffusivity
θ	tangential coordinate
λ	temporal growth rate ($= \lambda_R + j\lambda_I$)
λ_I	imaginary component of the temporal growth rate (a frequency)
λ_R	real component of the temporal growth rate
λ_W	wavelength
ν	kinematic viscosity
ρ	density
ρ_0	reference density
ϕ	scaled streamfunction ($= \frac{\psi}{r}$)
ψ	streamfunction
Ω	angular rotational speed of cavity
ω	vorticity (two–dimensional flow)

Subscripts

$_B$	base quantity
$_{crit}$	critical value

$_{dim}$	dimensional value
$_{max}$	maximum value
$_{min}$	minimum value

Superscripts

*	rotating frame reference value
^	perturbation quantities

Chapter 1

Introduction

The high operating temperatures encountered in modern gas turbine engines means that the accurate prediction of the temperature distribution and heat transfer within rotating cavities is very important. Effective cooling in such engines can improve efficiency and increase their operating life. The prediction of the temperature distribution in sealed rotating cavities is also of importance as this must account for the heat transfer conditions encountered elsewhere in the engine.

In the period from 1940, inlet temperatures have increased substantially from about 900 K to 1600 K resulting in the need for improved material properties to cope with the resulting large thermal stresses, and also an improved understanding of basic–flow structures within internal turbine cavities to aid cooling design. A typical cross–section through a gas turbine showing the internal air system may be seen in Figure 1.1. It is rare that sealed cavities occur within gas turbine cooling disk systems as a throughflow of cooling air is normally required, however an example of a sealed disk space with all surfaces rotating at the same angular

speed is presented in Figure 1.2. In order to investigate fully the flow within both sealed and non–sealed cavities, initial fundamental investigations are required for rotating systems with a simple geometry. This will aid the understanding of the increasingly complicated geometries and throughflow systems encountered in turbines. For forced convection problems at turbomachinery operating conditions, the flow within these air–filled cavities is expected to be turbulent. However, for buoyancy–induced flows, there is strong evidence that the flow remains laminar throughout the operating conditions encountered (Bohn, Dibelius, Deuker and Emunds, 1994). Laminar flow conditions only are therefore considered here. Turbulent flow modelling is beyond the scope of this thesis, but some reference is made to turbulent flow conditions in the review of previous work.

The main configuration being considered may be seen schematically in Figure 1.3. The outer cylindrical surface (shroud), is uniformly heated and the inner cylindrical surface (hub), uniformly cooled. The side walls (disks), are assumed to be perfectly insulated, (adiabatic). The cavity is sealed and rotates at a constant speed, Ω. If no heating were present (i.e. isothermal conditions prevail), the fluid within the cavity would be in solid body rotation with all the fluid particles rotating at the same angular velocity, Ω. The temperature difference between inner and outer cylindrical walls, if sufficiently large, may give rise to a buoyancy–induced flow due to centrifugal effects. Gravitational buoyancy effects are neglected in this computational study since the ratio $\frac{g}{\Omega R^2}$ is unlikely to be greater than 0.1 at turbomachinery operating conditions. The configuration is analogous to Bénard convection in confined cavities where gravitational buoyancy effects are the driving force (Figure 1.6). Indeed, in the limit as $\frac{a}{R} \rightarrow 1$ the LST tends to the Bénard limit with the centrifugal force taking the place of the gravitational force.

A further sealed geometry considered as part of the thesis is shown in Figure 1.7. Here, the shroud is stationary with all other surfaces rotating. The outer shroud and inner hub are assumed adiabatic with the disks either isothermal or at different constant temperatures. This geometry is relevant to some gas turbines where there is a peripheral flow of cooling air entering and leaving the cavity through the outer casing. However, solutions are obtained only for cases where there is no peripheral flow of cooling air in order to investigate fully the fundamental flow structures, and in particular, the temporal instabilities of the flow. Although the primary flow is in the tangential direction, a secondary radial/axial flow exists which takes the form of two counter–rotating circulations. It is shown that this secondary flow travels radially outward on the disks and radially inward at the mid–axial plane (located midway between the rotating disks as depicted by the dividing streamline in Figure 1.7).

The thesis broadly takes the following format. Chapter 2 contains a review of previous work on buoyancy–induced flows, and includes both stationary and rotating systems. In chapter 3, two dimensional radial/axial axisymmetric flow is first considered (figure 1.4). A Linear Stability Theory method is adopted to predict the conditions necessary for the onset of convecting flow. Numerical simulations of the full two–dimensional non–linear equations are then undertaken in order to simulate the form of the ensuing axisymmetric convection. Another study is undertaken in Chapter 4 where no convection is assumed to occur in the axial direction, and therefore a radial/tangential flow is studied (figure 1.5). Once again, a Linear Stability Theory is used in order to obtain the conditions necessary for the onset of convective instability and the results of detailed Numerical Simulations are presented. Chapter 5 describes the numerical simulation of the full three–dimensional problem and includes detail concerning the methods

of solution and assumptions made. A Fourier decomposition of the temperature field is also obtained. The effect of introducing buoyancy corrections to the Coriolis force is also discussed for two–dimensional and full three–dimensional simulations.

Chapter 6 describes the development of the axisymmetric radial/axial code to include the use of a non–uniform grid and then its subsequent use in predicting the flow inside a sealed cavity with stationary shroud. The effects of unsteadiness are investigated and comparison is made where possible, with experimental results. Solutions are also obtained using a suitably modified version of the uniform grid code developed in Chapter 3.

Conclusions and recommendations for future work are presented in Chapter 7.

Chapter 2

Review of previous work

2.1 Introduction

In this chapter a review of that previous work which is relevant to this thesis is presented. The problem of natural convection in stationary cavities is first considered. A strong similarity exists between the stationary and rotating cavity problems, where the gravitational field of the former is replaced by centrifugal force effects in the latter as the body force generating free convective flows. Much attention has been given to buoyancy induced flow in sealed stationary cavities due to its wide ranging applications. Less attention, however, has been given to natural convection in sealed rotating systems, with many authors considering forced convection problems only. Several authors have also considered the predominantly forced convection problem of flow and heat transfer in rotating cavities with a stationary shroud with or without a peripheral flow of cooling air. These will be reviewed here also. Some numerical methods are also considered and presented. In particular, various formulations and solution methodologies for the Navier–Stokes equations are reviewed.

In addition to the work presented below, two monographs by Owen and Rogers (1989,1995) give detailed reviews of flow and heat transfer in both rotor–stator systems and rotating cavities. Of particular interest and relevance is the review of buoyancy induced flow in rotating cavities where experimental, analytical and numerical work is covered in detail.

2.2 Natural convection in stationary cavities

Many authors have investigated natural convection in stationary cavities and this generic fundamental fluid problem has a long history. The problem for differentially heated side walls and adiabatic upper and lower surfaces, sometimes known as the double–glazing problem, has been investigated widely due to its associated applications. These include horizontal transport in water bodies, reactor cooling systems, building insulation and crystal growth procedures. Consequently, this has become one of the classical heat and mass transfer problems with significance for fundamental fluid mechanics. The buoyancy–induced flow between horizontal surfaces heated from below is another classic fluid dynamics problem. Rayleigh–Bénard convection has many wide ranging applications, having been the subject of numerous early investigations. Here, only a brief review of selected literature is presented.

2.2.1 Differentially heated side walls

Vest and Arpaci (1969) investigated analytically and experimentally the stability of natural convection of a viscous fluid in a vertical slot with differentially heated

side walls. At low Rayleigh numbers (Ra_b; see nomenclature), heat is transferred across the slot primarily by conduction. At higher Rayleigh numbers heat transfer is due primarily to convection with thin boundary–layers forming on the sidewalls and surrounding an isothermal core. The authors produced neutral stability curves for both the conduction and boundary–layer regimes and concluded that natural–convective flow is unstable with respect to two–dimensional stationary modes of disturbance which are fixed in space.

Unsteady natural convection in a rectangular cavity with differentially heated side walls was studied by Patterson and Imberger (1980). The Boussinesq approximation was assumed to be valid (see Tritton, (1977) for detailed description of the approximation) and the side walls were instantaneously heated and cooled to temperatures $T_0 + \frac{\Delta T}{2}$ and $T_0 - \frac{\Delta T}{2}$, where T_0 was taken as the initial fluid temperature. The flow that evolves, consists of narrow boundary–layers on the vertical walls exiting from the downstream corners in heated and cooled intrusions. A combination of scale analysis and a numerical simulation was used to show that a number of initial flow types are possible dependent upon the Rayleigh number, aspect ratio (height / width) and Prandtl number. They showed however, that these initial flow types tended toward either convective, conductive or transitional steady flow types. They also showed that the flow changes from being conduction dominated to being convection dominated for increasing Rayleigh number with a constant aspect ratio and Prandtl number. Further increases in Rayleigh number were shown to give rise to internal wave motion in the side wall boundary–layers.

De Vahl Davis (1983) produced a bench mark numerical solution for a buoyancy–driven flow in a square sealed stationary cavity in a gravitational field. The

vertical sides were differentially heated and horizontal surfaces adiabatic. Time independent solutions were obtained for Rayleigh numbers of $10^3, 10^4, 10^5$ and 10^6 using a streamfunction–vorticity formulation. The time–dependent form of the equations were utilised and advanced in time using the method of the false transient, (Mallinson and de Vahl Davis, 1973), until a steady state was reached. First order accurate forward differences were used for the time derivatives and central second–order accurate differences for spatial derivatives. Uniform grids were used which facilitated the use of the Richardson's extrapolation technique to obtain more accurate solutions. These fourth order accurate solutions were obtained by using solutions on two different meshes, the finer grid having half the grid spacing of the coarser.

Further investigations were conducted by Patterson and Armfield (1990). Here, a combined numerical and experimental approach was used to investigate the transient start–up corresponding to the instantaneous heating and cooling of the side walls of the cavity. Good comparisons were obtained indicating that the numerical simulations captured the important features of the flow. They showed the presence of travelling wave instabilities on the vertical wall boundary–layers and horizontal intrusion flows. The interaction of the intrusions with the opposing vertical boundary–layers were also shown to give rise to cavity–scale oscillations.

Schladow (1990) investigated the oscillatory motion in the side–heated cavity using a direct simulation method. The results obtained were for an aspect ratio of unity and chosen Rayleigh and Prandtl numbers. Both long–period cavity–scale and short–period boundary–layer instabilities were shown to be present for the transient start–up problem. The former was concluded to be as a result of the horizontal pressure gradients established by the tilting of the intrusion

isotherms caused by the strong buoyancy–induced vertical jets turning the corner and intruding horizontally across the cavity. The latter was deemed to be as a result of the 'leading–edge' effect at start–up and the interaction between the intrusion flows and opposite boundary–layers.

Armfield and Patterson (1992) investigated the wave properties associated with the starting boundary–layer. A comparison of experimental, numerical and analytical results were presented, indicating that the early part of the development of the thermal boundary–layer is approximately one–dimensional. They also showed that the divergence from the one–dimensional boundary–layer is followed by oscillation as a result of temperature overshoot from the steady state in the hot boundary–layer, and amplification of the travelling waves.

Further investigation was carried out by Schöpf and Patterson (1995). Here, a shadowgraph technique was used for visualising the early stages of the flow near start up. They present a clear visualisation of the first group of waves travelling up the hot boundary–layer, the initial horizontal intrusion flow and the second group of waves resulting from the interaction between the intrusion and boundary–layers.

2.2.2 Rayleigh–Bénard convection

Rayleigh–Bénard convection has been the subject of many reviews, much of which is beyond the scope of this thesis. However the brief description of some fundamental ideas and findings presented here is based on the review of Koschmieder (1993).

Bénard performed the first systematic investigation of convection in a shallow fluid layer heated from below with a free surface boundary above. He found a stable, steady–state regular pattern of hexagonal convection cells when viewed from above, with fluid rising at the centre and falling at the hexagonal edges. Rayleigh later explained this in terms of a buoyancy–driven instability. It was later understood that in buoyancy–driven convection, the expected pattern would be convection in the form of rolls, rather than the cellular pattern observed by Bénard. The convection observed by Bénard is now understood to be driven by temperature–dependent surface tension forces rather than by buoyancy. Rayleigh also discovered that a critical temperature difference must exist for the onset of instability, at which the buoyancy of the fluid is able to overcome the dissipation due to viscosity and thermal diffusivity of the fluid. The critical Rayleigh number (Ra_b), critical wavenumber and critical wavelength for the three possible horizontal boundary conditions are presented in Table 2.1.

Boundaries	$Ra_{crit.}$	k_{crit}	$\lambda_{W\,crit}$
Rigid–rigid	1707.8	3.117	2.016
Rigid–free	1100.7	2.682	2.342
Free–free	657.5	2.221	2.828

Table 2.1: Critical conditions for instability

Rayleigh–Bénard convection in a rotating fluid layer of infinite radial extent rotating about a vertical axis, heated uniformly from below has also been investigated by many authors. It was noted that rotation had a stabilising effect on the onset of convection due to the presence of the Coriolis force which makes the path of rising parcels of fluid curved and therefore longer. As a result, the parcels will experience more dissipation, and in order to overcome the increased dissipation a larger temperature difference has to be applied to begin convection. The convection pattern noted by several authors has the form of concentric circular rolls.

At larger rotational rates, the rolls align in the radial direction as a result of the shear of the centrifugal circulation becoming increasingly dominant.

Further work was conducted by Schlüter, Lortz and Busse (1965). They presented the finite–amplitude steady solutions for an infinitely long horizontal layer using successive approximations. They concluded that not every linear steady solution is a stable solution of the non–linear problem but yet there still exists an infinite number of finite–amplitude solutions. Their stability theory suggested that three–dimensional flows are unstable with respect to infinitesimal disturbances and that a class of two–dimensional solutions in the form of rolls are indeed stable, but this depends heavily on the wavelength. However, it was noted that their stability conclusions were obtained up to third–order in the expansion, and any small change in the Boussinesq equations being used could alter the behaviour.

Busse (1967), (reported in Koschmieder, 1993), made the first theoretical study of supercritical convection on an infinite plane and for an infinite Prandtl number (equivalent to neglecting inertia forces). He investigated the stability of the steady solutions of the convection equations by introducing non–oscillatory two–dimensional disturbances. He concluded that stationary two–dimensional supercritical rolls are stable in only a part of the range given by the neutral curve of linear theory and that there are no stable time–independent motions above a certain critical value of Rayleigh number.

2.3 Natural convection in rotating cavities

Many authors have considered rotating flow in sealed rotating cavities with either an axial or a radial heat flux. The former bears a strong similarity to the stationary sealed system in a gravitational field, (double–glazing problem), discussed above. Here, however, the direction of flow in the boundary–layer on the heated disk opposes the direction of centrifugal acceleration and is radially inward toward the centreline. Conversely, the flow in the boundary–layer formed on the cooled disk is radially outward. The latter case with a radial heat flux is generally more complex, and bears strong similarities to Rayleigh–Bénard convection. Here, the flow is likely to be three dimensional and unsteady.

2.3.1 Axial heat flux

Numerical predictions for centrifugally driven free convection in sealed rotating cavities were presented by Chew (1985). Results were obtained for both air and high–viscosity silicone oil filled cavities. Finite difference solutions in primitive variable form were obtained for the axisymmetric equations of momentum, mass and energy conservation on a staggered grid using the 'SIMPLE' algorithm of Patankar (1980). Step changes on the grid size near the boundaries were also implemented in order to resolve fully the boundary–layer regions. Chew utilised a first–order accurate hybrid upwinding scheme for the advection terms. The boundary conditions applied to the silicone oil simulations corresponded to different, but uniform, temperatures on the disks, adiabatic conditions on the outer cylindrical surface and symmetry boundary conditions at the axis of rotation. The investigation for low Reynolds number (Re) where conduction effects dom-

inate showed good comparison with the similarity solution of Dorfman (1968). At higher values of Reynolds number and of $\beta\Delta T$, the numerical results depart from the similarity solution which assumes a linear temperature profile across the cavity in the solution for the flow field between two infinite disks. The presence of the outer cylindrical surface is also shown to affect the heat transfer throughout the cavity.

Chew then considered the air–filled cavity and, in particular, concentrated on the effects of the thermal boundary condition applied at the outer cylindrical surface and non–uniform disk temperature distributions. Results were again compared with a similarity solution where the author showed reasonable comparison. It was shown however, that the replacement of the adiabatic condition on the outer cylindrical surface with a linear distribution, reduced significantly the heat transfer to the disks.

Bohn, Dibelius, Deuker and Emunds (1994) investigated numerically the temperature distribution and heat transfer within a square–section rotating annulus with constant but different temperature distributions at the walls, (disks). Furthermore, the inner and outer cylindrical surfaces were assumed to be insulated. The computational model included also the effects of introducing a sectored cavity by using adiabatic radial walls which made the flow three dimensional. Their code solved the compressible steady–state equations for the conservation of mass, momentum and energy. They evaluated the density using the ideal gas law assuming the cavity to be air–filled. Compressibility effects were neglected in the viscous terms of the equations as the velocities of these types of flow are generally small. In the energy equations the dissipation and the pressure changes were also assumed to be negligible. Laminar flow conditions only were investigated.

A finite volume scheme was introduced using the 'SIMPLE' pressure correction and hybrid upwinding schemes for the advective terms. Both three–dimensional sectored cavity and two–dimensional non–sectored cavity solutions were obtained.

Bohn *et al.* (1994) first showed that, for the two–dimensional computations, fluid circulates around the walls in boundary–layers with little motion in the core region. The heat transfer was shown to increase with increasing Grashof number at a constant Reynolds number. It was also shown that increasing the Reynolds number at constant Grashof number decreases the heat transfer. They concluded therefore that the flow was driven by the buoyancy force and damped by the Coriolis force. They also studied the effect of curvature on the cavity by varying the ratio between the mean radial extent ($\frac{1}{2}(R-a)$) and the cavity height ($R-a$). The heat transfer was found to be greater at large values of this aspect ratio.

When the cavity was sectored by radial walls the flow was found to be three–dimensional. The section angle was varied between 5^o and 180^o. The circumferential velocity was weakened and Coriolis forces were found to decrease resulting in an increase in the heat transfer. They also found that a significant increase in heat transfer occurs for section angles less than 30^o. They suggested that, for very small section angles (less than 5^o), viscous action would be dominant over the entire annulus, slowing down the motion and thus decreasing the heat transfer. No evidence of this was presented as the section angle was never decreased below 5^o.

Bohn, Emunds, Gorelitz and Krüger (1996) investigated both experimentally and theoretically the heat transfer in closed gas–filled rotating annuli with a

purely axial heat flux. The experimental rig consisted of insulated inner and outer cylindrical walls, one electrically heated and one cooled side wall. The experiments were conducted for one geometric configuration which facilitated comparison with the radial heat flux case presented below. They proposed a heat transfer law for the axial heat flux case,

$$Nu = 0.346 Ra^{0.124}. \tag{2.1}$$

where $Ra = \frac{r_m \Omega^2 \Delta T d^3}{T_m \nu \kappa}$ and $Nu = \frac{\dot{q}}{\dot{q}_\lambda}$. The law was evaluated between the range $2 \times 10^8 \leq Ra \leq 5 \times 10^{10}$. For the radial heat flux case, for comparison the heat transfer was given by

$$Nu = 0.246 Ra^{0.228}. \tag{2.2}$$

They therefore showed that the heat transport in the case of the radial heat flux is much greater, (approximately twice), than the one with pure axial heat flux over the whole range of Rayleigh number they considered.

The numerical investigation included the use of both two–dimensional and three–dimensional codes as described above by Bohn *et al.* (1994). They found again that the fluid circulates around the walls in boundary–layers with almost stagnant fluid in the core region. Comparisons between the two–dimensional code and experiment showed that the Nusselt numbers agreed well for $Ra < 2 \times 10^9$. They found that when the Rayleigh number is above 2×10^9, the comparison becomes increasingly poor. This they attributed to the two–dimensional and adiabatic cylindrical wall assumptions made for the numerical investigation. In particular, the assumption of adiabatic cylindrical surfaces could not be realised in the experiment. Results presented for the three–dimensional calculations show similar temperature distributions to the two–dimensional code. However, in the

regions where the cold fluid reaches the hot wall a significantly different temperature gradient was shown to occur. They also showed that for increasing Reynolds number ($Re = \frac{r_m \Omega d}{\nu}$), large differences between the two–dimensional and three–dimensional solutions became apparent. The authors suggested that, for further work, investigation into the conditions for the flow to change from two–dimensional to three–dimensional is particularly important.

2.3.2 Radial heat flux

Experimental and theoretical investigations of heat transfer in closed gas–filled rotating annuli were conducted by Bohn, Deuker, Emunds and Gorelitz (1995). Experimental and numerical results were presented for cavities with a radial heat flux at conditions very close to turbomachinery operation. The experimental rig comprised a uniformly heated outer copper ring, uniform water cooled inner hub and heat insulating annular disks. They considered experimentally three different geometric configurations. All three cavities had an inner radius of $125mm$ and axial width $120mm$. However, cavity A had an outer radius of $355mm$, with cavity B and C having an outer radius of $240mm$. In addition, cavity C was divided into 45^o segments by eight heat–insulating radial walls. They produced the following correlations from their experimental data between Nusselt and Rayleigh numbers for the three configurations:

$$Nu_A = 0.246 Ra^{0.228} \text{ for } \mathrm{Re_A} = 0.733 \mathrm{Ra}^{0.573}, \tag{2.3}$$

$$Nu_B = 0.317 Ra^{0.211} \text{ for } \mathrm{Re_B} = 1.441 \mathrm{Ra}^{0.557}, \tag{2.4}$$

$$Nu_C = 0.365 Ra^{0.213} \text{ for } \mathrm{Re_C} = 1.615 \mathrm{Ra}^{0.556}. \tag{2.5}$$

where $Ra = \frac{r_m \Omega^2 \Delta T d^3}{T_m \nu \kappa}$, $Re = \frac{r_m \Omega d}{\nu}$ and $Nu = \frac{\dot{q}}{\dot{q}_\lambda}$. They deduced that the insertion of separation walls attenuated the tangential velocity field resulting in a decrease in the radial component of the Coriolis force and thus increasing the heat transfer. Although the correlations for Nusselt numbers for geometries A and B are very similar, they noted that for a given Rayleigh number, the associated Reynolds number in case B was nearly twice that in case A. They obtained no experimental data on the flow structure.

The numerical investigation was concentrated only on configuration C due to the number of grid points involved with the computation of the entire cavity. They completed both steady and unsteady computations on the sectored cavity and showed that the flow is possibly unsteady. The steady state computations showed good agreement with the experimental data when they took into consideration the heat loss through the radial side walls for the experiment. The flow field evaluated showed that the air circulated mainly in boundary–layers with little motion occurring in the core. They concluded that the mean flow occurred in the radial/circumferential plane. The temperature in the core region was shown to be uniform at a value approximately midway between hot and cold wall temperatures.

2.3.3 Axial throughflow

Long and Tucker (1994) investigated numerically a heated rotating cavity with an axial throughflow of cooling air. The full three–dimensional, time–dependent, compressible equations were solved using a finite–volume approach. Various disk and shroud temperature distributions were investigated for a rotational Reynolds

number of 1.3×10^4 and axial throughflow Reynolds number of 2180, where this Reynolds number is defined as $Re = \frac{2Wa}{\nu}$. The mesh contained $17 \times 21 \times 40$ grids (in the axial, radial and tangential directions respectively). Both disks were heated with the same axisymmetric temperature distribution which either decreased or increased with radius. They found that the flow structure was three-dimensional and exhibited a cyclic form of time–dependence. The flow entered the cavity in radial arms with regions of cyclonic/anti–cyclonic circulation forming. They noted that where there exists a region of cyclonic flow, fluid moves axially away from the disk surface, and, for regions of anti–cyclonic flow, the reverse applies. It was found that for an unheated peripheral shroud, the number of radial arms, and hence the number of cyclonic/anti–cyclonic regions increases as the location of the maximum disk surface temperature moves radially outward. They also concluded that, when the shroud is heated, there are many radial arms which exchange fluid with the boundary–layer on the shroud.

2.4 Rotating cavity with stationary shroud

In some gas turbine engines, the corotating disks are cooled by air introduced at the periphery of the system. The air enters through holes in a stationary peripheral casing and leaves through the rim seals between the casing and the disks. The flow between shrouded corotating disks is also a key factor in the performance of disk drives where the temperature distribution and the resulting thermal distortion are critical to the performance of the drive. Many authors have considered flow and heat transfer in sealed systems with a stationary shroud, but little work has been undertaken into cavities with a peripheral flow of cooling air.

2.4.1 Sealed rotating cavity

Morse (1991) studied the case of corotating disks with a stationary outer shroud. He assumed axisymmetry and obtained numerically a flow structure with two symmetric recirculations about the mid–axial plane. He concluded that the direction of flow is radially outward over the disks and radially inward in the centre of the cavity. No comparisons with experimental data were made for the velocity profiles. He also commented that only about 0.5% of recirculated mass flow reaches the mid radial location for a gap ratio ($\frac{s}{R}$) of 0.1 and $Re = 10^6$.

Abrahamson, Eaton and Koga (1989) conducted experimental work to study the flow between corotating disks with a stationary shroud in a computer disk drive application. Experiments using water as a working fluid, were carried out for varying Eckman numbers (E) and gap ratios. They observed the existence of three distinct regions for a rotation speed of $1.57 rad/sec$ ($E = 2.1 \times 10^{-6}$) and gap ratio of 0.05:

- polygonal shaped inner region characterised by solid body rotation,
- an outer region dominated by large contra–rotating vortices in the secondary flow,
- boundary–layer region on the stationary shroud.

Flow visualisation showed a sharp transition between the inner and outer regions. For axisymmetric flow, the boundary between these two regions must be circular, while the existence of large vortical structures create a polygonal boundary between the two regions in the circumferential plane.

They also showed that the thin shroud boundary–layer region is three dimensional and includes a pair of toroidal vortices whose vorticity axis lies in the $\pm\theta$ direction in cylindrical polar coordinates. The locus of the axes of these vortices was found to be a circle with diameter slightly smaller than the diameter of the shroud. They also concluded that the size of the outer region increases as the axial separation of the disks increases, and the strength of the shroud boundary–layer region increases as E decreases. In this region, there was a large velocity gradient from zero at the stationary shroud to the disk speed at its tip. The results suggest that the axisymmetric assumption is not valid near the outer shroud where the flow is highly turbulent and three–dimensional.

Further parameter studies showed that increasing the gap ratio results in the decrease in the number of vortical structures in the outer region. Furthermore, they also showed that increasing the rotation rate results generally in a decrease in the number of vortical structures.

Herrero, Humphrey and Giralt (1994) conducted a numerical study using a primitive variable formulation to solve for axisymmetric laminar flow and heat transfer between corotating disks with both rotating and stationary outer casings. The authors used a staggered–grid, control volume discretisation approach to derive finite difference forms of the equations. The time integration was performed using a second–order accurate Runge–Kutta scheme. The range of the Reynolds numbers in both cases was $3.7 \times 10^3 \leq Re \leq 1.8 \times 10^4$. They showed that for the stationary shroud case with isothermal boundary conditions, there is a symmetric flow structure about the axial mid–plane. In the non–isothermal case where there exists a temperature difference between the disks, the symmetric flow structure breaks down, and the degree of asymmetry increases with increasing temperature

difference.

Wilson, Arnold, Lewis, Mirzaee, Rees and Owen (1997) investigated numerically the flow and heat transfer between contra–rotating disks with a stationary shroud. They presented results, in particular, for an axisymmetric steady state code and showed that for a Reynolds number (Re) of 10^4 and gap ratio of 0.3, the solution residual reduced to a minimum point where the secondary flow was shown to be symmetric about the mid–axial plane. Further iterations then displayed an increase in the residuals until they became oscillatory. The secondary flow, was shown to be asymmetric, with the left and right toroidal vorticies alternating in dominance. They concluded therefore that the axisymmetric flow was likely to be unsteady.

2.4.2 Cavity with peripheral flow

Gan, Mirzaee, Owen, Rees and Wilson (1996) studied the cavity with stationary shroud with a superimposed peripheral flow using both experimental and numerical approaches. They suggested that the stationary outer casing creates a secondary recirculation in the cavity which in turn creates a Rankine vortex in which,

$$\frac{v}{\Omega r} = Ax^{-2} + B, \tag{2.6}$$

where A and B are invariant with x, the non–dimensional radial coordinate, r is the dimensional radial coordinate and v the dimensional tangential velocity in a stationary frame. Incompressible flow calculations were carried out using an axisymmetric finite–volume solver for the discretised forms of the steady–flow, Reynolds averaged Navier–Stokes and energy equations. They also utilised a low–

Reynolds number k–ϵ turbulence model. They found that the measured values of tangential velocity in the core conformed to a Rankine vortex. However, poor agreement between some of the computed and measured velocities was evident, which was attributed to the deficiencies of the turbulence model. The computed and measured values of radial velocity do however confirm the recirculating nature of the secondary flow. The associated heat transfer is presented in Mirzaee, Gan, Wilson and Owen (1997).

Mirzaee (1997) studied numerically the flow and heat transfer in a rotating cavity with peripheral flow. Two different outer shroud geometries were tested: the flat shroud and the stepped shroud cases. For the flat shroud case, in an attempt to improve the agreement between computed and measured velocities, he made modifications to the computational model. He concluded that none of the corrections produced satisfactory comparisons. For the stepped shroud case, no velocity measurements were available, however, he was able to make heat transfer comparisons. He concluded that for the majority of the cases considered, the agreement between computed and experimental Nusselt numbers was very good. Mirzaee suggested from his findings, particularly pertaining to the flat shroud case, that the flow may be three–dimensional and time–dependent.

2.5 Numerical methods

Various formulations may be used for the Navier–Stokes equations. In particular, the three–dimensional formulations for the equations are considered in this section. Vorticity–velocity formulations are reviewed in particular for both two–dimensional and three–dimensional problems, both of which require grid–

staggering strategies.

Stella, Guj, Leonardi and de Vahl Davis (1988) compared the vorticity–velocity and vorticity–vector potential formulations in three dimensions. They commented that the boundary conditions for the vector potential formulation required special attention, however, the equation of continuity is satisfied without the need to stagger the mesh. They utilised a staggered grid for the vorticity–velocity formulation, with the velocities located at the centre of the faces which are normal to the velocity vector. The vorticity components were located at the mid–point of the edge of the cube, parallel to the corresponding axis. The temperature was located at the centre of the cube faces. Results were obtained for the problem of natural convection in a rectangular cavity. They showed the equivalence of the two formulations and concluded that the vorticity–velocity formulation ran approximately $20 - 30\%$ slower than the vorticity–vector potential code.

A MAC–type (Marker and Cell) staggering scheme was suggested by Guj and Stella (1988). In two dimensions the vorticity is located at the intersection of the reference grid lines with the velocities located at the centre of the cell sides which are normal to the corresponding velocity vector. They utilised an alternating direction implicit procedure to integrate in time the governing equations and applied it to the driven cavity and backward facing step test cases. Comparisons with the standard streamfunction–vorticity and primitive variable formulations show excellent agreement provided an equivalent second–order spatial approximation is utilised.

A numerical method for solving the steady–state vorticity–velocity form of the Navier–Stokes equations in two and three–dimensions was presented by Napoli-

tano and Pascazio (1991). For the three–dimensional case they suggested a grid–staggering approach as presented above by Guj and Stella (1988) in order to better satisfy continuity. They solved the driven–cavity problem in both two and three–dimensions.

Huang and Li (1997) investigated finite difference approximations for the vorticity–velocity formulation on staggered and non–staggered grids. They considered four different grid layouts, from a MAC staggering through to semi–staggered and non–staggered grid layouts. Asymptotic error analysis and numerical experiments pertaining to the two–dimensional driven cavity problem were used to show that the MAC grid gives the best results in that the errors are smaller. They also concluded that a non–staggered grid may be used provided that the mesh is fine enough or higher–order discretisations are employed. Integration in time also suggested that the numerical solution does not drift away from the exact solution.

Shen and Loc (1997) presented a finite difference method to solve the three–dimensional Navier–Stokes equations in vorticity–velocity form. They utilised a semi–implicit Adams–Bashforth Crank–Nicolson scheme to advance the solution in time. They utilised a staggered grid with the collocation points for unknown velocities located at the centre of the cube edges parallel to the corresponding velocity vector with the vorticity components located directly at the centre of the cuboidal faces, normal to the corresponding vorticity vector. The spatial discretisation took the form of a standard second–order centred difference scheme. Numerical results were obtained for flow around a cube and sphere and compared with a velocity–pressure formulation and experimental data respectively with the comparisons showing satisfactory agreement.

Chapter 3

2D axisymmetric radial/axial flow

3.1 Summary

First, an axisymmetric cavity is considered. A schematic of the configuration may be seen in Figure 1.4. The cavity is sealed and all surfaces rotate at a uniform angular velocity. The outer cylindrical shroud of the cavity is assumed to be uniformly hot whilst the inner cylindrical hub is assumed to be uniformly cool. The disk surfaces are taken to be adiabatic. This configuration is analogous in many ways to that of a stationary cavity in a gravitational field where Bénard cell structures arise. Here, the buoyancy force is due to centrifugal force effects, whilst for the stationary case, the buoyancy force is due to gravitational field effects.

A Linear Stability Theory is first used to obtain neutral stability curves for instability in the form of toroidal vortices. The effect on the critical Rayleigh number of varying the wavenumber, Reynolds number and inner radius is investigated.

The non–linear computations give further insight into the roles of the various non–dimensional parameters for various geometries, although it will be shown later that this is not the preferred mode of convection. It is however useful as a validation aid for the full three–dimensional computations which follow.

3.2 Governing equations

Flow in a rotating cavity may be described by the continuity and Navier–Stokes equations for unsteady three–dimensional flow of an incompressible fluid. The governing equations may be written in a rotating frame of reference where the circumferential velocity (v), polar angle (θ) and time variables (t) are given by,

$$v = v^* + \Omega r, \tag{3.1}$$

$$\theta = \theta^* + \Omega t, \tag{3.2}$$

$$t = t^*, \tag{3.3}$$

where * denote quantities relative to a rotating frame of reference. A further simplification is made by assuming that the density, ρ, depends linearly on the temperature, T, and not on the pressure – this is similar to the Boussinesq approximation and therefore we take,

$$\rho = \rho_0(1 - \beta(T - T_c)), \tag{3.4}$$

where $\beta(T - T_c) << 1$ would correspond to the Boussinesq approximation. It is assumed that in the Coriolis and centrifugal terms, (3.4) holds but that the density is constant elsewhere. Buoyancy and Coriolis terms are thus incorporated into the dimensional governing equations with coupling now present between the

temperature and momentum equations. The flow is assumed to be axisymmetric and therefore we set,

$$\frac{\partial}{\partial\theta} = 0. \tag{3.5}$$

The tangential momentum equation, however, is maintained with the pressure term neglected. Dropping the asterisks introduced in (3.1)–(3.3), the continuity, momentum and energy governing equations in a rotating frame of reference are given by,

$$\frac{\partial u}{\partial r} + \frac{1}{r}u + \frac{\partial w}{\partial z} = 0, \tag{3.6}$$

$$\frac{\partial u}{\partial t} + (\underline{u}.\nabla)u - \frac{v^2}{r} - \frac{\rho}{\rho_0}(2\Omega v + \Omega^2 r) = -\frac{1}{\rho_0}\frac{\partial P}{\partial r} + \nu(\nabla^2 u - \frac{u}{r^2}), \tag{3.7}$$

$$\frac{\partial v}{\partial t} + (\underline{u}.\nabla)v + \frac{uv}{r} + \frac{\rho}{\rho_0}(2\Omega u) = \nu(\nabla^2 v - \frac{v}{r^2}), \tag{3.8}$$

$$\frac{\partial w}{\partial t} + (\underline{u}.\nabla)w = -\frac{1}{\rho_0}\frac{\partial P}{\partial z} + \nu\nabla^2 w, \tag{3.9}$$

$$\frac{\partial T}{\partial t} + (\underline{u}.\nabla)T = \kappa\nabla^2 T, \tag{3.10}$$

where the 2–D divergence and Laplace operators are given respectively by,

$$(\underline{u}.\nabla) = u\frac{\partial}{\partial r} + w\frac{\partial}{\partial z}, \qquad \nabla^2 = \frac{\partial^2}{\partial r^2} + \frac{1}{r}\frac{\partial}{\partial r} + \frac{\partial^2}{\partial z^2}.$$

A streamfunction–vorticity formulation is utilised to overcome the difficulties arising from having to determine the pressure boundary values associated with a primitive variable formulation. The streamfunction–vorticity form is also used in preference to the vorticity–velocity formulation as the latter requires about 50% more operations due to the presence of an additional Poisson equation. It is also necessary to use a staggered grid in order to obtain divergence–free velocity and vorticity fields, thus, further reducing the efficiency of the resulting code.

The vorticity, ω, is therefore introduced in order to eliminate the pressure terms

by taking the curl of equations (3.7) and (3.9) where,

$$\omega = \frac{\partial u}{\partial z} - \frac{\partial w}{\partial r}. \tag{3.11}$$

The streamfunction, ψ, is introduced, satisfying the continuity equation exactly where,

$$u = \frac{1}{r}\frac{\partial \psi}{\partial z}, \qquad w = -\frac{1}{r}\frac{\partial \psi}{\partial r}, \tag{3.12}$$

and is rescaled for convenience using,

$$\psi = r\phi.$$

Non–dimensionalisation is undertaken using the substitutions,

$$r = R\bar{r}, \qquad z = R\bar{z}, \qquad v = \frac{\kappa}{R}\bar{v}, \qquad t = \frac{R^2}{\kappa}\bar{t},$$

$$\omega = \frac{\kappa}{R^2}\bar{\omega}, \qquad \phi = \kappa\bar{\phi}, \qquad \bar{T} = \frac{T - T_c}{T_h - T_c},$$

where over–bars denote non–dimensional variables and T_h and T_c are the temperatures of the hot and cold walls respectively. The characteristic length scale, R, is taken to be the outer radius of the cavity and the characteristic vorticity, streamfunction velocity and time scales are based on κ, the thermal diffusivity of the medium within the cavity. The rotational Rayleigh, rotational Reynolds and Prandtl numbers are also introduced and are given by,

$$Ra = \frac{R\Omega^2\beta(T_h - T_c)R^3}{\nu\kappa}, \qquad Re = \frac{\Omega R^2}{\nu}, \qquad Pr = \frac{\nu}{\kappa}.$$

Dropping the over–bar notation, the non–dimensional form of the governing equations is given by,

$$\omega = \nabla^2\phi - \frac{1}{r^2}\phi, \tag{3.13}$$

$$\frac{1}{Pr}\Big[\frac{\partial \omega}{\partial t} + J(\omega,\phi) - \frac{1}{r}(\phi\frac{\partial \omega}{\partial z} + \omega\frac{\partial \phi}{\partial z}) - \frac{2v}{r}\frac{\partial v}{\partial z}\Big] - 2Re\frac{\partial v}{\partial z} + \frac{2Ra}{RePr}(T\frac{\partial v}{\partial z} + v\frac{\partial T}{\partial z})$$

$$+rRa\frac{\partial T}{\partial z} = \nabla^2\omega - \frac{1}{r^2}\omega, \tag{3.14}$$

$$\frac{1}{Pr}\Big[\frac{\partial v}{\partial t} + J(v,\phi) + \frac{1}{r}(v\frac{\partial \phi}{\partial z} - \phi\frac{\partial v}{\partial z})\Big] + 2Re\frac{\partial \phi}{\partial z} - \frac{2Ra}{RePr}T\frac{\partial \phi}{\partial z} = \nabla^2 v - \frac{1}{r^2}v, \tag{3.15}$$

$$\frac{\partial T}{\partial t} + J(T,\phi) - \frac{1}{r}\phi\frac{\partial T}{\partial z} = \nabla^2 T, \tag{3.16}$$

where the Jacobian is given by,

$$J(A,B) = \frac{\partial A}{\partial r}\frac{\partial B}{\partial z} - \frac{\partial B}{\partial r}\frac{\partial A}{\partial z}.$$

Both the rotational Reynolds and Rayleigh numbers appear in the governing equations. The Reynolds number multiplies the Coriolis terms and the Rayleigh number the buoyancy term. The buoyancy correction to the Coriolis force terms are multiplied by a $\frac{2Ra}{RePr}$ factor. The effect of these terms will be considered and discussed in detail. The Prandtl number is a combination of fluid properties, and is related to the ratio of the thermal and viscous diffusivities. It does not change significantly with temperature variations and is assumed to be constant for the purposes of this investigation. Note that,

$$\frac{Ra}{RePr} = Re\beta\Delta T, \tag{3.17}$$

and therefore the buoyancy correction to the Coriolis force is negligible when the Boussinesq approximation is valid (i.e. when $\beta\Delta T << 1$). The factor $\beta\Delta T$ which occurs in (3.17) must also be less than 1 since, from (3.4), this would result in negative fluid densities.

3.3 Boundary conditions

The cavity is assumed sealed with no slip boundaries, adiabatic disks, heated shroud and cooled hub. The following boundary conditions are therefore prescribed:

At the heated shroud, $r = 1$, the boundary conditions are that,

$$\phi = 0, \qquad \frac{\partial \phi}{\partial r} = 0, \qquad v = 0, \qquad T = 1.$$

At the cooled hub, $r = r_0$, the boundary conditions are that,

$$\phi = 0, \qquad \frac{\partial \phi}{\partial r} = 0, \qquad v = 0, \qquad T = 0.$$

At the disks, $z = 0, z_{\max}$, the boundary conditions are that,

$$\phi = 0, \qquad \frac{\partial \phi}{\partial z} = 0, \qquad v = 0, \qquad \frac{\partial T}{\partial z} = 0.$$

It is noted that Ra, Re, Pr, r_0 and $z_{\max}$ are all parameters to vary.

3.4 Linear stability theory

3.4.1 Stability equations

Linear stability theory (LST) is used to ascertain the conditions required for the flow to convect strongly, becoming unstable to infinitesimal disturbances. Here, a base solution of the equations of motion is assumed corresponding to the non–convecting state of zero flow in the cavity with a temperature field corresponding

to that due to pure conduction where,

$$v_B = 0, \qquad \phi_B = 0, \qquad \omega_B = 0, \qquad T_B = g(r) = 1 - \frac{\ln r}{\ln r_0}. \tag{3.18}$$

Where $_B$ denotes base solution quantities. The perturbations are therefore given by,

$$v = v_B + \hat{v}, \qquad \phi = \phi_B + \hat{\phi}, \qquad \omega = \omega_B + \hat{\omega}, \qquad T = T_B + \hat{T}. \tag{3.19}$$

All the terms involving the square of the perturbation amplitudes are neglected thus linearising the perturbation equations. Due to the linearity, no interactions occur between different Fourier components, and thus the perturbation components may be written in the form,

$$\begin{pmatrix} \hat{v} \\ \hat{T} \\ \hat{\phi} \\ \hat{\omega} \end{pmatrix} = e^{\lambda t} \begin{pmatrix} \hat{v}(r)\cos(kz) \\ \hat{T}(r)\cos(kz) \\ \hat{\phi}(r)\sin(kz) \\ \hat{\omega}(r)\sin(kz) \end{pmatrix}, \tag{3.20}$$

where k is the wavenumber and λ is the complex temporal growth rate where,

$$\lambda = \lambda_R + j\lambda_I. \tag{3.21}$$

A temporal growth rate of greater than zero (i.e. $\lambda_R > 0$) corresponds to an exponential growth in the disturbance. A negative value of λ_R means that the base solution is stable to all infinitesimal disturbances. The solution for $\lambda_R = 0$ is therefore of interest in order to determine the conditions for this transition to take place. Due to the instability being stationary and steady–state, the imaginary part of the temporal growth rate is taken as, $\lambda_I = 0$. The resulting perturbation ordinary differential equations are given by,

$$\hat{\omega} = \hat{\phi}'' + \frac{1}{r}\hat{\phi}' - k^2\hat{\phi} - \frac{1}{r^2}\hat{\phi}, \tag{3.22}$$

$$\Big[(2Re) - (\frac{2Ra}{RePr})g(r)\Big]k\hat{v} - (rRa)k\hat{T} = \hat{\omega}'' + \frac{1}{r}\hat{\omega}' - k^2\hat{\omega} - \frac{1}{r^2}\hat{\omega}, \tag{3.23}$$

$$\Big[(2Re) - (\frac{2Ra}{RePr})g(r)\Big]k\hat{\phi} = \hat{v}'' + \frac{1}{r}\hat{v}' - k^2\hat{v} - \frac{1}{r^2}\hat{v}, \tag{3.24}$$

$$-\Big(\frac{1}{r\ln r_0}\Big)k\hat{\phi} = \hat{T}'' + \frac{1}{r}\hat{T}' - k^2\hat{T}. \tag{3.25}$$

The above is a 9^{th} order eigenvalue problem in Ra as a function of both Re and k and are solved satisfying the boundary conditions:

At the cooled hub, $r = r_0$, the initial boundary conditions are that,

$$\hat{\phi} = 0, \qquad \hat{\phi}' = 0, \qquad \hat{v} = 0, \qquad \hat{T} = 0. \tag{3.26}$$

At the heated shroud, $r = 1$, the final boundary conditions are that,

$$\hat{\phi} = 0, \qquad \hat{\phi}' = 0, \qquad \hat{v} = 0, \qquad \hat{T} = 0. \tag{3.27}$$

The additional initial normalising condition at $r = r_0$ is also required and is taken as,

$$\hat{T}' = 1. \tag{3.28}$$

A more complete parameter investigation may be obtained if the equations are minimised over the wavenumber where,

$$\frac{\partial Ra}{\partial k} = 0.$$

Minimising equations (3.22)–(3.25) over k results in an 18^{th} order system with Ra and k being eigenvalues as a function of Re and r_0. The following additional equations therefore require to be solved simultaneously,

$$\underline{\omega} = \underline{\phi}'' + \frac{1}{r}\underline{\phi}' - k^2\underline{\phi} - 2k\underline{\phi} - \frac{1}{r^2}\underline{\phi}, \tag{3.29}$$

$$\Big[(2Re) - (\frac{2Ra}{RePr})g(r)\Big](k\underline{v} + \hat{v}) - (rRa)(k\underline{T} + \hat{T}) = \underline{\omega}'' + \frac{1}{r}\underline{\omega}' - k^2\underline{\omega} - 2k\hat{\omega} - \frac{1}{r^2}\underline{\omega}, \tag{3.30}$$

$$\Big[(2Re) - (\frac{2Ra}{RePr})g(r)\Big](k\underline{\phi} + \hat{\phi}) = \underline{v}'' + \frac{1}{r}\underline{v}' - k^2\underline{v} - 2k\hat{v} - \frac{1}{r^2}\underline{v}, \tag{3.31}$$

$$-\Big(\frac{1}{r\ln r_0}\Big)(k\underline{\phi} + \hat{\phi}) = \underline{T}'' + \frac{1}{r}\underline{T}' - k^2\underline{T} - 2k\hat{T}. \tag{3.32}$$

where,

$$\underline{\omega} = \frac{\partial\hat{\omega}}{\partial k}, \qquad \underline{\phi} = \frac{\partial\hat{\phi}}{\partial k}, \qquad \underline{v} = \frac{\partial\hat{v}}{\partial k}, \qquad \underline{T} = \frac{\partial\hat{T}}{\partial k}.$$

At the cooled hub, $r = r_0$, the additional initial boundary conditions are that,

$$\underline{\phi} = 0, \qquad \underline{\phi}' = 0, \qquad \underline{v} = 0, \qquad \underline{T} = 0. \tag{3.33}$$

At the heated shroud, $r = 1$, the final additional boundary conditions are that,

$$\underline{\phi} = 0, \qquad \underline{\phi}' = 0, \qquad \underline{v} = 0, \qquad \underline{T} = 0. \tag{3.34}$$

3.4.2 Solution methods

The system of equations are reduced to first order form and the eigenvalues obtained using a fourth–order Runge Kutta scheme allied with the shooting method, which involves a multi–dimensional Newton–Raphson iteration scheme and Gaussian elimination.

3.4.3 Results

All solutions are obtained assuming air to be the medium within the cavity for which the Prandtl number is taken to be, $Pr = 0.7$.

Solutions for $\frac{Ra}{RePr} = 0$

Here, the ratio $\frac{Ra}{RePr}$ is assumed to be negligible and given that $\frac{Ra}{RePr} = Re\beta\Delta T$, this case corresponds to when $\beta\Delta T << 1$, i.e. for which the Boussinesq approximation applies, and the buoyancy correction to the Coriolis force is negligible. Buoyancy is not zero when $\beta\Delta T << 1$. Only the buoyancy correction to the Coriolis force. Figure 3.1 displays neutral stability curves for various Reynolds and wavenumbers $r_0 = 0.5$, which were obtained by solving equations (3.22)–(3.25) subject to boundary conditions (3.26)–(3.28). An increase in the Reynolds number causes an increase in the critical Rayleigh number, and this is consistent with the damping effect of the Coriolis force reported by previous authors. A large increase in the critical Rayleigh number for a given Reynolds number is also apparent for small wavenumbers in particular, where the relationship between the wavenumber and the wavelength, λ_W, is given by,

$$\lambda_W = \frac{2\pi}{k}.$$

Figure 3.2 displays neutral stability curves for $1000 \leq Re \leq 5000$. The same trends are again apparent, but it should be noted that the minimum Rayleigh number for the onset of convection occurs at decreasing wavenumbers, (increasing wavelengths), when Re increases. Results for $10000 \leq Re \leq 50000$ are presented in Figure 3.3 and show further evidence of this trend, with increase in the Reynolds number damping the instability. For large Reynolds numbers, the minimum critical Rayleigh numbers is also large, (e.g.for $Re = 50000$, $Ra_{crit} \approx 7 \times 10^9$).

Figures 3.4–3.6 display neutral stability curves for various Reynolds numbers and

wavenumbers for $r_0 = 0.3$. Comparison with the $r_0 = 0.5$ results suggests that decreasing the inner radius has a stabilising effect, (for $Re = 50000$, $Ra_{crit} \approx 1.2 \times 10^{10}$). However, for a more complete parameter investigation, equations (3.22)–(3.25) and (3.29)–(3.32) are solved subject to boundary conditions (3.26)–(3.28) and (3.33)–(3.34). Figure 3.7 displays neutral stability curves where Ra_{crit} has been minimised over k for various Reynolds numbers and inner radii. Again, the damping effect of the Coriolis force is apparent but the effect of varying r_0 is also displayed here. Generally, for increasing r_0 there is a decrease in Ra_{crit} until a turning point is apparent at approximately $0.7 \leq r_0 \leq 0.8$. Values of Ra_{crit} thereafter increase sharply suggesting that when the inner radius approaches the outer radius, no convective state exists. Figure 3.8 shows neutral stability curves for $1000 \leq Re \leq 5000$. The turning point here, occurs at approximately $r_0 \approx 0.9$. Further increase in the range of Reynolds number is displayed in Figure 3.9. Here again, the turning point occurs at increasing inner radii. The damping effects of the Reynolds number is therefore more effective at either small inner radii or for $r_0 \to 1$.

Scaling the Rayleigh number on the gap length scale, $R - a$, using the following relation,

$$Ra_{gap} = Ra \times \left(1 - r_0\right)^3.$$

where,

$$Ra = \frac{(R\Omega^2)\beta(T_h - T_c)R^3}{\nu\kappa}, \qquad Ra_{gap} = \frac{(R\Omega^2)\beta(T_h - T_c)(R-a)^3}{\nu\kappa},$$

and extrapolating to the limit $r_0 \to 1$ for a range of Re, (see Figure 3.10), it is found that onset of convection occurs at $Ra = 1707.8$. The configuration is analogous to the first onset of convection in a stationary cavity in a gravitational

field with a heated bottom wall and a cooled upper wall with no end effects (Koschmieder, 1993). The onset of convection in this stationary configuration is predicted to occur at $Ra_{gap} = 1707.8$ as shown in Table 2.1. There is therefore good confidence in the numerical procedure.

Solutions for non–zero values of $\frac{Ra}{RePr}$

Here we consider flows for which $\beta\Delta T \neq 0$ and hence the buoyancy correction to the Coriolis force is significant.

Figure 3.11 displays neutral stability curves for non–zero $\frac{Ra}{RePr}$ and $200 \leq Re \leq 500$. Direct comparison with the small $\frac{Ra}{RePr}$ results displays significantly reduced stability levels. The form of the curves are however largely unchanged, with increases in Ra_{crit} at small and large wavenumbers apparent. Figure 3.12 displays results for larger Re numbers which again display reduced stability levels when compared with the solutions obtained under the small $\frac{Ra}{RePr}$ assumption. The form of the curves is now modified with no well–defined minimum point apparent. For a given Reynolds number, Ra_{crit} is approximately constant for $k > 5$ over the range of wavenumbers computed. The effect of further increases in the Reynolds number is presented in Figure 3.13. Once again, the almost constant nature of Ra_{crit} is apparent with reduced stability levels from direct comparison with the small $\frac{Ra}{RePr}$ solutions. The buoyancy correction to the Coriolis force therefore has a destabilising effect which opposes the stabilising effect of the Coriolis force at the onset of convecting flow.

Further solutions for $r_0 = 0.3$ are presented under the assumption of non–zero values of $\frac{Ra}{RePr}$ in Figures 3.14–3.16. Again, values of Ra_{crit} are approximately one

tenth of the corresponding values under the assumption of small $\frac{Ra}{RePr}$. It is noted that in Figure 3.14, the neutral stability curves for $Re = 400$ and $Re = 500$ intersect at the larger values of wavenumber computed. The neutral stability curves for smaller Reynolds numbers also suggest the same trend, but solutions were very difficult to obtain using the available solution procedure for large wavenumbers. Figures 3.15–3.16 again display an approximately constant critical Rayleigh number over a large range of values of k. Comparison with the $r_0 = 0.5$ calculations shows relatively small increases in Ra_{crit} as the Reynolds number increases. This suggests that the larger variations in Ra_{crit} with r_0 are greatly exaggerated under the assumption of small $\frac{Ra}{RePr}$.

Solutions to equations (3.22)–(3.25) and (3.29)–(3.32) under the non–zero $\frac{Ra}{RePr}$ assumption could not always be successfully obtained using the shooting method code. The reasons for this were not clearly identified but may very well be associated with the growth of unwanted parasitic (i.e. exponentially growing) eigensolutions.

3.5 Non–linear computations

3.5.1 Finite difference approximations

The system of partial differential equations (3.13)–(3.16) is solved numerically using a finite difference scheme on a collocated uniform grid. Finite difference approximations (FDA) are utilised which are second–order accurate in space. These approximations are based on Taylor–Series expansions and their derivation is generally well known, (Wendt, 1992) and will not be repeated here. They

have been used in preference to finite–volume approximations due to the simplicity of application associated with them. Solutions on uniform grids only are presented here, and therefore the first and second derivative central difference approximations for typical variable ζ are given by,

$$\frac{\partial \zeta}{\partial x} \approx \frac{\zeta_{i+1} - \zeta_{i-1}}{2\delta x}, \qquad \frac{\partial^2 \zeta}{\partial x^2} \approx \frac{\zeta_{i+1} - 2\zeta_i + \zeta_{i-1}}{\delta x^2}$$

where x is a representative independent variable. The grid is defined by $x_i = i\delta x$ where δx is the constant step length, and ζ_i is the numerical approximation to $\zeta(x_i)$. In general ζ will be a function of time and either two or three spatial variables.

The advective, non–linear terms in the equations are evaluated using the Arakawa formulation (Arakawa, 1966). This method overcomes non–linear instabilities associated with other central difference approximations for the Jacobian. The mean vorticity, mean kinetic energy and mean square vorticity is conserved in time by combining three different approximations to the Jacobian and is given by,

$$\begin{aligned} J(A,B) = \frac{\partial A}{\partial x}\frac{\partial B}{\partial y} - \frac{\partial B}{\partial x}\frac{\partial A}{\partial y} = \Big[\frac{1}{12\delta x \delta y}\Big]\Big[&(A_{i+1,j} - A_{i-1,j})(B_{i,j+1} - B_{i,j-1}) \\ &-(A_{i,j+1} - A_{i,j-1})(B_{i+1,j} - B_{i-1,j}) \\ &+(A_{i+1,j})(B_{i+1,j+1} - B_{i+1,j-1}) - (A_{i-1,j})(B_{i-1,j+1} - B_{i-1,j-1}) \\ &-(A_{i,j+1})(B_{i+1,j+1} - B_{i-1,j+1}) + (A_{i,j-1})(B_{i+1,j-1} - B_{i-1,j-1}) \\ &+(B_{i,j+1})(A_{i+1,j+1} - A_{i-1,j+1}) - (B_{i,j-1})(A_{i+1,j-1} - A_{i-1,j-1}) \\ &-(B_{i+1,j})(A_{i+1,j+1} - A_{i+1,j-1}) + (B_{i-1,j})(A_{i-1,j+1} - A_{i-1,j-1})\Big] \end{aligned}$$

where the grid is defined by $x_i = i\delta x$ and $y_j = j\delta y$. This formulation is easier to

implement and less numerically diffusive than upwinding schemes for example, whilst retaining second–order accuracy. One drawback however, is that it may only be applied to uniform grids in its present form. Its application to non–uniform meshes has not been investigated and is beyond the scope of this thesis.

3.5.2 Finite difference approximations at the boundaries

The vorticity, ω, is defined at the boundaries in terms of the streamfunction, ϕ. For example, at the $r = 0$ boundary,

$$\omega_{0,j} = \frac{\partial^2 \phi}{\partial r^2}\Big|_{0,j}. \tag{3.35}$$

In central–finite difference (second–order accurate) form,

$$\omega_{0,j} \approx \frac{\phi_{1,j} - 2\phi_{0,j} + \phi_{-1,j}}{\delta r^2} \tag{3.36}$$

However, since $\frac{\partial \phi}{\partial r} = 0$, it may be shown that $\phi_{-1,j} = \phi_{1,j}$. Noting that $\phi_{0,j} = 0$, the vorticity at the $r = 0$ boundary may now be expressed in terms of ϕ on internal points only, and is given by,

$$\omega_{0,j} \approx \frac{2\phi_{1,j}}{\delta r^2}. \tag{3.37}$$

The other problematic boundary condition is that for the adiabatic temperature distribution on the disks, where

$$\frac{\partial T}{\partial z} = 0. \tag{3.38}$$

In central–finite difference form it may be shown that,

$$T_{i,j-1} = T_{i,j+1}. \tag{3.39}$$

This definition is used in conjunction with the FDA of the full equations at the disk boundaries in order to determine the adiabatic disk temperatures.

3.5.3 Transient method

The time–dependent vorticity, tangential velocity and energy equations are arranged explicitly using second–order accurate FDA to the time derivatives. The well–known Du–Fort Frankel method is used, where values of the dependent variable are substituted by averages of previous and new time values. For example, Fourier's two–dimensional equation in cartesian coordinates,

$$\frac{\partial \zeta}{\partial t} = \frac{\partial^2 \zeta}{\partial x^2} + \frac{\partial^2 \zeta}{\partial y^2}, \tag{3.40}$$

is rewritten in finite difference form as,

$$\zeta_{i,j}^{n+1}\left[\frac{1}{2\delta t} + \frac{1}{\delta x^2} + \frac{1}{\delta y^2}\right] = \zeta_{i,j}^{n-1}\left[\frac{1}{2\delta t} - \frac{1}{\delta x^2} - \frac{1}{\delta y^2}\right] + \frac{\zeta_{i+1,j}^{n} + \zeta_{i-1,j}^{n}}{\delta x} + \frac{\zeta_{i,j+1}^{n} + \zeta_{i,j-1}^{n}}{\delta y}. \tag{3.41}$$

This method is unconditionally stable for the one, two and three–dimensional Fourier's equation. A great advantage of the Du–Fort Frankel method is that it is technically an implicit method, but that it may be encoded as an explicit scheme, thereby combining the advantages of both implicit and explicit schemes. On the other hand the Crank–Nicholson method, which is frequently used for problems similar to that of (3.40), requires iteration at each timestep and iterative convergence is not guaranteed for non–linear equations.

The maximum timestep for stability is dependent on many factors. Of particular importance and interest is the dependence on grid size. To show this, the following test equation (Fourier's equation in one dimension) is considered,

$$\frac{\partial \zeta}{\partial t} = \frac{\partial^2 \zeta}{\partial x^2}, \tag{3.42}$$

subject to

$$0 \leq x \leq 1.$$

In finite difference form using a first–order forward–difference time approximation and a second–order central–difference spatial approximation, the above test equation may be rewritten as,

$$\frac{\zeta_i^{n+1} - \zeta_i^n}{\delta t} = \frac{\zeta_{i-1}^n - 2\zeta_i^n + \zeta_{i+1}^n}{\delta x^2}. \tag{3.43}$$

Rearranging the equation explicitly and assuming a solution of the form,

$$\zeta_i^n = A_n \sin(j\pi x_i), \tag{3.44}$$

where $0 \leq i \leq i_{max}$ and $0 < j < i_{max}$. It may be shown that for stability,

$$\delta t \leq \frac{\delta x^2}{2}. \tag{3.45}$$

A similar analysis for the Du–Fort Frankel method shows that it is unconditionally stable. However, when non–linear terms are added to the governing equations, the method loses this property. Factors which determine the stability limit on the timestep include, in particular, the magnitude of the non–dimensional rotational Rayleigh and Reynolds numbers. For the computation of steady–state flows using the above methods, the convergence criteria used is that $\max_i \left|\zeta_i^{n+1} - \zeta_i^n\right|$ should be less than some very small value. This was taken to be 10^{-6} and was found to

be adequate for all values of δt considered.

3.5.4 Multigrid method

The Poisson equation for the streamfunction, (3.13) is solved using a Multigrid (Correction Scheme) routine to accelerate iterative convergence. It incorporates V–cycling and a line relaxation scheme. The method is based on that described in Briggs (1987). The system of linear equations may be written in the form

$$Au = f, \tag{3.46}$$

where u is the exact solution of the FDA of the partial differential equation, A represents the finite difference operator and f is the right–hand–side function. If an approximate solution, v, is given then the error is expressed as,

$$e = u - v. \tag{3.47}$$

The residual, r, is a measure of the amount by which the approximation v fails to satisfy the system of equations and is defined by,

$$r = f - Av. \tag{3.48}$$

A very useful relationship between the error and the residual, known as the residual equation, may therefore be formed,

$$Ae = r. \tag{3.49}$$

Typical relaxation schemes possess what is known as the *smoothing property* which makes them very effective at eliminating high–frequency, oscillatory com-

ponents of the error, but they are far less effective at removing low–frequency, smooth components. On a coarse grid, the low–frequency errors from the point of view of the fine grid, look more oscillatory (i.e. are higher frequency errors) and therefore the *smoothing property* of the relaxation scheme is more effective on the coarse grid. This forms the basis of the Multigrid method where the residual equation is used to relax on the error on successively coarser grids.

For a two–level grid, with the fine grid having half the grid spacing of the coarse grid, the routine loosely follows the following strategy where superscripts denote the steplength corresponding to the grid being considered,

- Relax on $A^h u^h = f^h$ on Ω^h to obtain an approximation v^h,
- Compute the residual $r^h = f^h - A^h v^h$,
- Transfer (restrict) the residual from grid Ω^h to Ω^{2h}: $r^h \rightarrow r^{2h}$,
- Relax on the residual equation $A^{2h} e^{2h} = r^{2h}$ on Ω^{2h} to obtain an approximation to the error e^{2h},
- Transfer (prolong) the error from grid Ω^{2h} to Ω^h: $e^{2h} \rightarrow e^h$,
- Correct the approximation obtained on Ω^h with the error estimate obtained on Ω^{2h}: $v^h \rightarrow v^h + e^h$.

where Ω^h and Ω^{2h} define the fine and coarse grids respectively (h denotes the steplength). When the maximum residual, as defined in equation (3.48), falls below a suitably small limit (here we used a value of 10^{-6} since this gives highly accurate solutions of the difference equations), the procedure is deemed to have

converged. The prolongation operator is a straightforward linear interpolation routine given by $I_{2h}^{h}V^{2h} = V^{h}$, where

$$v_{2i,2j}^{h} = v_{i,j}^{2h}$$

$$v_{2i+1,2j}^{h} = \frac{1}{2}(v_{i,j}^{2h} + v_{i+1,j}^{2h})$$

$$v_{2i,2j+1}^{h} = \frac{1}{2}(v_{i,j}^{2h} + v_{i,j+1}^{2h})$$

$$v_{2i+1,2j+1}^{h} = \frac{1}{4}(v_{i,j}^{2h} + v_{i+1,j}^{2h} + v_{i,j+1}^{2h} + v_{i+1,j+1}^{2h}) \tag{3.50}$$

The restriction operator takes the form of a full weighting routine defined by $I_{h}^{2h}V^{h} = V^{2h}$, where

$$v_{i,j}^{2h} = \tfrac{1}{16}[(v_{2i+1,2j+1}^{h} + v_{2i-1,2j-1}^{h} + v_{2i+1,2j-1}^{h} + v_{2i-1,2j+1}^{h})$$

$$+2(v_{2i+1,2j}^{h} + v_{2i-1,2j}^{h} + v_{2i,2j+1}^{h} + v_{2i,2j-1}^{h}) + 4v_{2i,2j}^{h}]. \tag{3.51}$$

The alternative would be to utilise an injection operator, where the coarse grid value is taken directly from the corresponding fine grid point – such a method, though more straightforward to encode, results in a slightly less efficient algorithm.

The relaxation procedure utilised to solve for the approximation v and the error e is a straightforward line relaxation procedure. It uses the most recent approximation in order to calculate the new approximation. Sweeps are performed on the matrix of equations, which are in FDA form, in both radial and axial directions per relaxation procedure. Two relaxation procedures are undertaken on each level before moving on to either finer or coarser grids. The matrix is in tri–diagonal form for the radial/axial flow case, and is solved using a tri–diagonal matrix algorithm (TDMA). The details of the TDMA or Thomas algorithm is

generally well known and will not be repeated here.

3.5.5 Heat transfer

The heat transfer through the outer heated cylindrical surface into the fluid and out of the fluid through the cold inner cylindrical surface is evaluated in terms of a non–dimensional heat transfer value known as the Nusselt number, Nu. Two forms are defined, namely an average (total) or local heat transfer rate. The Nusselt number is defined as the ratio of heat transfer due to convection and conduction to that due to conduction alone and is given by,

$$Nu = \frac{\dot{q}}{\dot{q}_\lambda}, \tag{3.52}$$

where λ pertains to conduction quantities and the local rate of heat transfer is defined as,

$$\dot{q}_{local} = \frac{K\Delta T}{R}\frac{\partial T}{\partial r}. \tag{3.53}$$

The local Nusselt number is therefore given by,

$$Nu_{local} = -r\ln(r_0)\frac{\partial T}{\partial r}, \tag{3.54}$$

at $r = r_0$ or $r = 1$. The average or total heat transfer is expressed as,

$$\dot{q}_{total} = \frac{K\Delta T}{R}\int_0^{2\pi}\int_0^{z_{max}}\frac{\partial T}{\partial r}dz\, r\, d\theta \tag{3.55}$$

and therefore the average Nusselt number is therefore given by,

$$Nu_0 = -\frac{r\ln(r_0)}{z_{max}}\int_0^{z_{max}}\frac{\partial T}{\partial r}dz, \tag{3.56}$$

at either $r = r_0$ or $r = 1$. The average or total Nusselt number may therefore not be smaller than one as the total heat transfer from a surface must always be equal to or exceed the average heat transfer due to conduction effects alone.

The integral quantity is evaluated using the trapezoidal rule with the differential being approximated at the boundaries using a fourth–order accurate finite difference representation. The use of second–order accurate approximation rendered the solution inaccurate particularly on coarse grids.

3.5.6 Code structure

The structure of the solver for one timestep is characterised by the following numerical procedure:

- Initialise all variables for time $t = t_0 = 0$.
- Solve for $\omega^{n+1}, v^{n+1}, T^{n+1}$ at $t = t_{n+1}$ using the n^{th} and $n-1^{st}$ solutions on all internal grid points. (It is assumed that the solution at $t = t_{-1}$ is the same as that at $t = t_0$ in order to initiate the solution procedure.)
- Solve for T^{n+1} on adiabatic surfaces.
- Solve implicitly using the Multigrid method for ϕ^{n+1} using ω^{n+1} on the right–hand–side.
- Update values of ω^{n+1} on the boundaries using ϕ^{n+1}.

3.6 Code validation

3.6.1 Comparison with stationary cavity in gravitational field

De Vahl Davis (1983) produced a bench–mark numerical solution for a buoyancy–driven flow in a square sealed stationary cavity in a gravitational field. The vertical sides are differentially heated and horizontal surfaces are adiabatic. Time–independent solutions were obtained for Rayleigh numbers of $10^3, 10^4, 10^5$ and 10^6 using a streamfunction–vorticity formulation. A time–dependent form of the equations were used and the solution advanced in time using the method of the false transient (Mallinson and de Vahl Davis (1973)) until a steady state was reached. First–order (forward) differences were used for the time derivatives and second–order accurate central differences were used for spatial derivatives. Uniform grids were used which allowed the use of the Richardson's extrapolation technique. Fourth–order accurate solutions could therefore be obtained by using solutions on two different meshes, the finer grid having half the grid spacing of the coarser.

In the limit as $r \rightarrow 1$ with $Re = 0$, the rotating cavity reduces to the stationary cavity in a gravitational field if the disks are now differentially heated and cylindrical surfaces assumed adiabatic. $\frac{Ra}{RePr}$ is assumed to be small and terms of this order are neglected for the purposes of this validation. The Rayleigh numbers given by de Vahl Davis are based on the height of the cavity or gap, and therefore, must be scaled to correspond to the current formulation using the following

scaling,

$$Ra_R = \frac{Ra_{gap}}{(1-r_0)^3}.$$

Figure 3.17 shows the variation of maximum, minimum and average Nusselt numbers with inner radius for $Ra_{gap} = 10^3$ at the heated wall. Nu_0, Nu_{max} and Nu_{min} vary linearly with inner radius. Linear extrapolation may therefore be utilised to obtain these values in the limit, $r \to 1$. Comparisons are made with de Vahl Davis (1983) results for $Ra = 10^3, 10^4, 10^5$ and 10^6 and are presented in Table 3.1.

Ra_{gap}	Nu_0			Nu_{max}			Nu_{min}		
	(a)	(b)	%err	(a)	(b)	%err	(a)	(b)	%err
10^3	1.118	1.117	0.09	1.506	1.505	0.07	0.691	0.692	0.14
10^4	2.246	2.238	0.36	3.532	3.528	0.11	0.586	0.586	0.00
10^5	4.511	4.509	0.04	7.696	7.717	0.27	0.730	0.729	0.14
10^6	8.833	8.817	0.18	17.926	17.925	0.01	0.984	0.983	0.10

Table 3.1: Comparison of average, maximum and minimum Nusselt numbers for various Rayleigh numbers: (a) Current computations (b) de Vahl Davis (1983)

Richardson's extrapolation is used to render the approximations fourth–order accurate for direct comparison with the results of de Vahl Davis,

$$\bar{y}_{2N} = \frac{2^\alpha y_{2N} - y_N}{2^\alpha - 1} \tag{3.57}$$

where $\bar{y}_{2N}$ is the fourth–order approximation, y_{2N} and y_N are the approximations on the finer and coarser grids respectively and α is the current order of accuracy of the method which is $\alpha = 2$. All but the $Ra = 10^6$ case were computed on 32×32 and 64×64 interval grids. The $Ra = 10^6$ case utilised 40×40 and 80×80 grids. All cases were computed for $r_0 = 0.8$ and $r_0 = 0.9$ and linearly extrapolated to the $r_0 \to 1$ limit.

There is good agreement between the computed results and those of de Vahl Davis

(1983). A relatively large discrepancy occurs for the maximum local Nusselt number for the $Ra = 10^5$ case. No extrapolation process is used to locate a more accurate location and thus obtain a more accurate approximation for Nu_{max} on the heated surface. De Vahl Davis (1983) did use such an extrapolation process and was not limited by grid resolution. Excellent agreement between the minimum Nusselt numbers is apparent since these are always located at the same vertical location, $\bar{y} = 1$. There is reasonable agreement between the average Nusselt numbers. Discrepancies may be due to de Vahl Davis (1983) use of the fourth–order accurate Simpson's rule, whilst the computations presented here, use the inferior second–order accurate trapezoidal rule to evaluate the integral. But since the basic data used in the integration is second–order accurate, both integrators yield second–order accurate results.

3.6.2 Comparison with linear stability theory results

As a further means of validating the numerical computations, a comparison is made with linear stability theory results for onset of convection. The trivial case, $Re = 0$, is chosen, where no Coriolis forces are present and the model is analogous to natural convection in a non–rotating enclosure where the only body force is that due to gravity. The onset of convection is predicted by the numerical model by considering the average heat transfer, Nu_0, for various Rayleigh numbers above that predicted by LST.

Extrapolating the Nu_0 versus Ra lines to $Nu_0 = 1$ gives an approximation to the Rayleigh number for onset. Figure 3.18 displays the predicted Rayleigh number required for the onset of convection on two meshes, the finer having half the

grid spacing of the coarser gird. Richardson's extrapolation technique is also used here in order to render the approximation fourth–order accurate, being analogous therefore with the LST treatment. The calculations are based on a cavity geometry of $r_0 = 0.5, z_{\max} = 0.50514$. The axial dimension is obtained from LST results such as to accommodate one single rotating cell corresponding to one half of a wavelength.

In the fully numerical simulation, the boundary conditions at $z = 0, z_{\max}$ correspond to periodic conditions and are,

$$\omega = \phi = 0, \qquad \frac{\partial T}{\partial z} = 0.$$

Linear stability theory suggests that convection first occurs at $Ra_{crit} = 19033$. The Ra_{crit} predicted by the numerical simulation technique bears good comparison with the LST treatment, being less than 0.25% in error. Calculations for $Ra = 20000$ could not easily be obtained as the run times became excessive for Rayleigh numbers just above that which gives onset of convection due to the very slow transient nature of the flow.

3.7 Initial conditions

At time $t = 0$, the initial conditions, satisfying the boundary conditions, are that,

$$\phi = 0, \qquad \omega = 0, \qquad v = 0, \qquad T = 1 - \frac{\ln r}{\ln r_0}. \tag{3.58}$$

This corresponds to solid body rotation and a conduction dominated temperature field which is an exact solution of equations (3.13)–(3.16). In order to perturb this

initial solution, a small point perturbation in the temperature field is introduced at $r = \frac{1}{4}(1 - r_0)$ and $z = \frac{1}{4}z_{max}$. At this location, the local temperature is modified and is given by,

$$T(\tfrac{1}{4}(1 - r_0), \tfrac{1}{4}z_{max}) = T_B(\tfrac{1}{4}(1 - r_0), \tfrac{1}{4}z_{max}) + 0.01. \tag{3.59}$$

If this modification were not introduced, the perturbation would eventually be introduced into the system by means of amplification of the round–off errors. This would however increase significantly the computational time.

A further method employed for initialisation of the computations, involved the input of the starting conditions from a previously saved file. For example, the solution from another computation was frequently used as the initial condition for a new computation.

3.8 Numerical simulation results

The results presented here indicate in qualitative forms how the flow varies with Ra and Re. Extensive time and mesh refinement results are not presented, but grid refinement and decrease in timestep produce no qualitative changes to the flow structure.

The presented streamlines, iso–therms and tangential velocity iso–lines correspond to the flow structure at the end of the presented computation. It is important to note that in some cases this structure represents one "snapshot" of a time–periodic flow.

It is important to note that some of the solutions presented here correspond to values of Ra, Re and Pr for which $\frac{Ra}{Re^2 Pr} = \beta\Delta T > 1$. As mentioned earlier, the form of the pressure/density relation which is assumed to hold and which is given in equation (3.4), yields negative densities. Therefore results for which $\beta\Delta T > 1$ can only be regarded as giving a qualitative indication of the resulting flow and heat transfer.

3.8.1 Solutions for $Ra = 10^6$, $r_0 = 0.5$ & $z_{max} = 0.5$

Solutions were obtained for the above conditions with 64×64 interval grids and a timestep corresponding to $\delta t = 5 \times 10^{-5}$.

Figure 3.19 displays the results for a Reynolds number of 400. The flow is in the form of a single toroidal vortex, (Figure 3.19a), rotating in the clockwise sense. Convection is weak as displayed by the small deviation in the isotherms, (Figure 3.19b) and the level of Nu_0, (Figure 3.19d). Indeed, solutions for Reynolds numbers much less than the presented $Re = 400$ case, correspond to solid body rotation and purely conducting temperature fields. A decrease in the rotational Reynolds number from the conditions presented, therefore stabilises the flow. This effect may be attributed to the buoyancy correction to the Coriolis force terms which are multiplied by the factor $\frac{Ra}{RePr}$. For fixed values of Ra and Pr an increase in the magnitude of the buoyancy correction has a stabilising effect on the flow, which is consistent with a decrease in the rotational Reynolds number. The resulting decrease in the magnitude of the pure Coriolis terms attribute to a destabilising effect. The buoyancy correction to the Coriolis force is dominant at the low Reynolds numbers discussed here, for its magnitude is about 10 times

greater at the outer regions of the cavity near the heated cylindrical surface than the Coriolis force.

A region of positive tangential velocity is apparent in Figure 3.19c, located at the right side of the tangential velocity iso–line plot. Again, this is due to the buoyancy correction to the Coriolis terms, which tends to result in positive regions of tangential velocity for positive radial velocity. Conversely, the pure Coriolis force drives a negative region of tangential velocity in regions of positive radial velocity.

Figure 3.19e displays the variation in the local Nusselt numbers on the inner hub and outer shroud regions. Where the flow impinges on the inner and outer radii maxima in the local heat transfer occurs due to the large temperature gradients. Similarly, minima in the heat transfer arise where the flow moves away from these surfaces.

Figure 3.19f shows the variation in the tangential velocity normalised on the local disk speed against the radius at the mid–axial plane of the cavity. The plane bisects the region of negative tangential velocity, with a minimum fluid tangential velocity of approximately 0.8 times the disk speed occurring.

Figure 3.20 displays the results for $Re = 500$. Here, the flow is in the form of a pair of counter–rotating toroidal vortices. Radial outflow occurs at the mid–axial plane of the cavity, where a positive region of tangential velocity is apparent. Radial inflow occurs near the disk surfaces where fluid motion is from the outer toward the inner cylindrical surface. Due to the relatively small Reynolds number and consequently low rotation rate being considered, the centrifugal effects

opposing the radial inflow of fluid motion at the disk surfaces is small. The solution is periodic in time, (Figure 3.20d), and takes the form of periodic motion in the upper regions of the cavity where rotational effects are stronger. An overall increase in the total heat transfer is apparent with increase in Reynolds number. The buoyancy correction to the Coriolis force terms and its associated stabilising effect is less dominant with the pure Coriolis terms becoming increasingly important. The former, however remains several orders of magnitude greater than the latter at the outer regions of the cavity.

Further increases in the rotational Reynolds number, (Figure 3.21), again display the toroidal pair solution. The solution is however steady–state as shown in Figure 3.21d. The region of positive tangential velocity apparent in Figure 3.20c is not maintained. The buoyancy correction to the Coriolis force terms are now reduced to a factor of two greater than the pure Coriolis terms at the outer part of the cavity, where the temperature is at its maximum. In regions of small values of temperature, the Coriolis forces dominate. Again, an increase in the heat transfer and therefore, the strength of the flow is apparent.

Figure 3.22 displays the results for $Re = 900$. The solution here has returned to the form of a single toroidal vortex, rotating in the anti–clockwise sense. The tangential velocity field is purely negative, with magnitudes of both the Coriolis and buoyancy correction to the Coriolis terms approximately matching for these conditions. The toroidal vortex is therefore precessing relative to the surfaces, with the minimum tangential velocity being approximately half the local disk speed, (Figure 3.22f). Local values of heat transfer, (Figure 3.22e), show peaks in local Nusselt number at $z \approx 0.05$ on the hub and $z \approx 0.4$ on the shroud.

The results of further increase in the Reynolds number to $Re = 1200$ is displayed in Figure 3.23. The results bear a strong resemblance to the $Re = 900$ case, however a region of positive tangential velocity (Figure 3.23c) has appeared near the hub. The pure Coriolis force dominates the buoyancy correction to the Coriolis force, particularly in the colder regions of the cavity. Hence, in regions of negative radial velocity, a positive tangential velocity field is expected.

The final case presented here is for $Re = 1600$. The increase in the rotational Reynolds number and hence the Coriolis force has resulted in substantial damping of the flow as is depicted in Figure 3.24d. The buoyancy force which is opposed by the damping effect of the Coriolis force is thus insufficient to maintain the strong convection. Further increases in the rotational Reynolds number result in the reappearance of the solid body rotation solution with a purely conducting temperature field. Little variation in the tangential velocity field is then apparent.

3.8.2 Solutions for $Ra = 10^7$, $r_0 = 0.5$ & $z_{max} = 0.5$

Solutions were obtained for the above conditions with 64×64 interval grids and a timestep corresponding to $\delta t = 10^{-5}$. The results display good qualitative comparison with the $Ra = 10^6$ computations presented above. Therefore, in particular some ideas on mechanisms of transition from one form of instability to another is presented.

Figure 3.25 displays the results for $Re = 10^3$. Again, solutions for Reynolds numbers much less than the one presented is solid body rotation. A two–cell structure is not possible to obtain, regardless of the initial conditions utilised under these conditions. The periodic variation in the flow structure, as displayed in Figure

3.25d, takes the form of unsteady motion in the left hand side of the cavity. The radial asymmetry causes the outward and inward steady–state boundary–layers to be different, unlike in the Bénard problem. The outward boundary–layer is clearly more susceptible to a travelling wave instability that in inward boundary–layer. Increasing the Reynolds number from this initial condition results in a growth in the disturbance and eventually a toroidal vortex pair structure results as shown for $Re = 2 \times 10^3$ in Figure 3.26. The solution presented here is again periodic with an average Nusselt number of approximately 3.7. Radial outflow occurs at the mid–axial plane with radial inflow occurring near the disk surfaces.

A further increase in the Reynolds number to $Re = 3 \times 10^3$ from the initial conditions presented in Figure 3.26 displays a steady state solution with the vortex pair structure maintained and an average Nusselt number of $Nu_0 \approx 6.4$. Figure 3.27 however displays a single steady state toroidal vortex solution for $Re = 3 \times 10^3$. This latter solution corresponds to a point perturbation initial condition as described in section 3.7. Two solutions have therefore been obtained for the same operating conditions, but the one realised is dependent on the form of the initial condition. Two or more stable states are therefore possible for the same conditions. The core of the single vortex structure is approximately isothermal as is displayed in Figure 3.27b with a non–dimensional temperature of approximately 0.7. The tangential velocity field suggests a minimum of approximately 0.4 of the local disk speed with a smaller steady–state heat transfer than for the corresponding vortex pair solution.

For a Reynolds number of 4×10^3, Figure 3.28 shows once again a vortex pair structure. However, it is seen from the isotherm plot that radial inflow now occurs at the axial mid–plane, (c.f. Figure 3.26). Due to the increase in the rotational

Reynolds number and consequent increase in the rotational speed of the cavity, the centrifugal forces imparted on the fluid by the disks has also increased and has become dominant over the buoyancy forces in these regions. Again, the cores of the circulation region appear to be almost isothermal, (Figure 3.28b), with the maximum temperature gradients occurring at the inner cylindrical surface. In this same region, an area of positive tangential velocity is displayed in Figure 3.28c, predominantly due to the effects of the Coriolis force. Similarly, in the regions where there exists radial outflow of fluid, regions of negative tangential velocity are apparent.

Finally, further increases in the rotational Reynolds number increasingly dampens the strength of the flow and results for $Re = 5 \times 10^3$ are presented in Figures 3.29. Large peaks in the local Nusselt numbers (Figure 3.29e) occur at approximately $z = 0.02$ and $z = 0.48$ at the inner and outer cylindrical surfaces respectively. Little variation in the tangential velocity is however apparent, (Figure 3.29f). A toroidal vortex pair structure could not be obtained regardless of the initial conditions used.

3.8.3 Solutions for $Re = 5 \times 10^3$, $r_0 = 0.5$ & $z_{max} = 0.5$

The changes related to the variation in the rotational Rayleigh number alone is investigated here for a constant geometry and rotational Reynolds number of 5×10^3. Two meshes were used for these computations and corresponded to 64×64 and 80×80 grids. The time steps utilised varied between $\delta t = 5 \times 10^{-6}$ to $\delta t = 2 \times 10^{-6}$ for the finer mesh.

The solution for $Ra = 10^7$ has been previously presented in Figure 3.29. A single

toroidal vortex is apparent which is steady with time. Further increase in the Rayleigh number is presented in Figure 3.30 and corresponds to $Ra = 2\times10^7$. The rate of heat transfer has increased, (Figure 3.30d), with the flow being unsteady and periodic with a number of frequencies. This time–periodicity takes the form of either the clockwise or counter–clockwise circulation becoming dominant over the other. Due to the highly transient nature of the flow, the total heat transfer on the inner surface exceeds that on the outer surface at this particular time, (Figure 3.30e). Integration of the heat transfer over a time period would however provide equal rates of heat transfer from the inner and outer cylindrical surfaces as expected.

Figure 3.31 displays the solution for $Ra = 3 \times 10^7$. Increase in the Rayleigh number increases both the magnitude of the pure buoyancy and buoyancy correction to the Coriolis force. The former plays a destabilising role with the latter contributing toward stabilising the flow. At this Rayleigh number, radial outflow now occurs in the mid–axial plane of the cavity with radial inflow on the disks. The time–dependency takes the form of unsteadiness between the two circulations, one becoming dominant over the other. Between times $t \approx 0.05$ and $t \approx 0.085$, the solution is approximately symmetrical about the mid–axial plane. Subsequently the symmetry is destroyed and the flow becomes asymmetric and aperiodic.

A mono–periodic solution is obtained for $Ra = 5\times10^7$ as displayed in Figures 3.32. Little change in the level of the total heat transfer is apparent with comparison with Figure 3.31d, suggesting that the stabilising role played by the buoyancy correction to the Coriolis terms counteracts the destabilising role of the buoyancy term. Radial outflow at the mid–axial plane of the cavity is apparent, with the

local heat transfer at the end of the computation being a maximum near the disks on the inner cylindrical surface and a maximum either side of the mid–axial plane on the outer cylindrical surface as shown in Figure 3.32e. Initially the structure is asymmetric due to the point perturbation introduced with symmetric flow subsequently evolving.

Figure 3.33 displays the results for $Ra = 10^8$. Radial outflow is maintained on the mid–axial plane with radial inflow on the disks of the enclosure. A definite decrease in the total heat transfer level has resulted from the increase in the magnitude of the buoyancy correction to the Coriolis force terms, this becoming increasingly dominant over the pure buoyancy force. Figures 3.33c,f display a region of positive tangential velocity near the outer cylindrical shroud surface, again, suggesting that the $\frac{Ra}{RePr}$ terms are becoming dominant, particularly in regions of temperature approaching that of the heated (outer) surface. An increase in the frequency of the periodic motion is apparent with increase in Rayleigh number.

Further increase in the rotational Rayleigh number is presented in Figure 3.34. The flow structure is becoming increasingly unsymmetrical about the mid–axial plane with the a decrease in the strength of convection and hence rate of heat transfer being apparent. Again, radial outflow occurs roughly at the mid–axial plane with a positive region of tangential velocity predicted near the heated outer cylindrical surface. The basic two–cell structure is however maintained.

Another periodic state is predicted for $Ra = 5 \times 10^8$. The fundamental twin cell structure is again maintained as depicted in Figure 3.35a with similar characteristics to the results presented in Figures 3.34. However, the average heat

transfer (Figure 3.35d) is now significantly reduced. Further increase in the rotational Rayleigh number will result in the base solution of solid body rotation and purely conducting temperature field.

The effect of increasing the Rayleigh number on the heat transfer is counter–intuitive. Initially, an increase in heat transfer with increasing Rayleigh number is observed followed by a turning point and then a decrease in heat transfer with increasing Rayleigh number. Numerically, it is hypothesised that the increase in the magnitude of the buoyancy correction to the Coriolis terms with increase in Rayleigh number, counteracts the effects of both the buoyancy and Coriolis forces. In particular, the stabilising effect on the buoyancy force becomes increasingly important at larger Rayleigh numbers and is more dominant than the correction to the Coriolis terms.

3.8.4 Solutions for $Ra = 10^7$, $r_0 = 0.3$ & $z_{max} = 0.5$

The effects of geometry are investigated here for an enclosure with aspect ratio, $AR \approx 0.714$ (where $AR = \frac{z_{max}}{1-r_0}$). The grid comprises 96 intervals radially and 64 intervals axially. The timestep utilised corresponded to $\delta t = 10^{-5}$ and was obtained from stability and temporal accuracy considerations. Solutions are again presented for a range of Reynolds numbers.

Figures 3.36 display the solution for $Re = 10^3$. An anti–clockwise circulation is apparent in the lower regions of the cavity with little motion apparent in the outer regions near the heated cylindrical surface. Indeed, the fluid is in approximately solid body rotation near $r = 1$ as is seen in Figure 3.36f. Direct comparison with the square cavity of Figures 3.25, display very similar flow characteristics. In

particular, however, the total heat transfer level is reduced for the small aspect ratio cavity with the solution being steady–state.

Similarities again pertain between the narrow cavity solution of Figures 3.37 and the square cavity solutions of 3.26. Radial outflow occurs in the mid–axial plane of the enclosure with radial inflow at the disks. Again a region of positive tangential velocity is apparent near the heated boundary, (Figure 3.37f). Again, a mono–periodic solution exists with approximately the same period as for the square enclosure, but the rate of heat transfer is now smaller.

The solutions at $Re = 3 \times 10^3$ are presented in Figures 3.38. A twin cell structure results with radial outflow occurring in the mid–axial plane. The solution is not unique as a single–cell solution may equally be obtained using appropriate initial conditions. The toroidal vortex pair are precessing with respect to the enclosure walls, (Figures 3.38c,f).

Further increase in the rotational Reynolds number to $Re = 5 \times 10^3$ provides a steady–state single vortex solution presented in Figures 3.39. The results display the characteristics of the square aspect ratio cavity shown in Figures 3.29. Most of the fluid motion occurs along the surfaces of the enclosure with relatively little motion in the central regions. It is also noted that the value of the steady–state average Nusselt number is below that of the square cavity case.

3.8.5 Solutions for $Ra = 10^7$, $r_0 = 0.5$ & $z_{max} = 1.0$

Further investigations have been conducted for an enclosure of aspect ratio $AR = 2.0$. The grid utilised is comprised of 64 radial intervals and 96 axial intervals with

a timestep corresponding to $\delta t = 10^{-5}$. Again, a range of Reynolds number solutions are obtained for constant geometry and Rayleigh numbers. Comparisons are also made with both square and $AR = 0.714$ geometries where appropriate.

Figures 3.40 displays the periodic solution obtained for $Re = 10^3$. An overall single–cell solution is found which rotates in the clockwise sense. The periodicity takes the form of flow unsteadiness near the left hand disk of the cavity. In this region, a positive area of tangential velocity is apparent, (Figure 3.40c), driven by the buoyancy correction to the Coriolis force. Again, the average heat transfer, (Figure 3.40d) is less than that for the square aspect ratio cavity presented in Figures 3.25 due to the increase in viscous dissipation experienced by the fluid in the larger geometry cavity.

Further increase in the Reynolds number to $Re = 2 \times 10^3$ gives a chaotic solution, (Figures 3.41). An overall twin cell solution is however apparent with radial outflow of fluid occurring at $z \approx 0.3$ and radial inflow of fluid near the disk surfaces. Various relatively small–scale cells appear within the main two–cell pattern. A positive region of tangential velocity again exists near the heated outer cylindrical surface where the radial jet impinges on the shroud. This may again be attributed to the buoyancy correction to the Coriolis force which dominates over the pure Coriolis force in this region. The mean total Nusselt number is approximately equal to the $AR = 0.714$ case presented in Figures 3.37.

Figures 3.42 display the solution for $Re = 3 \times 10^3$. The two–cell structure again prevails with radial outflow occurring approximately in the mid–axial plane and radial inflow on the disks. The solution shows no tendency towards a steady or periodic solution. The streamline plot, (Figure 3.42a), displays weak counter–

rotating regions of circulation driven by the main circulations with the entire region precessing relative to the rotating surfaces.

A twin circulation solution is obtained for $Re = 4 \times 10^3$ and presented in Figures 3.43. However, radial inflow now occurs at the mid–axial plane with radial outflow on the disks. It is also noted that the solution is steady with time, and the cores of the two recirculating regions are approximately isothermal. Increase in the rotational Reynolds numbers therefore stabilises the flow, the Coriolis forces becoming increasingly dominant.

The twin cell structure shown in Figure 4.43a is reminiscent of Bénard convection, but when Re is increased to 5000 (Figures 3.44) this gives way to a much weaker single–cell structure with the flow travelling in boundary–layers on the disks of the enclosure and along the inner and outer cylindrical surfaces in layers detached from the surfaces. If the approximation that the density varies linearly with temperature is not applied to the Coriolis force, the solution is solid body rotation and a conducting temperature field. A positive region of tangential velocity exists on the left hand disk and a negative region on the right hand disk driven by the Coriolis forces, the buoyancy correction to the Coriolis force being weak for large Reynolds number.

3.9 Brief conclusions

In this Chapter, a radial/axial axisymmetric flow has been investigated which takes the form of toroidal vortices. The fundamental roles of the forces and hence non–dimensional parameters have been determined using both a linear stability

method and non–linear numerical simulations:

- The magnitude of the buoyancy force is proportional to the Rayleigh number and an increase in its magnitude destabilises the flow.
- The magnitude of the Coriolis force, (proportional to the rotational Reynolds number), stabilises the flow.
- The buoyancy correction to the Coriolis force, (multiplied by the factor $\frac{Ra}{RePr}$), again stabilises the flow when its magnitude is non–zero. This occurs for large amplitude instabilities or small rotational Reynolds numbers.

It is unlikely that this radial/axial flow is the dominant flow regime, with variations in the tangential direction likely to occur. In the next chapter, a radial/tangential two–dimensional configuration is therefore considered in order to determine azimuthal variations in the flow structure.

A much fuller discussion of the flows presented here is given in Chapter 7 where it will be compared with results detailed in Chapters 4 and 5.

Chapter 4

2D radial/tangential flow

4.1 Summary

Here we study the case where the flow occurs in the r–θ plane and is axially invariant. A schematic of the configuration may be seen in Figure 1.5. The cavity is assumed to be sealed with the outer cylindrical shroud at a uniformly hot temperature and the inner cylindrical hub at a uniformly cold temperature. Once again this is analogous to Bénard convection in confined stationary cavities and a gravitational field.

The flow computed bears a strong qualitative resemblance to the three–dimensional flow presented later in Chapter 5. Four different flow regimes are identified. Initially, when the Rayleigh number is small, only solid–body rotation of the fluid in the cavity occurs and the heat is transferred across the cavity by conduction alone. When the Rayleigh number is large and the Reynolds number small, then convection takes the form of rolls which precess relative to the rotating surfaces (i.e. slower than the angular velocity of the cavity). When the Reynolds number

is large then the rolls are stationary relative to the rotating cylindrical surfaces. A further increase in the Rayleigh number results in the plume regions between the rolls becoming unsteady.

4.2 Governing equations

Again a rotating frame of reference is introduced and the density assumed to vary linearly with temperature. The velocity in the axial direction is neglected thereby reducing the dimensional governing equations to the following form,

$$\frac{\partial u}{\partial r} + \frac{1}{r}u + \frac{1}{r}\frac{\partial v}{\partial \theta} = 0, \tag{4.1}$$

$$\frac{\partial u}{\partial t} + (\underline{u}.\nabla)u - \frac{v^2}{r} - \frac{\rho}{\rho_0}(2\Omega v + \Omega^2 r) = -\frac{1}{\rho_0}\frac{\partial P}{\partial r} + \nu(\nabla^2 u - \frac{2}{r^2}\frac{\partial v}{\partial \theta} - \frac{u}{r^2}), \tag{4.2}$$

$$\frac{\partial v}{\partial t} + (\underline{u}.\nabla)v + \frac{uv}{r} + \frac{\rho}{\rho_0}(2\Omega u) = -\frac{1}{\rho_0 r}\frac{\partial P}{\partial \theta} + \nu(\nabla^2 v + \frac{2}{r^2}\frac{\partial u}{\partial \theta} - \frac{v}{r^2}), \tag{4.3}$$

$$\frac{\partial T}{\partial t} + (\underline{u}.\nabla)T = \kappa(\nabla^2 T). \tag{4.4}$$

where the 2–D divergence and Laplace operators are given respectively by,

$$(\underline{u}.\nabla) = u\frac{\partial}{\partial r} + \frac{v}{r}\frac{\partial}{\partial \theta}, \qquad \nabla^2 = \frac{\partial^2}{\partial r^2} + \frac{1}{r}\frac{\partial}{\partial r} + \frac{1}{r^2}\frac{\partial^2}{\partial \theta^2}.$$

A streamfunction–vorticity formulation is again introduced,

$$u = \frac{1}{r}\frac{\partial \psi}{\partial \theta}, \qquad v = -\frac{\partial \psi}{\partial r}, \tag{4.5}$$

$$\omega = -\frac{\partial v}{\partial r} - \frac{1}{r}v + \frac{1}{r}\frac{\partial u}{\partial \theta}. \tag{4.6}$$

where ψ is not the same as that introduced in section 2.1 for radial/axial flow. The non–dimensionalisation is similar to that introduced for the radial/axial

configuration and is given by,

$$r = R\bar{r}, \qquad t = \frac{R^2}{\kappa}\bar{t}, \qquad \omega = \frac{\kappa}{R^2}\bar{\omega}, \qquad \psi = \kappa\bar{\psi}, \qquad \bar{T} = \frac{T - T_c}{T_h - T_c}.$$

where overbars denote non–dimensional variables and T_h and T_c are the temperatures of the hot and cold walls respectively. The characteristic length scale, R, is taken to be the outer radius of the cavity and the characteristic vorticity, streamfunction and time scales are based on κ, the thermal diffusivity of the fluid within the cavity. Dropping the overbar and rotating frame notation, the resulting non–dimensional form of the governing equations for radial/circumferential flow in streamfunction–vorticity form are expressed as,

$$\omega = \nabla^2\psi, \tag{4.7}$$

$$\frac{1}{Pr}\Big[\frac{\partial\omega}{\partial t} + \frac{1}{r}J(\omega,\psi)\Big] + \frac{2Ra}{r\,Re\,Pr}J(T,\psi) + Ra\frac{\partial T}{\partial\theta} = \nabla^2\omega, \tag{4.8}$$

$$\frac{\partial T}{\partial t} + \frac{1}{r}J(T,\psi) = \nabla^2 T \tag{4.9}$$

where the Jacobian is given by,

$$J(A,B) = \frac{\partial A}{\partial r}\frac{\partial B}{\partial\theta} - \frac{\partial B}{\partial r}\frac{\partial A}{\partial\theta}$$

It is noted that the usual Coriolis term is eliminated with the introduction of the streamfunction–vorticity formulation. The flow however, is not independent of the Reynolds number for it appears explicitly in the buoyancy correction to the Coriolis term. The pure buoyancy term is multiplied by the rotational Rayleigh number as expected.

4.3 Boundary conditions

The cavity is assumed to be sealed with a heated shroud and cooled hub. The following boundary conditions are therefore prescribed:

At the heated shroud, $r = 1$, the boundary conditions are that,

$$\psi = 0, \qquad \frac{\partial \psi}{\partial r} = 0, \qquad T = 1.$$

At the cooled hub, $r = r_0$, the boundary conditions are that,

$$\psi = 0, \qquad \frac{\partial \psi}{\partial r} = 0, \qquad T = 0.$$

At $\theta = 0$ and 2π, periodic boundary conditions are applied.

4.4 Linear stability theory (LST)

4.4.1 Stability equations

Again, a linear stability theory is applied to predict the conditions necessary for the onset of convection for the radial/circumferential flow. A base solution of the governing equations corresponding to the non–convecting state of solid body rotation with a purely conducting temperature field is assumed.

$$\psi_B = 0, \qquad \omega_B = 0, \qquad T_B = \Big(1 - \frac{\ln r}{\ln r_0}\Big). \tag{4.10}$$

Where $_B$ denotes base solution quantities. The perturbations are therefore given by,

$$\psi = \psi_B + \hat{\psi}, \qquad \omega = \omega_B + \hat{\omega}, \qquad T = T_B + \hat{T}.$$

The governing equations are linearised by introducing periodic perturbations of infinitesimal amplitude with the wavenumber, n, taking only integer values.

$$\begin{pmatrix} \hat{\psi} \\ \hat{\omega} \\ \hat{T} \end{pmatrix} = e^{njθ+\lambda t} \begin{pmatrix} \hat{\psi}(r) + j\underline{\psi}(r) \\ \hat{\omega}(r) + j\underline{\omega}(r) \\ \hat{T}(r) + j\underline{T}(r) \end{pmatrix}. \tag{4.11}$$

where _ denotes the imaginary part of the complex perturbation solution and λ is the complex temporal growth rate given by,

$$\lambda = \lambda_R + j\lambda_I. \tag{4.12}$$

Solutions for $\lambda_R = 0$ are sought in order to investigate the neutral stability of the flow with λ_I non–zero to allow precession of the rolls. Resolving into real and imaginary parts, the resulting linear differential perturbation equations are,

$$\hat{\omega} = \hat{\psi}'' + \frac{1}{r}\hat{\psi}' - \frac{n^2}{r^2}\hat{\psi}, \tag{4.13}$$

$$\underline{\omega} = \underline{\psi}'' + \frac{1}{r}\underline{\psi}' - \frac{n^2}{r^2}\underline{\psi}, \tag{4.14}$$

$$-\frac{1}{Pr}\lambda_I\underline{\omega} + (\frac{2Ra}{RePr})(\frac{n}{r^2 \ln r_0})\underline{\psi} - Ra\, n\underline{T} = \hat{\omega}'' + \frac{1}{r}\hat{\omega}' - \frac{n^2}{r^2}\hat{\omega}, \tag{4.15}$$

$$\frac{1}{Pr}\lambda_I\hat{\omega} - (\frac{2Ra}{RePr})(\frac{n}{r^2 \ln r_0})\hat{\psi} + Ra\, n\hat{T} = \underline{\omega}'' + \frac{1}{r}\underline{\omega}' - \frac{n^2}{r^2}\underline{\omega}, \tag{4.16}$$

$$-\lambda_I\underline{T} + \frac{n}{r^2 \ln r_0}\underline{\psi} = \hat{T}'' + \frac{1}{r}\hat{T}' - \frac{n^2}{r^2}\hat{T}, \tag{4.17}$$

$$\lambda_I\hat{T} - \frac{n}{r^2 \ln r_0}\hat{\psi} = \underline{T}'' + \frac{1}{r}\underline{T}' - \frac{n^2}{r^2}\underline{T}, \tag{4.18}$$

$$Ra' = 0, \tag{4.19}$$

$$\lambda_I' = 0. \tag{4.20}$$

The above is a 14^{th} order eigenvalue problem in Ra and λ_I as a function of n and r_0 and the full system is solved subject to the boundary conditions:

$$\hat{\psi} = \underline{\psi} = 0, \qquad \hat{\psi}' = \underline{\psi}' = 0, \qquad \hat{T} = \underline{T} = 0 \quad \text{on} \quad r = r_0 \tag{4.21}$$

and

$$\hat{\psi} = \underline{\psi} = 0, \qquad \hat{\psi}' = \underline{\psi}' = 0, \qquad \hat{T} = \underline{T} = 0 \quad \text{on} \quad r = 1. \tag{4.22}$$

Additional normalising conditions at $r = r_0$ are also required and are taken to be,

$$\hat{T}' = 1, \qquad \underline{T}' = 0. \tag{4.23}$$

4.4.2 Solution method

Solutions for the eigenvalues Ra and λ_I are obtained using the method described in Section 3.4.2. The equations are reduced to first–order form and the eigenvalues obtained using a fourth–order Runge Kutta scheme allied with the shooting method, which involves a multi–dimensional Newton–Raphson iteration and Gaussian elimination scheme.

4.4.3 Results

Air is assumed to be the fluid within the cavity for which the Prandtl number is taken as $Pr = 0.7$.

Solutions for $\frac{Ra}{Re\,Pr} = 0$

Neglecting the buoyancy correction to the Coriolis force is equivalent to setting $\beta\Delta T << 1$ and hence the Boussinesq approximation is valid. Buoyancy is not zero when $\beta\Delta T << 1$. Only the buoyancy correction to the Coriolis force. In this case the numerical results indicate that $\lambda_I = 0$ which corresponds to stationary rolls, i.e. precession of the flow pattern does not occur and the rolls are locked to the rotating surfaces.

Figure 4.1 displays critical Rayleigh number curves for a range of inner radii and discrete wavenumbers. For a given wavenumber and increasing inner radii, the critical Rayleigh number initially decreases until a minimum is reached. A rapid increase in the critical Rayleigh number then occurs with a further increase in inner radii. This variation is more prominent for larger wavenumber convection (i.e. for large values of n) and less prominent for small wavenumbers. Indeed, for the $n = 2$ solution, only a very small initial decrease in Ra_{crit} is apparent with increasing inner radii. For small inner radii, the lowest values of Ra_{crit} correspond to small wavenumber instability, with increasing wavenumber solutions possible for increasing Ra_{crit}. As the inner radius increases, the minimum value of Ra_{crit} occurs at increasing wavenumbers.

Figure 4.2 displays gap–based critical Rayleigh numbers for varying inner radius and wavenumbers where,

$$Ra_{gap} = Ra_R \times \left(1 - r_0\right)^3.$$

The shape of the critical Rayleigh number lines bears a strong similarity to the those of Figure 4.1, the interpretation of both figures being the same, namely,

at a given value of r_0, the first curve which is crossed in the Ra–direction yields the critical value of Ra_{gap} and the value of n. At certain values of r_0 (e.g. at approximately 0.31 in Figure 4.2) two curves cross; at such points it is possible to have two modes ($n = 2$ and $n = 4$ in this case) becoming unstable simultaneously. The subsequent interaction requires non–linear simulations.

Extrapolation of the minimum points of the curves in Figure 4.2 for the larger wavenumbers toward the $r_0 = 1$ limit, gives a critical Rayleigh number corresponding to $Ra_{crit} \approx 1700$. This again corresponds to the critical Rayleigh number for the onset of Bénard convection in confined stationary cavities and a gravitational field. (c.f. Table 2.1). Good confidence therefore prevails in the numerical procedure.

Solutions for non–zero values of $\frac{Ra}{Re\,Pr}$

The buoyancy correction to the Coriolis force is assumed to be significant here in order to determine the effect of precession on neutral stability. As in Section 3, attention is drawn to the fact that flows for which $\frac{Ra}{Re^2 Pr} = \beta\Delta T > 1$ may only be regarded as being qualitatively correct as the fluid takes negative densities in part of the computational domain. The frequency (λ_I) is non–zero and results are presented for three different inner radii and various Reynolds numbers and wavenumbers. Solutions at large values of $\frac{Ra}{Re\,Pr}$ could not be obtained.

Figure 4.3 displays the stability curves for $r_0 = 0.7$ and Re in the range $0 \rightarrow 1000$. The effect of the buoyancy correction is prominent here for small values of Re only and hence for large magnitudes of the buoyancy correction terms. In particular, the first curve crossed in the Ra direction ($n = 8$ in Figure 4.3) is the critical

value of Ra and the effect of the buoyancy correction at small Re is constrained to $Re < 200$ approximately. For larger values of Ra_{crit}, where larger or smaller wavenumbers become stable, the buoyancy correction is observed to modify the neutral stability curves over a wider range of Reynolds numbers. It is noted in particular that for wavenumbers $n \leq 8$, the buoyancy correction has a stabilising effect, whereas for $n > 8$ flow destabilisation occurs at small values of Re.

Similar observations are made for $r_0 = 0.5$ (Figure 4.4). Here however, the primary mode of instability is $n = 4$ over a large range of values of Re but other modes take over as Re becomes small.

Figure 4.5 shows the neutral stability curves for $r_0 = 0.1$. It is noted that for all the wavenumbers presented, destabilisation occurs at small Reynolds numbers with no neutral stability curve observed to cross another for $r_0 = 0.1$. The effect of the Reynolds number on the neutral stability curves is more prominent for large wavenumbers, n, with the variation for small wavenumbers being small.

4.5 Non–linear computations

4.5.1 Finite difference approximations

Second–order accurate finite–difference approximations are utilised in space on a uniform grid. The non–linear advective terms are again approximated by the formulation presented by Arakawa (1966), in order to aid the stability of the numerical procedure. The application of the periodic boundary conditions is straightforward and will not be repeated here.

4.5.2 Transient method

The vorticity and temperature equations are arranged explicity using second–order accurate central differences for the time derivatives based on the Du–Fort Frankel method. Once again, values of the dependant variable at the n^{th} timestep are exchanged for averages of new and old time values to improve the stability of the method.

4.5.3 Multigrid method

The Poisson equation for the streamfunction is solved using a Multigrid routine to accelerate convergence as described in Section 3.5.4. A line relaxation scheme is utilised incorporating V–cycling. However, when relaxing in the θ direction the tri–diagonal matrix algorithm cannot be used. The periodic boundary condition applied in the θ direction causes the iteration matrix to have additional elements in the top right and bottom left entries as follows:

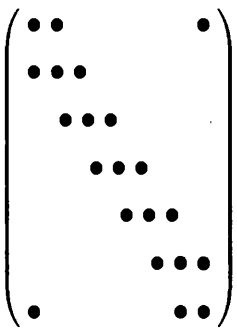

The resulting matrix is therefore solved using a periodic tri–diagonal matrix algorithm to obtain approximations to the solution and the error. Although there are only two extra entries in the above matrix, the number of arithmetic operations is approximately twice that of the TDMA (Tri–Diagonal Matrix Algorithm or Thomas–Algorithm). Once again, two relaxation sweeps based on the Gauss–

Seidel method are undertaken in both the radial and tangential directions before moving to finer or coarser grids.

4.5.4 Heat transfer

The definition of the total or average heat transfer is not the same as that for radial/axial flow and is expressed as,

$$Nu_0 = -\frac{r\ln(r_0)}{2\pi}\int_0^{2\pi}\frac{\partial T}{\partial r}d\theta. \tag{4.24}$$

The integral quantity is again evaluated using the trapezoidal rule with the differential being approximated using a fourth–order accurate finite difference representation.

The local Nusselt number remains unchanged from that presented in Section 3.5.5 and is repeated here for completeness,

$$Nu_{local} = -r\ln(r_0)\frac{\partial T}{\partial r}. \tag{4.25}$$

4.5.5 Precession of rolls

A measure of the rate of precession of the cyclonic/anti–cyclonic pairs is determined by evaluating even and odd Fourier components of the temperature solution with time. At each timestep therefore, the following integrals are evaluated,

$$I_s^n = \int_{r_0}^1\int_0^{2\pi} T(r,\theta)\sin(n\theta)r\,dr\,d\theta, \tag{4.26}$$

$$I_c^n = \int_{r_0}^1\int_0^{2\pi} T(r,\theta)\cos(n\theta)r\,dr\,d\theta, \tag{4.27}$$

where $n = 1, N$. Here N is the number of modes (cyclonic pairs) to be resolved and is typically taken to be $N = 10$. The integral quantities are evaluated using the trapezoidal rule at each time–step. One time period of the fundamental mode corresponds to the time taken for one cyclonic/anti–cyclonic pair to pass a given point. It is useful to relate this precession velocity relative to the disk speed. Relative to a stationary frame of reference, the rotational velocity of the surfaces is obtained form the Reynolds number and is given by,

$$\Omega = \frac{Re\,\nu}{R^2}. \tag{4.28}$$

In a rotating frame, the tangential distance precessed in dimensional time $\frac{PR^2}{\kappa}$, where P, is the non–dimensional time period of the dominant cosine and sine Fourier components, is,

$$\frac{2\pi}{n}, \tag{4.29}$$

where n is the dominant wavenumber. Hence, the speed of precession of the cyclonic/anti–cyclonic pairs is,

$$\frac{2\pi\kappa}{nPR^2}. \tag{4.30}$$

The parameter, γ is introduced and is defined as the ratio of the rotational speed of the circulations to that of the disks and is given by,

$$\gamma = \frac{\frac{Re\nu}{R^2} - \frac{2\pi\kappa}{nPR^2}}{\frac{Re\nu}{R^2}}, \tag{4.31}$$

which simplifies to,

$$\gamma = 1 - \frac{2\pi}{Re\,Pr\,n\,P}. \tag{4.32}$$

4.5.6 Code structure

The structure of the solver for one timestep is given by the following numerical procedure,

- Initialise all variables for time $t = 0$.
- Solve for ω^{n+1}, T^{n+1} using the solutions at t^n and t^{n-1} on all internal grid points.
- Evaluate $I_s^{n=1,10}, I_c^{n=1,10}$ and Nu_0 using values of T^{n+1}.
- Solve implicitly for ψ^{n+1} using values of ω^{n+1} on the right hand side using the Multigrid method.
- Update values of ω^{n+1} on the boundaries using values of ψ^{n+1}.

4.6 Code validation

Comparisons are made with LST results in order to validate the numerical simulation procedure. A discrete wavenumber solution corresponding to $n = 4$ is considered with $r_0 = 0.5$. The numerical simulations use initial conditions for the temperature field corresponding to the following distribution,

$$T = T_B + A(1 - r)(r - r_0)\cos(n\theta), \tag{4.33}$$

in order to perturb the solution toward the correct number of cyclonic/anti–cyclonic pairs. Again, solutions are sought for large Reynolds numbers, (i.e. $\frac{Ra}{Re\,Pr} = 0$), in order to correspond with the LST treatment.

Figure 4.6 displays both the numerical and LST results for the prediction of Ra_{crit} for an $n = 4$ instability. The numerical simulation results were obtained on 32×64 and 64×128 radial/tangential interval grids. The solutions are rendered fourth–order accurate using the Richardson's extrapolation technique, (equation 3.51). A polynomial extrapolation procedure is used in order to obtain a more accurate prediction for Ra_{crit} and is of the form,

$$y = ax^3 + bx^2 + cx + d.$$

The extrapolation procedure allied with the Richardson's extrapolation technique gave a value of $Ra_{crit} = 19228$ for the numerical simulation result. The LST treatment gave a value $Ra_{crit} = 19217$. A good comparison therefore exists between the LST treatment and numerical simulation techniques for the prediction of the critical Rayleigh number with the numerical simulation result being less than 0.1% in error of the LST prediction.

4.7 Initial conditions

The initial conditions correspond to solid–body rotation with a conducting temperature field and is given by,

$$\psi = 0, \qquad \omega = 0, \qquad T = 1 - \frac{\ln r}{\ln r_0}.$$

In order to perturb this initial solution, two methods are used. A point perturbation may be introduced in the temperature field where,

$$T(\tfrac{1}{4}(1 - r_0), 0) = T_B(\tfrac{1}{4}(1 - r_0), 0) - 0.02. \tag{4.34}$$

Alternatively, if a solution at a predetermined wavenumber is required, the following perturbation to the temperature field is introduced,

$$T = T_B + A(1-r)(r-r_0)\cos(n\theta), \tag{4.35}$$

where n is the wavenumber and A the perturbation amplitude which is typically within the range,

$$0 \leq A \leq 0.5.$$

4.8 Numerical simulation results

The flow is characterised by cyclonic/anti–cyclonic pairs of circulating flow. The cyclonic regions rotate in the same sense as the disks, whereas the anti–cyclonic regions rotate in the opposite sense. The streamline and isotherm contour plots are presented such that the cyclonic regions rotate in the clockwise sense and the anti–cyclonic regions rotate anti–clockwise. The streamlines, isotherms and local heat transfer results presented correspond to the flow structure after the decay of transients when the flow has settled into a time–periodic state.

Although the Coriolis force terms do not appear in the non–dimensional governing equations in streamfunction–vorticity form, the role played may be investigated by considering the tangential momentum equation for steady, incompressible and inviscid flow,

$$2\Omega u = -\frac{1}{\rho r}\frac{\partial P}{\partial \theta} \tag{4.36}$$

From the inspection of equation 4.36, it is evident that there can only be a radial velocity if there is a tangential variation in the pressure field which is provided by

a cyclone/anti–cyclone pair. Radial inflow therefore occurs if $\frac{\partial P}{\partial \theta} > 0$ and radial outflow occurs if $\frac{\partial P}{\partial \theta} < 0$.

As in Section 3, attention is drawn to the fact that flows for which $\frac{Ra}{Re^2 Pr} = \beta \Delta T > 1$ may only be regarded as being qualitatively correct as the fluid takes negative densities in part of the computational domain.

4.8.1 Solutions for various wavenumbers with $Ra = 10^6$,$Re = 10^3$ and $r_0 = 0.5$

Typical grids utilised for these computations comprised 64 radial intervals and 128 to 160 tangential intervals, (the larger number of intervals being used for the larger wavenumber solutions). The initial perturbation is given by equation (4.35). As deduced from the LST treatment, various wavenumber instabilities may appear for a given geometry and operating conditions. A range of different wavenumbers are therefore considered here for otherwise identical operating conditions and geometries.

Figures 4.7 displays the results of an initial $n = 2$ perturbation to the base flow. Two cyclonic/anti–cyclonic pairs are apparent with two radial outflow and two radial inflow arms exchanging fluid between the inner and outer cylindrical surfaces. Maxima in the local heat transfer (Figure 4.7d) correspond to regions where these radial arms of fluid impinge on the cylindrical surfaces with different maxima for inner and outer surfaces. The isotherms show that at the centre of the rolls, the fluid is approximately isothermal and at a scaled temperature of approximately 0.6. This is due to the fact that little fluid motion occurs at the centre of the cyclonic/anti–cyclonic regions.

The total heat transfer variation with time (Figure 4.7c) suggests that the flow is steady–state. However, the Fourier decomposition of the temperature field with time suggests a different story. A pure precession of the rolls occurs, with the total heat transfer evaluated at the cooled cylindrical surface, remaining constant throughout. The form of the cyclonic/anti–cyclonic pairs is therefore constant with time, with precession occurring in the anti–clockwise direction as defined in Figures 4.7a.

Figure 4.7e shows that the $n = 2$ mode dominates, (the fundamental), with higher harmonics of the fundamental also evident. It is noted in particular that the second harmonic of the fundamental is small with the third harmonic being significant. This may be due to the integral being evaluated over the radius in addition to the tangential direction and thus only odd harmonics of the fundamental are apparent.

Figures 4.8 display the solution for an initial $n = 3$ perturbation. Three cyclonic/ anti–cyclonic pair regions are now evident with arms of radial inflow and outflow between the rolls. Comparison with Figure 4.7c shows a significant increase in the total heat transfer with little difference in the maxima and minima of the local heat transfer. The increase in the number of radial arms is therefore the main contributor to this increase in the heat transfer. Again, the Fourier decomposition of the temperature field with time, shows that the third harmonic of the fundamental frequency is more prominent than the second harmonic.

A further increase in the wavenumber of the initial perturbation is presented in Figures 4.9. Here an $n = 4$ initial perturbation is introduced. The rolls now have a more "square" aspect ratio, with the isothermal regions at the centre of the rolls

becoming quite small. Again, a small increase in the average Nusselt number is apparent on comparison with Figure 4.8c. The increase in heat transfer associated with an increase in the number of radial arms offsetting the decrease in heat transfer due to the reduced strength of the rolls themselves. The precession of the cyclonic/anti–cyclonic pairs is again evident, with the fundamental component of the Fourier decomposition, (Figure 4.9e), dominating. It is anticipated that higher modes are also significant, however, only the integral quantities up to and including $\cos(10\theta)$ and $\sin(10\theta)$ are evaluated. The amplitudes of the second harmonic are again very small.

Figures 4.10 display solutions for an $n = 5$ perturbation. It is apparent from Figures 4.10a,b that the cyclonic regions are slightly stronger than their anti–cyclonic counterparts. This effect is due to the precessing motion of the rolls which occurs in the anti–clockwise sense, which in turn is due to the Coriolis correction to the buoyancy term. At the heated outer cylindrical surface, the shear between the cyclonic regions and the surface strengthens the cyclones. Conversely, at the cooled inner cylindrical surface, the shear strengthens the anti–cyclonic regions and weakens the cyclones. However, this effect is less prominent due to the smaller radial location of the inner cylindrical surface. This is analogous to the driven–cavity problem where the motion of a surface causes a recirculation. In this instance, in a frame of motion rotating with the rolls, the motion of the outer cylindrical surface increases the strength of the cyclones. This effect will become more prominent for smaller Reynolds numbers where the magnitude of the Coriolis correction to the buoyancy terms, and hence the rate of precession, increases.

Figures 4.11 displays the solution for an $n = 6$ perturbation. A very slight

increase in the rate of heat transfer is again apparent, with six arms of radial outflow and six arms of radial inflow exchanging fluid between the heated and cooled cylindrical surfaces. The Fourier decomposition of the temperature solution with time, (Figure 4.11e), shows only the dominant fundamental frequency. Higher harmonics were not evaluated but are not thought to be significant, given earlier results.

A periodic solution is obtained for an $n = 7$ perturbation. This unsteadiness takes the form of motion between the cyclonic/anti–cyclonic pairs. At the end of the computation, the streamlines (Figure 4.12a) show that the cyclonic regions are dominant over the anti–cyclonic regions. This may be due to the flow unsteadiness and also the velocity imparted on the fluid by the rotating surfaces as discussed above. A decrease in the mean total heat transfer from that presented in Figure 4.11c is also evident. The increase in the heat transfer associated with an increase in the number of radial arms impinging on the surfaces is not adequate here to offset the decrease in the heat transfer due to the reduced strength of the rolls. The small wriggles in Figures 4.12e are due to the flow unsteadiness between the cyclonic/anti–cyclonic pairs, where one roll becomes dominant over the other.

The solutions presented in Figures 4.13, correspond to an initial $n = 8$ perturbation. The resulting structure however, comprises of four cyclonic/anti–cyclonic pairs. The transition from the initial periodic $n = 8$ instability to the steady $n = 4$ instability occurs approximately at a non–dimensional time corresponding to $t \approx 0.45$. This is easily identified from both Figures 4.13c and 4.13e which show the total heat transfer and the Fourier decomposition of the temperature field with time respectively. Given the form of the initial profile, the $n = 8$ solution is therefore unstable with respect to $n = 4$ disturbances and the only way

the flow may be contaminated by an $n = 4$ component is via round–off error in the solution procedure. The initial periodic unsteadiness in the regions between the cyclones and anti–cyclones may be due to the relatively large velocity gradients between the cyclonic/anti–cyclonic circulations as a result of the relative proximity of the rolls.

For the results presented above, the rate of precession is very small with γ, (equation 4.32), approaching unity. The number of cyclonic/anti–cyclonic pairs has only a small effect on the value of γ for the wavenumber instabilities considered here due to the relatively small magnitude of the buoyancy correction to the Coriolis term. The preferred number of cyclonic/anti–cyclonic pairs which form for a given geometry and operating conditions is likely to be that which approximately maximises the overall heat transfer. For a point perturbation initial condition, the preferred number of pairs corresponds to an $n = 5$ solution which both maximises the heat transfer and is also steady with time. A pure precession of the rolls therefore occurs.

4.8.2 Solutions for various inner radii with $Ra = 10^6$ and $Re = 10^3$

The solutions presented here are evaluated on grids with between 64 and 80 radial intervals and 128 tangential intervals. The initial point perturbation corresponds to equation (4.34) for all the computations presented.

Figures 4.14 show the solution for a small inner radius ($r_0 = 0.1$). An $n = 1$ wavenumber solution results with the cyclonic circulation being dominant over the anti–cyclonic circulation at the end of the computation. The resulting small

wavenumber solution comprises of only one region each of radial outflow and radial inflow of fluid, with the location of the impingement of fluid on the outer surface being the location of the largest peak in the local Nusselt number (Figure 4.14d). It is also noted that the regions at the centre of the cyclones and anti–cyclones are highly isothermal. The solution is periodic as displayed in the variation with time of the total heat transfer and the Fourier decomposition of the temperature field. This periodicity takes the form of flow unsteadiness between the counter–rotating vortices. The simulations suggest a steady precession of the convective cells with a superimposed fast oscillation.

A transition in the flow occurs at $t \approx 0.2$ where prior to this time, the $\sin(2\theta)$ and $\cos(2\theta)$ modes in the Fourier decomposition are dominant, (Figure 4.14e). Wavenumber halving therefore occurs at this time with an associated reduction in the heat transfer, (Figure 4.14c).

An $n = 2$ solution is obtained for an inner radius of $r_0 = 0.3$, (Figures 4.15). The increase in the total heat transfer, (c.f. Figure 4.14c), is due to the increase in the number of radial arms of circulating fluid and the decrease in gap between the inner and outer cylindrical surfaces. A pure precession of the rolls occurs with no periodic motion evident at the impingement and radial arm regions. Again, a transition in the dominant mode is apparent at $t \approx 0.25$. Prior to this, the $n = 3$ mode dominates and subsequently decays as it is likely to have a faster linearised growth rate than the $n = 2$ mode.

A further increase in the inner radius to $r_0 = 0.6$ is presented in Figures 4.16. Here, a substantial increase in the wavenumber is apparent with the rolls maintaining an approximately square aspect ratio. Due to the small gap between the

cylindrical surfaces, an increase in the heat transfer is expected. However, the increase in the number of cyclonic/anti–cyclonic pairs and the viscous effects between these rolls counteracts the increase in both the number of radial arms and the effect of the small gap. The number of pairs which form however approximately maximises the heat transfer. A transition in the flow occurs at $t \approx 0.2$ and may be identified from Figures 4.16c,e. Before this time, various modes in the Fourier decomposition are significant due to the instability consisting of 8 cyclonic/anti–cyclonic pairs of various sizes, but an $n = 7$ solution forms the final flow pattern.

Further increase in the inner radius results in an increase in the number of cyclonic/anti–cyclonic pairs with further decrease in the total rate of heat transfer. The approximately square aspect ratio of the rolls is also maintained.

4.8.3 Solutions for various Re with $Ra = 10^5$ and $r_0 = 0.5$

The variation of the precession speed relative to the cylindrical surfaces, γ, (equation (4.32)), of the cyclonic/anti–cyclonic pairs with Reynolds number is considered. The grids used for these computations comprised 32×128 radial and tangential intervals respectively and a non–dimensional timestep of $t = 0.0005$.

The precession of the cyclonic/anti–cyclonic pairs is dependant only on the magnitude of the buoyancy correction to the Coriolis term. When the magnitude of the factor $\frac{Ra}{Re\,Pr}$ is large, then the rolls precess relative to the rotating cylindrical surfaces. Conversely, when the magnitude of the buoyancy correction to the Coriolis term is small, then the cyclonic/anti–cyclonic pairs are rigidly fixed to the cylindrical surfaces. The results of varying the Reynolds number, and hence

the magnitude of the buoyancy correction to the Coriolis term are presented in Figure 4.17 with the Reynolds number axis presented on a logarithmic scale. The speed of precession of the rolls rises sharply from $\gamma \approx 0.9$ at $Re = 100$ to $\gamma \approx 1.0$ at $Re = 1000$. A further increase in the Reynolds number has little effect on the precession speed relative to the rotating cylindrical surfaces, with the rolls locked to the surfaces.

The effect of this precession on the heat transfer is shown in Figure 4.18 with the Reynolds number again presented on a logarithmic axis. A decrease in the total heat transfer occurs for decreasing Reynolds number. Smaller values of Re (increasing influence of the buoyancy correction) causes an increase in the speed of precession. This results in a reduction in the strength of the rolls and a consequent decrease in the rate of heat transfer. A further reduction in the Reynolds number from that presented, results in further stabilisation of the flow, and for small Reynolds numbers, a solid body rotation flow field and conducting temperature field is obtained. The reduction in the Reynolds number and hence the centrifugal forces becomes insufficient to support buoyancy induced flow due to centrifugal force effects.

4.8.4 Solutions for various Ra with $Re = 10^3$ and $r_0 = 0.5$

To investigate the variation in the flow structure with increase in the dimensional temperature difference, the Reynolds number is held fixed and the Rayleigh number is allowed to vary. For the computations presented here, between 32 and 80 radial intervals and between 128 and 160 tangential intervals were used. The finer grid structures correspond to the larger Rayleigh number investigations.

The non–dimensional timestep used ranged from $\delta t = 5 \times 10^{-4}$ down to 10^{-6}.

Figures 4.19 displays the solution for $Ra = 10^5$. The preferred number of cyclonic/anti-cyclonic pairs here is six with the core of the rolls not displaying the isothermal nature of larger Rayleigh number flows. The strength of these pairs is therefore relatively weak with steady precession occurring at an average Nusselt number of approximately 2.5.

Increase in the Rayleigh number results in a decrease in the preferred number of pairs observed and a return to more isothermal cores. Figures 4.20 show the simulation results for $Ra = 10^6$. An increase in the heat transfer is apparent, (c.f. Figure 4.19c), with a discontinuity occurring at a time $t \approx 0.35$. The Fourier decomposition of the temperature field may however be separated into four distinct regions. Up to a time, $t \approx 0.02$, localised amplification of the point perturbation occurs, with little growth in the flow field. Subsequently, up to a time $t \approx 0.07$, the disturbance propagates around the enclosure with many Fourier modes being prominent. Following this the $n = 6$ mode dominates with the transition to an $n = 5$ mode occurring finally at $t \approx 0.35$. It is unclear precisely why this latter transition should take place, but it is evident from Figure 4.20e that many other competing modes exist just before $t = 0.35$; we suspect strongly that different initial conditions would yield an $n = 6$ solution. Note that the final solution is identical to that presented in Figure 4.10.

It is however unclear from the results as to why this latter modal transition should occur as a very small reduction in the heat transfer occurs, thus it may not be said that the preferred number of rolls exactly maximises the heat transfer here.

Figures 4.21 displays the solution for $Ra = 4 \times 10^6$. The total heat transfer is periodic in time, (Figure 4.21c), and is caused by the flapping motion of the radial arms. It is noted that this flapping does not occur in the usual manner, but period doubling occurs characterised by the opposing arms of radially out–flowing fluid moving in the tangentially opposite sense to the other two opposing arms or neighbouring arms being out of phase, (n.b. this can not occur for an odd value of n). A decrease in the number of cyclonic/anti–cyclonic pairs is again apparent with increasing Rayleigh number with an associated increase in the heat transfer also occurring.

The time history of the transient isotherms is presented in Figures 4.22 from a time $t = 0.005$ through to $t = 0.05$. Initially, the amplification of the point perturbation introduced at $\theta = 0$ is small, with only a small deviation of the isotherms from the base conducting solution. At a time $t = 0.0075$, the amplification of the point perturbation is evident with two regions of radial inflow and one more pronounced region of radial outflow. A pair of cyclonic/anti–cyclonic rolls are therefore present. At larger times, the instability is seen to travel around the cavity faster in the clockwise sense than in the anti–clockwise direction. It may be expected, that the disturbance would travel faster in the direction of precession, however, the precession rate of the rolls is small in comparison with the diffusion of the instability around the cavity. This effect therefore may be attributed to the rotating surfaces aiding the disturbance in the clockwise sense around the cavity. At a time $t = 0.015$, the disturbance has spread throughout the enclosure, with coherent cyclonic/anti–cyclonic features becoming increasingly evident. Six radially out–flowing arms of fluid are apparent at a time $t = 0.0175$ with five distinct arms occurring at time $t = 0.02$. At larger times, the $n = 4$ solution asserts itself, with two radial arms of fluid merging and thus

reducing the characteristic wavenumber.

Further increase in the Rayleigh number is characterised by an increasingly chaotic solution. Figures 4.23 show simulation results for $Ra = 5 \times 10^6$ with the preferred number of pairs corresponding to an $n = 4$ solution. Once again, period doubling occurs with higher harmonics apparent in the total heat transfer variation with time plot. The Fourier decomposition shows the two dominant modes, with many of the higher Fourier modes also prominent due to the flapping motion between the cyclonic/anti–cyclonic pairs.

Figures 4.24 display a chaotic solution for $Ra = 10^7$ with an increase in the wavenumber apparent. The core of the rolls are also becoming increasingly isothermal, with the large temperature gradients occurring near the cylindrical surfaces and in the radial plumes of fluid.

Further increases in the Rayleigh number result in increasingly chaotic flows. Figures 4.25 show an $n = 6$ instability for $Ra = 2 \times 10^7$. Increasingly large peaks in the local heat transfer are evident in Figure 4.25d with the form of the rolls becoming less smooth and with the cyclones becoming increasingly dominant over the anti–cyclones due to an increase in the rate of precession of the rolls themselves.

Figures 4.26 show the numerical simulation results for $Ra = 5 \times 10^7$. Large chaotic fluctuations in the total heat transfer are apparent with the streamlines and isotherms showing characteristic signs of these fluctuations. It is hypothesised that the reduction in the resulting wavenumber instability, $(n = 4)$, is due to these violent fluctuations causing the breakdown of larger wavenumber instabilities

which were likely to be prominent between $t \approx 0.002$ and $t \approx 0.01$. The Fourier decomposition of the temperature field with time shows that the rolls precess steadily with higher modes also significant due to the time dependence of the simulation.

The effect of the Rayleigh number on the precession rate relative to the rotating surfaces, γ, is presented in Figure 4.27. An increase in the Rayleigh number results in an associated increase in both the buoyancy force and the magnitude of the buoyancy correction to the Coriolis force. Due to this latter effect, a decrease in γ with increasing Rayleigh number occurs. The variation is approximately linear, however, discontinuities arise due the different characteristics of the various resulting wavenumber instabilities considered. Had the variation been considered for flows with the same wavenumber, then a more smooth variation in the precession rate relative to the rotating surfaces may be expected.

4.9 Brief conclusions

The radial/tangential instability takes the form of cyclonic/anti–cyclonic pairs, where the cyclones rotate in the same sense as the disks and the anti–cyclones in the opposite sense. The regime is independent of the Coriolis force, but the buoyancy correction to the Coriolis force remains significant in the governing equations. The buoyancy force is proportional to the Rayleigh number and has a destabilising effect on the flow. The primary effect of the buoyancy correction term is to cause precession of the rolls relative to the disk surfaces. This occurs for small Reynolds numbers in particular. For large Reynolds numbers, the cyclonic/anti–cyclonic pairs tend to be locked to the rotating surfaces. This

precession is also prevalent at large Rayleigh numbers. Various wavenumber solutions are stable for a given Rayleigh number, Reynolds number and inner radius, with the preferred number of cyclonic/anti–cyclonic pairs (obtained using a point perturbation initial condition) approximately maximising the rate of heat transfer.

As in Section 3, attention is drawn to the fact that flows for which $\frac{Ra}{Re^2 Pr} = \beta\Delta T > 1$ may only be regarded as being qualitatively correct as the fluid takes negative densities in part of the computational domain.

The effect of the disk boundaries on the flow characteristics is however thought to be important. In order to determine the influence of a fully enclosed cavity, the full three–dimensional equations of motion are considered and solutions presented in the next chapter.

Once more the results are discussed more fully in the contexts of those of Chapters 3 and 5 in Chapter 7.

Chapter 5

3D flow simulation

5.1 Summary

To investigate fully the flow structures within the present geometry, it is necessary to solve the full three–dimensional equations of motion. In particular, a fully enclosed cavity will modify the flow compared with the results of the previous two chapters. A representation of the three–dimensional cavity being considered is presented in Figure 1.3. As in the tangentially axisymmetric case, the disks are assumed to be adiabatic, the outer cylindrical shroud uniformly hot and the inner cylindrical hub uniformly cold.

Due to the very large number of grid points required, this chapter presents a qualitative investigation of the resulting flows. A more detailed, quantitatively accurate investigation would require much more computing power than is currently available at the University of Bath. The formulation is such that three Poisson equations are required to be solved at each timestep, and this consumes a large proportion of computational time. The spatial resolution therefore, tends

to be poor compared to what may be achieved with the two–dimensional codes which are in streamfunction–vorticity form. This limits the range of Rayleigh numbers which may be investigated. The use of a non–uniform grid distribution would aid in the resolution of flow in any boundary–layers, but this would require a marked increase in the complexity of the code. Therefore solutions on uniform meshes are presented.

5.2 Governing equations

The three–dimensional Navier–Stokes and energy equations in a rotating frame of reference and polar coordinates, subject to the assumption that the density varies linearly with temperature, are given by,

$$\frac{\partial u}{\partial r} + \frac{1}{r}u + \frac{1}{r}\frac{\partial v}{\partial \theta} + \frac{\partial w}{\partial z} = 0, \tag{5.1}$$

$$\frac{\partial u}{\partial t} + (\underline{u}.\nabla)u - \frac{v^2}{r} - \frac{\rho}{\rho_0}(2\Omega v + \Omega^2 r) = -\frac{1}{\rho_0}\frac{\partial P}{\partial r} + \nu(\nabla^2 u - \frac{2}{r^2}\frac{\partial v}{\partial \theta} - \frac{u}{r^2}), \tag{5.2}$$

$$\frac{\partial v}{\partial t} + (\underline{u}.\nabla)v + \frac{uv}{r} + \frac{\rho}{\rho_0}(2\Omega u) = \frac{1}{\rho_0 r}\frac{\partial P}{\partial \theta} + \nu(\nabla^2 v - \frac{v}{r^2}), \tag{5.3}$$

$$\frac{\partial w}{\partial t} + (\underline{u}.\nabla)w = -\frac{1}{\rho_0}\frac{\partial P}{\partial z} + \nu(\nabla^2 w), \tag{5.4}$$

$$\frac{\partial T}{\partial t} + (\underline{u}.\nabla)T = \kappa(\nabla^2 T) \tag{5.5}$$

where the three–dimensional divergence and Laplace operators are given respectively by,

$$(\underline{u}.\nabla) = u\frac{\partial}{\partial r} + \frac{v}{r}\frac{\partial}{\partial \theta} + w\frac{\partial}{\partial z}, \qquad \nabla^2 = \frac{\partial^2}{\partial r^2} + \frac{1}{r}\frac{\partial}{\partial r} + \frac{1}{r^2}\frac{\partial^2}{\partial \theta^2} + \frac{\partial^2}{\partial z^2}.$$

In order to eliminate the pressure field and its associated numerical difficulties, two different formulations may be used: these are vorticity–velocity and vorticity–

vector potential formulations. However, problems exist with the application of the boundary conditions for the latter method since the non–uniqueness of the vector potential allows multiple forms of its boundary formulation. One important advantage of the vector potential–vorticity formulation is that a collocated grid may be utilised, but, to avoid the difficulties arising as a result of applying the boundary conditions, it was decided to use the vorticity–velocity formulation, being the preferred formulation in the literature that was surveyed. Two different forms of the vorticity–velocity formulations exist characterised by the method used for determining the velocity vector; see Shen and Loc (1997).

- The first order or div–curl form where the velocity components are computed by solving the coupled problem of the divergence constraint and the definition of the curl of the velocity vector.
- The second–order form where Poisson equations are obtained by taking the curl of the vorticity definition and utilising the continuity equation.

The latter, classical form, of the vorticity–velocity formulation was selected for simplicity, with three uncoupled Poisson equations chosen in preference to the coupled problem which would be further complicated by the use of a staggered grid. The three–dimensional vorticity is therefore defined such that,

$$\underline{\omega} = \nabla \times \underline{u} = \frac{1}{r} \begin{vmatrix} \underline{i} & r\underline{j} & \underline{k} \\ \frac{\partial}{\partial r} & \frac{\partial}{\partial \theta} & \frac{\partial}{\partial z} \\ u & rv & w \end{vmatrix} \tag{5.6}$$

where $\underline{i}, \underline{j}$ and $\underline{k}$ are unit vectors in r, θ and z directions respectively. The three components of vorticity are therefore given by,

$$A = \frac{1}{r}\frac{\partial w}{\partial \theta} - \frac{\partial v}{\partial z}, \qquad B = \frac{\partial u}{\partial z} - \frac{\partial w}{\partial r}, \qquad C = \frac{\partial v}{\partial r} + \frac{v}{r} - \frac{1}{r}\frac{\partial u}{\partial \theta} \tag{5.7}$$

where $\underline{\omega} = (A, B, C)$. The pressure terms in the above equations may therefore be eliminated in the usual manner by cross–differentiation. The non–dimensionalisation is the same as that for radial/axial flow and is repeated here for completeness,

$$r = R\bar{r}, \qquad z = R\bar{z}, \qquad (u, v, w) = \frac{\kappa}{R}(\bar{u}, \bar{v}, \bar{w}), \qquad t = \frac{R^2}{\kappa}\bar{t},$$

$$(A, B, C) = \frac{\kappa}{R^2}(\bar{A}, \bar{B}, \bar{C}), \qquad \bar{T} = \frac{T - T_c}{T_h - T_c}$$

where overbars denote non–dimensional variables and T_h and T_c are the temperatures of the hot and cold walls respectively. The characteristic length scale, R, is taken to be the outer radius of the cavity and the characteristic vorticity, velocity and time scales are based on κ, the thermal diffusivity of the medium within the cavity rather than on ν, the kinematic viscosity. The rotational Rayleigh, rotational Reynolds and Prandtl numbers are also introduced and are given by,

$$Ra = \frac{R\Omega^2\beta(T_h - T_c)R^3}{\nu\kappa}, \qquad Re = \frac{\Omega R^2}{\nu}, \qquad Pr = \frac{\nu}{\kappa}.$$

The resulting, non–dimensional governing equations are given by,

$$\frac{1}{Pr}\Big[\frac{\partial A}{\partial t} + (\underline{u}.\nabla)A - \frac{\partial u}{\partial r}A - \frac{1}{r}\frac{\partial u}{\partial \theta}B - \frac{\partial u}{\partial z}C\Big] - 2Re\frac{\partial u}{\partial z} + \frac{2Ra}{RePr}(T\frac{\partial u}{\partial z} + u\frac{\partial T}{\partial z})$$
$$= \nabla^2 A - \frac{2}{r^2}\frac{\partial B}{\partial \theta} - \frac{1}{r^2}A, \tag{5.8}$$

$$\frac{1}{Pr}\Big[\frac{\partial B}{\partial t} + (\underline{u}.\nabla)B - (\frac{\partial v}{\partial r} - \frac{v}{r})A - \frac{1}{r}(u + \frac{\partial v}{\partial \theta})B - \frac{\partial v}{\partial z}C\Big] - 2Re\frac{\partial v}{\partial z} + \frac{2Ra}{RePr}(T\frac{\partial v}{\partial z} + v\frac{\partial T}{\partial z})$$
$$+ rRa\frac{\partial T}{\partial z} = \nabla^2 B + \frac{2}{r^2}\frac{\partial A}{\partial \theta} - \frac{1}{r^2}B, \tag{5.9}$$

$$\frac{1}{Pr}\Big[\frac{\partial C}{\partial t} + (\underline{u}.\nabla)C - \frac{\partial w}{\partial r}A - \frac{1}{r}\frac{\partial w}{\partial \theta}B - \frac{\partial w}{\partial z}C\Big] - 2Re\frac{\partial w}{\partial z} + \frac{2Ra}{RePr}(T\frac{\partial w}{\partial z} - u\frac{\partial T}{\partial r} - \frac{v}{r}\frac{\partial T}{\partial \theta})$$
$$- Ra\frac{\partial T}{\partial \theta} = \nabla^2 C. \tag{5.10}$$

The Poisson equations for velocity are formulated using the equation of continuity and the vorticity definitions. The equations for the velocity are thus expressed

in terms of vorticity on the right hand side and are given by,

$$\nabla^2 w = \frac{1}{r}\frac{\partial A}{\partial \theta} - \frac{\partial B}{\partial r} - \frac{B}{r}, \tag{5.11}$$

$$\nabla^2 v + \frac{2}{r}\frac{\partial v}{\partial r} + \frac{v}{r^2} = \frac{\partial C}{\partial r} + \frac{2C}{r} - \frac{\partial A}{\partial z}, \tag{5.12}$$

$$\nabla^2 u + \frac{2}{r}\frac{\partial u}{\partial r} + \frac{u}{r^2} = \frac{\partial B}{\partial z} - \frac{1}{r}\frac{\partial C}{\partial \theta} - \frac{2}{r}\frac{\partial w}{\partial z}. \tag{5.13}$$

It is noted that equation (5.13) for velocity u is expressed in terms of the axial velocity field, w and may not be defined explicitly in terms of the vorticity vector. Therefore, the axial velocity field must be calculated in order to obtain the radial velocity distribution for a given time.

The energy equation for temperature is expressed in the usual manner and is given by,

$$\frac{\partial T}{\partial t} + (\underline{u}.\nabla)T = \nabla^2 T. \tag{5.14}$$

Once again, it is noted that the Coriolis force is proportional to the Reynolds number and the magnitude of the buoyancy force is proportional to the Rayleigh number. The buoyancy correction to the Coriolis terms is proportional to the factor $\frac{Ra}{RePr}$. When the rotational Reynolds number is large, then this factor becomes negligible if Ra and Pr are held fixed.

5.3 Boundary conditions

The boundary conditions are that $u = v = w = 0$ such that all surfaces are no–slip and impermeable. The disks are assumed to be adiabatic whilst the outer cylindrical shroud is at a uniform hot temperature and the inner cylindrical hub is assumed to be uniformly cold. The boundary conditions for the vorticity

components are derived from their definition in terms of the curl of the velocity. The boundary conditions are therefore expressed as:

At the heated shroud, $r = 1$, the boundary conditions are that,

$$u = v = w = 0, \qquad A = 0, \qquad B = -\frac{\partial w}{\partial r}, \qquad C = \frac{\partial v}{\partial r}, \qquad T = 1.$$

At the cooled hub, $r = r_0$, the boundary conditions are that,

$$u = v = w = 0, \qquad A = 0, \qquad B = -\frac{\partial w}{\partial r}, \qquad C = \frac{\partial v}{\partial r}, \qquad T = 0.$$

At the disks, $z = 0, z_{\max}$, the boundary conditions are that,

$$u = v = w = 0, \qquad A = -\frac{\partial v}{\partial z}, \qquad B = \frac{\partial u}{\partial z}, \qquad C = 0, \qquad \frac{\partial T}{\partial z} = 0.$$

At $\theta = 0, 2\pi$, periodic boundary conditions are applied.

5.4 Non–linear computations

5.4.1 Staggered grid

In order to obtain a divergence–free velocity and vorticity vector distributions it is necessary to implement a staggered grid strategy. For a non–staggered grid, the divergence constraints for velocity and vorticity are not numerically satisfied. The staggering scheme used is presented in Figure 5.1 and is the same as that used by Stella *et al.* (1988), but here has been adapted to a polar grid. The velocities are located at the midpoint of the cube faces whilst the components of vorticity are located at the mid points of cube edges, parallel to the axis of the vorticity components. The location of the velocities assures the global conservation of the

flow rate within the cubical element. The location of the vorticities minimises the discretisation error in the right hand side of the Poisson equations for velocity. The temperature is located at the centre of the cube.

In order to minimise the complexity of the numerical approach and hence computational expenditure per iteration, a uniform mesh is utilised.

If the nodal point (i, j, k) denotes the physical nodal location $(i\delta r + r_0, j\delta\theta, k\delta z)$ then,

- Velocity u is located at $(i, j + \frac{1}{2}, k + \frac{1}{2})$
- Velocity v is located at $(i + \frac{1}{2}, j, k + \frac{1}{2})$
- Velocity w is located at $(i + \frac{1}{2}, j + \frac{1}{2}, k)$
- Vorticity A is located at $(i + \frac{1}{2}, j, k)$
- Vorticity B is located at $(i, j + \frac{1}{2}, k)$
- Vorticity C is located at $(i, j, k + \frac{1}{2})$
- Temperature T, is located at $(i + \frac{1}{2}, j + \frac{1}{2}, k + \frac{1}{2})$

5.4.2 Finite–difference approximations

Second–order finite difference spatial approximations become more complicated on a staggered grid. Linear or bi–linear interpolation techniques are used in order to evaluate the finite difference approximations. For example, in equation (5.8) for the vorticity component, A, vorticity components B and C are obtained using

bi–linear interpolation where,

$$B_{(i+\frac{1}{2},j,k)} = \frac{1}{4}(B_{(i,j+\frac{1}{2},k)} + B_{(i+1,j+\frac{1}{2},k)} + B_{(i,j-\frac{1}{2},k)} + B_{(i+1,j-\frac{1}{2},k)}),$$

$$C_{(i+\frac{1}{2},j,k)} = \frac{1}{4}(C_{(i,j,k+\frac{1}{2})} + C_{(i+1,j,k+\frac{1}{2})} + C_{(i,j,k+\frac{1}{2})} + C_{(i+1,j,k+\frac{1}{2})}).$$

Finite–difference approximations (FDA), to $\frac{\partial u}{\partial z}$ in equation (5.8) is expressed by taking a bi–linear approximation of u at $(i+\frac{1}{2}, j, k+\frac{1}{2})$ and $(i+\frac{1}{2}, j, k-\frac{1}{2})$ then forming the FDA in the usual manner using,

$$\frac{\partial u_{(i+\frac{1}{2},j,k)}}{\partial z} \approx \frac{u_{(i+\frac{1}{2},j,k+\frac{1}{2})} - u_{(i+\frac{1}{2},j,k-\frac{1}{2})}}{\delta z}.$$

Further difficulties arise at the boundaries where an extra storage location is used. For example, the FDA to $\frac{\partial^2 A}{\partial r^2}$ at one radial storage location from the inner cylindrical hub boundary is approximated by a four–point approximation in order to obtain second–order accuracy and is given by,

$$\frac{\partial^2 A_{(\frac{1}{2},j,k)}}{\partial r^2} \approx \frac{3.2A_{(0,j,k)} - 5A_{(\frac{1}{2},j,k)} + 2A_{(\frac{3}{2},j,k)} - 0.2A_{(\frac{5}{2},j,k)}}{\delta r^2}.$$

Similarly, a second–order accurate approximation for $\frac{\partial A}{\partial r}$ at one radial storage location from the inner cylindrical hub boundary is approximated by a three point approximation and is expressed as,

$$\frac{\partial A_{(\frac{1}{2},j,k)}}{\partial r} \approx \frac{-\frac{4}{3}A_{(0,j,k)} + A_{(\frac{1}{2},j,k)} + \frac{1}{3}A_{(\frac{3}{2},j,k)}}{\delta r}.$$

5.4.3 Application of boundary conditions

The main difficulty in applying the boundary conditions are those associated with the vorticity vector. No–slip boundary conditions applied to the velocity field are not problematical. In order to satisfy the vorticity boundary conditions at the

same time level, the boundary conditions for the vorticity and velocity equations must be resolved simultaneously. The velocity Poisson equations therefore differ at one location in from the boundaries from those applied in the core region. In order to demonstrate this, the $r = r_0$ boundary is considered for velocity w and vorticity B boundary condition, centred at $(\frac{1}{2}, j+\frac{1}{2}, k)$. In second–order accurate finite difference form it is expressed as,

$$\frac{-5w_{\frac{1}{2},j+\frac{1}{2},k} + 2w_{1\frac{1}{2},j+\frac{1}{2},k} - 0.2w_{\frac{3}{2},j+\frac{1}{2},k}}{\delta r^2} + \frac{1}{r}\left(\frac{w_{\frac{1}{2},j+\frac{1}{2},k} + \frac{1}{3}w_{1\frac{1}{2},j+\frac{1}{2},k}}{\delta r}\right)$$

$$+\frac{w_{\frac{1}{2},j-\frac{1}{2},k} - 2w_{\frac{1}{2},j+\frac{1}{2},k} + w_{\frac{1}{2},j+\frac{3}{2},k}}{\delta\theta^2} + \frac{w_{\frac{1}{2},j+\frac{1}{2},k-1} - 2w_{\frac{1}{2},j+\frac{1}{2},k} + w_{\frac{1}{2},j+\frac{1}{2},k+1}}{\delta z^2}$$

$$\approx \frac{1}{r}\frac{A_{\frac{1}{2},j+1,k} - A_{\frac{1}{2},j,k}}{\delta\theta} - \frac{B_{1,j+\frac{1}{2},k} - B_{0,j+\frac{1}{2},k}}{\delta r} - \frac{B_{1,j+\frac{1}{2},k} + B_{0,j+\frac{1}{2},k}}{2r} \qquad (5.15)$$

The value of $B_{0,j+\frac{1}{2},k}$ is as yet unknown, since the boundary vorticity is expressed in terms of the velocity field at the same timestep. At the $r = r_0$ boundary, $B = -\frac{\partial w}{\partial r}$. In second–order finite difference form this is expressed as,

$$B_{0,j+\frac{1}{2},k} \approx -\frac{3w_{\frac{1}{2},j+\frac{1}{2},k} - \frac{1}{3}w_{1\frac{1}{2},j+\frac{1}{2},k}}{\delta r} \qquad (5.16)$$

Substituting this expression into (5.15) above, the finite difference approximation to the axial velocity Poisson equation is obtained and is given by,

$$\frac{-2w_{\frac{1}{2},j+\frac{1}{2},k} + \frac{5}{3}w_{1\frac{1}{2},j+\frac{1}{2},k} - 0.2w_{\frac{3}{2},j+\frac{1}{2},k}}{\delta r^2} + \frac{1}{r}\left(\frac{-\frac{1}{2}w_{\frac{1}{2},j+\frac{1}{2},k} + \frac{1}{2}w_{1\frac{1}{2},j+\frac{1}{2},k}}{\delta r}\right)$$

$$+\frac{w_{\frac{1}{2},j-\frac{1}{2},k} - 2w_{\frac{1}{2},j+\frac{1}{2},k} + w_{\frac{1}{2},j+\frac{3}{2},k}}{\delta\theta^2} + \frac{w_{\frac{1}{2},j+\frac{1}{2},k-1} - 2w_{\frac{1}{2},j+\frac{1}{2},k} + w_{\frac{1}{2},j+\frac{1}{2},k+1}}{\delta z^2}$$

$$\approx \frac{1}{r}\frac{A_{\frac{1}{2},j+1,k} - A_{\frac{1}{2},j,k}}{\delta\theta} - \frac{B_{1,j+\frac{1}{2},k}}{\delta r} - \frac{B_{1,j+\frac{1}{2},k}}{2r}. \qquad (5.17)$$

Similar expressions are evaluated for the remaining boundaries and velocity equations to satisfy the vorticity boundary conditions at the same timestep.

During validation, it was found that the implementation of second–order accurate vorticity boundary conditions for the tangential velocity equations produced unsatisfactory results. It was found however, that good comparisons could be obtained using first–order vorticity boundary conditions. The reason for this could not be clearly identified and may have been due to one or more of the following reasons,

- The second–order conditions may not have been applied correctly in the code.
- The mesh utilised may have been too coarse near the boundaries rendering the second–order approximation inaccurate.
- Stability problems occurred with the higher–order approximations.

5.4.4 Transient method

The vorticity transport and temperature transport equations are discretised using first–order accurate forward–difference approximations for the time derivatives. Values of the dependent variable are substituted by averages of previous and new time values, stabilising the numerical approach significantly in the same manner as the Du–Fort Frankel method. For example, Fourier's two–dimensional equation in Cartesian coordinates,

$$\frac{\partial \zeta}{\partial t} = \frac{\partial^2 \zeta}{\partial x^2} + \frac{\partial^2 \zeta}{\partial y^2} \tag{5.18}$$

is rewritten in finite difference form as,

$$\zeta_{i,j}^{n+1}\Big[\frac{1}{\delta t}+\frac{1}{\delta x^2}+\frac{1}{\delta y^2}\Big]=\zeta_{i,j}^{n-1}\Big[-\frac{1}{\delta x^2}-\frac{1}{\delta y^2}\Big]+\frac{\zeta_{i,j}^{n}}{\delta t}+\frac{\zeta_{i+1,j}^{n}+\zeta_{i-1,j}^{n}}{\delta x}+\frac{\zeta_{i,j+1}^{n}+\zeta_{i,j-1}^{n}}{\delta y}. \tag{5.19}$$

5.4.5 Multigrid method

Again the multigrid method is based on that presented in Chapter 3. However, due to having three spatial dimensions, the prolongation and restriction operators are different from the forms previously quoted. If $I_{2h}^{h}V^{2h} = V^h$ denotes the prolongation operator where h is the steplength, then the components of V^h are given by

$$\begin{aligned}
v_{2i,2j,2k}^{h} &= v_{2i,2j,2k}^{2h} \\
v_{2i+1,2j,2k}^{h} &= \frac{1}{2}(v_{2i,2j,2k}^{2h}+v_{2i+1,2j,2k}^{2h}) \\
v_{2i,2j+1,2k}^{h} &= \frac{1}{2}(v_{2i,2j,2k}^{2h}+v_{2i,2j+1,2k}^{2h}) \\
v_{2i,2j,2k+1}^{h} &= \frac{1}{2}(v_{2i,2j,2k}^{2h}+v_{2i,2j,2k+1}^{2h}) \\
v_{2i,2j+1,2k+1}^{h} &= \frac{1}{4}(v_{2i,2j,2k}^{2h}+v_{2i,2j+1,2k}^{2h}+v_{2i,2j,2k+1}^{2h}+v_{i,j+1,k+1}^{2h}) \\
v_{2i+1,2j,2k+1}^{h} &= \frac{1}{4}(v_{2i,2j,2k}^{2h}+v_{2i+1,2j,2k}^{2h}+v_{2i,2j,2k+1}^{2h}+v_{i+1,j,k+1}^{2h}) \\
v_{2i+1,2j+1,2k}^{h} &= \frac{1}{4}(v_{2i,2j,2k}^{2h}+v_{2i+1,2j,2k}^{2h}+v_{2i,2j+1,2k}^{2h}+v_{i+1,j+1,k}^{2h}) \\
v_{2i+1,2j+1,2k+1}^{h} &= \frac{1}{8}(v_{2i,2j,2k}^{2h}+v_{2i+1,2j,2k}^{2h}+v_{2i,2j+1,2k}^{2h}+v_{i+1,j+1,k}^{2h} \\
&\quad +v_{2i,2j,2k+1}^{2h}+v_{i+1,j,k+1}^{2h}+v_{i,j+1,k+1}^{2h}+v_{i+1,j+1,k+1}^{2h})
\end{aligned} \tag{5.20}$$

The restriction operator again takes the form of a full weighting operator defined by $I_h^{2h}V^h = V^{2h}$, where

$$v_{i,j,k}^{2h} = \frac{1}{64}[(v_{2i+1,2j+1,2k+1}^h + v_{2i+1,2j+1,2k-1}^h + v_{2i+1,2j-1,2k+1}^h + v_{2i+1,2j-1,2k-1}^h$$

$$+v_{2i-1,2j-1,2k+1}^h + v_{2i-1,2j-1,2k-1}^h + v_{2i-1,2j+1,2k+1}^h + v_{2i-1,2j+1,2k-1}^h)$$

$$+2(v_{2i+1,2j+1,2k}^h + v_{2i+1,2j-1,2k}^h + v_{2i-1,2j+1,2k+1}^h + v_{2i-1,2j-1,2k}^h$$

$$+v_{2i+1,2j,2k+1}^h + v_{2i+1,2j,2k-1}^h + v_{2i-1,2j,2k+1}^h + v_{2i-1,2j,2k-1}^h$$

$$+v_{2i,2j+1,2k+1}^h + v_{2i,2j+1,2k-1}^h + v_{2i,2j-1,2k+1}^h + v_{2i,2j-1,2k-1}^h)$$

$$+4(v_{2i+1,2j,2k}^h + v_{2i-1,2j,2k}^h + v_{2i,2j+1,2k}^h + v_{2i,2j-1,2k}^h$$

$$+v_{2i,2j,2k+1}^h + v_{2i,2j,2k-1}^h) + 8v_{2i,2j,2k}^h]. \tag{5.21}$$

Modification of the weighting near the boundaries due to the staggered grid strategy was not found to be required since little loss in performance was evident using the presented weighting operator. Two line relaxation sweeps are undertaken in radial, tangential and axial directions at each Multigrid level to resolve the velocity vector. The scheme is said to have converged when the absolute value of the residual is below 10^{-6}. This was found to give highly accurate results.

5.4.6 Heat transfer

The heat transfer through the outer heated cylindrical surface into the fluid and out of the fluid through the cold inner cylindrical surface is evaluated in terms of a non–dimensional heat transfer quantity known as the Nusselt number, Nu. Two forms are defined, dependent on whether it pertains to an average (total) or local heat transfer rate. The Nusselt number is defined as the ratio of heat

transfer due to convection and conduction to that due to conduction alone and is given by,

$$Nu = \frac{\dot{q}}{\dot{q}_\lambda}, \tag{5.22}$$

where λ pertains to conduction quantities and the local heat transfer is defined as,

$$\dot{q}_{local} = \frac{K\Delta T}{R}\frac{\partial T}{\partial r}. \tag{5.23}$$

The local Nusselt number is therefore given by,

$$Nu_{local} = -r\ln(r_0)\frac{\partial T}{\partial r} \tag{5.24}$$

at either $r = r_0$ or $r = 1$. The average or total heat transfer is given by,

$$\dot{q}_{total} = \frac{K\Delta T}{R}\int_0^{2\pi}\int_0^{z_{max}}\frac{\partial T}{\partial r}dz\, r\, d\theta \tag{5.25}$$

The average Nusselt number is therefore given by,

$$Nu_0 = -\frac{r\ln(r_0)}{z_{max}\,2\pi}\int_0^{2\pi}\int_0^{z_{max}}\frac{\partial T}{\partial r}d\theta\, dz \tag{5.26}$$

at either $r = r_0$ or $r = 1$. The average or total Nusselt number may therefore not be smaller than 1 as the total heat transfer from a surface must always be equal to or exceed the average heat transfer due to conduction effects alone.

The integral quantity is evaluated using the trapezoidal rule with the differential being approximated at the boundaries utilising a fourth–order accurate finite difference representation. The use of second–order approximation rendered the solution inaccurate particularly on coarse grids.

5.4.7 Precession of rolls

A measure of the rate of precession of the cyclonic/anti–cyclonic pairs is determined by evaluating even and odd Fourier components of the temperature solution with time. At each timestep therefore, the following integrals are evaluated,

$$I_s^n = \int_{r_0}^{1}\int_0^{2\pi}\int_0^{z_{max}} T(r,\theta,z)\sin(n\theta) r\, dr\, d\theta\, dz, \tag{5.27}$$

$$I_c^n = \int_{r_0}^{1}\int_0^{2\pi}\int_0^{z_{max}} T(r,\theta,z)\cos(n\theta) r\, dr\, d\theta\, dz, \tag{5.28}$$

where $n = 1, N$. Where N is the number of modes (cyclonic pairs), to be resolved and is typically taken as $N \leq 8$. These integral quantities are also evaluated using the trapezoidal rule at each timestep. One time period of the fundamental mode (e.g. $n = 6$ mode for six cyclonic/anti–cyclonic pairs solution) corresponds to the time taken for one cyclonic/anti–cyclonic pair to pass a given point and thus the rate of precession may be evaluated.

5.4.8 Code structure

The three–dimensional code strategy is very similar to the axisymmetric treatment and is loosely based on the following,

- Initialise all variables at time $t = 0$.
- Evaluate $A^{n+1}, B^{n+1}, C^{n+1}, T^{n+1}$ using the n^{th} and $n - 1^{st}$ solutions on all internal grid points.
- Compute T^{n+1} on adiabatic surfaces.
- Evaluate $I_s^{n=1,6}, I_c^{n=1,6}$ and Nu_0 using values of T^{n+1}.

- Solve the velocity equations implicitly using the Multigrid method using values of vorticity at time level $^{n+1}$ on the right–hand–side and subject to the vorticity boundary conditions.
- Update A^{n+1}, B^{n+1} and C^{n+1} on all boundaries.

The solutions do not reach a steady–state regime as the disk surfaces cause precession of the flow pattern. For this reason, no convergence criteria is specified.

5.5 Code validation

Comparisons are made with two–dimensional solutions obtained using the codes described in Chapters 3 and 4. Appropriate initial conditions and geometries are used to allow the comparisons to be made.

5.5.1 Comparison with radial/axial flow

Results obtained from the three–dimensional code may be compared with two–dimensional axisymmetric solutions if variations in the tangential direction are suppressed by using appropriate initial perturbations to the temperature field. It was found that axisymmetric solutions using the three–dimensional code were difficult to obtain unless the factor $\frac{Ra}{RePr}$ was assumed small. All the terms involving the buoyancy correction to the Coriolis force were therefore neglected for the purposes of this validation exercise.

Heat transfer comparisons at the inner and outer cylindrical surfaces are presented in Figure 5.2 for $Ra = 10^5$, $Re = 100$ and $r_0 = 0.5$. The three–dimensional

solution is computed on both $16 \times 64 \times 16$ and $24 \times 64 \times 24$ (radial, tangential and axial) grids respectively. The axisymmetric solution is grid independent and uses a 64×64 (radial/axial) grid. There is very good comparison between the solutions at locations where the local Nusselt number is relatively small. However, a poor comparison is apparent for the peak Nusselt number at the outer radius. It is anticipated that this discrepancy, in particular, is due to the poor grid definition associated with the three–dimensional simulations, with the trend suggesting improved comparisons for finer three–dimensional meshes.

Figure 5.3 again displays local Nusselt number comparisons at the inner and outer cylindrical surfaces for a larger Reynolds number. This time, a very good comparison is apparent at the outer radius with significant differences in the peak Nusselt number at the inner radius. Again, it is anticipated that this is due to the coarse nature of the grid used for the three–dimensional computation, with increase in the grid resolution suggesting an improved comparison once again.

5.5.2 Comparison with radial/tangential flow

The two–dimensional, axially invariant computations may be compared with the three–dimensional code results for cavities of large axial extent. At the mid–axial plane, no axial velocity occurs for a constant wavenumber solution. In addition, all derivatives with respect to the axial coordinate are approximately zero.

In order to evaluate the desired axial extent of the cavity for the solution at the mid–axial plane to be approximately independent of the disks, solutions for the variation of the local heat transfer at the mid–axial plane of the inner hub for various maximum axial dimensions are presented in Figure 5.4. An initial

$n = 6$ perturbation to the base solution results in a steady precession of six cyclonic/anti–cyclonic pairs. An increase in the maximum axial dimension, z_{max}, of the cavity results in an increase in the peak Nusselt numbers. For the smaller dimensions considered, the effect of the disks at the mid–axial plane is very significant. The $z_{max} = 4.0$ and $z_{max} = 6.0$ solutions show that any further increase in the axial dimension should have a negligible effect on the mid–axial plane heat transfer. Thus, for the comparison with the two–dimensional axisymmetric code, the axial dimension of the cavity is taken as $z_{max} = 6.0$.

Figure 5.5 shows this comparison for various radial grid intervals as this has a strong effect on the three–dimensional solutions. It is noted, that an increase in the radial definition results in a reduction of the peak Nusselt number toward the two–dimensional solution. Only small differences around the minima in the heat transfer appear. It is anticipated that a further increase in the number of radial intervals would reduce the peak in the heat transfer toward the two–dimensional and a grid–independent solution. It is also important to note, that comparisons are being drawn based on collocated and staggered methodologies with first–order accurate vorticity boundary conditions being applied to the tangential velocity Poisson equation in the three–dimensional code. The influence of the number of axial intervals on the solution has not been investigated fully due to the additional computational expense. This may however have a further influence on the maximum Nusselt numbers.

The local Nusselt numbers considered for the radial/tangential flow are far in excess of those corresponding to radial/axial flow. Thus, it may be expected that inaccuracy in evaluating the temperature derivative at the boundaries to be amplified significantly by the use of a relatively coarse grid structure.

5.6 Computational expense

Due to the three Poisson equations for velocity to be resolved at each timestep, the scheme is computationally expensive. The work required to resolve each Poisson equation adequately such that the maximum residual is less than 10^{-6}, ranges between 10 and 25 V–cycles, depending on the grid distribution, time–step and values of non–dimensional parameters. In particular, the number of V–cycles is minimised when individual cells are approximately square. An increase in the grid resolution also has an adverse effect on the maximum timestep for stability as has been shown in Section 3.5.3. This is particularly restrictive when the maximum number of timesteps is limited.

For any given simulation, the minimum number of timesteps evaluated is 5000 with a maximum number of 15000 timesteps for larger Rayleigh number flows. The computational time in real terms therefore varies between three and nine days on a Silicon Graphics Power Challenge with a R10000 processor and 256 Mb RAM.

5.7 Initial conditions

The initial conditions again correspond to solid–body rotation with a conducting temperature field which is given by,

$$A = B = C = 0, \qquad u = v = w = 0, \qquad T = 1 - \frac{\ln r}{\ln r_0}.$$

In order to perturb this initial solution, two methods are used. A point perturbation may be introduced in the temperature field where,

$$T(\tfrac{1}{4}(1-r_0),\pi,\tfrac{1}{4}z_{max}) \rightarrow T_B(\tfrac{1}{4}(1-r_0),\pi,\tfrac{1}{4}z_{max}) - 0.02. \qquad (5.29)$$

Alternatively, if a predetermined azimuthal wavenumber is required, then the following perturbation to the temperature field is introduced,

$$T = T_B + A(1-r)(r-r_0)\cos(n\theta), \qquad (5.30)$$

where n is the wavenumber and A the perturbation amplitude which is typically within the range,

$$0 < A \leq 0.5.$$

5.8 Numerical simulation results

The results presented here are of a qualitative nature and are not intended for quantitative comparison. The spatial resolution in particular, tends to be poor for the larger Rayleigh number cases considered here with a minimum of $16 \times 128 \times 16$ (radial, tangential and axial) intervals respectively being used and a maximum grid resolution for the larger Rayleigh number cases corresponding to $24 \times 128 \times 24$ (radial, tangential and axial) intervals.

The cyclonic regions rotate in the anti–clockwise sense and in the same sense as the direction of rotation of the cavity. The anti–cyclonic regions rotate in the opposite sense to the cavity walls and correspond to clockwise rotation. In general, it is difficult to determine the direction of rotation of the circulations due to the poor resolution in the vector plotting package, but the direction of

rotation may be obtained by examination of the isotherms.

Again some solutions presented here correspond to cases for which $\beta\Delta T > 1$ and these have to be treated with caution.

5.8.1 Solutions for various initial profiles with $Ra = 10^5$, $Re = 10^3$, $r_0 = 0.5$ and $z_{max} = 0.5$.

In order to investigate the dependence of the solution on the wavenumber of the initial disturbance, the rotational Rayleigh and Reynolds numbers are held fixed for a constant geometry cavity. The initial temperature field profile corresponds to that presented in equation (5.30) and solutions are evaluated on a $16 \times 128 \times 16$ grid with a non–dimensional timestep corresponding to $\delta t = 0.0002$.

Figures 5.6 show the flow vectors and corresponding isotherms at three axial locations for an $n = 6$ perturbation. The primary flow is in the radial/tangential plane with little variation in the structure in the axial direction. Very near to the disk surfaces, the cyclonic/anti–cyclonic pairs weaken due to the no–slip velocity boundary conditions with little variation in the form of the isotherms apparent. Six identical cyclonic/anti-cyclonic pairs have developed, with the cyclonic regions dominating in size. This is due to the outer heated cylindrical shroud acting to strengthen the precessing cyclonic regions and suppress the precessing anti–cyclonic regions as is shown in Figure 5.7 which displays the cavity in a rotating frame which is fixed to the precessing rolls. At the inner, cooled cylindrical hub, the converse holds but the effect is less dominant due to the smaller radius.

Figures 5.8a–c display axial velocity iso–lines at identical axial locations to those presented in Figures 5.6. Figures 5.8a,c corresponds approximately to locations where the axial velocities are at their maximum. At $z = 0.09375$, cyclonic regions correspond to positive axial velocities. Conversely, where there is a region of anti–cyclonic circulation, a region of negative axial velocity occurs with the cores of maximum or minimum axial velocity corresponding to the cores of the rolls. At $z = 0.25$, which corresponds to the mid–axial plane, the axial velocity is zero. At $z = 0.40625$, a cyclone corresponds to a negative region of axial velocity, and where there is an anti–cyclone, a positive region of axial velocity is apparent.

Therefore, where there is a cyclone, fluid moves axially away from the disks and where there is an anti–cyclone, fluid moves axially toward the disks. This corresponds to the findings of Long and Tucker (1994), who studied a buoyancy–induced flow in a cavity with axial through–flow.

For unsteady, inviscid slow flow, the axial momentum equation may be rewritten,

$$\frac{\partial w}{\partial t} = -\frac{1}{\rho_0}\frac{\partial P}{\partial z}. \tag{5.31}$$

From inspection of equation (5.31), it may be seen that axial velocity may only be induced if there is an axial variation in the pressure distribution. This occurs in particular near the disks, where the pressure of the fluid on the disk surfaces differs from that in the cyclonic/anti–cyclonic regions away from the disks. As has been discussed in Section 4.8, radial inflow occurs if $\frac{\partial P}{\partial \theta} > 0$ and radial outflow occurs if $\frac{\partial P}{\partial \theta} < 0$. Hence, the pressure at the core of a cyclonic region is less than that at the core of an anti–cyclonic circulation. The pressure of the fluid at the disk surface may be assumed to be at a pressure midway between the cyclonic/anti–cyclonic region pressures. Thus, for increasing axial dimension away from the

disk, at a tangential location where there exists a cyclonic region, $\frac{\partial P}{\partial z} < 0$ and hence a positive region of axial velocity occurs, (away from the disk). Similarly, for increasing axial dimension away from the disk, at a tangential location where there exists an anti–cyclonic region, $\frac{\partial P}{\partial z} > 0$, resulting in a negative region of axial velocity toward the disk.

A similar argument may be used to justify the sign of the axial velocities near the remaining disk surface.

Figure 5.8d displays the variation of the total heat transfer with time. The Nusselt number stabilises at a constant value by a non–dimensional time of $t \approx 0.15$. The cyclones and anti–cyclones however precess in the clockwise sense as is depicted in Figure 5.8e. The Fourier decomposition of the temperature field with non–dimensional time shows that a steady precession of the rolls occur with the $n = 6$ modes dominating. No higher harmonics are apparent since only the first six Fourier components are evaluated for each computation. It is however anticipated that higher modes occur due to the mildly non–linear nature of the flow.

The solutions for an $n = 5$ initial perturbation to the temperature field are shown in Figures 5.9 and 5.10. The mid–axial plane flow vectors and isotherms, (Figure 5.9a,b), show that the resulting structure consists of five cyclonic/anti–cyclonic pairs consisting of five arms each of radial outflow and radial inflow of fluid. Again the cyclonic regions dominate in size with the isothermal nature of the core of the circulations, prominent in the axisymmetric radial/tangential flow, not being apparent at these particular operating conditions. Axial velocity iso–lines between $z = 0$ and $z = 0.25$ are presented in Figures 5.9c–f. At the disk surface the axial velocity is zero with an increase in the magnitude away from

the disk. At $z = 0.09375$, the magnitude of the axial velocities is approximately a maximum with a significant decrease having occurred by $z = 0.1875$. At the mid–axial plane, there is zero axial velocity. Figures 5.10a–c are axial velocity iso–lines for the remaining half of the cavity and correspond to those of Figures 5.9. It is seen that the flow structure is exactly symmetric about the mid–axial plane.

The magnitude of the maximum axial velocity is approximately 30% of the maximum radial velocity and approximately 40% of the maximum tangential velocity magnitude. Thus, the axial flow corrections near the disk surfaces are significant.

Figure 5.10d shows a decrease in the heat transfer, (c.f. Figure 5.8d), as a result of the decrease in the number of cyclonic and anti–cyclonic pairs. Again, the Fourier decomposition of the temperature field shows that the rolls precess steadily relative to the rotating surfaces, with the $n = 5$ mode dominating.

The solutions from an initial $n = 4$ perturbation are presented in Figures 5.11. At the end of the computation, the flow comprises four anti–cyclonic regions and four larger cyclonic circulations. Figure 5.11d suggests that the flow is periodic in time with three distinct points of interest in the time period. At the minimum point, marked as (1), the flow structure corresponds to that presented in Figures 5.12 at a time $t = 0.40$. The cyclonic regions have split into two distinct circulations and at this time remain without an associated anti–cyclonic region in between. At the later time $t = 0.45$, where there is a bump in the heat transfer plot, (marked as (2)), associated anti–cyclonic regions are now apparent between the two cyclones. However, two of the cyclones are more dominant than the remaining two. At time $t = 0.48$, (marked as (3)), the $n = 8$ mode has decayed and the $n = 4$ solution

now dominates again. The flow structure therefore periodically changes from an $n = 4$ instability to a non–uniform $n = 8$ instability. Figure 5.11d shows the dominant $n = 4$ and $n = 8$ modes and records the precession of the rolls with time.

Figures 5.13 display the solutions using an initial $n = 3$ perturbation to the temperature field profile. The mid–axial plane flow vectors and isotherms show that the resulting instability corresponds to an $n = 6$ flow, with the $n = 3$ disturbance growing initially, but eventually decaying as the $n = 6$ solution grows. The axial velocity iso–lines show that the flow moves axially away from the disk in regions of anti–cyclonic behaviour and toward the disk in regions of cyclonic circulation. Figure 5.13e displays the Fourier decomposition of the temperature field. The initial $n = 3$ perturbation is dominant up to a time $t \approx 0.07$, but is subsequently stabilised with the $n = 6$ mode dominating and displaying the characteristic precession of the cyclonic/anti–cyclonic pairs.

Further decrease in the initial wavenumber profile is presented in Figures 5.14. Here, an $n = 2$ perturbation is used, but this mode is found not to persist. Non-linear effects give rise to $n = 4$ components and the resulting flow is very similar to that for the initial $n = 4$ perturbation to the temperature field, with the instability periodically changing from the $n = 4$ structure to an $n = 8$ structure. Figure 5.14e shows the initial $n = 2$ profile decaying and subsequently the domination of the $n = 4$ mode. The mid–axial plane flow vectors and isotherms, show four main cyclonic regions with the opposing anti–cyclonic region pairs differing in form. These regions are split into a further two distinct regions, whilst the remaining two anti–cyclones remain as single clockwise circulations. This may explain the higher mode activity present in Figure 5.14e, where the $n = 6$ modes

become prominent at certain times.

5.8.2 Solution for various Reynolds numbers with $Ra = 10^5$, $r_0 = 0.5$ and $z_{max} = 0.5$

To investigate the variation in the flow structure with change in the rotational Reynolds number, the Rayleigh number and the geometry are held fixed and the Reynolds number is allowed to vary. Solutions are again obtained on $16 \times 128 \times 16$ radial/tangential/axial interval grids and using a non–dimensional timestep of $\delta t = 0.0002$. Initial conditions correspond to a point perturbation to the temperature field as given by equation (5.29).

Figures 5.15 show the solutions for $Re = 200$. The mid–axial plane flow vectors and isotherms at the end of the computation show essentially an $n = 4$ wavenumber structure, with very limited axial variations in the flow structure apparent apart from that experienced at close proximity to the disk surfaces where the effect of the no–slip boundary conditions attenuates the flow. The four cyclonic/anti–cyclonic pairs are however not equally spaced and are not uniform in size. It is also noted that the cyclonic structures are smaller than the anti–cyclones with their cores located toward the outer heated cylindrical surface. Figure 5.15c shows a snapshot of axial velocity iso–lines near one of the disks. Unlike the cases considered earlier for $Re = 10^3$, in regions of cyclonic flow, the axial velocity is away from the disks and toward the disks in regions of anti–cyclonic activity. Although this effect is not entirely intuitive, it may be associated with the increase in the magnitude of the buoyancy correction to the Coriolis terms for small Reynolds numbers. Equation (5.3) may therefore be rewritten in dimensional form for steady and inviscid flow with buoyancy correction to the Coriolis

term included as,

$$2\Omega u - \beta(T - T_c)2\Omega u = 2\Omega u(1 - \beta(T - T_c)) = -\frac{1}{\rho_0 r}\frac{\partial P}{\partial \theta}. \qquad (5.32)$$

Hence, in the instance where the magnitude of the buoyancy correction to the Coriolis term is greater than the pure Coriolis term, the pressure at the core of a cyclonic region will be greater than that at the core of an anti–cyclonic region. This subsequently results in the flow moving axially away from the disks in anti–cyclonic regions and towards the disk in regions of cyclonic activity.

The variation of the total heat transfer with time suggests that the flow is unsteady but not periodic, (Figure 5.15d). The Fourier decomposition shows that up to a non–dimensional time $t \approx 0.25$, an $n = 6$ structure dominates with the structure changing to an $n = 4$ pattern. Although the flow is unsteady in time and the rolls unevenly spaced, the precession occurs at an approximately uniform rate as suggested by the almost constant wavelength of the $n = 4$ Fourier coefficients.

Figures 5.16 show the solutions for $Re = 300$. At the end of the computation, a four cyclonic/anti–cyclonic pair structure is apparent. The cores of the cyclones tend toward the outer heated cylindrical shroud whilst the position of the cores of the anti–cyclonic regions tend toward the cooled inner cylindrical hub. Again, little variation in the form of the solution is apparent axially, with the mid–axial plane vectors and isotherms being representative of the flow structure axially across the cavity. Due to the relatively large magnitude of the buoyancy correction to the Coriolis terms, fluid moves axially away from the disks in regions of anti–cyclonic flow and toward the disks in regions of cyclonic flow. This effect is less pronounced than for the lower Reynolds number case considered above,

with poor definition apparent between regions of positive and negative axial velocity. Figures 5.16d and 5.16e show that the flow is aperiodic with all the modes prominent up to a time $t \approx 0.85$. Subsequent to this, the $n = 4$ modes are prominent with the other Fourier components decaying. An increase in the heat transfer with increase in Reynolds number around these conditions also suggests the dominance of the buoyancy correction to the Coriolis terms.

A further increase in the Reynolds number results in an increase in the vigour of the flow. Figures 5.17 display solutions for a Reynolds number $Re = 500$. The flow vectors and the isotherms at the mid–axial plane suggest an $n = 6$ structure at the end of the computation with a very large cyclone in the lower right quarter of the cavity being present. In the upper region of the cavity, the cyclones and the anti–cyclones tend to be well matched in size with regions of cyclonic activity resulting in axial flow away from the disks and anti–cyclonic circulation resulting in axial flow velocities toward the disks, (Figure 5.17c). An increase in the level of the heat transfer suggests that initial increase in the Reynolds number results in amplification of the flow similar to the findings of the radial/axial axisymmetric computations presented in Chapter 3. The Fourier decomposition of the temperature field, (Figure 5.16e), shows that many of the Fourier modes evaluated are significant with the most dominant corresponding to $n = 3$ and $n = 6$ modes. It is however very difficult to evaluate a precession rate from this data, as the solution suggests that the size, position and the number of individual cyclones and anti–cyclones vary significantly with time.

Figures 5.18 show the solutions for a Reynolds number of $Re = 800$. Here, the mid–axial plane flow vectors and isotherms show a uniformly spaced $n = 5$ instability at the end of the computation. The cyclonic regions are once again,

dominant with respect to their size. Figure 5.18e displays the Fourier decomposition of the temperature field with time. Three distinct regions may be identified. Up to a time $t \approx 0.1$, amplification of the local point perturbation occurs, with the amplitude of the displayed Fourier components being approximately zero. Subsequently, an $n = 5$ mode grows with a subdominant $n = 6$ component still prominent. This situation remains until $t \approx 0.55$ when the characteristic wavenumber of the flow changes to $n = 6$ with six cyclonic/anti–cyclonic pairs appearing. At the point of transition between the $n = 5$ instability to the $n = 6$ instability, a sharp change in the total heat transfer occurs, (Figure 5.18d). A decrease in the heat transfer suggests that the preferred number of rolls does not correspond to the maximisation of the heat transfer. The increase in the Reynolds number from that presented in Figures 5.17 suggests that such an increase now stabilises the flow. It is also unlikely that at a future time the $n = 6$ instability will break down as the $n = 5$ Fourier component in the decomposition is seen to decay rapidly, but this has not been investigated.

Solutions for a Reynolds number $Re = 10^3$ show that the preferred number of cyclonic/anti–cyclonic pairs for the conditions considered is six. The flow is again seen to be further stabilised by this increase in the Reynolds number, (Figure 5.19d), with a steady precession of the cyclonic/anti–cyclonic pairs occurring, (Figure 5.19e).

Figures 5.20 display the early development of an $n = 5$ instability for $Re = 1.5 \times 10^3$. Again, the cyclonic/anti–cyclonic pairs are distributed evenly around the cavity with the cyclonic regions being dominant in size over the anti–cyclonic circulations. A further decrease in the heat transfer, (Figure 5.20d) with increase in the rotational Reynolds number has occurred. Further increases in the

Reynolds number up to $Re = 2000$, results in a full stabilisation of the flow, with the fluid being in solid–body rotation with a purely conducting temperature field.

5.8.3 Solution for various Reynolds numbers with $Ra = 10^6$, $r_0 = 0.5$ and $z_{max} = 0.5$

This increase in the Rayleigh number will cause an increase in the convection rates due to the strength of the buoyancy forces and hence velocity gradients will also increase. In order to resolve these higher gradients an increase in the grid resolution is required and therefore a mesh of $24 \times 128 \times 24$ intervals was used which consisted of approximately $80,000$ mesh points. The timestep used ranged between $\delta t = 0.00004$ and $\delta t = 0.00001$ and these levels were determined by eliminating numerical instabilities. Again a point perturbation of the base solution was used to start the computations presented below.

Initially, a small–Reynolds–number flow was considered where the magnitude of the buoyancy correction to the Coriolis term is very significant. Figures 5.21 display the solutions obtained for $Re = 500$. The flow is chaotic with large fluctuations in the heat transfer being apparent with time. This is also evident in the Fourier decomposition of the temperature field, which shows that all of the modes which are evaluated are significant. At the end of the computation, the flow structure at the mid–axial plane is that presented in Figures 5.21a and 5.21b. Anti–cyclones dominate due to the magnitude of the buoyancy correction to the Coriolis terms, with relatively small regions of cyclonic flow being apparent. The isotherms show that the cores of the anti–cyclonic regions are approximately isothermal with axial flow in these regions away from the disks, (Figure 5.21c).

Figures 5.22 show the solutions obtained for $Re = 10^3$. Again the flow is time–dependent with the Fourier decomposition of the temperature field showing that the $n = 3$ and $n = 6$ modes are dominant, particularly towards the end of the computation. The flow structure at the end of the computation consists of three distinct arms of radially out–flowing fluid. The flow structure and isotherms vary little axially, hence only those at the mid–axial plane are presented. The cyclonic regions tend to dominate in size. It is however unclear as to whether flow moves axially away or toward the disks in the regions of cyclonic flow. This is due to the magnitude of the Coriolis and the buoyancy correction to the Coriolis terms approximately balancing. An increase in the total heat transfer is also apparent with this initial increase in the Reynolds number to 1000 from 500.

A further increase in the Reynolds number to $Re = 2 \times 10^3$ results in the solutions presented in Figures 5.23. The cyclonic circulations appear to be increasingly dominant, with the anti–cyclonic regions being very small. Their locations may however be identified by the location of negative axial velocity in Figure 5.23c. Both the variation in heat transfer and the Fourier decomposition of the temperature field with time show the chaotic nature of the flow structure. The cores of the cyclonic regions display their characteristic isothermal temperature distribution with large gradients in the temperature evident near the inner cylindrical hub in particular.

Figures 5.24 display the solutions for $Re = 5 \times 10^3$. The buoyancy correction to the Coriolis force is now small in magnitude with the buoyancy and Coriolis forces dominating. The increase in the magnitude of the Coriolis force as a result of increase in the rotational Reynolds number has resulted in a decrease in the heat transfer due to the stabilising effect of the Coriolis terms, (Figure 5.24d).

The flow structure at the end of the computation comprises of three dominant radially out–flowing arms of fluid, (Figure 5.24b), with other weaker radial arms in evidence.

A further increase in the Reynolds number to $Re = 10^4$ results in a more coherent structure. Figure 5.25 shows the variation of the total heat transfer with time. The fluctuations apparent in previous calculations at lower Reynolds numbers have been substantially damped, at least, for the timescale considered here. Indeed, larger timescale fluctuations may occur, but this could not be investigated given the additional computational expenditure required. Figure 5.26 shows the Fourier decomposition of the temperature field. The dominant modes correspond to an $n = 6$ wavenumber, hence strongly suggesting that an $n = 6$ instability is dominant given the initial point perturbation starting condition. Figures 5.27 show the mid–axial plane flow vectors and isotherms at three points in time; $t = 0.05$, $t = 0.10$ and $t = 0.15$. At $t = 0.05$, the initial point disturbance is yet to penetrate the entire cavity with the area around $\theta = 0$ being undisturbed. Figures 5.27c and 5.26d show the flow structure at time $t = 0.1$. A coherent structure has evolved, with seven radial arms of fluid evident and corresponding to seven pairs of cyclones/anti–cyclones. The pairs are however not evenly distributed with the cyclones dominating in size over the anti–cyclones. Finally, at a time $t = 0.15$, the $n = 7$ pattern has decayed and an $n = 6$ structure is now apparent. Again, the anti–cyclonic regions are very small and correspond to regions of axial flow away from the disk surfaces.

The sizes of the cyclones and anti–cyclones vary significantly with the distance between the disks. For the hypothetical case where the disks are an infinite distance apart, their influence on the mid–axial plane flow is infinitesimally small,

and hence the cyclones and anti–cyclones would be dependent only on the magnitude of the buoyancy correction to the Coriolis force terms. Conversely, when the distance between the disks is small, the cyclonic circulations will tend to be larger than the anti–cyclonic circulations.

5.8.4 Solutions for various Reynolds numbers with $Ra = 10^6$, $r_0 = 0.3$ and $z_{max} = 0.5$

Two cases are considered here to gain an understanding of the changes to the flow due to a decrease in the inner radius. The mesh resolution corresponds to $32 \times 128 \times 24$ (radial/tangential and axial) intervals with a timestep corresponding to $\delta t = 0.00002$.

Significant changes in the buoyancy–induced flow structure arise as a result of the decrease in inner radius. At the end of the computation for $Re = 10^3$, the flow vectors and isotherms, (Figure 5.28a,b) show two main regions of radial outflow with the radial inflow regions being less distinct. At each of the outflow regions, a cyclonic/anti–cyclonic pair exists. In the mid-axial plane, fluid flows tangentially from the anti–cyclonic region of one pair toward the cyclonic region of the other. At some future time, the appearance of another radial arm of fluid may occur, as a small deviation of the isotherms is apparent at the inner cylindrical hub at $\theta \approx 100°$. The isotherms show the occurrence of relatively large isothermal areas at a temperature only slightly cooler than the hot cylindrical surface temperature. The temperature gradients at the inner hub are far in excess of those on the outer cylindrical shroud, (shown by the density of the isotherms in these areas). This occurs as a result of the small surface area of the inner hub in comparison with the outer shroud surface area.

Figure 5.28c shows the occurrence of a region of axial velocity toward the disks where there is anti–cyclonic flow with a region of axial velocity away from the disks near the inner cylindrical hub. This is due to the dominant magnitude of the buoyancy correction to the Coriolis force over the pure Coriolis terms. The variation of heat transfer with time, (Figure 5.28d), indicates the unsteady nature of the instability and comparison with Figure 5.22d shows only a small decrease in the level of the heat transfer as a result of the decrease in the inner radius. The Fourier decomposition of the temperature field shows the dominance of the $n = 2$ mode at the latter stages of the computation, with various modes dominating before this time.

The result of increasing the Reynolds number to $Re = 2 \times 10^3$ is shown in Figures 5.29. Three main regions of cyclonic flow are apparent, with smaller anti–cyclonic regions between. The regions of radial outflow are not as distinct on the isotherm plot, (Figure 5.29b), as for the previous, lower Reynolds number case. The cyclones and anti–cyclones may be more easily identified by using the axial velocity iso–line contour plot. Cyclonic activity occurs in regions of positive axial velocity and ani–cyclonic flow in areas of negative tangential velocity with the cores of these regions coinciding with the maxima and minima regions in Figure 5.29c. Two of the anti–cyclones have two distinct cores at the end of the computation; one is located near the outer cylindrical shroud and the other smaller core is near to the inner cold hub.

Figure 5.29d shows that an increase in the level of the heat transfer occurs with increase in the Reynolds number for the range of Reynolds number considered here. This is due to the decrease in magnitude of the buoyancy correction to the Coriolis force terms. The Fourier decomposition of the temperature field shows

that no single mode is dominant over the time period considered here due to the localised nature of the jets. At the initial stages as the disturbance travels around the cavity, the $n = 6$ modes dominate and subsequently decay with the $n = 2$ and $n = 3$ modes generally dominating at later times. This suggests that the flow structure does not vary significantly from that at the end of the computation.

Further simulations were attempted for larger Reynolds numbers but, due to constraints on the grid resolution and timestep, it was only possible to compute the initial amplification of the point perturbation and early stages of the disturbance travelling around the cavity given the computational time involved.

5.8.5 Solutions for various Rayleigh numbers with $Re = 10^3$, $r_0 = 0.5$ and $z_{max} = 0.5$

Two further computations were undertaken to investigate more fully the influence of the Rayleigh number on the flow characteristics for a constant Reynolds number and geometry.

Initially, the case for $Ra = 10^5$, presented in Figures 5.19 is summarised before introducing the results for higher Rayleigh numbers. At these operating conditions, a steady $n = 6$ flow develops, the cyclonic regions being larger than corresponding anti–cyclonic regions. The steady state average Nusselt number is $Nu_0 \approx 1.8$.

An increase in the Rayleigh number to $Ra = 2 \times 10^5$ (see Figures 5.30), results once again in a steady precessing state with a $n = 6$ structure apparent. A substantial increase in the heat transfer is observed, with the steady state total

Nusselt number being $Nu_0 \approx 2.6$. A small increase in the comparative sizes of the cyclonic to anti–cyclonic circulations is also apparent and is as a result of the increase in the magnitude of the buoyancy correction to the Coriolis terms which largely control the rate of precession of the rolls. The rate of precession is therefore seen to increase by inspection and comparison of the Fourier decomposition of the temperature field distributions with time.

Further increase in the Rayleigh number is presented in Figures 5.31 for $Ra = 5 \times 10^5$. The flow vectors and isotherms show four dominant arms of radial outflow present at the end of the computation. These are not however evenly distributed, with the cyclones and anti–cyclones being of various sizes and strengths. The flow is unsteady in time with no apparent prospect of steadily precessing flow. Again a further increase in the heat transfer occurs, with a mean total Nusselt number of $Nu_0 \approx 3.5$. The core of each cell becomes increasingly isothermal with increase in the Rayleigh number also.

A case considered and presented previously in Figures 5.22, is that for $Ra = 10^6$. At the end of the computation, the flow is of an $n = 3$ form and is unsteady with time. The mean total heat transfer is $Nu_0 \approx 4.5$, which represents another increase in the heat transfer rate, indeed it is likely that Nu_0 always increases with increasing Rayleigh number. Comparison with the $Ra = 5 \times 10^5$ case shows an increase in size of the isothermal regions at the core of the circulations, with large areas of flow with only small temperature gradients apparent.

5.8.6 Solution for cavity with $Ra = 10^5$, $Re = 10^3$, $r_0 = 0.5$ and $z_{max} = 0.3$

The effect of decrease in the maximum axial dimension of the cavity is considered here. The mesh used comprised of $24 \times 128 \times 16$ (radial, tangential, axial) and a non–dimensional time–step $\delta t = 0.0002$.

Figures 5.32a,b show the end point flow vectors and isotherms for an $n = 5$ instability. The cyclones and anti–cyclones are approximately uniformly distributed throughout the cavity, with size of the cyclonic regions far exceeding the size of the anti–cyclonic regions. Comparison with Figures 5.10 for a cavity with $z_{max} = 0.5$ however shows little difference in the comparative sizes of the cyclones and anti–cyclones between the two cases. The most apparent difference is in the heat transfer, with a reduction in the total Nusselt number with decrease in the axial–dimension of the cavity due to the retardation experienced as a result of the proximity of the disks. A distinct decrease in the rate of precession of the rolls is also apparent with the reduction in the gap between the disks.

5.9 Brief conclusions

Strong similarities in the flow structure exist between the three–dimensional and two–dimensional flow presented in Chapter 4. As for the radial/tangential flow, the instability takes the form of cyclonic/anti–cyclonic activity in the radial/tangential plane. In addition, when the Coriolis force is dominant over the buoyancy correction, where there is a cyclone, fluid moves axially away from the disks. In regions of anti-cyclonic activity, fluid moves axially toward the disk

surfaces. If the buoyancy correction dominates, the converse holds. Similarities with the two–dimensional radial/axial flow regime (presented in Chapter 3) are limited to the effect of the non–dimensional parameters, with the rotational axis of the circulations being parallel to the enclosure rotational axis.

As in Section 3, attention is drawn to the fact that flows for which $\frac{Ra}{Re^2 Pr} = \beta \Delta T > 1$ may only be regarded as being qualitatively correct as the fluid takes negative densities in part of the computational domain.

In general, the flow is more likely to be time–dependent as a result of introducing the disk boundaries, with wavenumber halving/doubling being one of the possible time–dependent regimes. The Coriolis, buoyancy and buoyancy correction to the Coriolis force terms, have the same stabilising/de–stabilising effect as concluded for the radial/axial flow. In addition, an increase in the magnitude of the buoyancy correction results in an increase in the rate of precession of the cyclonic/anti–cyclonic pairs as is concluded for the radial/tangential flow presented in Chapter 4. Further retardation of the cyclones and anti–cyclones occurs with decrease in the distance between the two disks.

The three–dimensional flow, therefore, includes characteristics of both the two–dimensional radial/axial and radial/tangential flows. In addition, significant three–dimensional effects are apparent particularly near the disk surfaces.

Chapter 6

Sealed cavity with a stationary shroud

6.1 Summary

A schematic of the geometry being considered is shown in Figure 1.7. The cavity is characterised by having a stationary shroud with all other surfaces rotating at a uniform angular velocity. The tangential velocity discontinuity between the rotating disks and the stationary shroud, for the sealed cases considered, is the source of flow motion. In this chapter the development of the axisymmetric code presented in Chapter 3 to include a non–uniform grid distribution is also discussed.

Two geometries are considered which relate to two practical engineering situations. Initially, a simplified model of co–rotating turbine disks is considered where the aspect ratio of the cavity is taken as $s/R = 0.3$. A further application investigated briefly is the air flow between disks where $s/R = 0.05$. Such a small gap–aspect–ratio cavity is typical of the those found in computer disk

drives (Abrahamson *et al.*, 1989), where the thermal distortion of a disk drive during the long start up transient requires to be minimised.

6.2 Governing equations

The non–dimensional governing equations in streamfunction–vorticity form for axisymmetric flow in a rotating frame of reference are exactly the same as those presented in §3.2, but are repeated here again for completeness,

$$\omega = \nabla^2\phi - \frac{1}{r^2}\phi, \tag{6.1}$$

$$\frac{1}{Pr}\Big[\frac{\partial\omega}{\partial t} + J(\omega,\phi) - \frac{1}{r}(\phi\frac{\partial\omega}{\partial z} + \omega\frac{\partial\phi}{\partial z}) - \frac{2v}{r}\frac{\partial v}{\partial z}\Big] - 2Re\frac{\partial v}{\partial z} + \frac{2Ra}{RePr}(T\frac{\partial v}{\partial z} + v\frac{\partial T}{\partial z})$$
$$+ rRa\frac{\partial T}{\partial z} = \nabla^2\omega - \frac{1}{r^2}\omega, \tag{6.2}$$

$$\frac{1}{Pr}\Big[\frac{\partial v}{\partial t} + J(v,\phi) + \frac{1}{r}(v\frac{\partial\phi}{\partial z} - \phi\frac{\partial v}{\partial z})\Big] + 2Re\frac{\partial\phi}{\partial z} - \frac{2Ra}{RePr}T\frac{\partial\phi}{\partial z} = \nabla^2 v - \frac{1}{r^2}v, \tag{6.3}$$

$$\frac{\partial T}{\partial t} + J(T,\phi) - \frac{1}{r}\phi\frac{\partial T}{\partial z} = \nabla^2 T \tag{6.4}$$

where the Jacobian is given by,

$$J(A,B) = \frac{\partial A}{\partial r}\frac{\partial B}{\partial z} - \frac{\partial B}{\partial r}\frac{\partial A}{\partial z}.$$

This is treated as an iso–thermal forced convection problem, unlike the buoyancy–induced flow problems considered previously. Free–convection effects are therefore neglected for the purposes of this investigation and hence the Rayleigh number is taken as $Ra = 0$. The buoyancy force and temperature equation are however retained in the governing equations for the purposes of code validation.

After validation isothermal flows are computed using equations (6.1)–(6.3) with

$Pr = 0.71$. We note that the non–dimensionalisation used to generate these equations are inappropriate for isothermal flows since they are independent of Pr. However, the solutions presented here may be regarded as a numerically scaled version of the appropriate non–dimensional equations: if we set $v = Prv^*$, $\phi = Pr\phi^*$, $\omega = Pr\omega^*$ and $t = Pr^{-1}t^*$ into equations (6.1)–(6.3) dropping the * notation we obtain

$$\omega = \nabla^2\phi - \frac{1}{r^2}\phi, \tag{6.5}$$

$$\frac{\partial\omega}{\partial t} + J(\omega,\phi) - \frac{1}{r}(\phi\frac{\partial\omega}{\partial z} + \omega\frac{\partial\phi}{\partial z}) - \frac{2v}{r}\frac{\partial v}{\partial z} - 2Re\frac{\partial v}{\partial z} = \nabla^2\omega - \frac{1}{r^2}\omega, \tag{6.6}$$

$$\frac{\partial v}{\partial t} + J(v,\phi) + \frac{1}{r}(v\frac{\partial\phi}{\partial z} - \phi\frac{\partial v}{\partial z} + 2Re\frac{\partial\phi}{\partial z} = \nabla^2 v - \frac{1}{r^2}v, \tag{6.7}$$

The results are presented in the form of solutions to equations (6.1)–(6.3) and only those figures involving the time (t) need to be interpreted with care.

For radial velocity comparisons to be made with experimental data, the vorticity definition (equation (3.11)) and divergence constraint (equation (3.6)) may be combined to give a Poisson equation for the radial velocity field which takes the form,

$$\nabla^2 u - \frac{1}{r^2}u = \frac{\partial\omega}{\partial z}. \tag{6.8}$$

6.3 Boundary conditions

The cavity is assumed to be sealed with no–slip boundaries and a negative dimensional outer cylindrical shroud velocity of $-\Omega R$ to take account of the rotating frame of reference. Using the same non–dimensionalisation as presented in Section 3.2 this corresponds to a non–dimensional tangential velocity of $-Re \times Pr$ (or equal to $-Re$ for equations (6.5)–(6.7)). The following boundary conditions

are therefore prescribed for equations (6.1)–(6.4),

At the shroud, $r = 1$, the boundary conditions are that,

$$\phi = 0, \qquad \frac{\partial \phi}{\partial r} = 0, \qquad v = -Re \times Pr, \qquad u = 0.$$

At the hub, $r = r_0$, the boundary conditions are that,

$$\phi = 0, \qquad \frac{\partial \phi}{\partial r} = 0, \qquad v = u = 0.$$

At the disk, $z = 0$, the boundary conditions are that,

$$\phi = 0, \qquad \frac{\partial \phi}{\partial z} = 0, \qquad v = u = 0.$$

At the disk, $z = z_{\max}$, the boundary conditions are that,

$$\phi = 0, \qquad \frac{\partial \phi}{\partial z} = 0, \qquad v = u = 0$$

The three non–dimensional parameters to vary are,

$$Re, \quad r_0 \quad \& \quad z_{max}.$$

6.4 Numerical method

6.4.1 Non–uniform grid approach

The flow in the enclosure presented consists of both primary and secondary flows. The primary flow in general consists of a sheared tangential velocity flow field, with solid–body rotation evident in the lower half of the cavity (in particular near the inner cylindrical hub) and large shear in the upper regions of the cavity

(in particular near the stationary outer cylindrical shroud), where the tangential velocity decreases from solid–body rotation in the core regions to the stationary shroud tangential velocity boundary condition. This shear is particularly large in the regions where the rotating disks and stationary shroud meet. The secondary flow field in general consists of radial outflow on the disks due to centrifugal force effects and radial inflow in the mid–axial plane of the cavity to satisfy continuity of mass. The boundary–layers which form on the disks become thinner with increasing Reynolds number due to the increase in inertial over viscous forces.

To ensure that these boundary–layers and regions of large tangential velocity gradients are sufficiently well resolved, a very fine uniform grid is required which increases the computational time significantly. Alternatively, a non–uniform grid structure may be adopted, with grid points concentrated in the boundary–layers and regions of large tangential velocity shear; this may be done in two ways:

- The physical non–uniform grid is transformed onto a uniform grid by use of a general transformation process that maintains the conservative form of the continuity equation.
- A method of coefficients may be adopted where second–order finite difference approximations are evaluated directly on the non–uniform mesh.

The latter method was chosen as it was deemed to give greater flexibility for creating various meshes and adapting the final code for other applications. Meshes are created using grid expansion factors (GEF) for the spatial intervals near the boundaries with the grid intervals, h, evaluated using

$$h_i = GEF \times h_{i-1}.$$

For the simulations which are presented later, the grid expansion factor was kept within the range,

$$1.1 \leq GEF \leq 1.2.$$

The size of the first interval, the grid expansion factor and the approximate distance over which to apply the expansion are defined initially. The remaining part of the computational domain is divided into equal intervals dependent upon the number of grid intervals defined by the user. The mesh is constructed such that it is symmetric about both the vertical and horizontal mid planes. This may however easily be modified to accommodate non–symmetric grid expansions. Examples of the non–uniform meshes used here may be seen in Figure 6.1. The mesh presented in Figure 6.1a is typical of that used for the co–rotating turbine disks model, with 128 × 96 radial/axial intervals. Figure 6.1b is typical of that used for the computer disk drive model and contains 128×64 intervals. In the core region a uniform grid is used with sufficient resolution to capture all the details of the flow. The increased resolution required near the boundaries is provided by the use of a non–uniform grid with $GEF = 1.15$. The largest interval in the variable grid region is approximately equal to that in the uniform core.

In order to demonstrate the method of evaluation of the coefficients, consider three Taylor series for a variable, u, at three neighbouring points where the second is considered the reference point and h_1 and h_2 are the respective intervals. This Taylor series expansion may be written in matrix form,

$$\begin{pmatrix} u(x_i - h_1) \\ u(x_i) \\ u(x_i + h_2) \end{pmatrix} \simeq \begin{pmatrix} 1 & -h_1 & \frac{h_1^2}{2!} & \frac{-h_1^3}{3!} & \frac{h_1^4}{4!} \\ 1 & 0 & 0 & 0 & 0 \\ 1 & h_2 & \frac{h_2^2}{2!} & \frac{h_2^3}{3!} & \frac{h_2^4}{4!} \end{pmatrix} \begin{pmatrix} u(x_i) \\ u'(x_i) \\ u''(x_i) \\ u'''(x_i) \\ u''''(x_i) \end{pmatrix}. \tag{6.9}$$

Difference approximations for the first two derivatives together with the magnitude of the $O(h^3)$ and $O(h^4)$ errors may be obtained by rearranging the above matrix into the following form,

$$\begin{pmatrix} 1 & -h_1 & \frac{h_1^2}{2!} \\ 1 & 0 & 0 \\ 1 & h_2 & \frac{h_2^2}{2!} \end{pmatrix} \begin{pmatrix} u(x_i) \\ u'(x_i) \\ u''(x_i) \end{pmatrix} = \begin{pmatrix} u(x_i - h_1) \\ u(x_i) \\ u(x_i + h_2) \end{pmatrix} - \begin{pmatrix} \frac{-h_1^3}{3!} & \frac{h_1^4}{4!} \\ 0 & 0 \\ \frac{h_2^3}{3!} & \frac{h_2^4}{4!} \end{pmatrix} \begin{pmatrix} u'''(x_i) \\ u''''(x_i) \end{pmatrix} + ... \tag{6.10}$$

Denoting the above by,

$$A\underline{x} = \underline{b} - B\underline{y}.$$

and multiplying both sides by the inverse matrix A^{-1} we obtain,

$$\underline{x} = A^{-1}\underline{b} - A^{-1}(B\underline{y}).$$

The inverse matrix is thus the matrix of coefficients required to evaluate the finite difference approximations and $A^{-1}(By)$ yields the magnitude of $O(h^3)$ and $O(h^4)$ errors where,

$$y = \begin{pmatrix} 1 \\ 1 \end{pmatrix}$$

The inverse matrix A^{-1} is evaluated using a Gaussian Elimination Scheme.

Second–order accuracy may be obtained for first spatial derivatives using a three point approximation. However, a four point approximation for the second derivative is required to maintain second–order accuracy in general; but when $h_1 = h_2$ three points suffice.

6.4.2 Approximations to the non–linear terms

As mentioned in Chapter 3, the Arakawa (1966), formulation for the Jacobians is useful in the form presented only on uniform grids. Its application to non–

uniform grid structures is beyond the scope of this thesis. Initially, second–order central difference approximations to the non–linear terms were implemented. It was found however, that these central differences produced solutions at high Reynolds numbers which were characterised by pointwise fluctuations. Both first and second–order upwinding schemes were implemented in turn, the bias of the differencing formula being determined by the local flow direction. It was found that the second–order upwinding scheme was numerically unstable when combined with the Du–Fort Frankel method for the transport equations. The first–order upwinding scheme (see Wendt, 1992) was found to be numerically stable and therefore it was applied, producing physically reasonable results which could be validated. A first–order scheme however, may produce unacceptable levels of numerical diffusion in regions of the flow where convective effects are small in relation to diffusive effects (e.g. near no–slip boundaries). The hybridised version, however, will produce more acceptable levels of numerical diffusion where it is not desirable, using the following hybrid strategy suggested by Spalding (1972).

If the local Peclet number is greater than two, an upwind FDA is used. Alternatively, second–order differences are used if the local Peclet number is smaller than two, where the Peclet number is defined as,

$$Pe = \frac{vh}{\nu}, \tag{6.11}$$

and where v is the local velocity and h is the local grid size. Using the non–dimensionalisation of Chapter 3, the local Peclet number is given by,

$$Pe = \frac{\bar{h}\bar{v}}{Pr}, \tag{6.12}$$

where overbars denote non–dimensional quantities.

When a radial derivative of the advective terms is considered, the non–dimensional local radial velocity and average local radial grid size are used to evaluate the local Peclet number. Similarly, where an axial derivative of the advective terms is considered, local axial velocity and average axial grid size are used to evaluate the local Peclet number.

6.4.3 Transient method

Forward first–order approximations are used for the time derivatives. Second–order central approximations were numerically stable only for small timesteps and stepwise fluctuations often appeared unless the timestep were very small. The transient treatment is based on the Du–Fort Frankel method where values of the dependent variable at the n^{th} timestep are exchanged for averages of new and old time values to improve the stability of the method. An example of the treatment applied to Fourier's two–dimensional equation is given in Section 5.4.4.

6.4.4 Multigrid method

The Multigrid method used to solve for the streamfunction and radial velocity fields is based on that described previously in Section 3.5.4. The relaxation procedure was modified in a straightforward way to accommodate the non–uniform grid structure and four–point difference approximations which resulted in additional elements in the iteration matrix on either the sub–sub–diagonal or super–super–diagonal. A penta–diagonal version of the tri–diagonal matrix (Thomas) algorithm was therefore used to obtain approximations to the solution and error. The prolongation and restriction operators remained unmodified in the non–uniform

grid regions with little loss in performance.

6.4.5 Mean and standard deviation

Due to the unsteady and often aperiodic nature of the flow and for comparison with experimental data, it is convenient to evaluate the standard deviation of the radial and tangential velocity fields about the respective mean. The variance is denoted by

$$S^2 = \frac{1}{n-1}\sum_{i=1}^{n}(\zeta_i - \bar{\zeta})^2, \tag{6.13}$$

where ζ is a generic variable and $\bar{\zeta}$ is the mean which is expressed as

$$\bar{\zeta} = \frac{1}{n}\sum_{i=1}^{n}\zeta_i. \tag{6.14}$$

Combining equations 6.13 and 6.14 above, the standard deviation may be written as

$$S = \sqrt{\frac{1}{n}\sum_{i=1}^{n}\zeta_i{}^2 - \frac{1}{n^2}(\sum_{i=1}^{n}\zeta_i)^2}. \tag{6.15}$$

6.5 Code validation

The benchmark solutions of de Vahl Davis (1983) were again used to validate the numerical method presented here. Comparisons were made with the stationary square cavity in the limit as $r \rightarrow 1$ for Ra_{gap} rising from 10^3 to 10^6. Richardson's extrapolation method was not used in this instance as a non–uniform mesh was used together with a hybrid upwinding method. The grid contained 80×80 intervals for all but the $Ra = 10^6$ computation which used a 96×96 grid. The mesh was contracted symmetrically towards the boundaries. The solutions were

obtained for $r_0 = 0.8$ and $r_0 = 0.9$ and extrapolated to the limit $r_0 = 1$. It was again assumed the ratio $\frac{Ra}{RePr}$ is negligible, as this term is absent in the Cartesian configuration of de Vahl Davis (1983). The average, maximum and minimum Nusselt numbers were compared at the heated surface and the results are presented in Table 6.1 below.

Ra_{crit}	Nu_0			Nu_{max}			Nu_{min}		
	(a)	(b)	%err	(a)	(b)	%err	(a)	(b)	%err
10^3	1.117	1.117	0.00	1.506	1.505	0.07	0.691	0.692	0.14
10^4	2.248	2.238	0.45	3.537	3.528	0.26	0.586	0.586	0.00
10^5	4.539	4.509	0.67	7.773	7.717	0.73	0.727	0.729	0.27
10^6	8.923	8.817	1.20	17.681	17.925	1.36	0.979	0.983	0.41

Table 6.1: Comparison of average, maximum and minimum Nusselt numbers for $Ra = 10^3, 10^4, 10^5$ and 10^6: (a) Current computations, (b) de Vahl Davis (1983).

The maximum error between the computed results and those of de Vahl Davis (1983) is approximately 1.5%. The main causes are likely to be the difference in grid distribution and in particular the upwinding scheme utilised in the above analysis. The numerical analysis of de Vahl Davis uses second–order accurate central difference approximations to all spatial derivatives and Richardsons extrapolation procedure leading to high accuracy benchmark solutions. The comparison, however, does provide a good level of confidence in the numerical procedure. Comparisons were also made with the uniform mesh code presented in Chapter 3. Good comparisons again prevailed.

6.6 Initial conditions

The fluid was initially at rest in the stationary frame of reference, and the rotating surfaces assumed a fixed given speed instantaneously at time $t = 0$. In the

rotating frame, the tangential velocity in the fluid is therefore given by,

$$v = -Pr \times Re \times r. \tag{6.16}$$

In order to perturb the solution from a symmetric twin recirculation structure, a small axially–varying perturbation to the tangential velocity field may be introduced. Amplification of the round–off errors in the solution were often found to be sufficient to perturb the flow over a sufficiently long time period as the Poisson solver does not impose the appropriate symmetry but breaks it slightly. The computational time required to achieve a non–symmetric state (should one exist) was minimised by introducing an axially varying perturbation to the tangential velocity field:

$$v = -Pr \times Re \times r + A \times z, \tag{6.17}$$

where z is the non–dimensional axial coordinate and A is the perturbation amplitude,

$$0 \leq A \leq 1.0.$$

No secondary convection in the radial/axial plane is assumed and therefore we set the following as initial conditions,

$$\phi = 0, \qquad \omega = 0. \tag{6.18}$$

6.7 Numerical simulation results

Solutions have been obtained using both the non–uniform grid code described above, and the uniform grid code described in Chapter 3 suitably modified to solve for the stationary shroud configuration. The poor spatial resolution achieved

using the uniform grid code meant that it is applied only to the low Reynolds number cases.

6.7.1 Results for $Re = 10^4$ and $r_0 = 0.5$

Initially, the uniform grid code, incorporating the Arakawa (1966) formulation for the non–linear convective terms was used for this low Reynolds number case. The grid comprised of 96×80 radial/axial intervals and the non–dimensional timestep used varied from $\delta t = 10^{-6}$ to $\delta t = 2 \times 10^{-6}$. These values were arrived at after numerical experiments involving stability, time and grid–independence considerations.

Figures 6.2 show the solution obtained using the uniform grid code with no initial axial variation in the tangential velocity field. The steady state streamfunction, achieved at $t \approx 0.01$ shows that the secondary flow is comprised of two symmetric counter–rotating vortices with stagnation points at the mid–axial points on the inner cylindrical hub and outer stationary cylindrical shroud. The core of these vortices are located in the bottom half of the cavity with fluid moving radially outward on the disk surfaces and radially inward in the mid–axial plane of the cavity. No exchange of fluid between the two vortices occurs. Figure 6.2b shows the tangential velocity iso–lines from a rotating perspective. Large tangential velocity gradients occur near the outer stationary shroud and the upper regions of the disks. In the lower regions, the fluid is approximately in solid–body–rotation, (i.e. the fluid rotates at approximately the same speed as the local disk speed). Indeed, a region of tangential velocity greater than the local disk speed occurs in the mid–axial plane around $r \approx 0.55$. This is due to the advection

by the secondary re–circulating flow of fluid near the disk surfaces in the upper region of the cavity toward the mid–axial lower regions via the central plume of fluid.

Figure 6.2c shows the variation of the maximum and minimum streamfunction values with time throughout the duration of the computation. Due to the initial tangential velocity profile used, with a zero axially varying component, the absolute values of the maxima and minima are the same at all times. The oscillations at early times are due to the appearance of vortices in the lower half of the cavity during start up. These are however observed to decay, but they maintain left–right symmetry.

If the computation were allowed to proceed further in time, asymmetries due to round–off errors would amplify, and the computed flow would become asymmetric with eventual attachment of the central plume to one of the disks. This process is accelerated in the next case investigated by the use of the axially varying initial perturbation to the tangential velocity field.

Figures 6.3 display the results of such a computation. The streamlines at the end point show the central plume is now attached to the right–hand–side disk with the clockwise rotating circulation dominating in size over the anti–clockwise circulation. The mechanism behind this process is known as the Coanda effect and a good description is given by Tritton (1977). A centrally placed plume entrains equal amounts of fluid from both sides. When it is perturbed, to the right, say, then the jet cannot entrain as much fluid from the right and therefore moves rightwards and in this instance, attaches to the right–hand–side disk. Two–dimensional flows tend to exhibit the Coanda effect more strongly than three–

dimensional flows as fluid entrainment can occur from the third dimension in the latter. It is anticipated therefore, that the Coanda effect may be less strong if the three–dimensional flow was considered and plume attachment therefore less likely to occur.

Again the horizontal aspect of the tangential velocity iso–lines away from the disks shows the existence of a region of solid body rotation near the inner cylindrical hub: see Figure 6.3b. However this is not a steady flow for the central plume moves slightly, but periodically. Figure 6.3c shows the periodic variation in the maximum and minimum streamfunction during the latter stages of the computation. This corresponds to a flapping motion of the region between the two circulations, with the mean values of maximum and minimum streamfunction remaining roughly constant. The jet therefore remains attached to the disk throughout the simulation. Animations of the secondary flow periodicity shows the unsteadiness to be small in comparison with the magnitude of the instability itself. Unsteady, periodic motion in the bottom region of the cavity also occurs. Subsequent computations carried out by Randriamampianina (1998), has verified the above computations and findings. That author used an accurate pseudo–spectral collocation method to investigate the axisymmetric instability. His work provides another confirmation of the accuracy of the present code.

The effect of varying the axial extent of the cavity is investigated by considering two different aspect ratios. Initially, a small gap aspect ratio is investigated and corresponds to a maximum axial dimension of $z_{max} = 0.1$. Figures 6.4 show the results for $Re = 10^4$ and include the use of an initial axially varying perturbation to the tangential velocity field. The initial asymmetric disturbance decays with time with two symmetric vortices resulting. The proximity of the disk surfaces

thus stabilises asymmetric disturbances at this Reynolds number compared with the $z_{max} = 0.3$ case shown in Figure 6.3. Figure 6.4b displays the occurrence of a large area of fluid in solid body rotation with the vortices accommodating less than half of the radial extent of the cavity. Figure 6.4c shows that a steady–state solution has been reached, with the absolute magnitude of the maximum and minimum streamfunction being exactly equal.

The results for a square aspect ratio cavity is presented in Figures 6.5. As the distance between the disks is relatively large, the solution is asymmetric and unsteady with the central plume not attaching to either disk. Again, radial outflow occurs near the disk surfaces, with radial inflow occurring in the central axial regions of the cavity. The unsteady behaviour is particularly noticeable in the lower reaches of the central plume of fluid, with the motion taking the form of the plume moving from one side to the other. Figure 6.5c shows that the computed flow is chaotic with time.

The results for the non–uniform grid code are presented in Figures 6.6 for the axial dimension $z_{max} = 0.3$. Comparison with Figures 6.3 show the apparent inaccuracies in the non–uniform grid code at predicting the correct form of the time–dependency of the flow. Again, an axially varying perturbation of the tangential velocity field was used in order to accelerate the evolution of the flow asymmetries. The non–uniform grid code, predicts a periodic flow with the clockwise and anti–clockwise circulations alternately dominating. No attachment of the plume to one of the disks therefore occurs, unlike the solution obtained by Randriamampianina (1998). Further comparison of the uniform and non–uniform grid codes suggest that the discrepancy is due to the approximation used for the non–linear advective terms in the non–uniform grid code, which takes the form

of a hybrid up–winding scheme.

6.7.2 Results for $Re = 1.46 \times 10^5$, $r_0 = 0.5$ and $z_{max} = 0.3$

Although doubt has been cast over the time accuracy of the non–uniform code, further computations and comparisons have been made with experimental data for this higher Reynolds number cases. It was found that the spatial resolution which could be obtained using the uniform grid code was insufficient to resolve the boundary–layers, hence this was the only available means of investigating the time–dependent nature of the flow.

For the computation presented below, the grid was comprised of 128×96 radial/axial intervals with a non–dimensional timestep of $\delta t = 5 \times 10^{-8}$. This case was selected for computation as it was the lowest rotational Reynolds number for which experimental velocity data were obtained in the study reported by Gan (1994). An axially–varying initial tangential velocity profile was used and the solution after a non–dimensional time $t = 0.0025$ is presented in Figures 6.7. The streamlines suggest that the secondary flow structure, as found for the low Reynolds number cases, has not formed a large coherent structure, but several cells appear. At this time however, Figure 6.7b demonstrates that the effects on the tangential velocity field of the instantaneous imposition of disk rotation at $t = 0$ have propagated throughout the cavity, with a layering of the iso–lines clearly visible. Figure 6.7c displays the variation of the tangential velocity profile at specific axial locations. In order to investigate the Rankine vortex behaviour of the primary tangential flow, the dimensional tangential velocity is normalised on the local disk speed and plotted against the inverse of the non–dimensional

radius squared, (r^{-2}). There is good comparison between the computed profile and the experimental data of Gan (1994), with the computed profile following the Rankine vortex type structure (equation 2.6) suggested by the experimental data. The spike which appears very near the stationary shroud ($r^{-2} \approx 1$ in Figure 6.7c) may be accounted for by considering the interaction between the primary and secondary flows. As the boundary–layers on the disk surfaces travel towards the disk tips, an increasing tangential component of velocity is imparted on them by the rotating disks. As these boundary–layers turn toward the stationary shroud surface, a large shear in tangential velocity results due to the large relative difference in the tangential velocities of the two surfaces. The size of this spike however reduces toward the mid–axial plane as diffusion effects play an important role.

At a later time, $t = 0.005$, the secondary flow structure takes the form of two distinct counter–rotating circulations with the clockwise circulation dominating, (Figures 6.8). At this time however, the predicted tangential velocity profile does not compare well with the experimental data, although the Rankine structure is again suggested.

Figures 6.9 show the simulation results at a time $t = 0.005$. Once again, there is good comparison between the computation and the experimental data at both the axial locations considered. The secondary flow structure is concentrated in the upper regions of the cavity and suggests significant variation with time. In order to investigate fully the effects of the time dependence on the flow structure, mean and standard deviation velocity profiles are evaluated over a non–dimensional time period of 0.005.

Figure 6.10a shows the good agreement obtained between the time–averaged tangential velocities for the unsteady computation and the experimental data. An axisymmetric steady computation carried out using the low Reynolds number turbulence model of Launder and Sharma (1974), failed to reproduce this behaviour and is in poor agreement with the data. Mirzaee (1997) found the turbulence model to be deficient for this flow. The standard deviation profiles are reasonably narrow, suggesting that the time variation of the tangential velocities are reasonably robust with time.

Comparison between the computed and measured radial velocities however, in general are not in good agreement. Again, the dimensional radial velocity is normalised on the local disk speed and the solutions are presented in Figures 6.10b,c,d for three different radial locations. At a radius $r = 0.55$, near the inner cylindrical hub, there is a very good comparison between the mean computed profile and the experimental data. However, the large fluctuations suggested by the standard deviation, is not supported by the experimental data. At $r = 0.75$, there is poor agreement between the computed and measured profiles, with the magnitude of the predicted velocities being significantly greater than that suggested by the experimental data. At a radius $r = 0.85$, there is a much better comparison, with the computed mean radial velocity profile following the same trends as the experimental data. It should however be noted that the experimental data is time averaged also, but over a substantially smaller time period. The large standard deviation about the computed mean value is not therefore confirmed by similar unsteadiness in the experimental observations made by Gan (1994).

Solutions for higher Reynolds numbers were obtained, but due to doubts about

the grid independent nature of the solutions, the comparisons with the available experimental data are not presented.

6.7.3 Results for $Re = 4.5 \times 10^5$, $r_0 = 0.5$ and $z_{max} = 0.05$

The investigation of the axisymmetric flow structure in the small gap cavity, investigated by Abrahamson *et al.* (1989), is presented here. The solutions were obtained using 128×64 radial/axial intervals and non–dimensional timestep $\delta t = 2 \times 10^{-8}$.

Instantaneous computed streamlines, shown in Figures 6.11a–c, again show two principal recirculations in the outer part of the cavity, affecting the radial inflow between the disks. The inflow was directed more toward the left or right hand disk at different times, depending on the relative size of the recirculating regions near the outer casing. At a time $t = 0.001$, the central plume takes the form of a wave–like structure, with several core regions of maximum and minimum streamfunction apparent. At a later time, $t = 0.002$, the radial inflow region supports an almost symmetric secondary flow structure in the upper regions of the cavity, with the characteristic wave shape appearing lower down in the plume. Figures 6.11c show the clockwise secondary circulation to be dominant at a time $t = 0.003$.

Figure 6.12 shows the behaviour of the streamfunction extrema with time for the entire computation, (requiring 150,000 timesteps), and Figure 6.13 shows the time–averaged mid–plane tangential velocity distribution in comparison with the measured data with the mean and standard deviation being computed between times $t = 0.002$ and $t = 0.003$. There is solid body rotation in the inner part of the

system, extending to around $r = 0.8$ for the computations. The measurements, inferred from flow visualisations by Abrahamson *et al.* (1989) and digitised here from the results presented, suggest further inward penetration of the recirculating flow than was predicted. The standard deviation from the mean suggests that the primary tangential flow is again influenced only slightly by the highly time–dependent nature of the secondary flow recirculation.

6.8 Brief conclusions

The two–dimensional axisymmetric computed flow can be time–dependent, but this is highly dependent on the aspect ratio of the cavity. In particular, the time–unsteadiness is stabilised by increase in the proximity of the disks. Conversely, destabilisation of the time variation occurs if the two disks are moved further apart. The attachment of the central plume of the secondary flow to one of the disks can occur and is thought to be due to the Coanda effect, where unequal fluid entrainment from either side of the jet causes the plume to move away from the side of greater fluid entrainment. Reasonable comparison has been achieved between experimental data and time–averaged computation for the higher Reynolds numbers considered and in particular for the tangential velocity profiles.

The hybrid upwinding scheme as an approximation to the non–linear advective terms is unsuitable for time–dependent flows, with comparisons between uniform and non–uniform grid codes showing fundamental differences in the primary flow structures.

Chapter 7

Conclusions and recommendations for future work

In this thesis, a computational study of the buoyancy–induced flow in a rotating cavity with differentially heated cylindrical surfaces has been carried out. The outer cylindrical surface has been assumed to be uniformly hot and the inner cylindrical surface uniformly cold thereby giving an unstably stratified fluid. Adiabatic boundary conditions were applied to the disk surfaces.

Gravitational acceleration is small in comparison with the centrifugal acceleration experienced at typical turbomachinery operating conditions and therefore, gravitational buoyancy effects were neglected for the purposes of this investigation in order to simulate more accurately the fluid flow in turbomachinery disk spaces.

Four different configurations were investigated with Linear Stability Theory applied to two of the flows in order to obtain neutral stability curves for various operating conditions. The configurations studied using Linear Stability The-

ory corresponded to two–dimensional radial/axial and radial/tangential flows. In these cases the equations were linearised using a non–convecting, conducting base solution of the equations and infinitesimal perturbations to the base flow.

For the non–linear two–dimensional numerical simulations, a streamfunction–vorticity approach and an explicit time dependent method were adopted to solve for buoyancy induced laminar flow, with coupling with the temperature equation achieved through the assumption that the density varies linearly with temperature. This was applied to the Coriolis force in addition to the centrifugal force. Multigrid acceleration was used to solve the Poisson equation for the streamfunction at each time level.

The three–dimensional numerical simulations were obtained using a vorticity–velocity formulation on a staggered mesh. Again, an explicit time dependent approach was adopted, with multigrid acceleration applied to the three Poisson equations for the three components of velocity at each time level.

Attention is drawn however to the fact that flows for which $\frac{Ra}{Re^2 Pr} = \beta \Delta T > 1$ may only be regarded as being qualitatively correct as the fluid takes negative densities in part of the computational domain.

The final study presented in this thesis is the computation of isothermal fluid flow for a sealed rotating cavity with a stationary shroud. The axisymmetric code developed for the buoyancy–induced radial/axial flow configuration was adapted to allow the use of non–uniform mesh distributions. Simulations were also conducted using a uniform grid code and comparisons were made with experimental data where this was available.

7.1 2D axisymmetric radial/axial flow

A tangentially axisymmetric flow was first considered with convection taking the form of toroidal vortices. Conclusions for the Linear Stability Theory are presented in section 7.1.1 and for the full non–linear investigation in section 7.1.2.

7.1.1 Linear Stability Theory

Solutions were obtained for two cases. In the first instance the Boussinesq approximation is applied and this is equivalent to $\beta\Delta T \approx 0$; this is equivalent to having no buoyancy correction to the Coriolis force. The second case has this correction and a linear variation in the density with temperature is taken.

- The effect of increasing the rotational Reynolds number is to stabilise the flow. Thus the critical Rayleigh number increases with increase in rotational Reynolds number.
- For small and decreasing wavenumber instability, (increasing wavelength), the critical Rayleigh number increases rapidly with the solutions suggesting that very small wavenumber instabilities occur at large values of Ra_{crit} only.
- For large and increasing wavenumbers, the growth in the critical Rayleigh number is small, with little suggestion of the rapid increase as observed for small wavenumbers. Definite turning points are however observed in the neutral stability curves.
- For increasing Reynolds numbers, and hence critical stability levels, the minima in the neutral stability curves occur at increasingly small wavenum-

bers.

- As the inner radius varies the critical Rayleigh number decreases at first and then increases yielding a well–defined minima. When the inner radius is large the flow consists of many small–wavelength cells, whereas two cells correspond to sufficiently small inner radii.

- In the limit as the inner non–dimensional radius tends to one, for $Re = 0$ the neutral stability curve tends to that of the classical Bénard problem.

- Introduction of the buoyancy correction to the Coriolis force destabilises the flow, resulting in a decrease in the neutral stability levels. The form of the curves remain largely unchanged for small Reynolds numbers. For larger Reynolds numbers, the neutral stability curves are of a flatter profile over a larger range of wavenumbers.

- Solutions minimised over the wavenumber and presented against the inner radius could not be obtained for large $\frac{Ra}{RePr}$ using the available methodology and may have been due to the stiffness of the equations.

7.1.2 Numerical simulation

Validation for the corresponding fully non–linear simulations was achieved using the benchmark solution of de Vahl Davis (1983), for a two–dimensional cavity with horizontal temperature gradient. In addition, comparison with LST results were also conducted.

- When the Reynolds number is increased from zero the flow strengthens at first due to the decreasing dominance of buoyancy correction to the

Coriolis force. Eventually the flow weakens again as the Coriolis force itself increases.

- For the geometries considered, in general, the flow at low Reynolds numbers consists of one toroidal vortex, with two vortices arising at slightly higher Reynolds number. These are characterised by radial outflow at the mid–axial plane and radial inflow near the disk surfaces. Further increase in Re results in either a return to a single toroidal vortex or to a twin recirculation with radial inflow occurring at the mid–axial plane. Non–unique solutions are also observed for this mid–range of Reynolds numbers. For large Reynolds numbers, where the stabilising effect of the Coriolis force dominates, the single vortex flow is re–established.

- Increase in the Rayleigh number for constant Reynolds number and geometry initially results in an increase in the heat transfer due to the associated increase in the buoyancy force. However, further increases in the Rayleigh number attenuates the flow due to the attendant increase in magnitude of the buoyancy correction. Solutions for large Rayleigh numbers also tend to result in periodic, time–dependent flow.

- Decrease in the inner radii tends to reduce the strength of the flow with a decrease in the heat transfer observed. Increase in the axial dimension of the cavity results in little change in the heat transfer, with the flow in general showing stronger fluctuations.

- For cases where the buoyancy correction to the Coriolis force is large, (i.e. for small Re given a fixed Ra), in regions of positive radial velocity the tangential velocity can also be positive. In general however, the toroidal vortices are found to precess relative to the rotating surfaces. For cases

where the Coriolis force is dominant, positive regions of tangential velocity occur in regions of radial inflow, where fluid near the outer cylindrical shroud is convected from outer radial regions toward the inner radial regions of the cavity.

7.2 2D radial/tangential flow

An axially independent flow was then considered with convection taking the form of rolls. Conclusions for the Linear Stability Theory are presented in section 7.2.1 and for the full non–linear investigation in section 7.2.2.

7.2.1 Linear Stability Theory

Solutions were again obtained for two cases. In the first instance the Boussinesq approximation was applied (equivalent to $\beta\Delta T \approx 0$ and hence no buoyancy correction to the Coriolis force). Subsequently, the buoyancy correction was introduced and its effect noted. For both the cases considered, the Coriolis force was found to scale out of the governing equations.

- For a given disturbance wavenumber, an initial increase in the inner radius destabilises the flow and corresponds to a decrease in the value of Ra_{crit}. As the inner radius increases further the critical Rayleigh number eventually begins to increase and very markedly as the non–dimensional inner radius approaches one. The curvature of the neutral curve (Ra_{crit} against inner radius) at the minimising value of r_0, for small wavenumbers is small, but is much larger for larger wavenumbers. In practice though, r_0 is fixed and

it is necessary to consider Figure 4.1 in detail to determine the wavenumber which minimises Ra_{crit}. For large r_0 this wavenumber is large reflecting the need for a large number of cells in the narrow annulus. For small r_0 the wavenumber is small.

- Increase in the the discrete wavenumber results in flow stabilisation for approximately $r_0 < 0.7$. The converse applies for $r_0 > 0.7$, where flow destabilisation occurs with increase in the wavenumber.

- At values of inner radii approaching that of the outer radius, Ra_{crit} increases without limit suggesting that no instability occurs in the limit $r_0 \to 1$. In such thin annuli viscous forces dominate buoyancy forces.

- Rescaling the critical Rayleigh number on the gap $(R - a)$ length scale results in more symmetric neutral stability profiles with increasingly narrow stability curves observed as the wavenumber increases. Large wavenumber convection is confined to large inner radii, with small wavenumber convection occurring over a broader band of inner radii.

- The introduction of the buoyancy correction affects the neutral stability criteria for values of Re less than approximately 200 for the cases considered. (Note that we assume that Ra and Pr are held fixed). At smaller values of Re the most dangerous wavenumber may alter.

- The buoyancy correction is found to either stabilise or destabilise the neutral stability dependent on the wavenumber and inner radius, although in terms of the value of Ra at which convection first appears convection is stabilised.

7.2.2 Numerical simulation

Conclusions are drawn for simulations which include the application of the buoyancy correction to the Coriolis force in addition to the centrifugal force. The pure Coriolis force was found to scale out of the governing equations. Validation was achieved by comparison with the Linear Stability analysis.

- For any given Rayleigh number, Reynolds number and geometry, it is possible for flows with different wavenumbers to be stable (i.e. with respect to small disturbances). These different wavenumber solutions are obtained using appropriate wavenumber perturbations to the initial conducting temperature profile.

- The resulting cyclonic and anti–cyclonic circulations consist of approximately isothermal cores with regions of radial outflow and inflow occurring between the cyclonic and anti–cyclonic pairs when Ra is sufficiently far above the critical value for the onset of convection.

- The steady precession of the cyclones and anti–cyclones is observed to be dependent on the Reynolds number or rather on the magnitude of the buoyancy correction to the Coriolis force terms. When the Reynolds number is large, and hence the magnitude of the correction small, the rolls are locked to the rotating surfaces and are equal in size. For small Reynolds numbers and consequent roll precession, the cyclones are observed to be of a larger size than the anti–cyclones.

- For large inner radii, the preferred number of cyclonic and anti–cyclonic pairs exceeds the preferred number that occurs for small inner radii. This

is in qualitative agreement with Linear Stability Theory results.

- The steady behaviour at relatively small Rayleigh numbers gives way to periodic flow and subsequently to chaotic flow for increasing Rayleigh numbers.

- An increase in the rate of heat transfer occurs with an increase in the Rayleigh number and hence the magnitude of the buoyancy force. Due to the Coriolis force scaling out of the governing equations, no stabilisation of the flow occurs with an increase in the Reynolds number.

- The preferred number of cyclonic and anti–cyclonic pairs is found to be such that the heat transfer is approximately maximised.

7.3 3D flow simulation

- A strong qualitative similarity exists between the three–dimensional flow and the radial/tangential two–dimensional flow studied previously. In particular, the three–dimensional mid–axial plane flow structure comprises of regions of cyclonic and anti–cyclonic activity with approximately zero axial velocity component apparent.

- Variations in this cyclonic/anti–cyclonic structure with the axial coordinate are found to be limited to variations in the axial velocity near the disk surfaces. The temperature distribution remains constant with variation in the axial coordinate for steady precessing flow.

- Near the disk surfaces, where the Coriolis force dominates over the buoyancy correction to the Coriolis force fluid moves axially away from the disks in the

cyclonic regions and toward the disks in anti–cyclonic regions. Conversely, when the buoyancy correction is dominant, fluid moves axially away from the disks in regions of anti–cyclonic flow and toward the disks in regions of cyclonic flow.

- A decrease in the axial–dimension of the cavity and hence the proximity of the disks to one another causes a stabilisation of the flow with a consequent decrease in the heat transfer being evident.

- As for the axisymmetric flow, it is possible for a range of different wavenumber flows to be stable for any given operating condition.

- The rate of precession of the cyclones and anti–cyclones depends on two factors: the magnitude of the buoyancy correction to the Coriolis force and the proximity of the two disks. The larger the magnitude of the buoyancy correction and the smaller the distance between the disks, the greater the rate of precession of the rolls.

- Increase in the Rayleigh number results in an increase in the heat transfer due to the associated increase in the buoyancy force.

- For small Reynolds numbers, initial increase in Re results in flow destabilisation as a consequence of the decrease in the magnitude of the buoyancy correction to the Coriolis force. Subsequent increases are found to stabilise the flow due to the increase in magnitude of the Coriolis force.

- The time–dependency of the flow is found to take several forms. Periodic wavenumber halving and subsequent doubling can occur, where for example, an $n = 4$ pattern changes to an $n = 8$ pattern and back periodically.

- Unsteady, chaotic flow is found to be more likely to arise at higher values of Rayleigh numbers.

7.4 Sealed cavity with stationary shroud

The radial/axial axisymmetric code developed for the buoyancy–induced flow study was further modified for use with a non–uniform grid distribution.The uniform grid code, using the Arakawa (1966) formulation was also modified and applied to the sealed cavity with stationary shroud geometry.

- A symmetric secondary flow distribution can be obtained using a symmetric initial tangential velocity profile and limited number of timesteps. It is found however, that amplification of the round–off errors become significant after a certain number of timesteps and results in asymmetries evolving in the secondary flow structure. In these cases the symmetric flows are unstable and are unlikely to appear in practice despite being a legitimate solution of the equations.

- In order to accelerate this non–symmetric "seeding" process, an artificial axially varying perturbation to the tangential velocity field is introduced. It is found that for $Re = 10^4$, the secondary flow is symmetric only for narrow geometries. Increases in the axial width result in periodic flow with the central plume of radial inflow tending toward one of the disks. Further increases in the axial dimension of the cavity results in chaotic flow becoming evident.

- The attachment of the central plume of fluid to one of the disks is a form of the Coanda effect, where unequal entrainment of fluid from either side of a perturbed jet causes the plume to shift in the direction of smaller fluid entrainment.

- Comparisons between with the non–uniform code results suggests that the up–winding scheme used for the non–linear convective terms is not suitable for time–dependent flow. This numerical problem was not resolved and merits closer scrutiny.

- Solutions are however obtained for larger Reynolds numbers and time–averaged comparisons with experimental data show good agreement for the tangential velocity profile. Radial velocity comparisons are however poor, for the large variations in the radial velocities apparent in the computations are not evident in the experimental data.

- The flow may be highly three–dimensional. The three–dimensionalities suggested by Abrahamson *et al.* (1989) may indeed be also significant for the turbomachinery cavities considered.

7.5 Recommendations for future work

This thesis has been concerned with idealised geometries related to cavities found in gas turbine engines. Although many non–linear phenomena are likely to apply to more realistic geometries there are few guides to predict which, and quantitative results are certain to change. It would therefore be interesting to extend the work presented in this thesis toward more realistic geometries and through–flow systems.

7.5.1 Buoyancy–induced flow

Solutions at typical turbomachinery operating conditions could not be obtained using the presented numerical procedure and the available computational resources. A more accurate methodology requires to be developed for a non–uniform grid distribution in order to minimise the number of mesh points required to resolve fully the flow structure at turbomachinery operating conditions. Comparison can then be made with the experimental results of Bohn *et al.* (1995) for validation. This may only be achieved with a substantial increase in processor speed.

Further difficulties arise for large–amplitude convection. The assumption that the density variations are independent of the pressure distribution becomes invalid. In particular, the Boussinesq approximation and the linear density/temperature relationship may not be confidently applied, and the full compressible governing equations have to be considered. These modifications may however be simplified in part by the assumption of incompressible flow in the viscous terms, as the velocities for natural convection flows are generally small in comparison with forced convection problems.

7.5.2 Sealed cavity with stationary shroud

As has previously been discussed, the flow in a rotating cavity with a stationary outer casing may be both unsteady and three–dimensional. Further experimental and theoretical investigations should be carried out to study the three–dimensionality of this flow. In particular, an accurate time–dependent code re-

quires to be developed to solve the flow in three–dimensions. Non–isothermal effects may subsequently be introduced and investigated as it is thought that buoyancy effects may be significant.

References

- Abrahamson, S.D., Eaton, J.K. & Koga, D.J., 1989, The flow between shrouded corotating disks, *Physics of Fluids*, **2**, pp.241–251.

- Arakawa, A., 1966, Computational design for long–term numerical integration of the equations of fluid motion: two–dimensional incompressible flow. Part 1, *Journal of Computational Physics*, **1**, pp.119–143.

- Armfield, S.W. & Patterson, J.C., 1992, Wave properties of natural–convection boundary layers, *Journal of Fluid Mechanics*, **239**, pp.195–211.

- Bohn, D., Deuker, E., Emunds, R. & Gorzelitz, V., 1995, Experimental and theoretical investigations of heat transfer in closed gas–filled rotating annuli, *Journal of Turbomachinery*, **117**, pp.175–183.

- Bohn, D., Dibelius, G.H., Deuker, E. & Emunds, R., 1994, Flow pattern and heat transfer in a closed rotating annulus, *Journal of Turbomachinery*, **116**, pp.542–547.

- Bohn, D., Emunds, R., Gorzelitz, V. & Krüger U., 1996, Experimental and theoretical investigations of heat transfer in closed gas–filled rotating annuli II, *Journal of Turbomachinery*, **118**, pp.11–19.

- Briggs, W. L., 1987, *A Multigrid Tutorial*, Lancaster press.

- Busse, F. H., 1967, On the stability of two–dimensional convection in a

layer heated from below, *Journal of Mathematical Physics*, **46**, pp.140–149.

- Chew, J. W., 1985, Computation of convective laminar flow in rotating cavities, *Journal of Fluid Mechanics*, **153**, pp.339–360.

- Dorfman, L. A., 1968, Laminar thermal convection in the rotating cavity between two disks, *Izv. A N SSSR. Mekhanika Ahidkosti i Gaza*, **3**, pp.40–46.

- Gan, X., 1994, Experimental study of rotating disks with peripheral flow, *Report No. 014/94, School of Mech. Eng., Univ. of Bath.*

- Gan, X., Mirzaee, I., Owen, J.M., Rees, D.A.S. & Wilson, M., 1996, Flow in a rotating cavity with a peripheral inlet and outlet of cooling air, *ASME Int. Gas Turbine and Aeroengine Cong., Birmingham, paper 96-GT-309*

- Guj, G. & Stella, F., 1988, Numerical solutions of high-Re recirculating flows in vorticity–velocity form, *International Journal for Numerical Methods in Fluids*, **8**, pp.405–416.

- Herrero, J., Humphrey, J.A.C. & Giralt, F., 1994, Comparative analysis of coupled flow and heat transfer between corotating disks in rotating and fixed cylindrical enclosures, *ASME Heat Transfer in Gas Turbines*, **300**, pp.111–121.

- Huang, H. & Li, M., 1997, Finite–difference approximations for the velocity–vorticity formulation on staggered and non–staggered grids, *Computers and Fluids*, **26**, pp.59–82.

- Koschmieder, E.L., 1993, *Bénard cells and Taylor vortices*, Cambridge University Press.

- Launder, B.E. and Sharma, B.L., 1974, Application of the energy dissipation model of turbulence to the calculation of flow near a spinning disc, *Letters in Heat and Mass Transfer*, **1**, pp.131-138.

- Long, C.A. & Tucker, P.G., 1994, Numerical computation of laminar flow in a heated rotating cavity with an axial throughflow of air, *International Journal of Numerical Methods in Heat and Fluid Flow*, **4**, pp.347–365.

- Mallinson, G.D. & de Vahl Davis, G., 1973, The method of the false transient for the solution of coupled partial differential equations, *Journal of Computational Physics*, **12**, pp.435.

- Mirzaee, I., Gan, X., Wilson, M. & Owen, J.M., 1997, Heat transfer in a rotating cavity with a peripheral inflow and outflow of cooling air, *ASME Int. Gas Turbine and Aeroengine Cong., Orlando, paper 97–GT–136*

- Mirzaee, I., 1997, *Computation of Flow and Heat Transfer in a Rotating Cavity with Peripheral Flow*, PhD thesis, University of Bath, U.K.

- Morse, A.P., 1991, Assessment of laminar–turbulent transition in closed disk geometries, *Journal of Turbomachinery*, **113**, pp.131–138.

- Napolitano, M. & Pascazio, G., 1991, A numerical method for the vorticity–velocity Navier–Stokes equations in two and three dimensions, *Computers and Fluids*, **19**, pp.489–495.

- Owen, J.M. & Rogers, R.H., 1989, *Flow and heat transfer in rotating–disc systems: rotor–stator systems*, Research Studies Press, Taunton, Somerset, England.

- Owen, J.M. & Rogers, R.H., 1995, *Flow and heat transfer in rotating–disc*

systems: rotating cavities, Research Studies Press, Taunton, Somerset, England.

- Patanker, S.V., 1980, *Numerical heat transfer and fluid flow*, Hemisphere, New York.

- Patterson, J.C. & Armfield, S.W., 1990, Transient features of natural convection in a cavity, *Journal of Fluid Mechanics*, **219**, pp.469–497.

- Patterson, J.C. & Imberger, J., 1980, Unsteady natural convection in a rectangular cavity, *Journal of Fluid Mechanics*, **100**, pp.65–86.

- Randriamampianina, A., 1998, Private Communication.

- Schladow, S.G., 1990, Oscillatory motion in a side–heated cavity, *Journal of Fluid Mechanics*, **213**, pp.589–610.

- Schlüter, A., Lortz, D. & Busse, F., 1965, On the stability of steady finite amplitude convection, *Journal of Fluid Mechanics*, **23**, pp.129–144.

- Schöpf, W & Patterson, J.C., 1995, Natural convection in a side–heated cavity: visualisation of the initial flow features, *Journal of Fluid Mechanics*, **295**, pp.357–379.

- Shen, W.Z. & Loc, T.P., 1997, Numerical method for unsteady 3D Navier–Stokes equations in velocity–vorticity form, *Computers and Fluids*, **26**, pp.193–216.

- Spalding, D.B., 1972, A novel finite difference formulation for differential expressions involving both first and second derivatives, *International Journal for Numerical Methods in Engineering*, **4**, pp.551–559.

- Stella, F., Guj, G., Leonardi E. & de Vahl Davis, G., 1988, The velocity/vorticity and vector potential/vorticity formulations in three–dimensional natural convection, 3^{rd} *Italian Conference of Computational Mechanica, Italian Association of Theoretical and Applied Mechanics. Palmero, Italy.*

- Tritton, D.J., 1977, *Physical fluid dynamics*, Van Norstrand Reinhold.

- de Vahl Davis, G., 1983, Natural convection of air in a square cavity: A benchmark numerical solution, *International Journal for Numerical Methods in Fluids*, **3**, pp.249–264.

- Vest, C.M. & Arpaci, V.S., 1969, Stability of natural convection in a vertical slot, *Journal of Fluid Mechanics*, **36**, pp.1–15.

- Wendt, J. F., 1992, *Computational Fluid Dynamics*, Springer–Verlag.

- M.Wilson, P.D.Arnold, T.W.Lewis, I.Mirzaee, D.A.S.Rees & J.M.Owen, 1997, Instability of flow and heat transfer in a rotating cavity with a stationary outer casing, *Eurotherm 55 (Heat transfer in Single Phase Flow) September 1997, Santorini, Greece.*

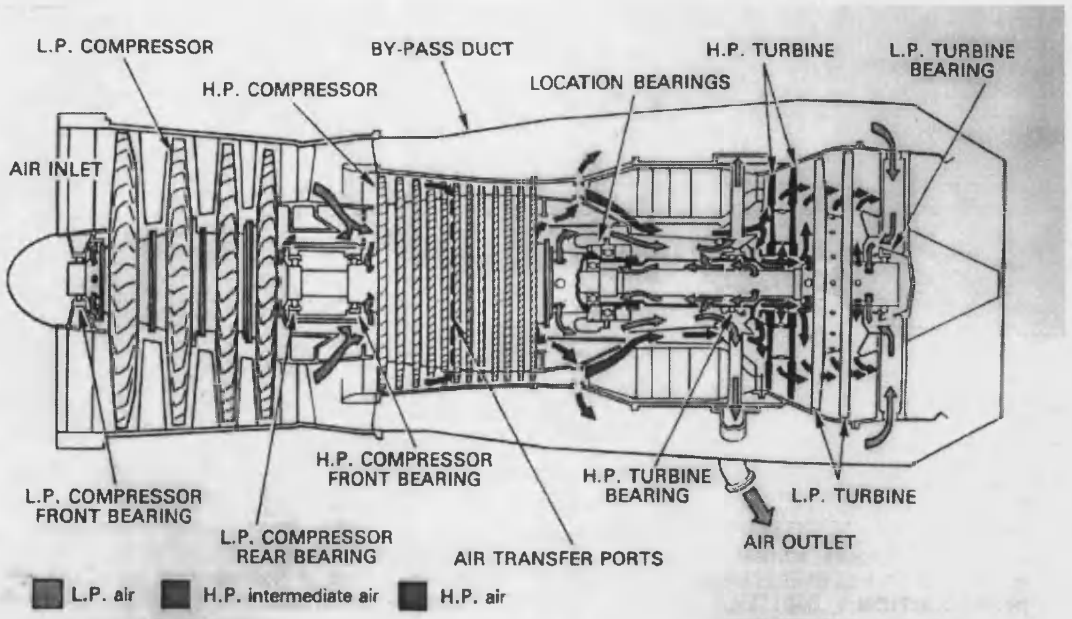

Figure 1.1. Internal air system in a gas turbine engine (The Jet Engine – Rolls–Royce PLC)

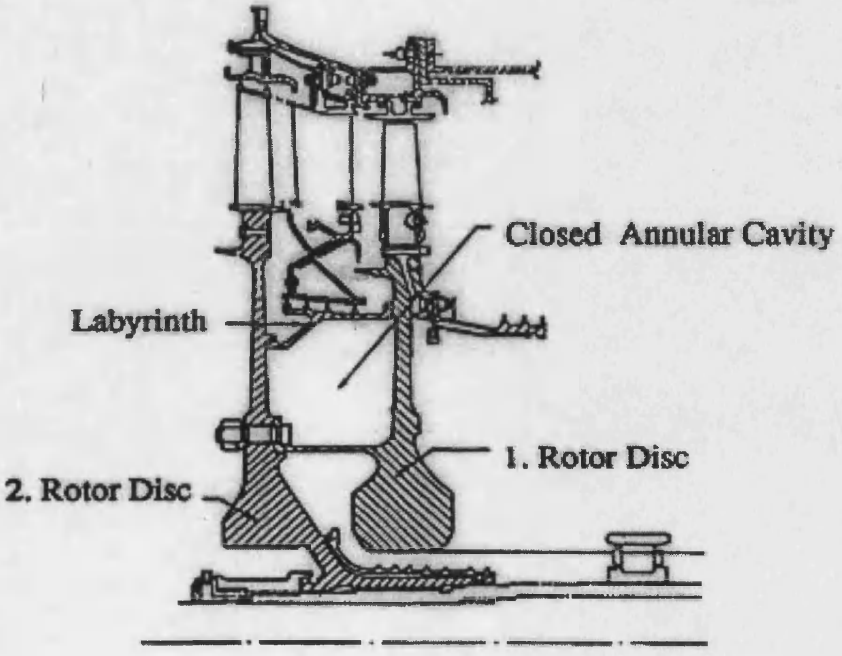

Figure 1.2. Cross–section through gas turbine showing closed annular cavity between two co–rotating rotor disks (Bohn *et al* (1996))

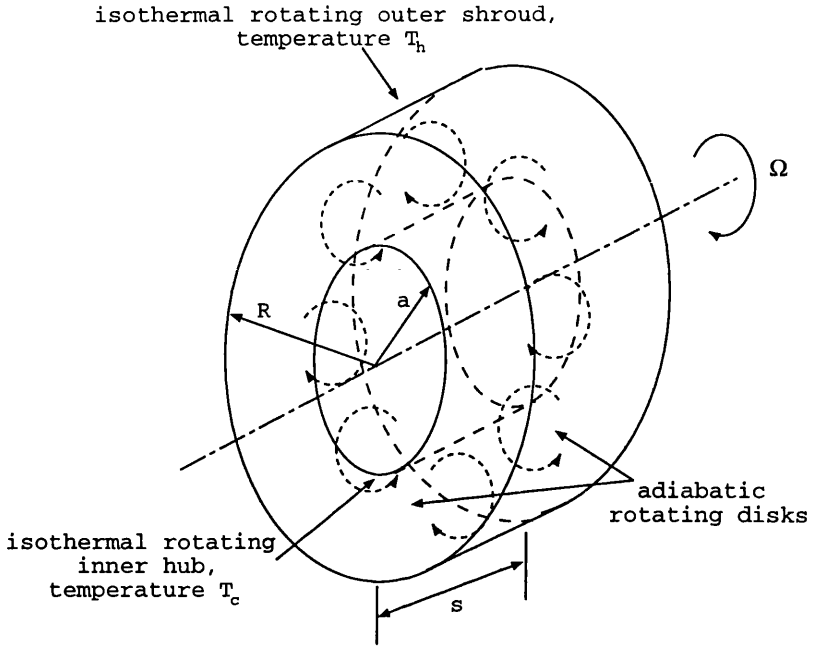

Figure 1.3. Schematic diagram of rotating cavity showing flow structure due to buoyancy effects.

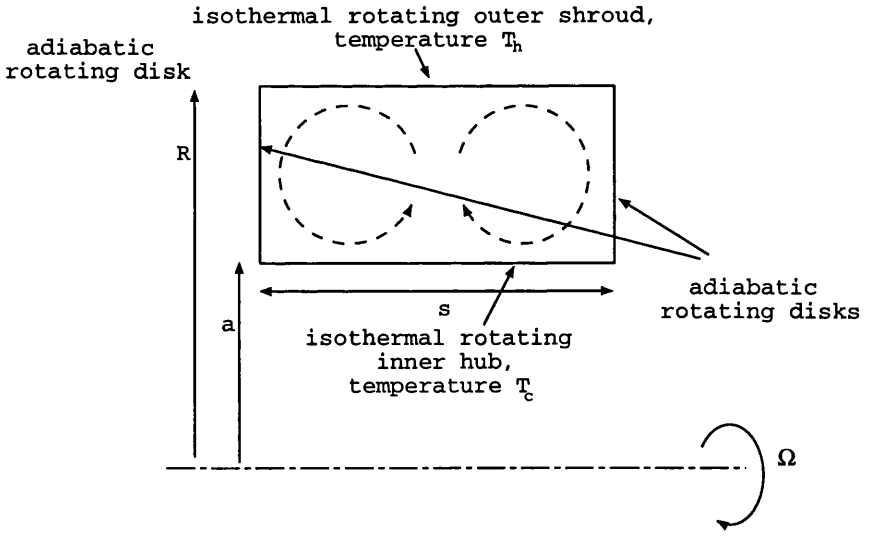

Figure 1.4. Schematic diagram of two–dimensional axisymmetric rotating cavity showing flow structure due to buoyancy effects.

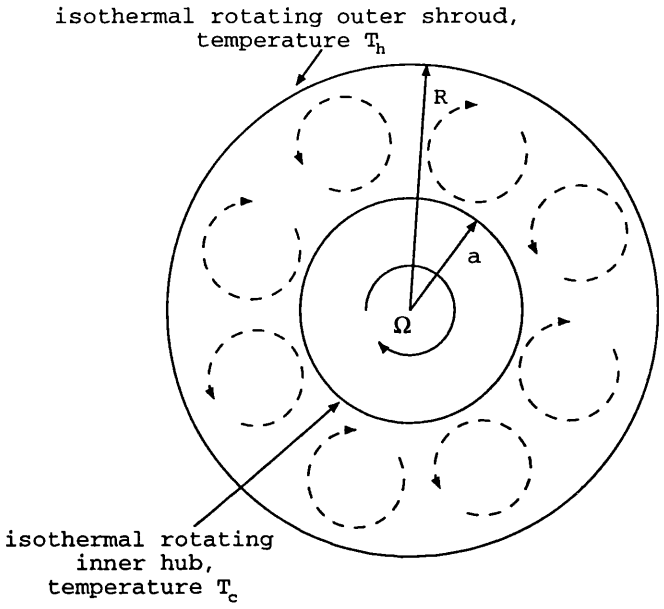

Figure 1.5. Schematic diagram of two–dimensional, radial–tangential rotating cavity showing flow structure due to buoyancy effects.

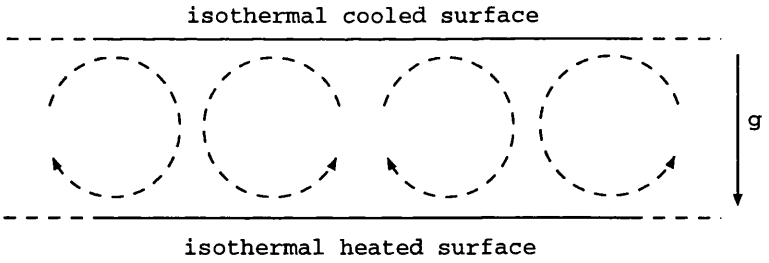

Figure 1.6. Schematic diagram of Rayleigh–Bénard convection in a graviational field characterised by parallel rolls.

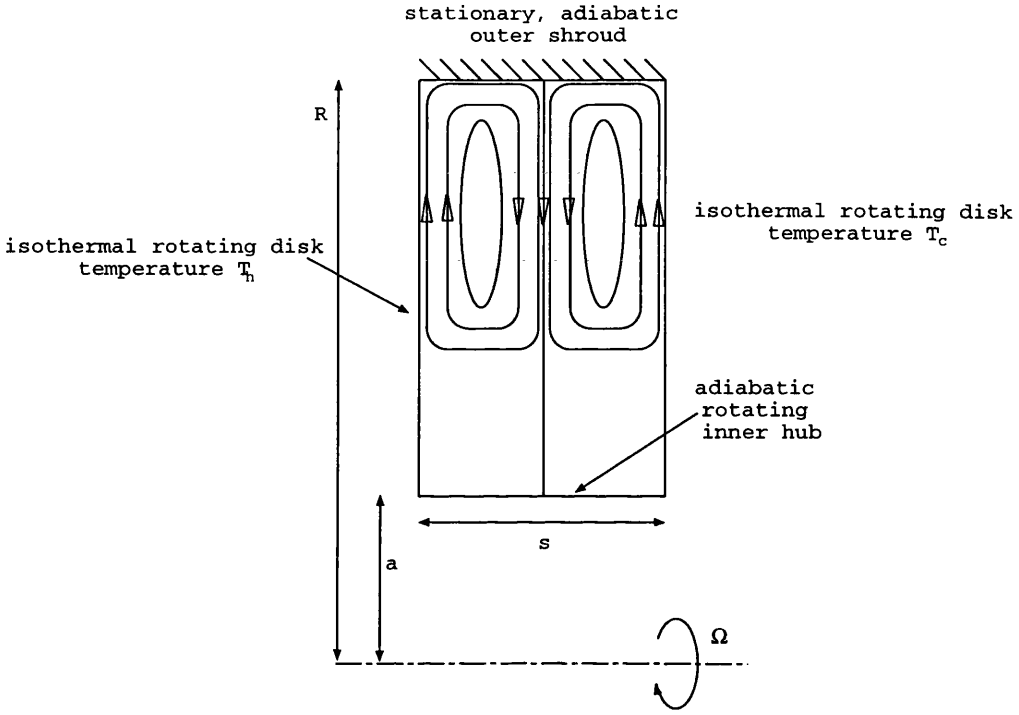

Figure 1.7. Schematic diagram of rotating cavity with stationary shroud showing secondary flow structure.

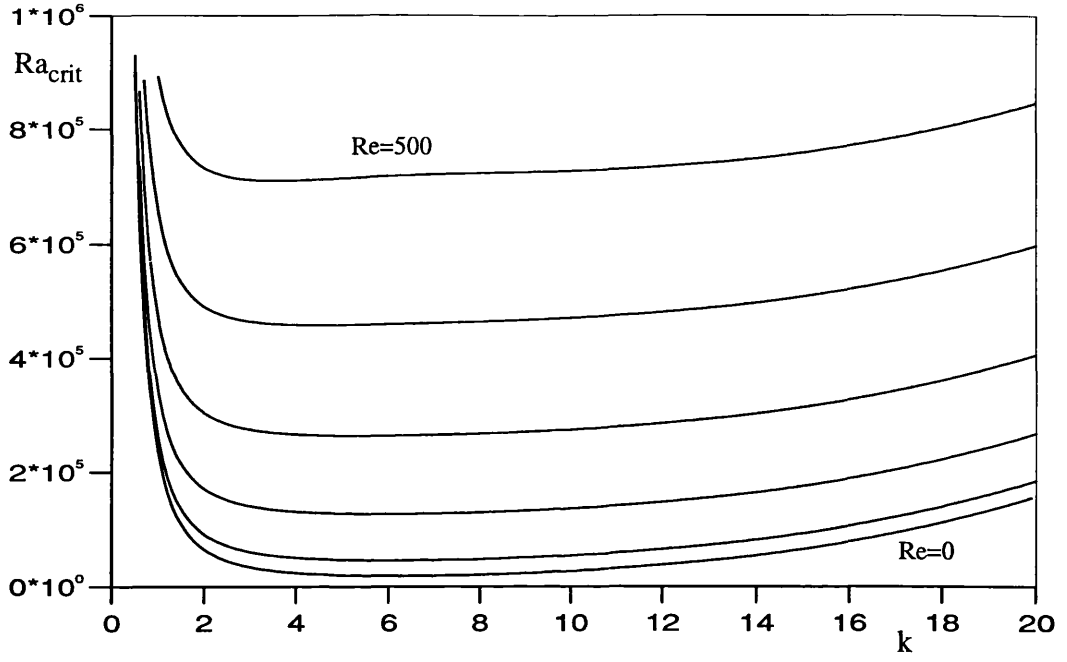

Figure 3.1. Neutral Stability curves for Re=0,100,200,.....,500 and range of wavenumbers for r_0=0.5 and small Ra/(Re Pr).

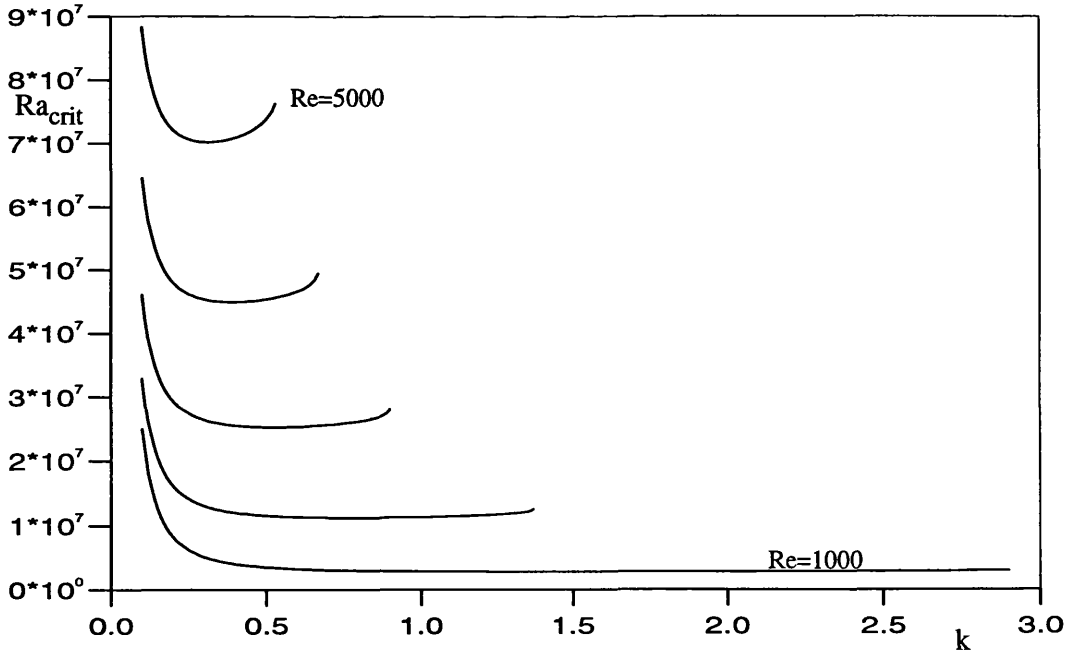

Figure 3.2. Neutral Stability curves for Re=1000,2000,.....,5000 and range of wavenumbers for r_0=0.5 and small Ra/(Re Pr).

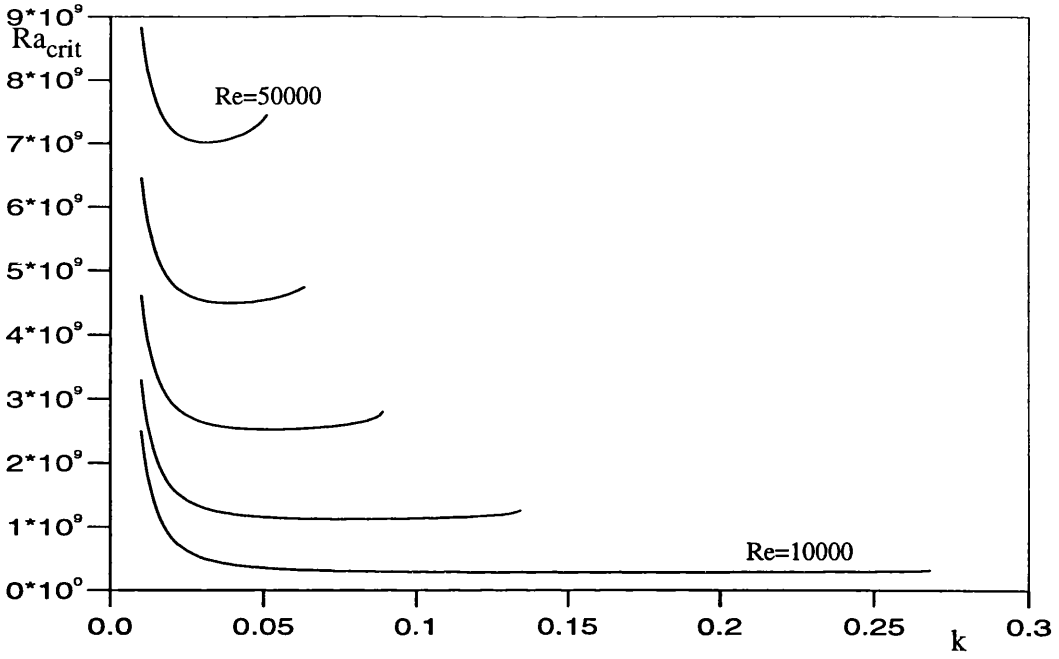

Figure 3.3. Neutral Stability curves for Re=10000,20000,.....,50000 and range of wavenumbers for r_0=0.5 and small Ra/(Re Pr).

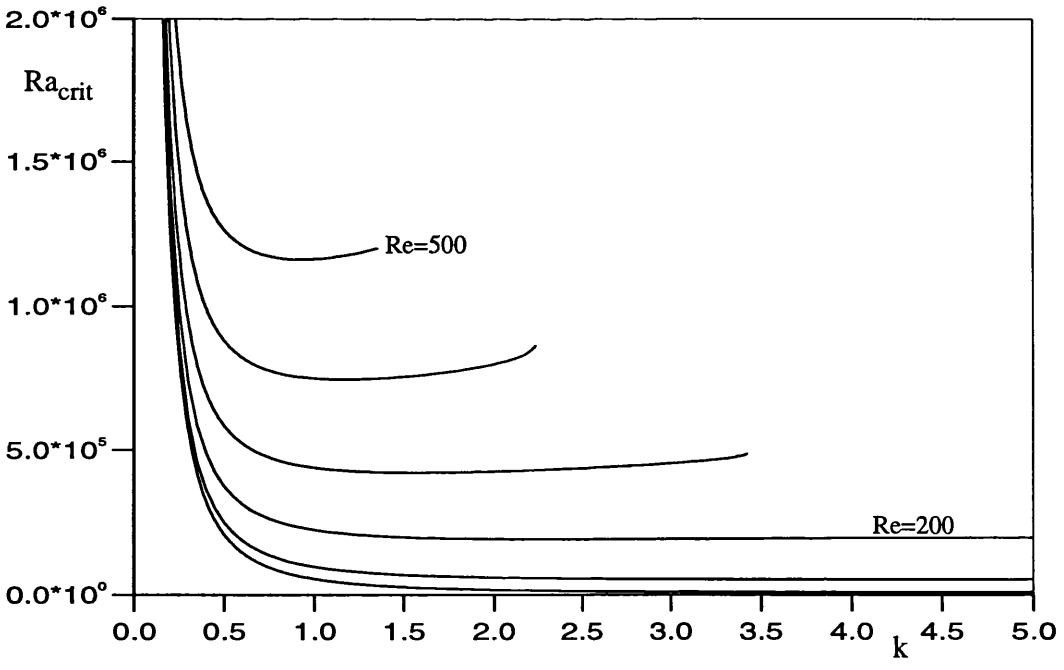

Figure 3.4. Neutral Stability curves for Re=0,100,.....,500 and range of wavenumbers for r_0=0.3 and small Ra/(Re Pr).

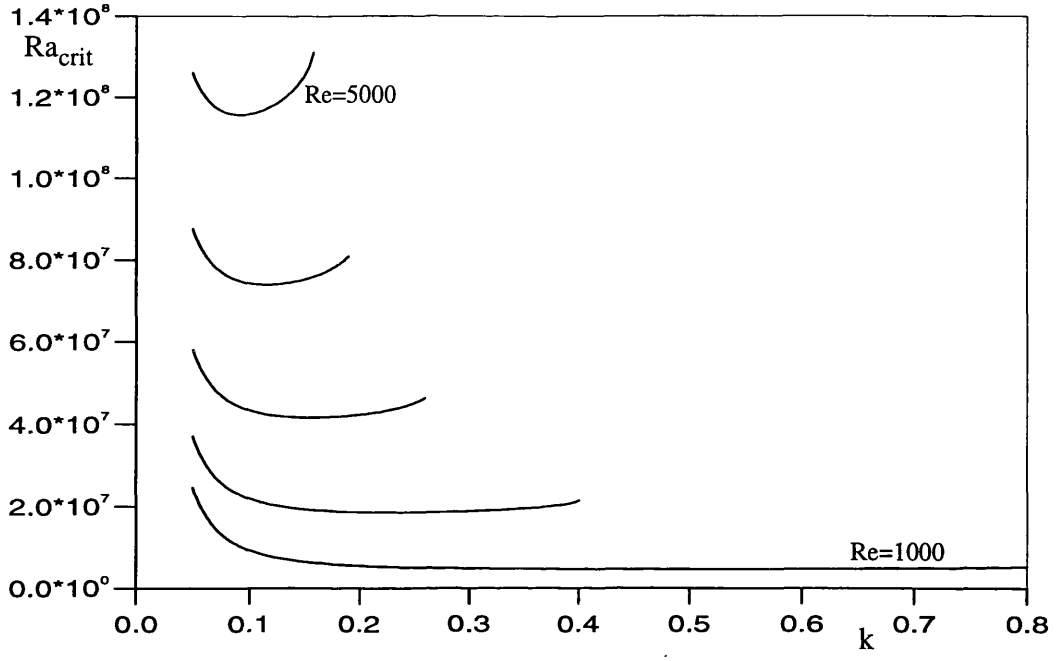

Figure 3.5. Neutral Stability curves for Re=1000,2000,.....,5000 and range of wavenumbers for r_0=0.3 and small Ra/(Re Pr).

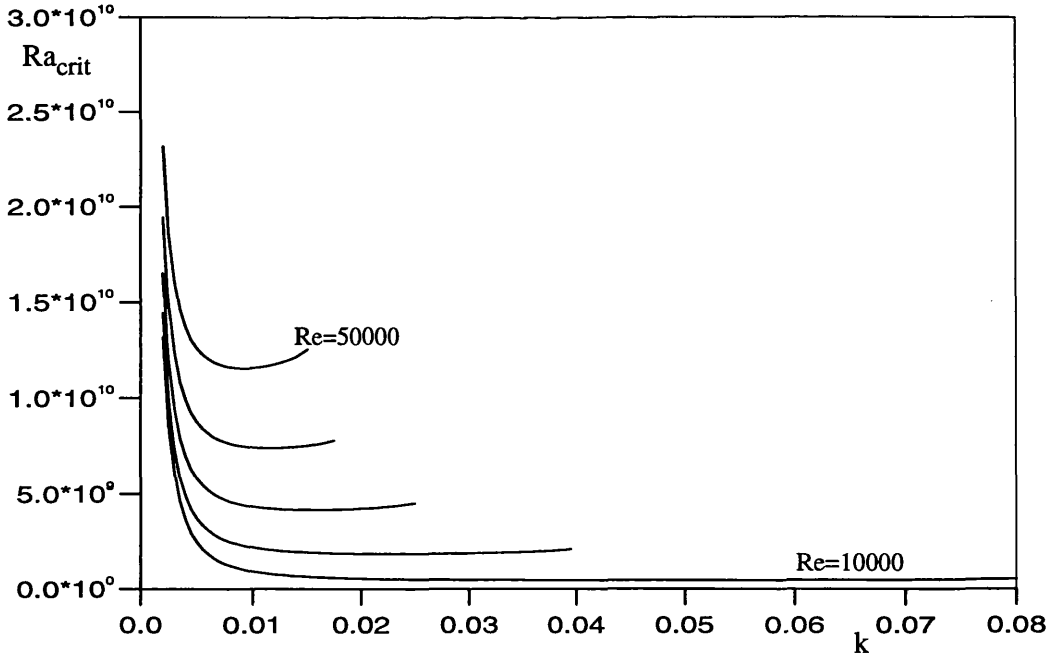

Figure 3.6. Neutral Stability curves for Re=10000,20000,.....,50000 and range of wavenumbers for r_0=0.3 and small Ra/(Re Pr).

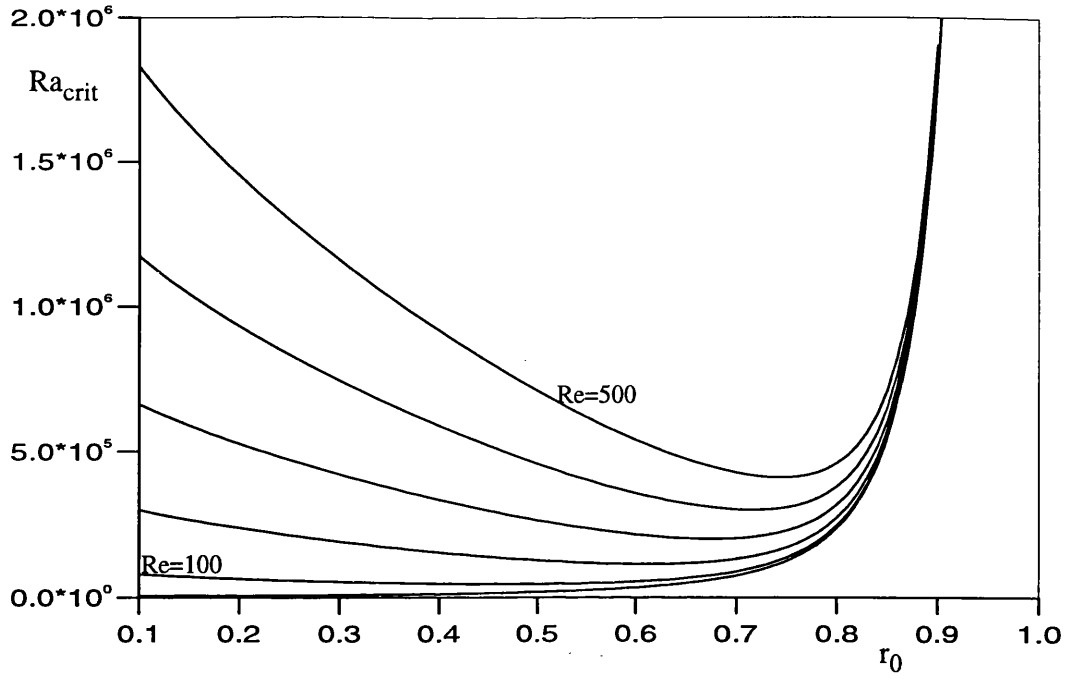

Figure 3.7. Neutral Stability curves for minimum k , range of inner radii and Re=0,100,.....,500 with Ra/(Re Pr) small.

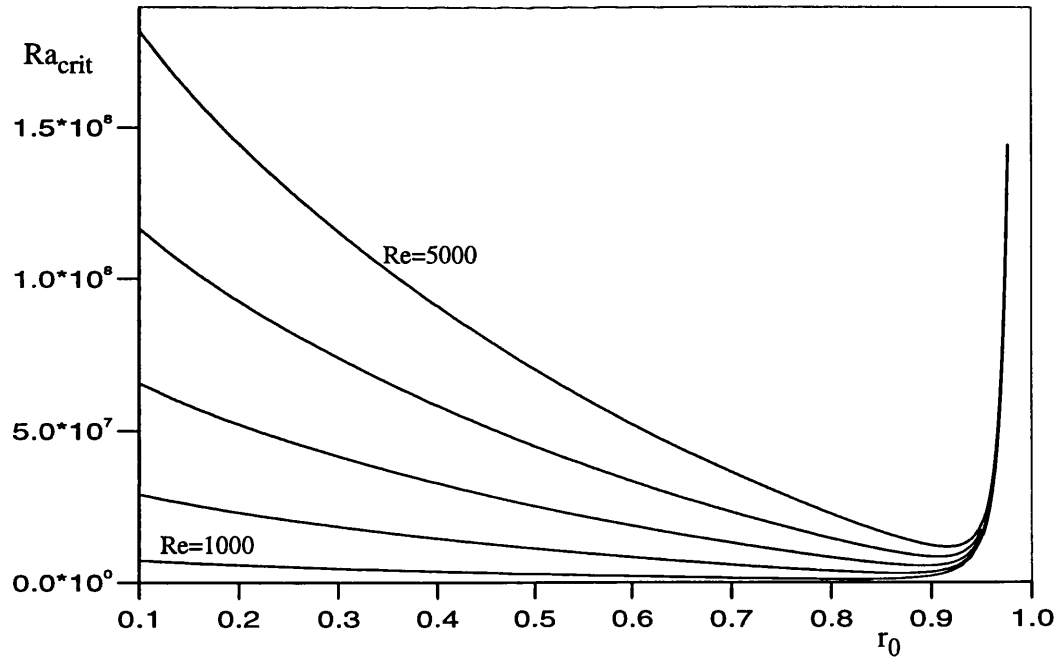

Figure 3.8. Neutral Stability curves for minimum k, range of inner radii and Re=1000,2000,.....,5000 with Ra/(Re Pr) small.

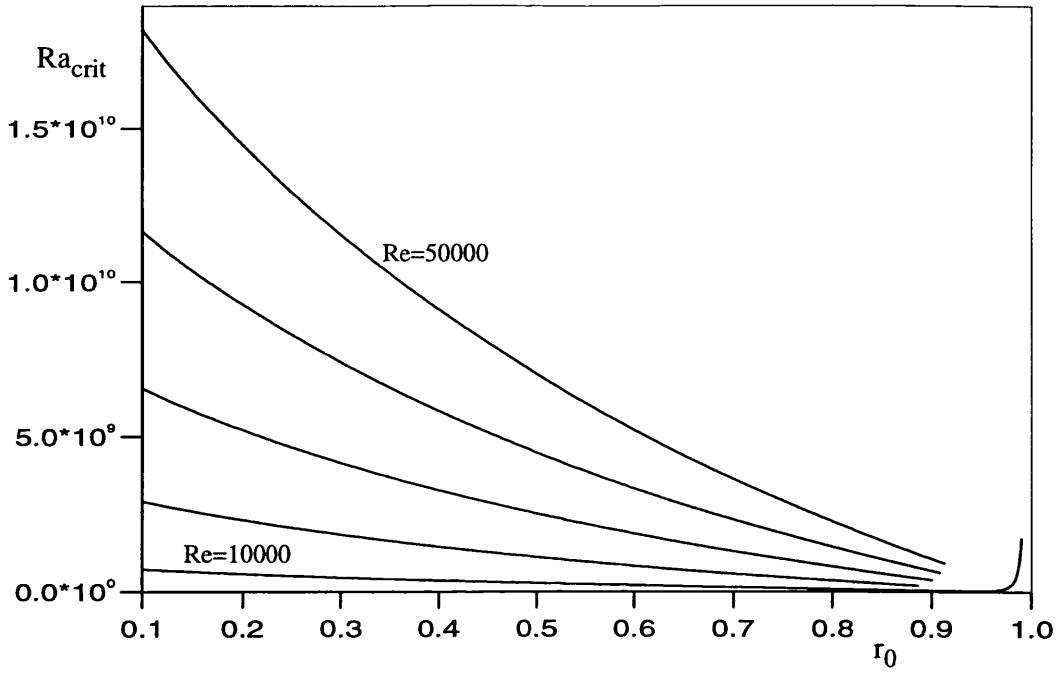

Figure 3.9. Neutral Stability curves for minimum k, range of inner radii and Re=10000,20000,.....,50000 with Ra/(Re Pr) small.

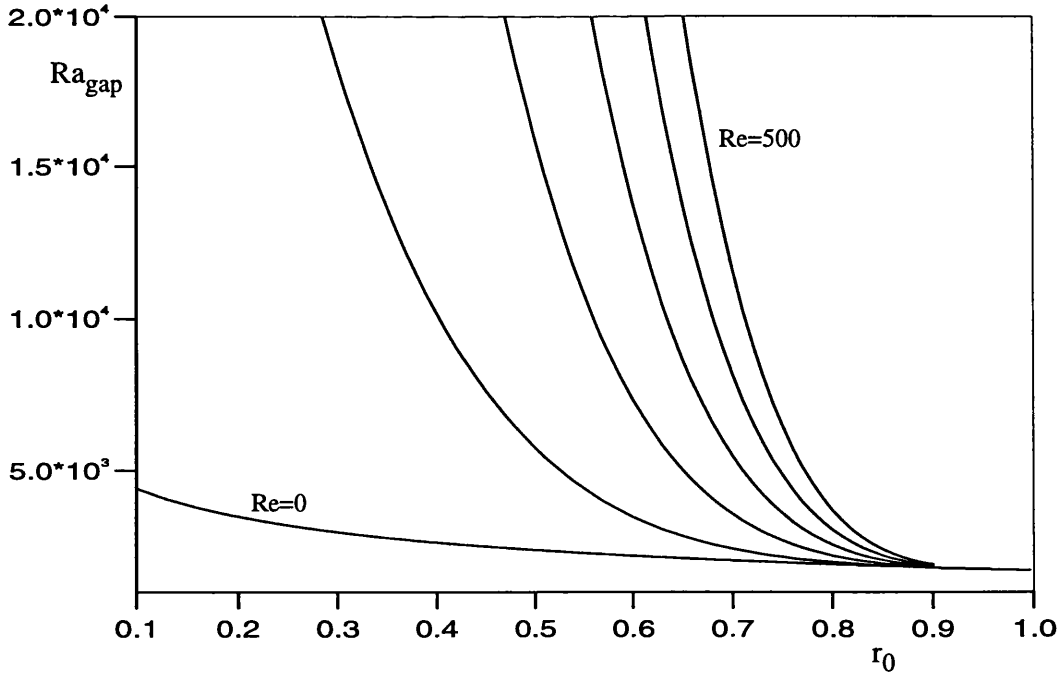

Figure 3.10. Critical Rayleigh number based on the gap for Re=0,100,.....,500. In the limit as $r_0 \longrightarrow 1$, the critical Rayleigh number tends to the plane wall Bénard value. Ra/(Re Pr) assumed small.

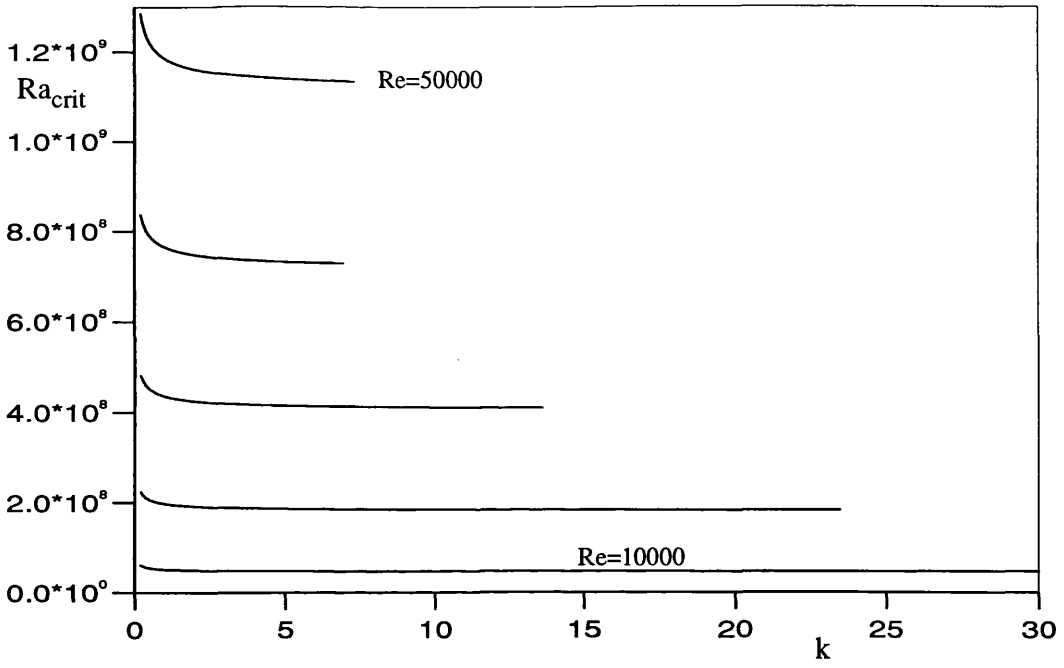

Figure 3.13. Neutral Stability curves for Re=10000,....,50000 and range of wavenumbers for r_0=0.5 and large Ra/(Re Pr).

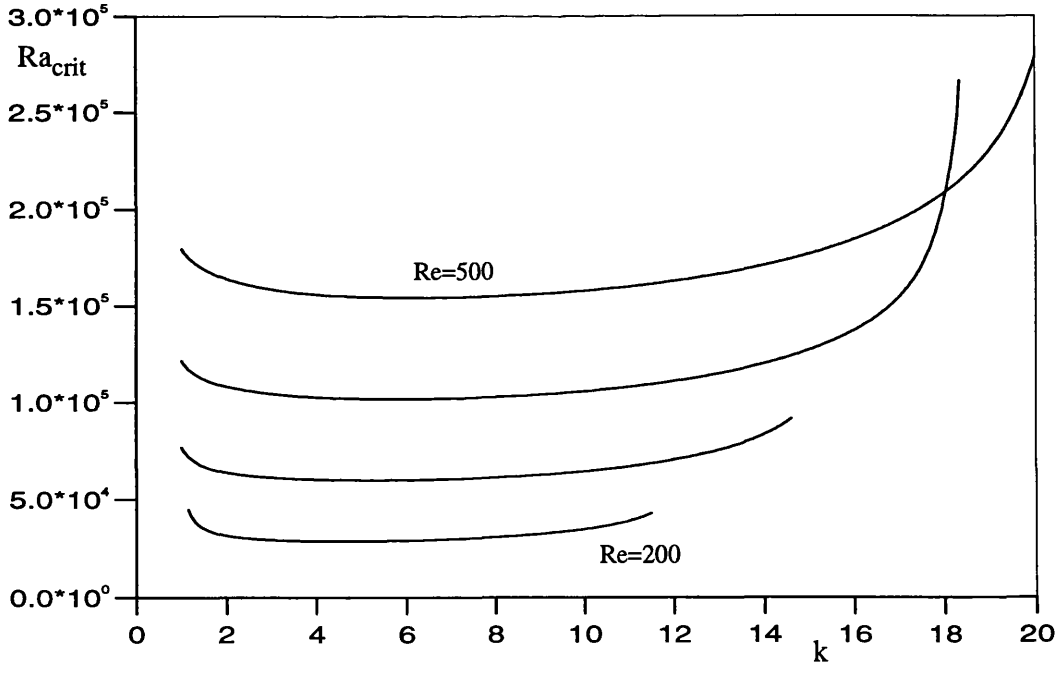

Figure 3.14. Neutral Stability curves for Re=200,300,...,500 and range of wavenumbers for r_0=0.3 and large Ra/(Re Pr).

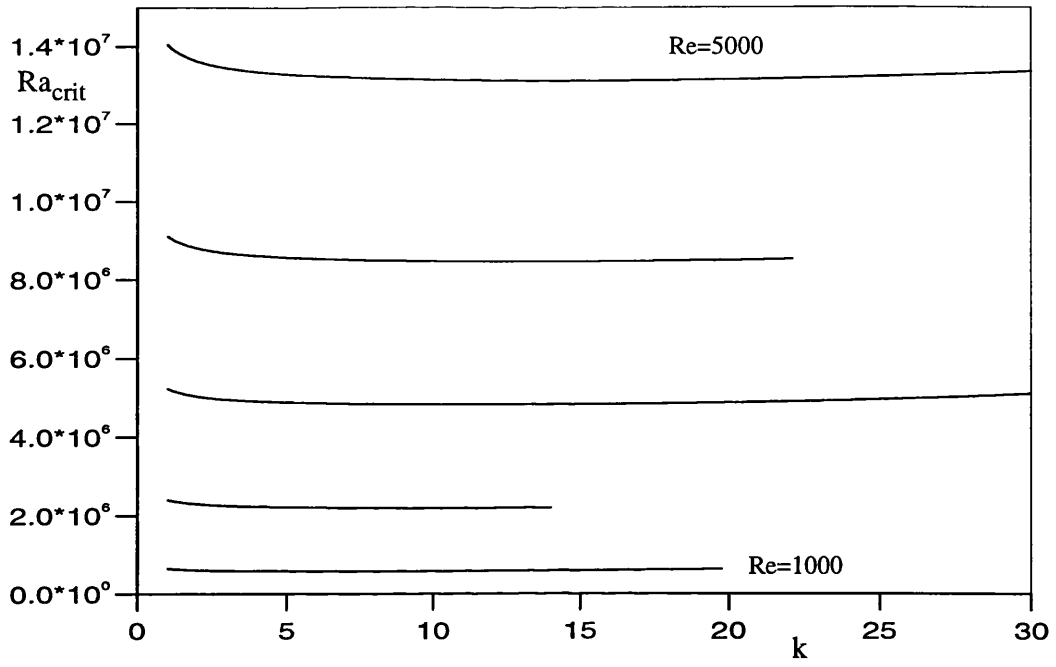

Figure 3.15. Neutral Stability curves for Re=1000,2000,.....,5000 and range of wavenumbers for r_0=0.3 and large Ra/(Re Pr).

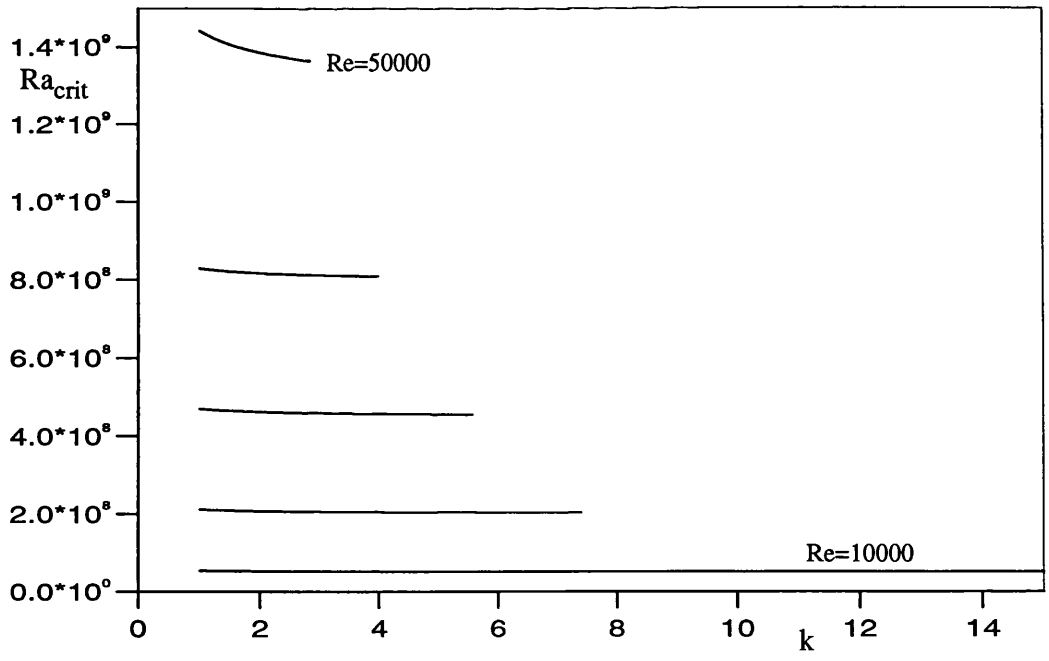

Figure 3.16. Neutral Stability curves for Re=10000,20000,.....,50000 and range of wavenumbers for r_0=0.3 and large Ra(Re Pr).

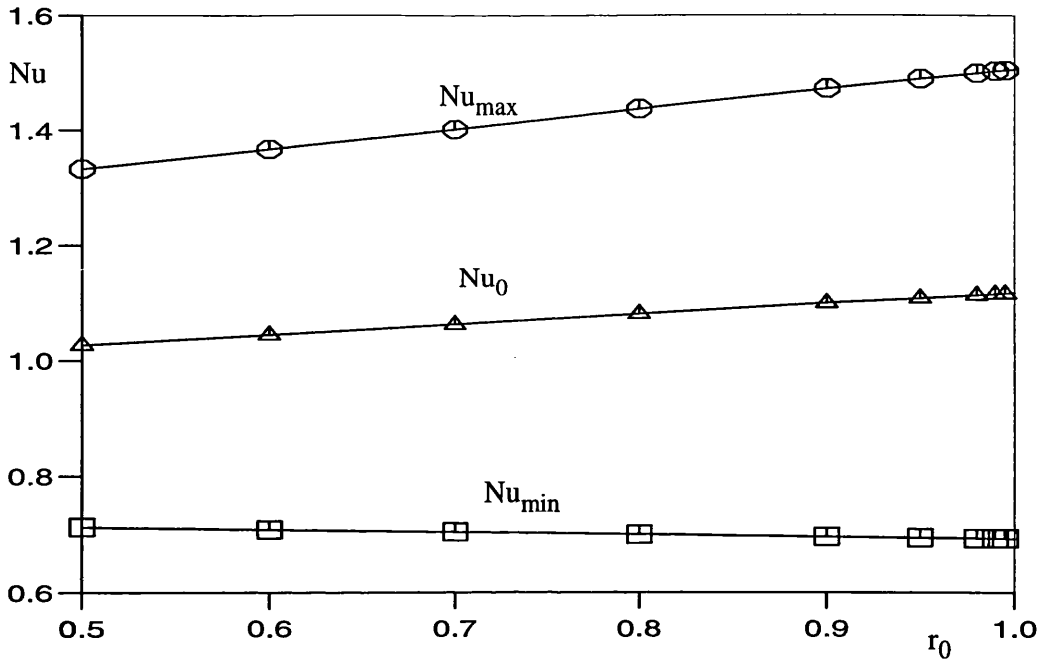

Figure 3.17. Linear variation of heat transfer at heated wall for $Ra_{gap}=10^3$, Re=0 and under the assumption of small Ra/(Re Pr).

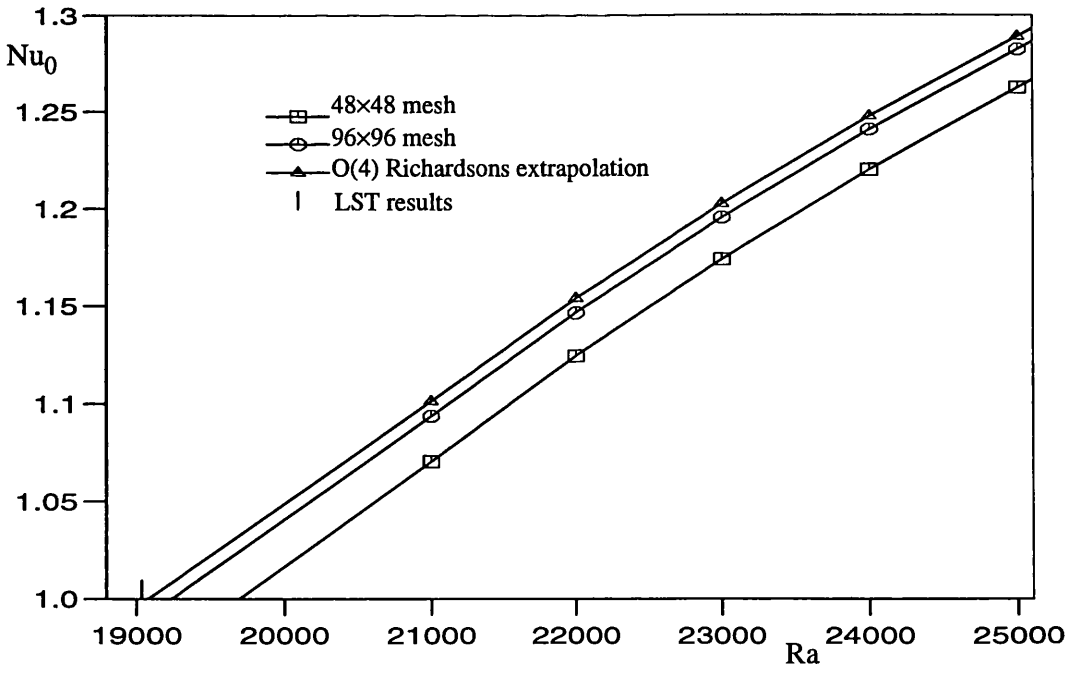

Figure 3.18. Heat transfer near onset of convection for validation with LST results for Re=0 and small Ra/(Re Pr).

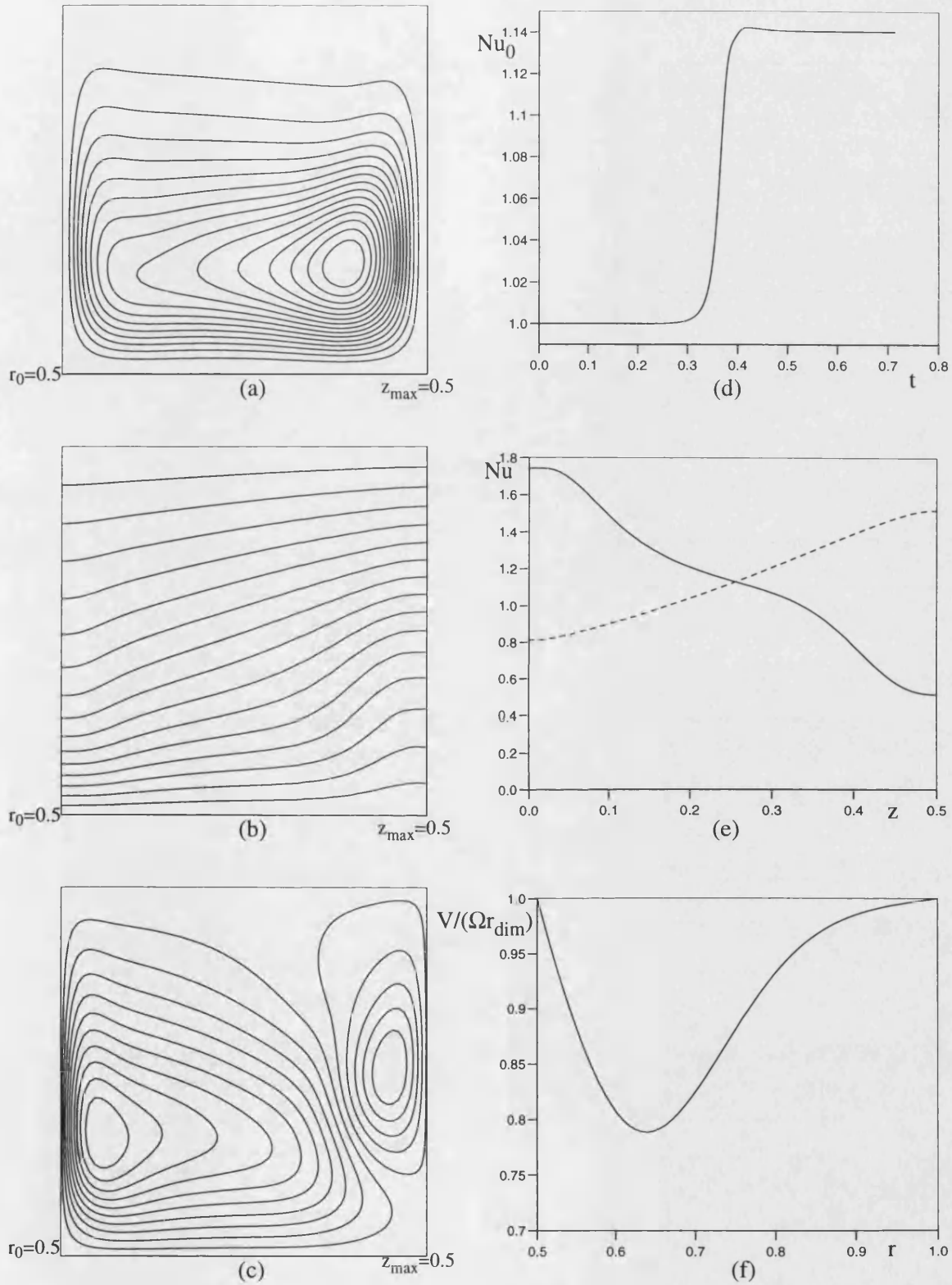

Figure 3.19. Solutions for axisymmetric radial/axial flow with $Ra=10^6$, $Re=400$, $r_0=0.5$ and $z_{max}=0.5$.

(a) streamlines (b) iso–therms
(c) tangential velocity iso–lines (d) total heat transfer
(e) local heat transfer ——— inner radius - - - - outer radius
(f) variation of tangential velocity at the mid–axial plane

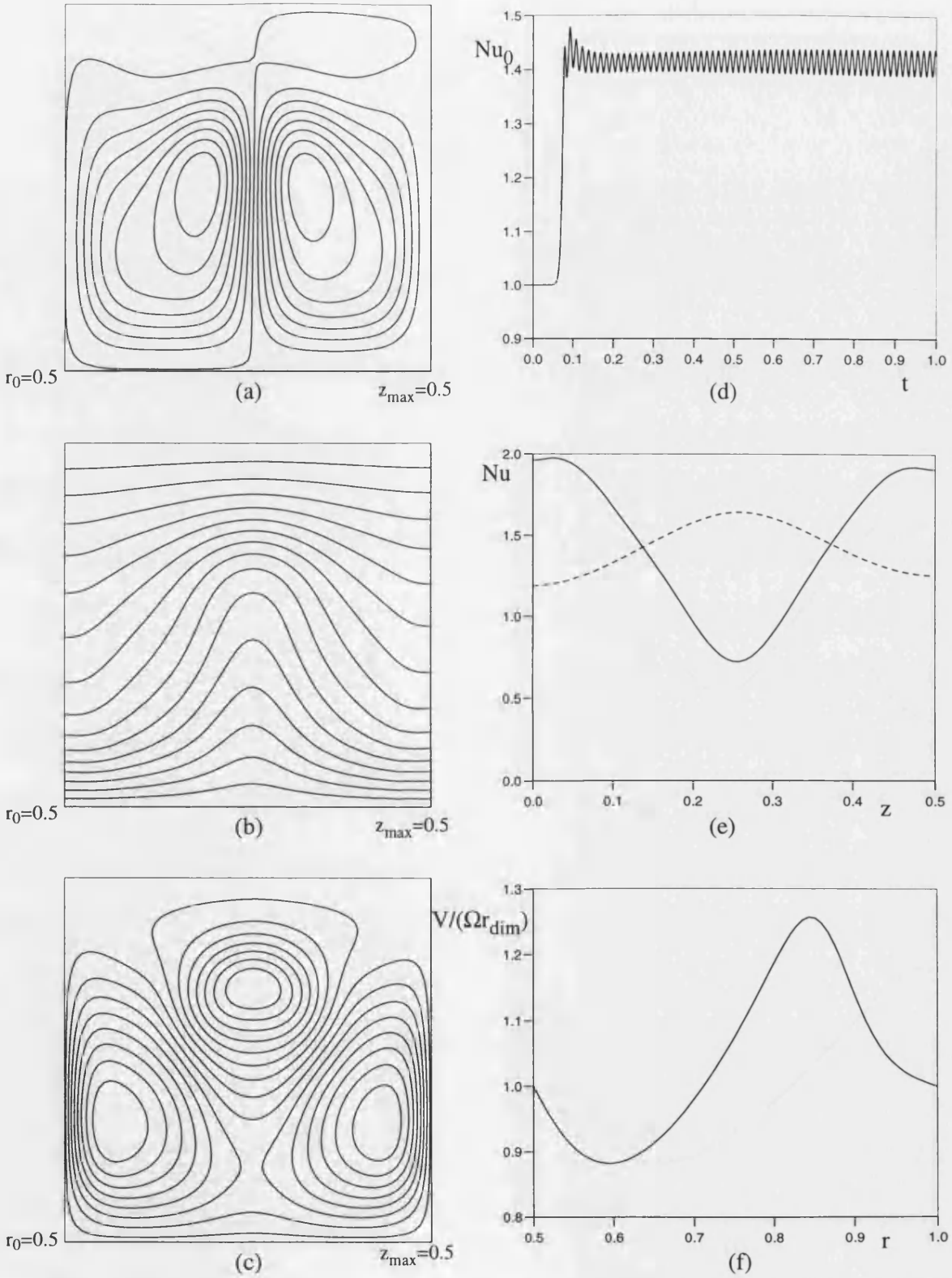

Figure 3.20. Solutions for axisymmetric radial/axial flow with $Ra=10^6$, $Re=500$, $r_0=0.5$ and $z_{max}=0.5$.
(a) streamlines (b) iso–therms
(c) tangential velocity iso–lines (d) total heat transfer
(e) local heat transfer ——— inner radius - - - - outer radius
(f) variation of tangential velocity at the mid–axial plane

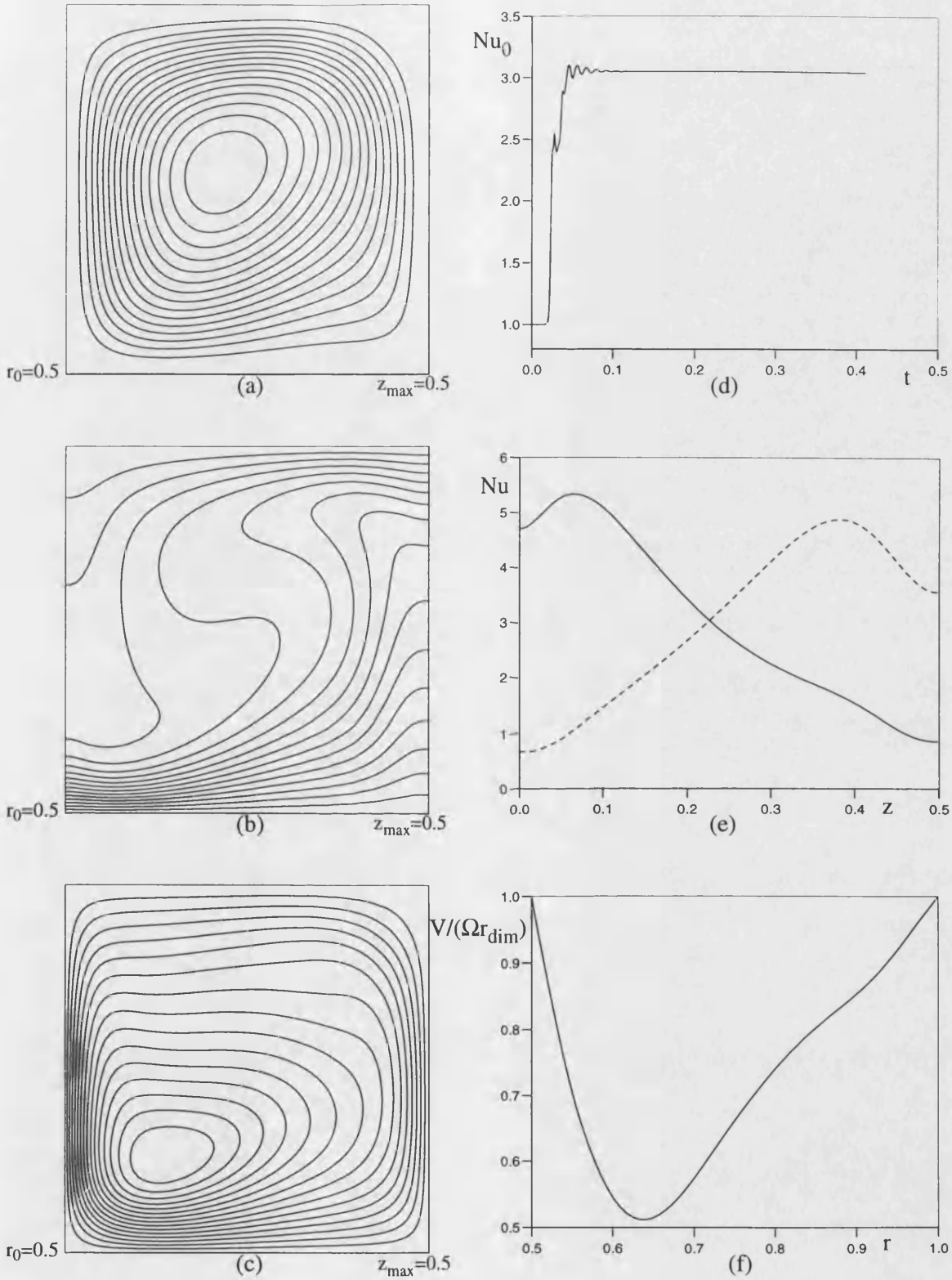

Figure 3.22. Solutions for axisymmetric radial/axial flow with $Ra=10^6$, $Re=900$, $r_0=0.5$ and $z_{max}=0.5$

(a) streamlines (b) iso–therms
(c) tangential velocity iso–lines (d) total heat transfer
(e) local heat transfer ——— inner radius - - - - outer radius
(f) variation of tangential velocity at the mid–axial plane

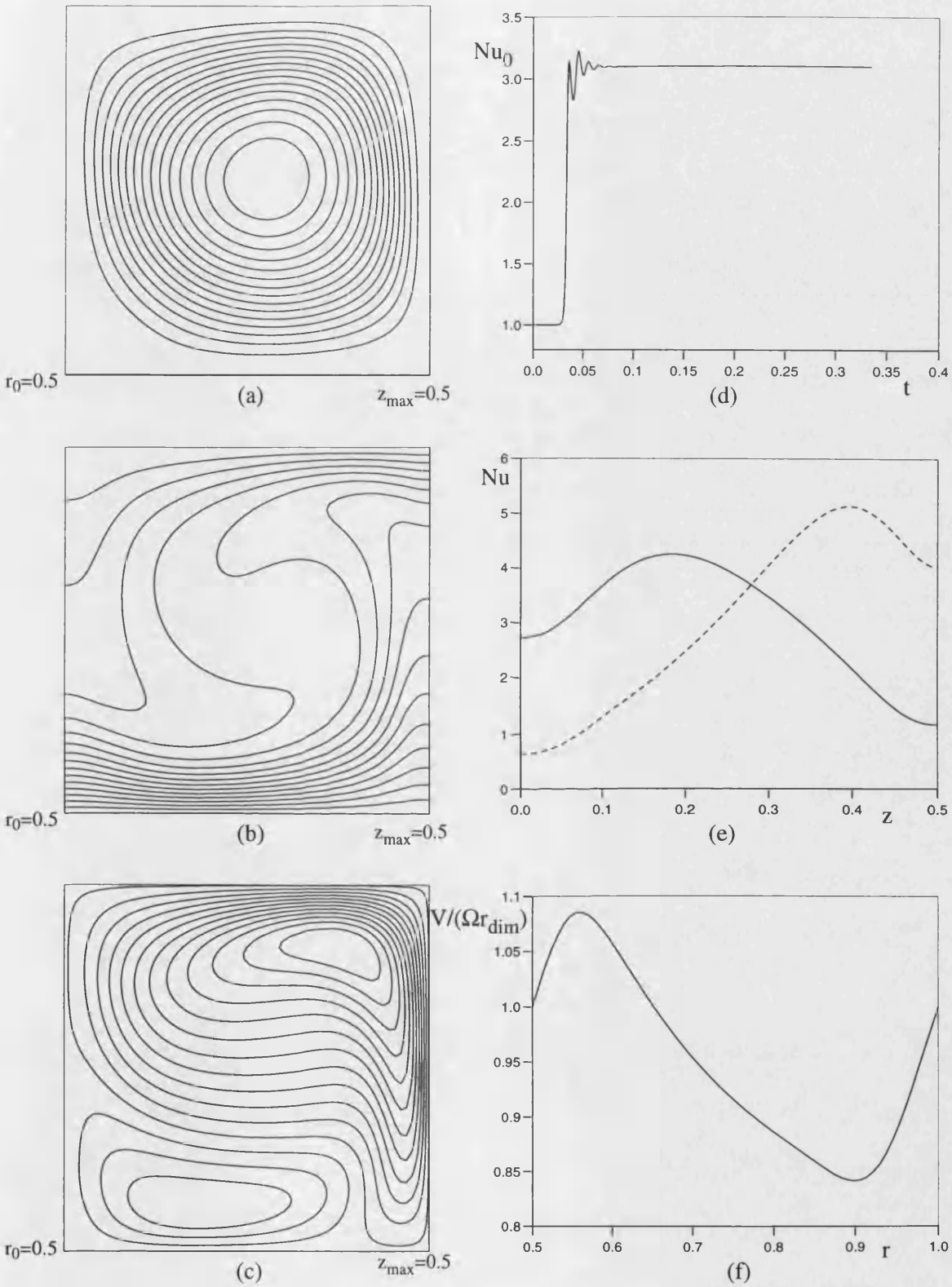

Figure 3.23. Solutions for axisymmetric radial/axial flow with $Ra=10^6$, $Re=1.2\times10^3$, $r_0=0.5$ and $z_{max}=0.5$.
(a) streamlines (b) iso–therms
(c) tangential velocity iso–lines (d) total heat transfer
(e) local heat transfer ——— inner radius - - - - outer radius
(f) variation of tangential velocity at the mid–axial plane

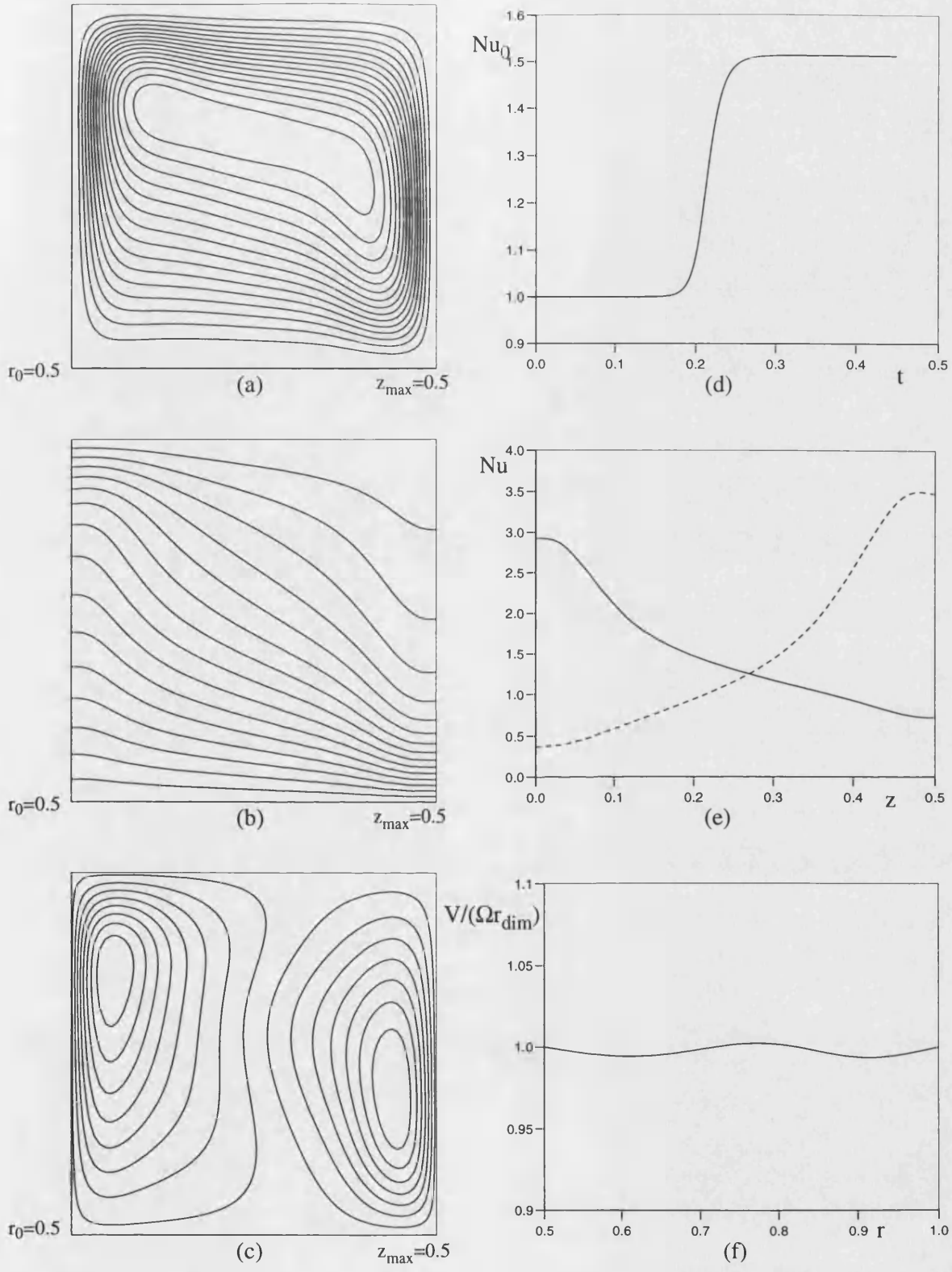

Figure 3.24. Solutions for axisymmetric radial/axial flow with $Ra=10^6$, $Re=1.6\times10^3$, $r_0=0.5$ and $z_{max}=0.5$.
(a) streamlines (b) iso–therms
(c) tangential velocity iso–lines (d) total heat transfer
(e) local heat transfer ——— inner radius - - - - outer radius
(f) variation of tangential velocity at the mid–axial plane

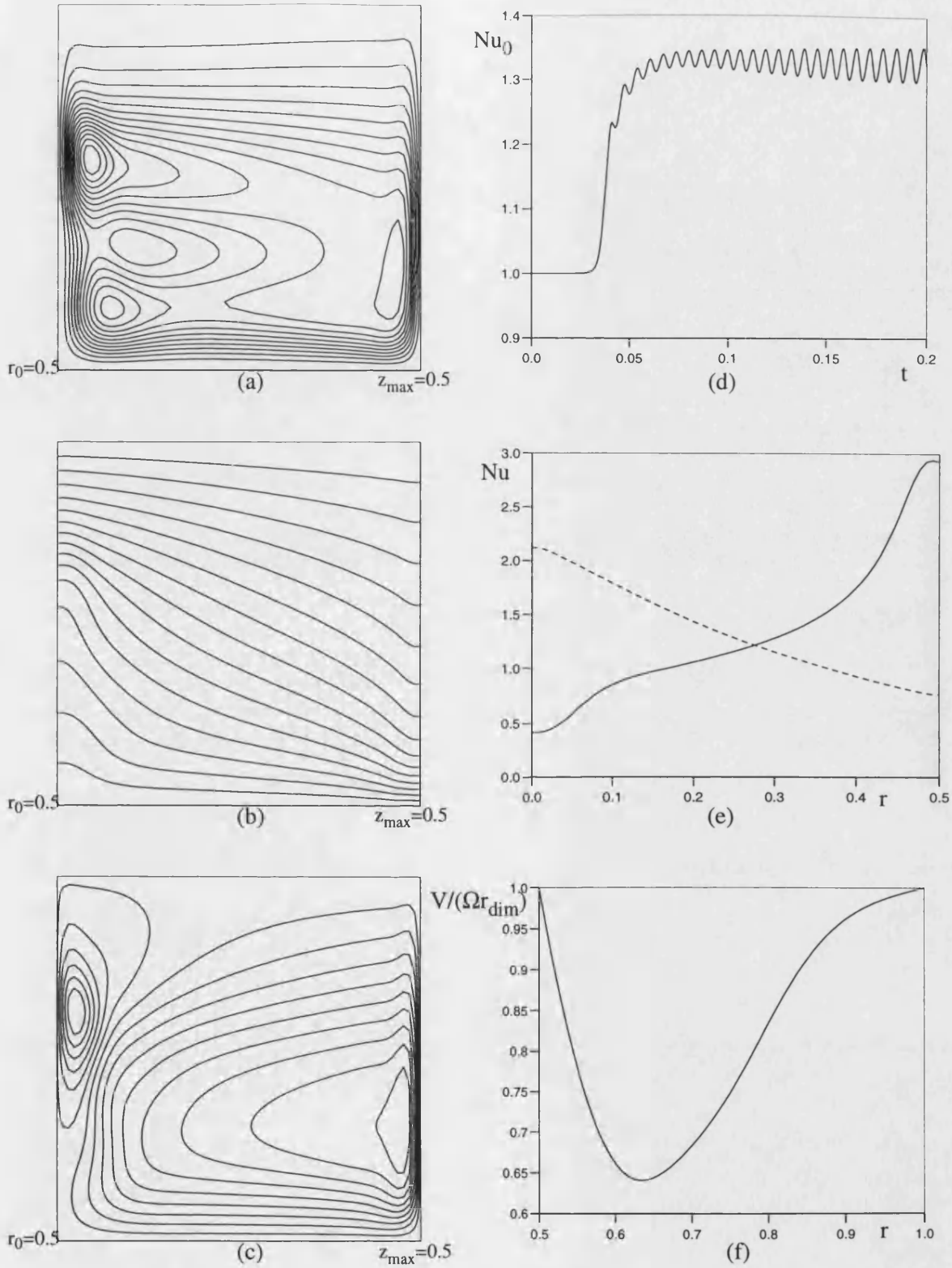

Figure 3.25. Solutions for axisymmetric radial/axial flow with $Ra=10^7$, $Re=10^3$, $r_0=0.5$ and $z_{max}=0.5$.
(a) streamlines (b) iso–therms
(c) tangential velocity iso–lines (d) total heat transfer
(e) local heat transfer ——— inner radius - - - - outer radius
(f) variation of tangential velocity at the mid–axial plane

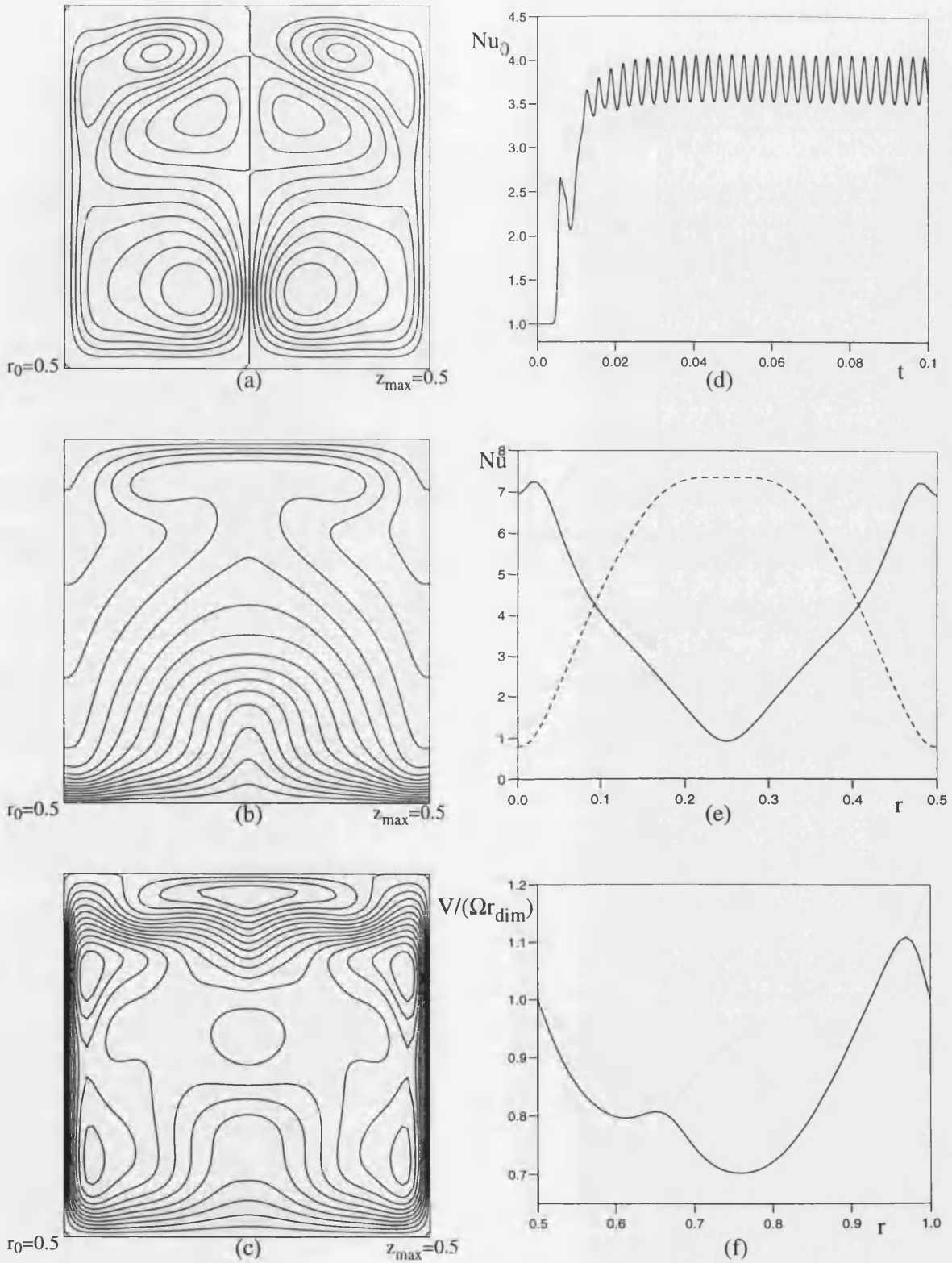

Figure 3.26. Solutions for axisymmetric radial/axial flow with $Ra=10^7$, $Re=2\times10^3$, $r_0=0.5$ and $z_{max}=0.5$.

(a) streamlines (b) iso–therms
(c) tangential velocity iso–lines (d) total heat transfer
(e) local heat transfer ——— inner radius - - - - outer radius
(f) variation of tangential velocity at the mid–axial plane

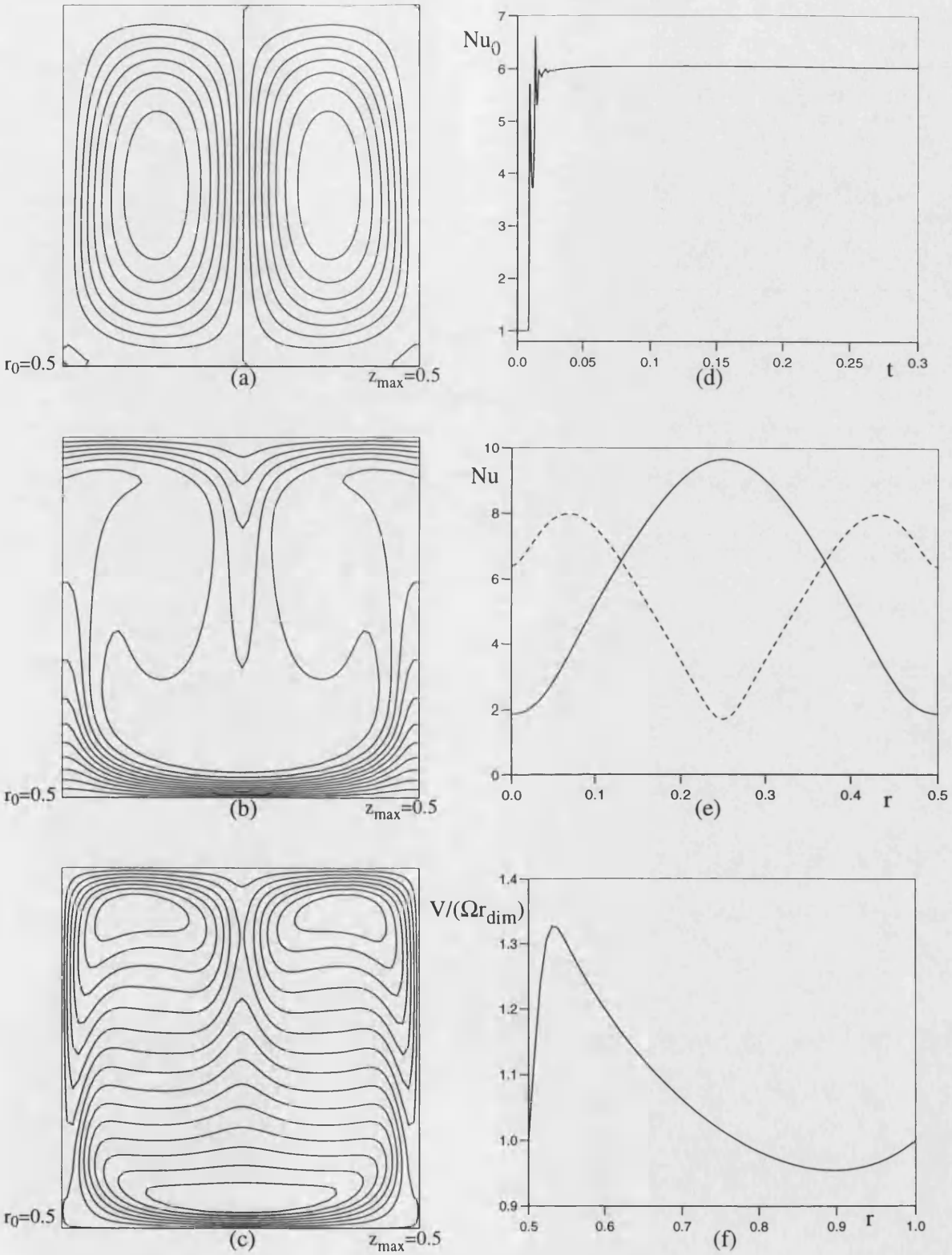

Figure 3.28. Solutions for axisymmetric radial/axial flow with $Ra=10^7$, $Re=4\times10^3$, $r_0=0.5$ and $z_{max}=0.5$.
(a) streamlines (b) iso–therms
(c) tangential velocity iso–lines (d) total heat transfer
(e) local heat transfer ——— inner radius - - - - outer radius
(f) variation of tangential velocity at the mid–axial plane

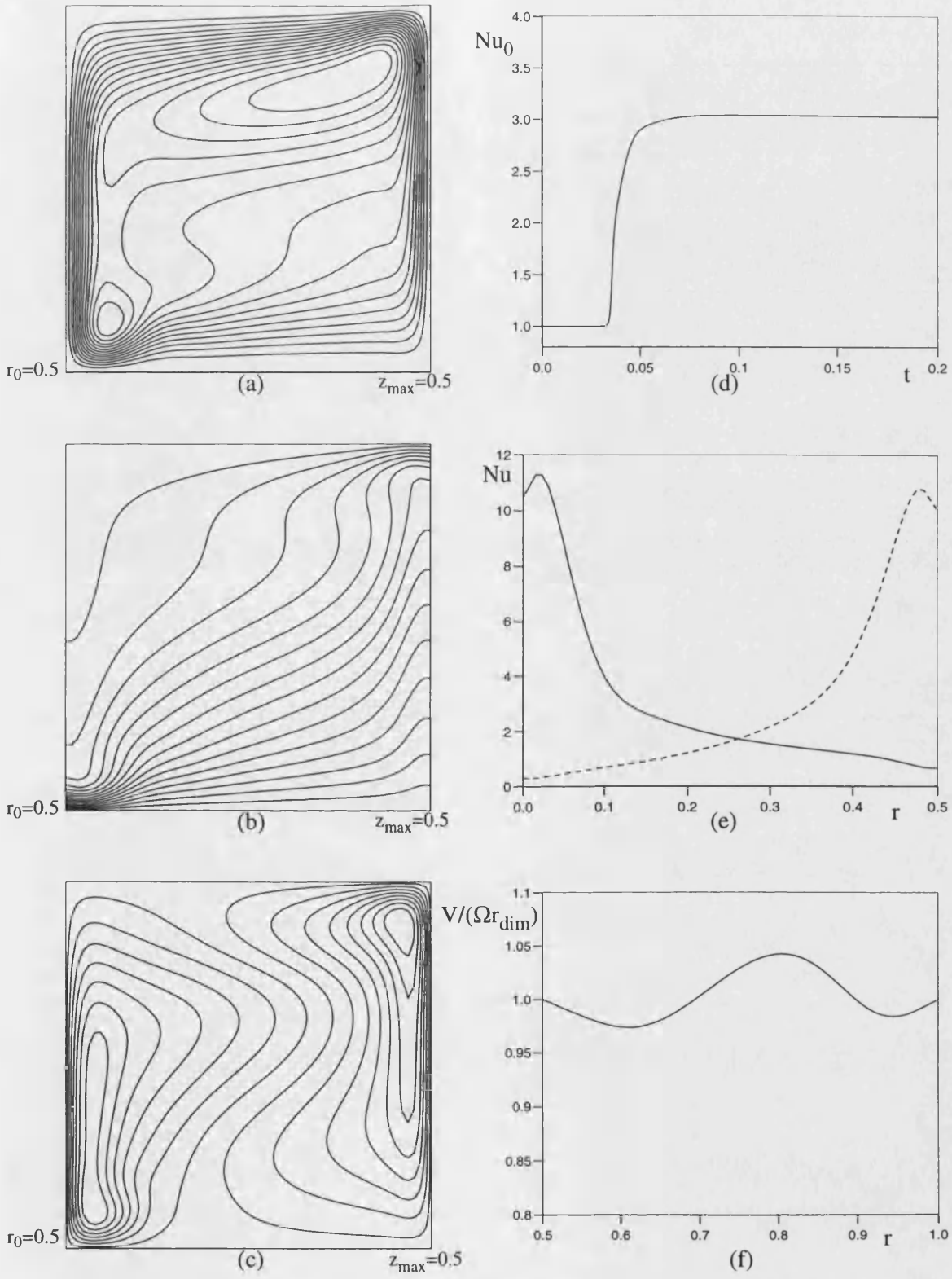

Figure 3.29. Solutions for axisymmetric radial/axial flow with $Ra=10^7$, $Re=5\times10^3$, $r_0=0.5$ and $z_{max}=0.5$.
(a) streamlines (b) iso–therms
(c) tangential velocity iso–lines (d) total heat transfer
(e) local heat transfer ——— inner radius - - - - outer radius
(f) variation of tangential velocity at the mid–axial plane

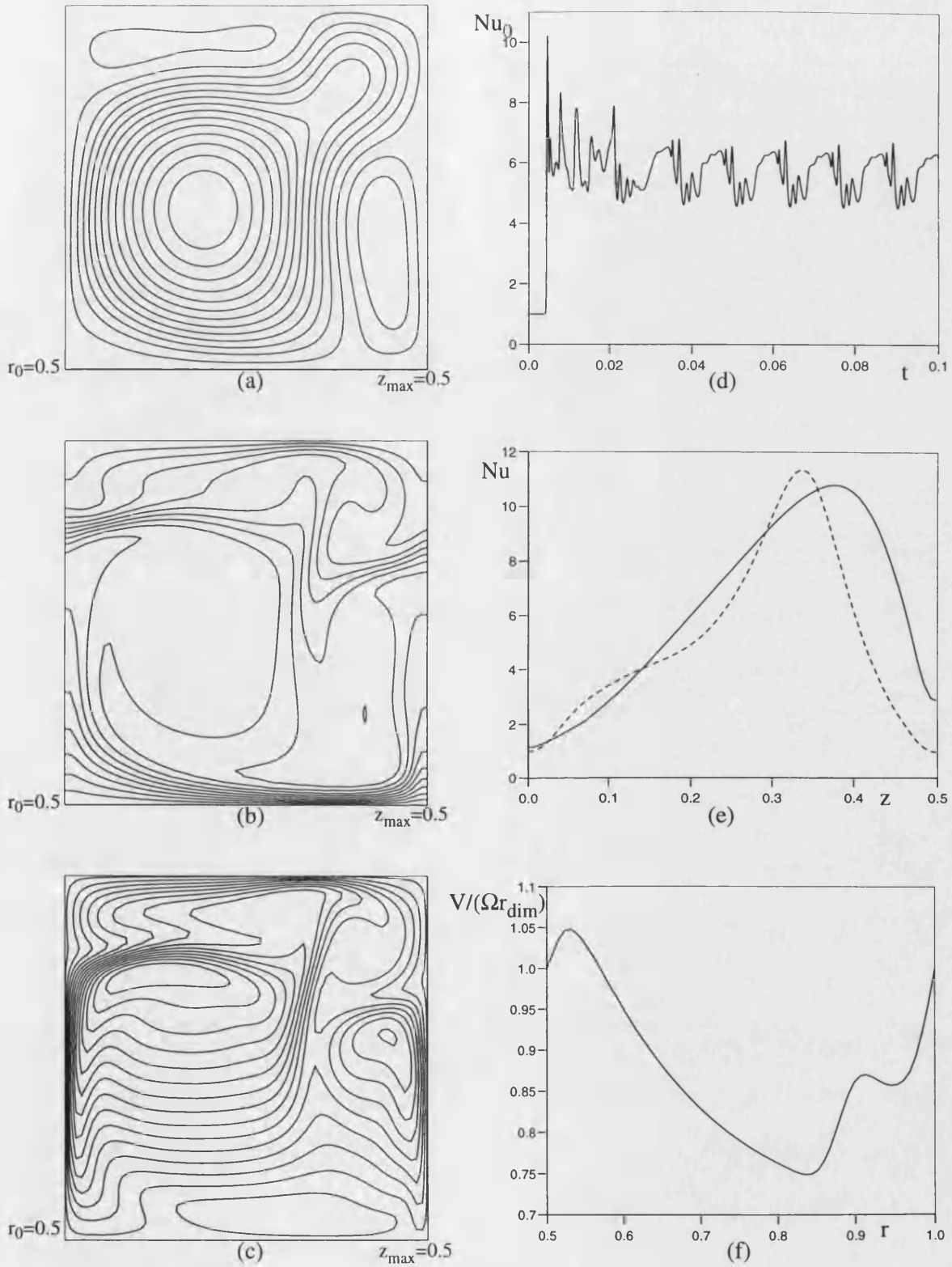

Figure 3.30. Solutions for axisymmetric radial/axial flow with $Ra=2\times10^7$, $Re=5\times10^3$, $r_0=0.5$ and $z_{max}=0.5$.
(a) streamlines (b) iso–therms
(c) tangential velocity iso–lines (d) total heat transfer
(e) local heat transfer ——— inner radius - - - - outer radius
(f) variation of tangential velocity at the mid–axial plane

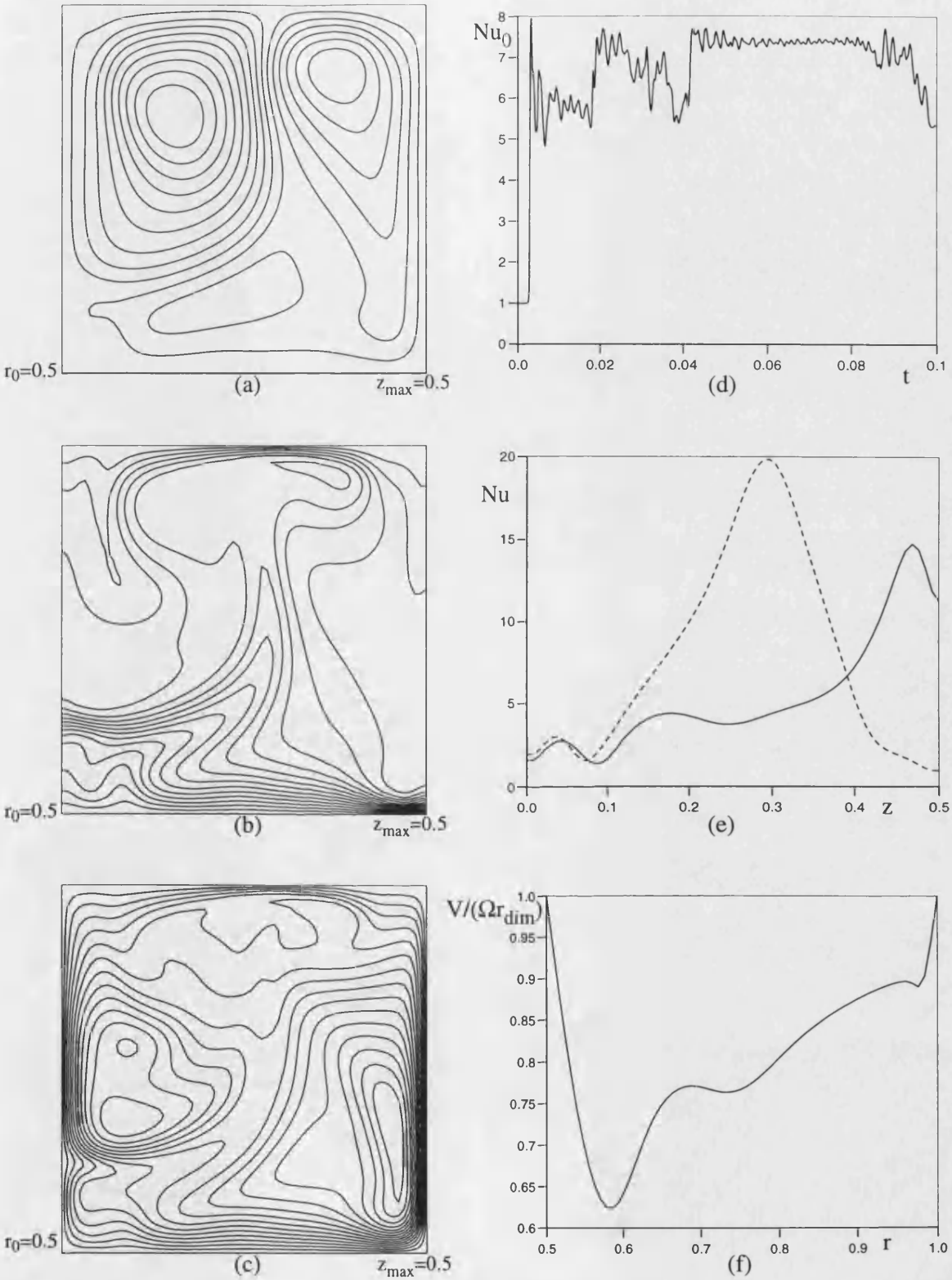

Figure 3.31. Solutions for axisymmetric radial/axial flow with $Ra=3\times10^7$, $Re=5\times10^3$, $r_0=0.5$ and $z_{max}=0.5$.
(a) streamlines (b) iso–therms
(c) tangential velocity iso–lines (d) total heat transfer
(e) local heat transfer ——— inner radius - - - - outer radius
(f) variation of tangential velocity at the mid–axial plane

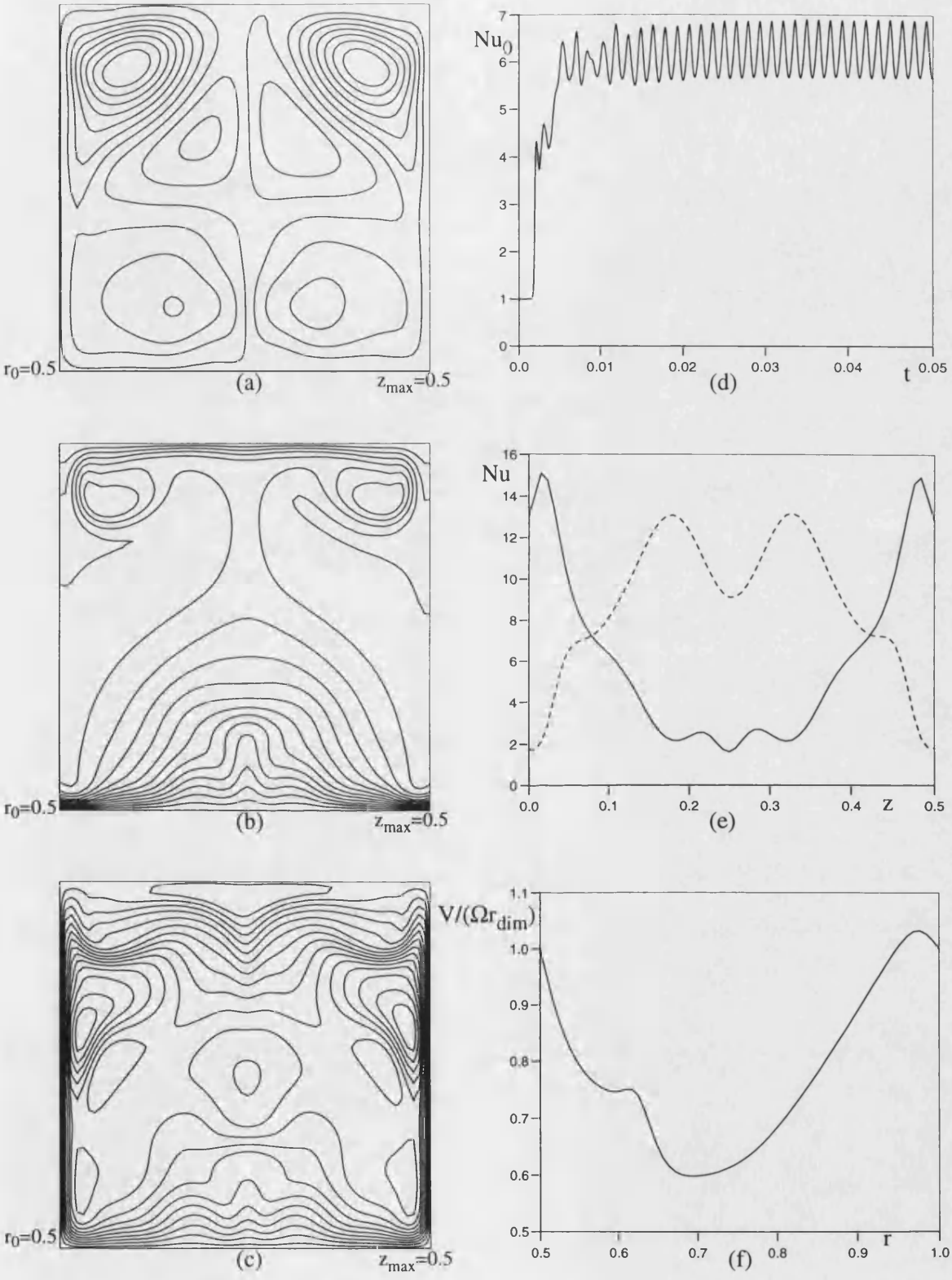

Figure 3.32. Solutions for axisymmetric radial/axial flow with $Ra=5\times10^7$, $Re=5\times10^3$, $r_0=0.5$ and $z_{max}=0.5$.
(a) streamlines (b) iso–therms
(c) tangential velocity iso–lines (d) total heat transfer
(e) local heat transfer ——— inner radius - - - - outer radius
(f) variation of tangential velocity at the mid–axial plane

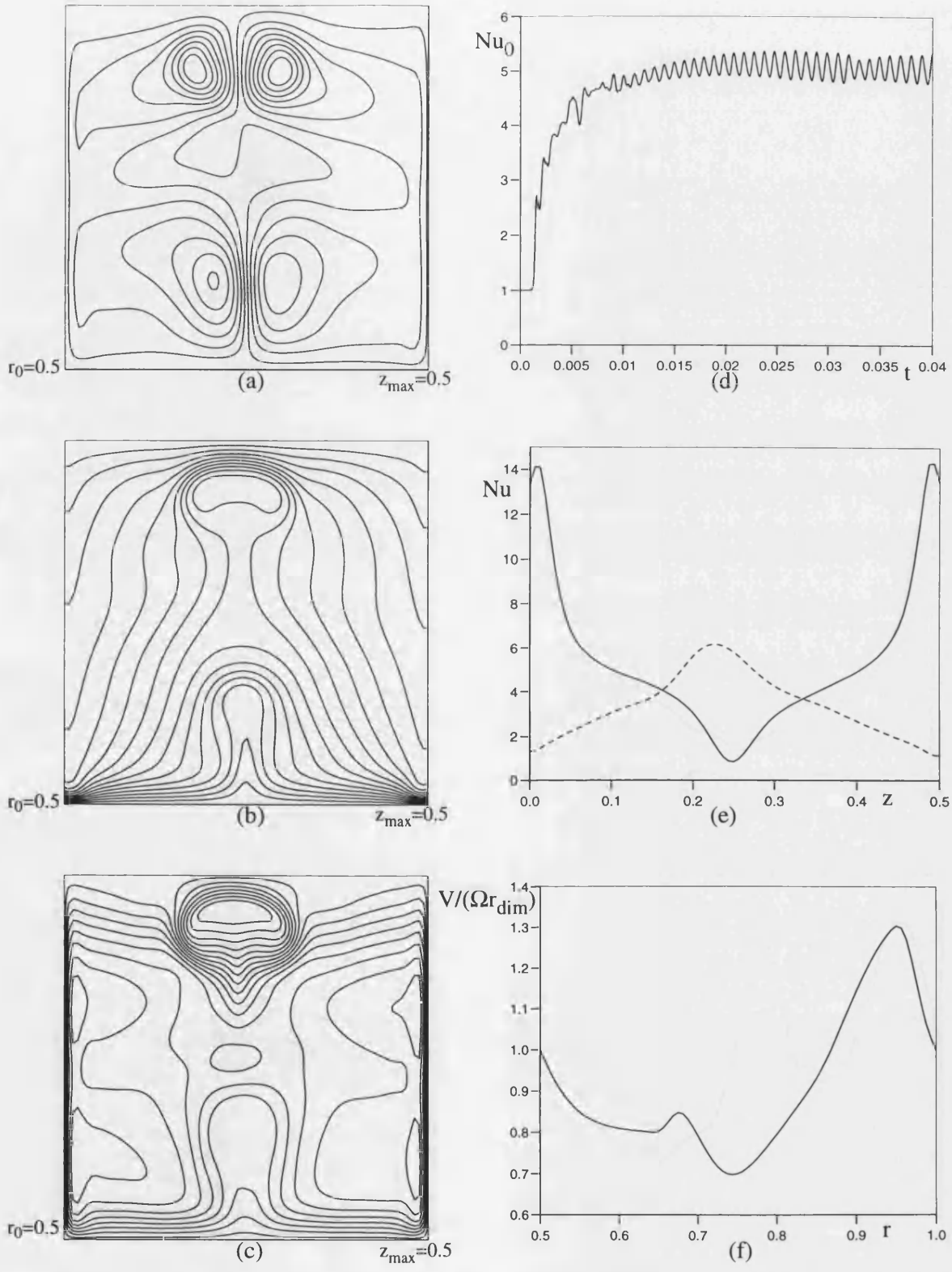

Figure 3.33. Solutions for axisymmetric radial/axial flow with $Ra=10^8$, $Re=5\times10^3$, $r_0=0.5$ and $z_{max}=0.5$.
(a) streamlines (b) iso–therms
(c) tangential velocity iso–lines (d) total heat transfer
(e) local heat transfer ——— inner radius - - - - outer radius
(f) variation of tangential velocity at the mid–axial plane

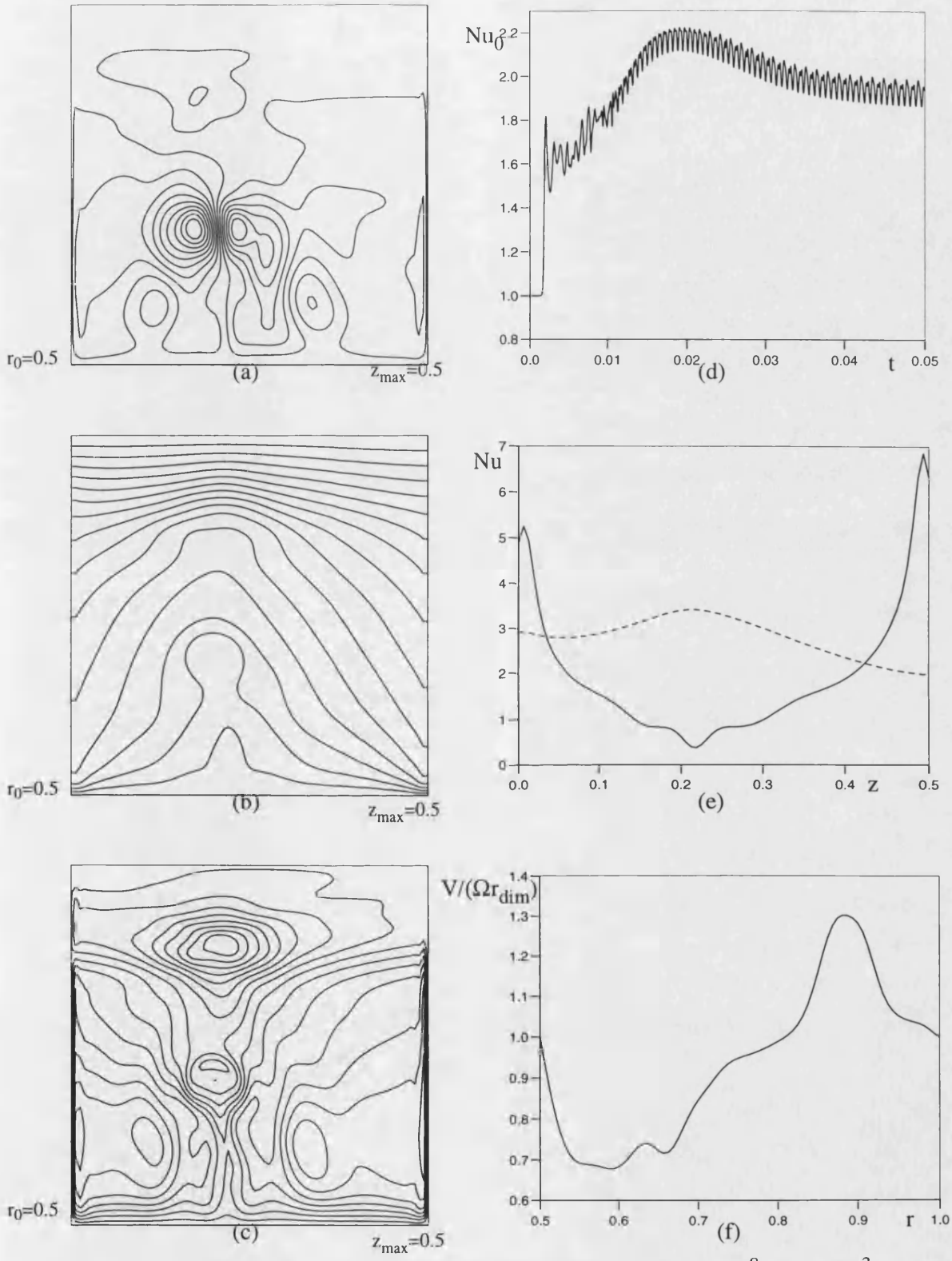

Figure 3.35. Solutions for axisymmetric radial/axial flow with $Ra=5\times10^8$, $Re=5\times10^3$, $r_0=0.5$ and $z_{max}=0.5$.
(a) streamlines (b) iso–therms
(c) tangential velocity iso–lines (d) total heat transfer
(e) local heat transfer ——— inner radius - - - - outer radius
(f) variation of tangential velocity at the mid–axial plane

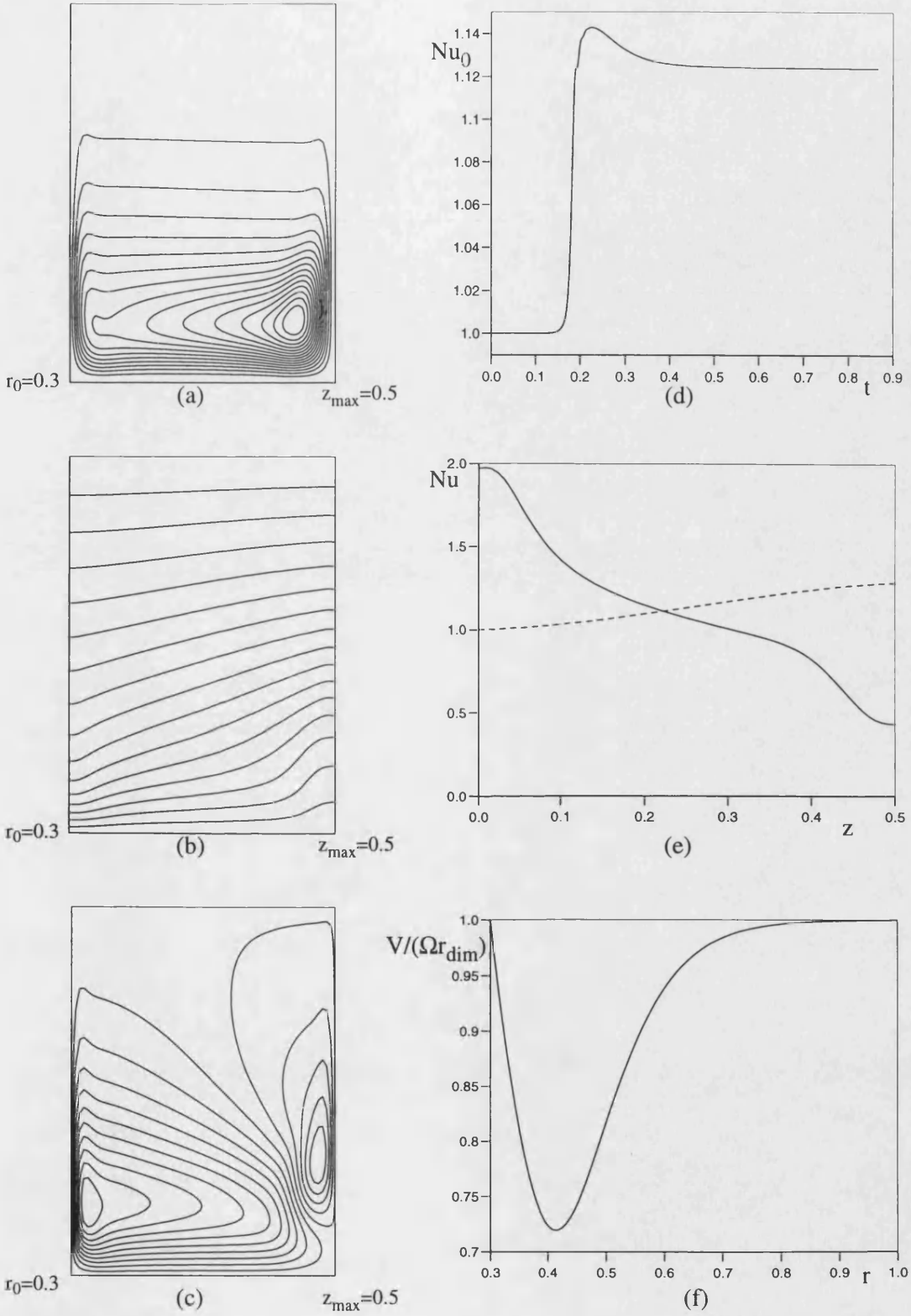

Figure 3.36. Solutions for axisymmetric radial/axial flow with $Ra=10^7$, $Re=10^3$, $r_0=0.3$ and $z_{max}=0.5$.
(a) streamlines (b) iso–therms
(c) tangential velocity iso–lines (d) total heat transfer
(e) local heat transfer ——— inner radius - - - - outer radius
(f) variation of tangential velocity at the mid–axial plane

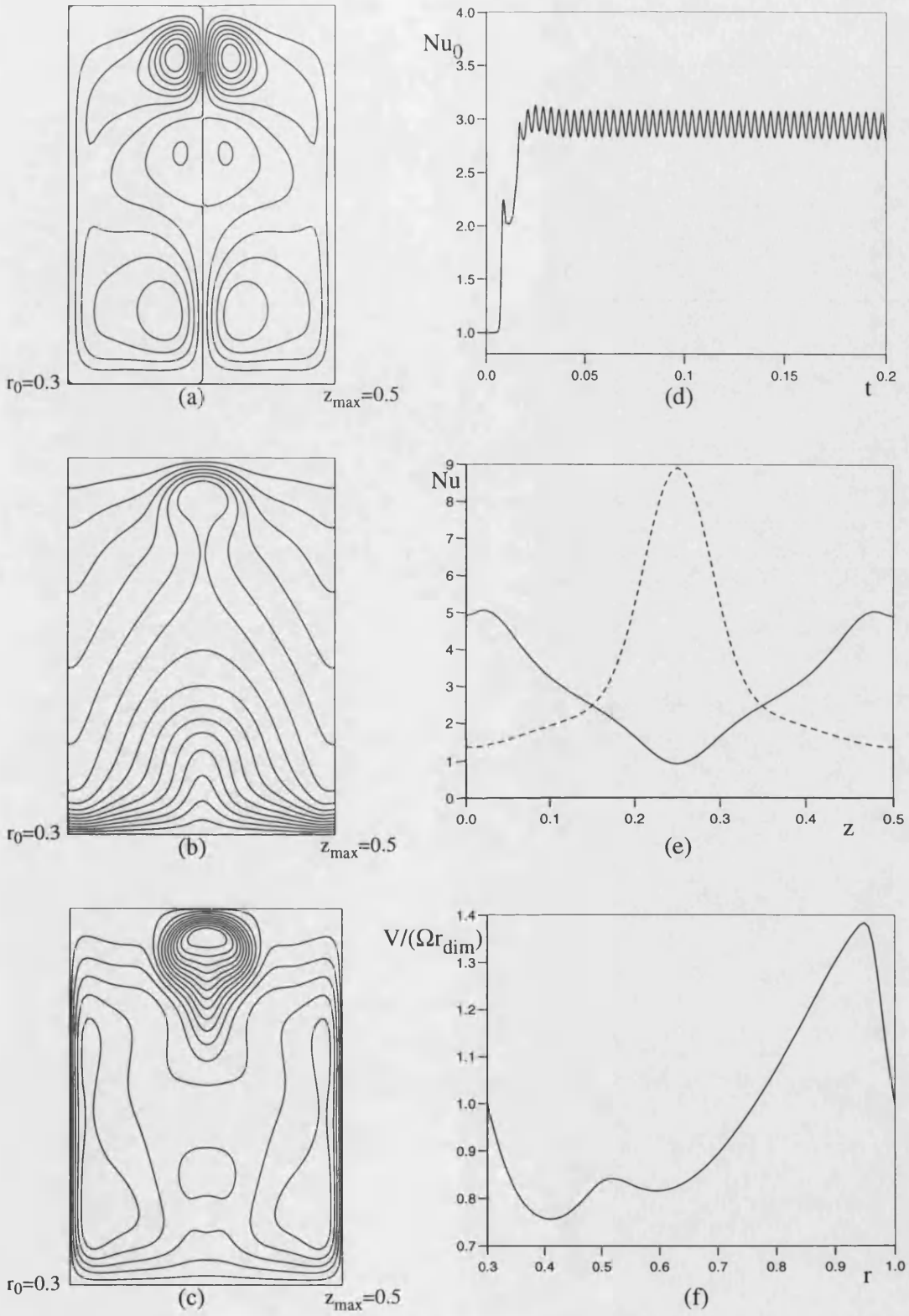

Figure 3.37. Solutions for axisymmetric radial/axial flow with $Ra=10^7$, $Re=2\times10^3$, $r_0=0.3$ and $z_{max}=0.5$.
(a) streamlines (b) iso–therms
(c) tangential velocity iso–lines (d) total heat transfer
(e) local heat transfer ——— inner radius - - - - outer radius
(f) variation of tangential velocity at the mid–axial plane

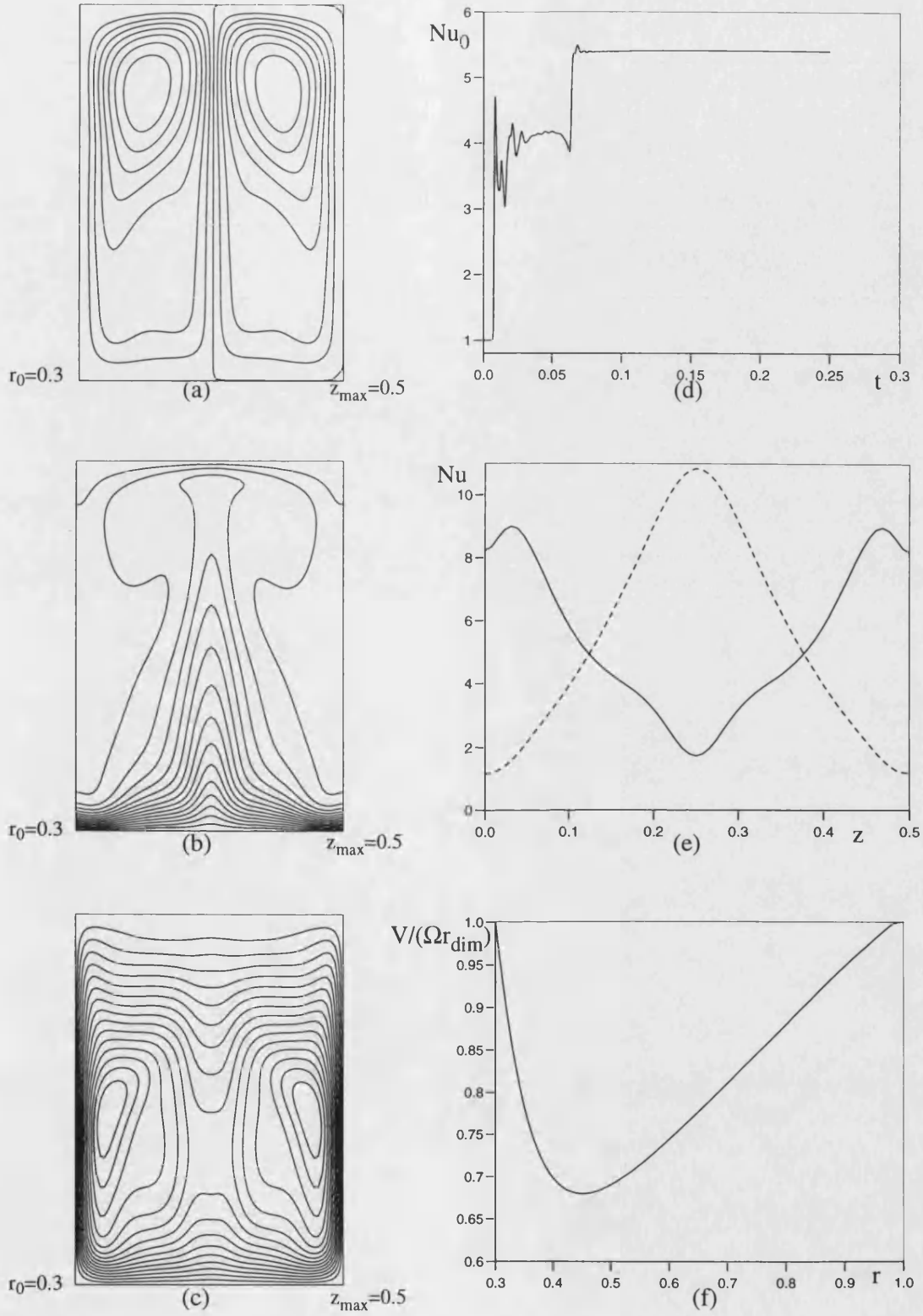

Figure 3.38. Solutions for axisymmetric radial/axial flow with $Ra=10^7$, $Re=3\times10^3$, $r_0=0.3$ and $z_{max}=0.5$.

(a) streamlines (b) iso–therms
(c) tangential velocity iso–lines (d) total heat transfer
(e) local heat transfer ——— inner radius - - - - outer radius
(f) variation of tangential velocity at the mid–axial plane

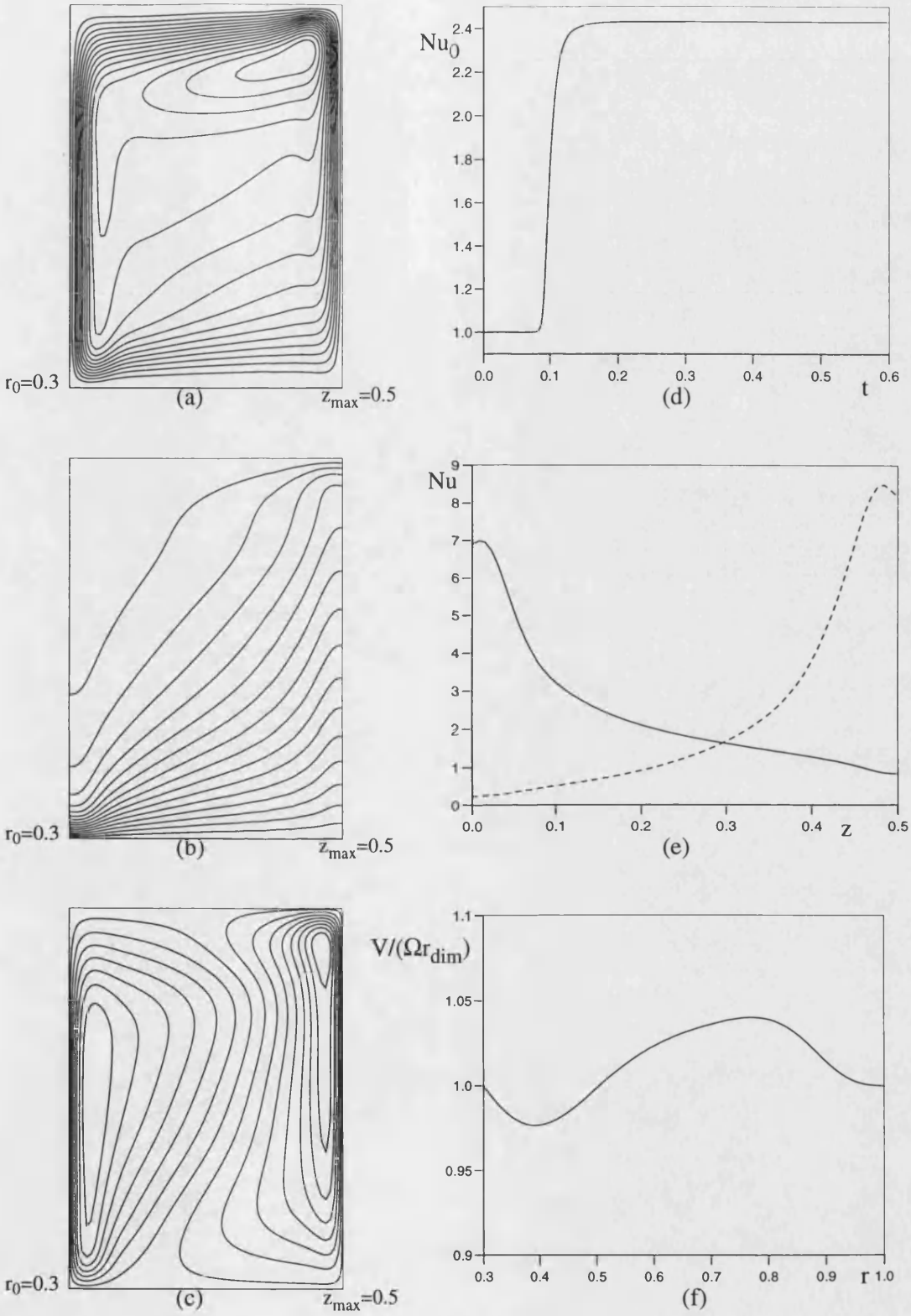

Figure 3.39. Solutions for axisymmetric radial/axial flow with $Ra=10^7$, $Re=5\times10^3$, $r_0=0.3$ and $z_{max}=0.5$.

(a) streamlines (b) iso–therms

(c) tangential velocity iso–lines (d) total heat transfer

(e) local heat transfer ——— inner radius - - - - outer radius

(f) variation of tangential velocity at the mid–axial plane

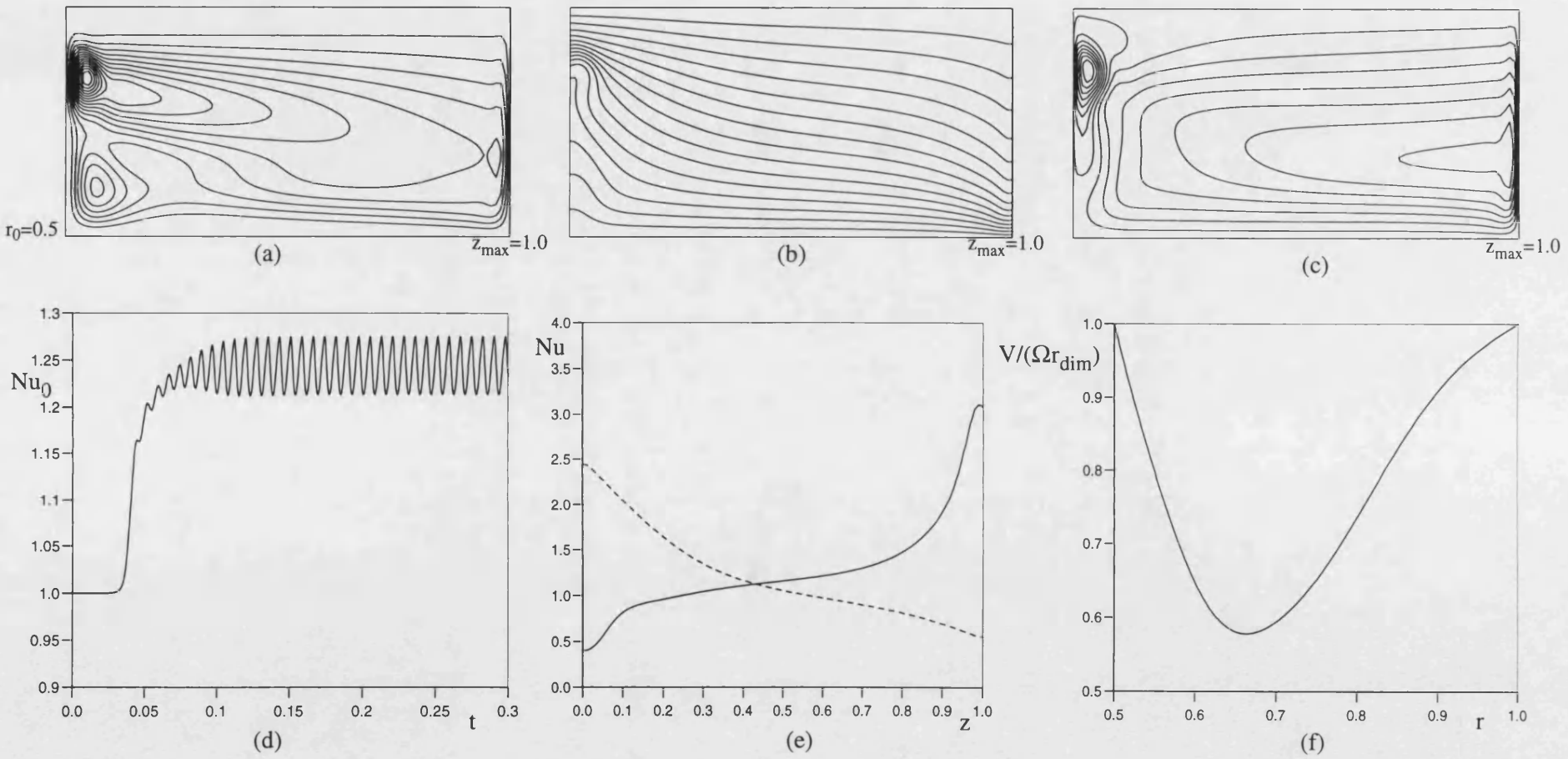

Figure 3.40. Solutions for axisymmetric radial/axial flow with $Ra=10^7$, $Re=10^3$, $r_0=0.5$ and $z_{max}=1.0$.
(a) streamlines (b) iso–therms
(c) tangential velocity iso–lines (d) total heat transfer
(e) local heat transfer ——— inner radius - - - - outer radius
(f) variation of tangential velocity at the mid–axial plane

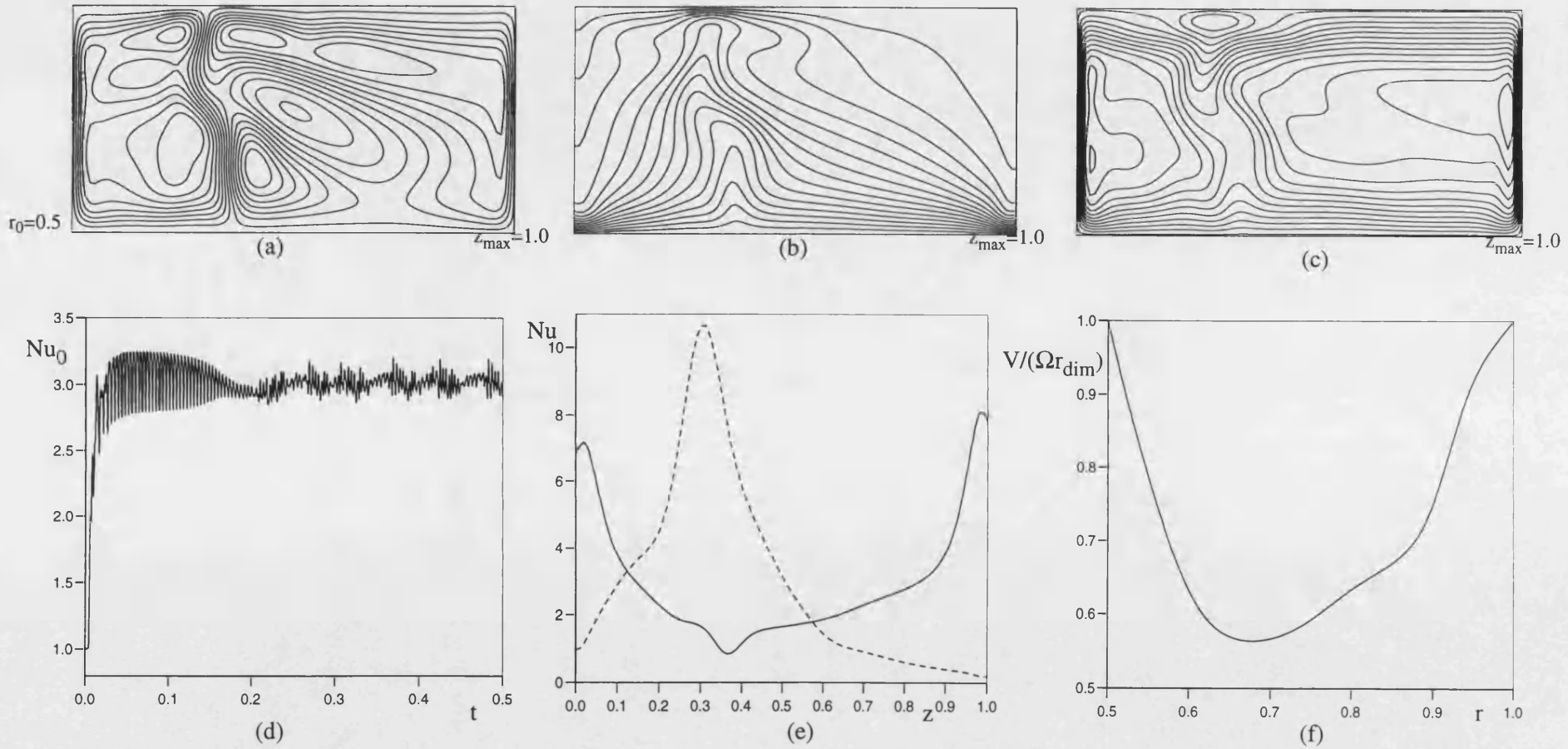

Figure 3.41. Solutions for axisymmetric radial/axial flow with $Ra=10^7$, $Re=2\times10^3$, $r_0=0.5$ and $z_{max}=1.0$.
(a) streamlines (b) iso–therms
(c) tangential velocity iso–lines (d) total heat transfer
(e) local heat transfer ——— inner radius - - - - outer radius
(f) variation of tangential velocity at the mid–axial plane

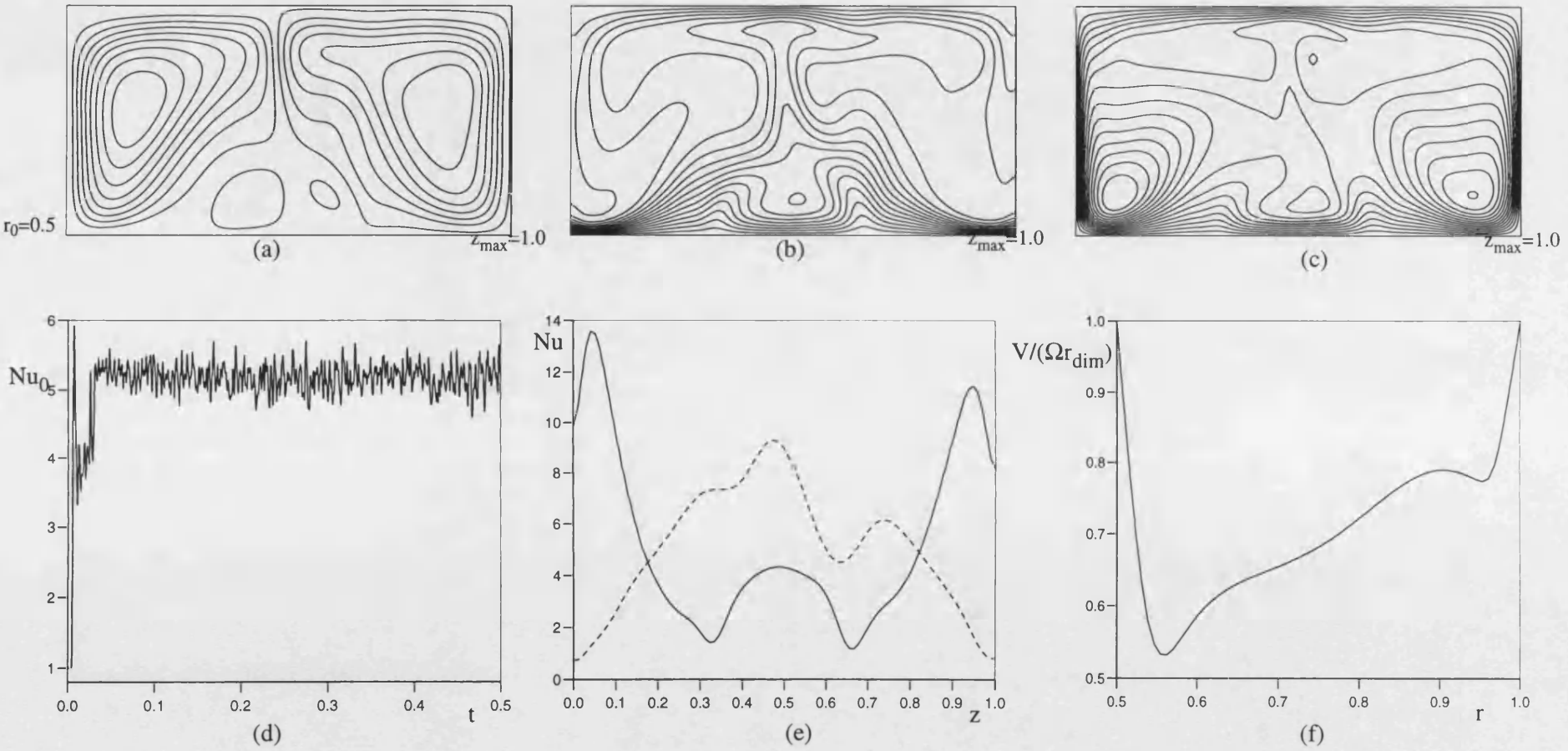

Figure 3.42. Solutions for axisymmetric radial/axial flow with $Ra=10^7$, $Re=3\times10^3$, $r_0=0.5$ and $z_{max}=1.0$.
(a) streamlines (b) iso–therms
(c) tangential velocity iso–lines (d) total heat transfer
(e) local heat transfer ——— inner radius - - - - outer radius
(f) variation of tangential velocity at the mid–axial plane

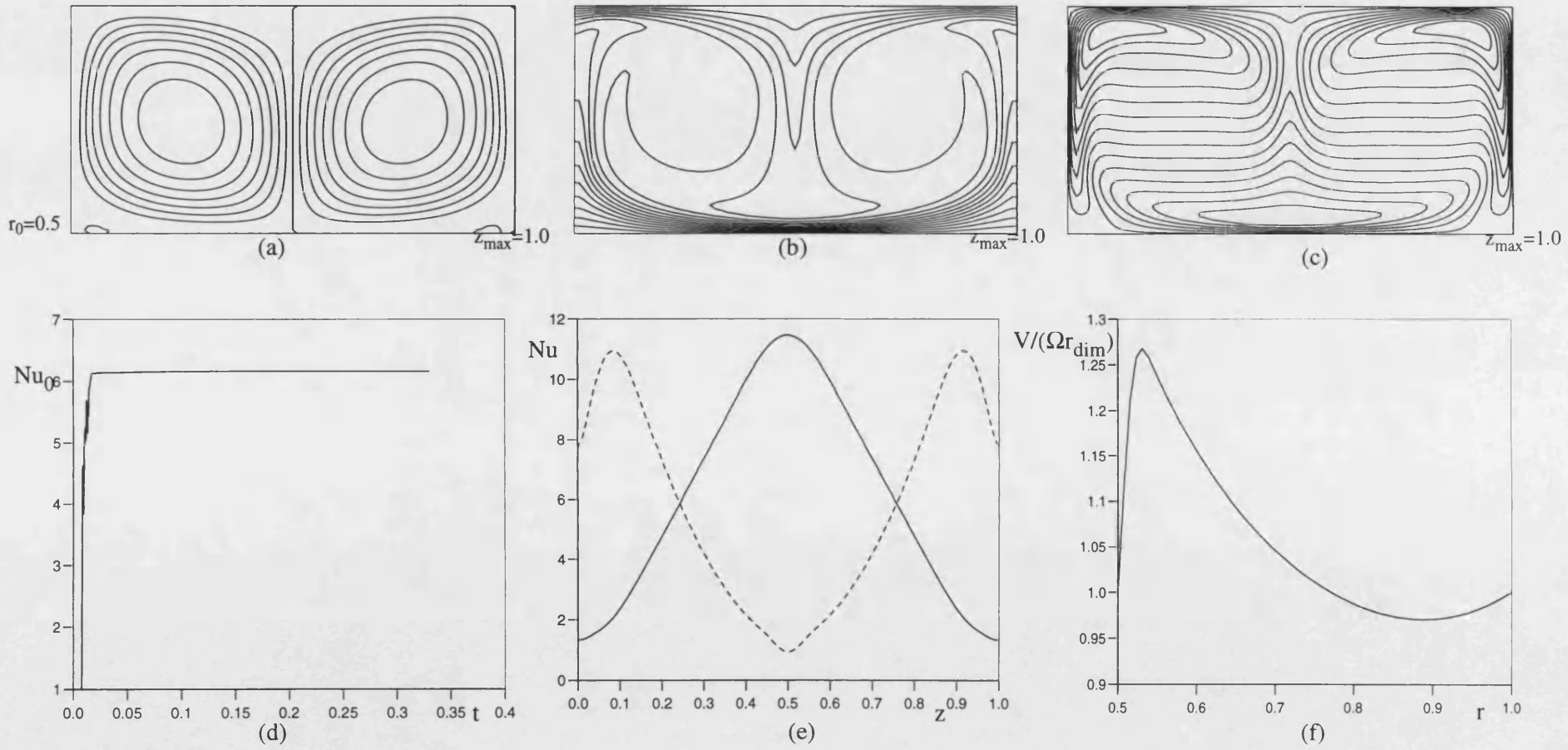

Figure 3.43. Solutions for axisymmetric radial/axial flow with $Ra=10^7$, $Re=4\times10^3$, $r_0=0.5$ and $z_{max}=1.0$.
(a) streamlines (b) iso–therms
(c) tangential velocity iso–lines (d) total heat transfer
(e) local heat transfer ——— inner radius - - - - outer radius
(f) variation of tangential velocity at the mid–axial plane

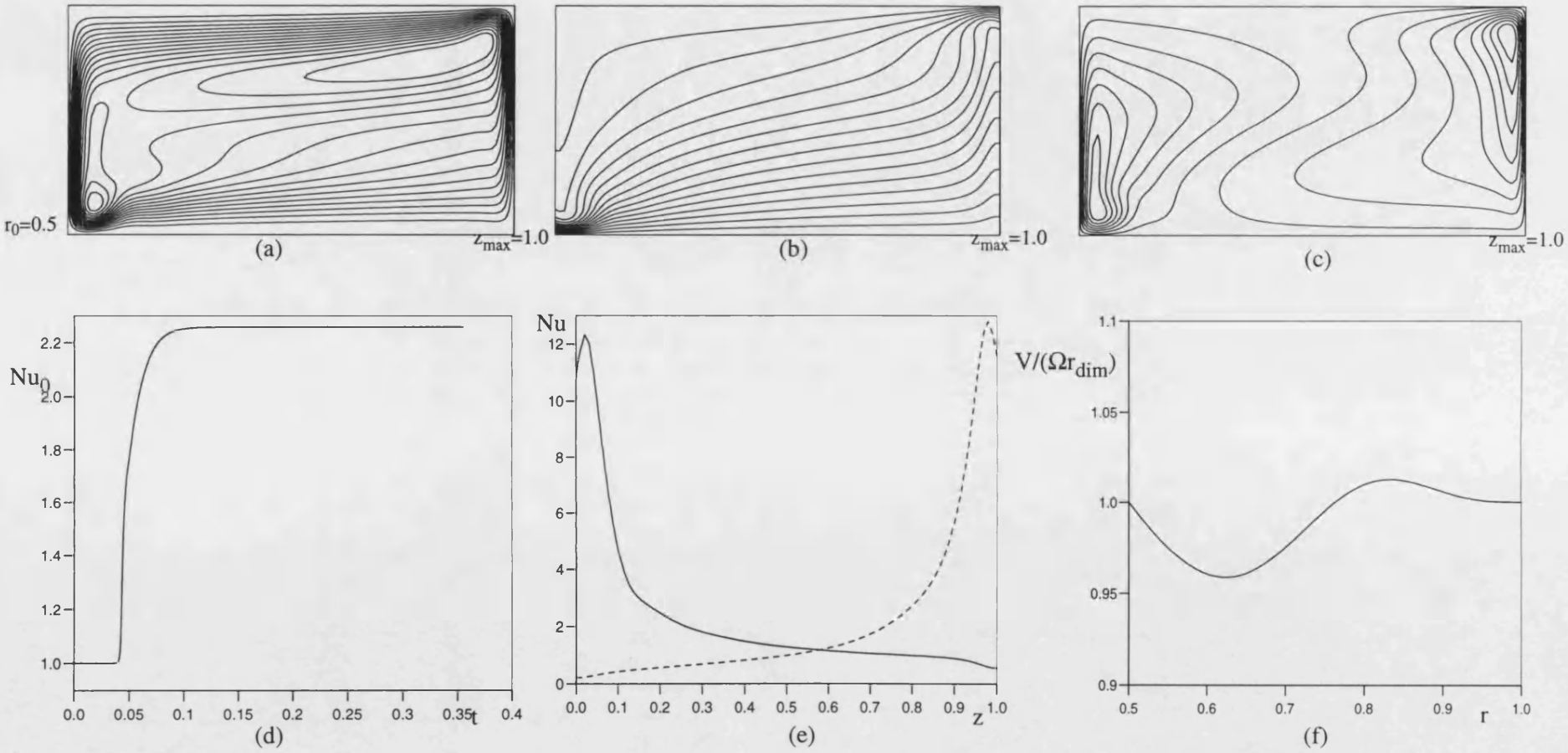

Figure 3.44. Solutions for axisymmetric radial/axial flow with $Ra=10^7$, $Re=5\times10^3$, $r_0=0.5$ and $z_{max}=1.0$.
(a) streamlines (b) iso–therms
(c) tangential velocity iso–lines (d) total heat transfer
(e) local heat transfer ——— inner radius - - - - outer radius
(f) variation of tangential velocity at the mid–axial plane

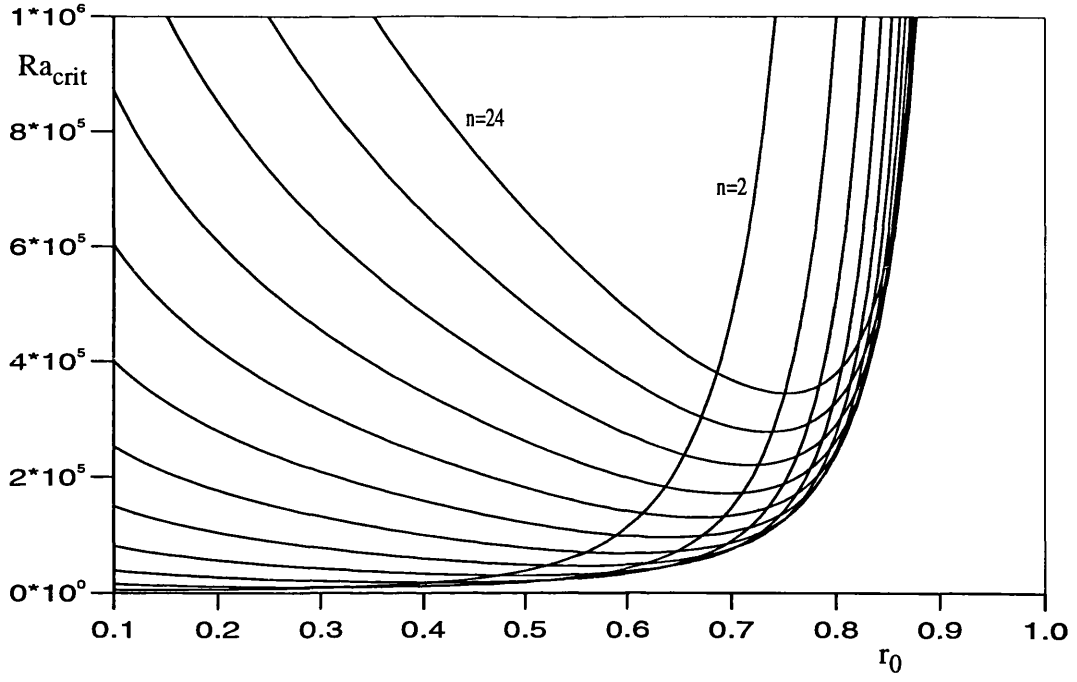

Figure 4.1. Neutral Stability curves for n=2,4,6,.....,24 and range of inner radii with Ra/(Re Pr) assumed small.

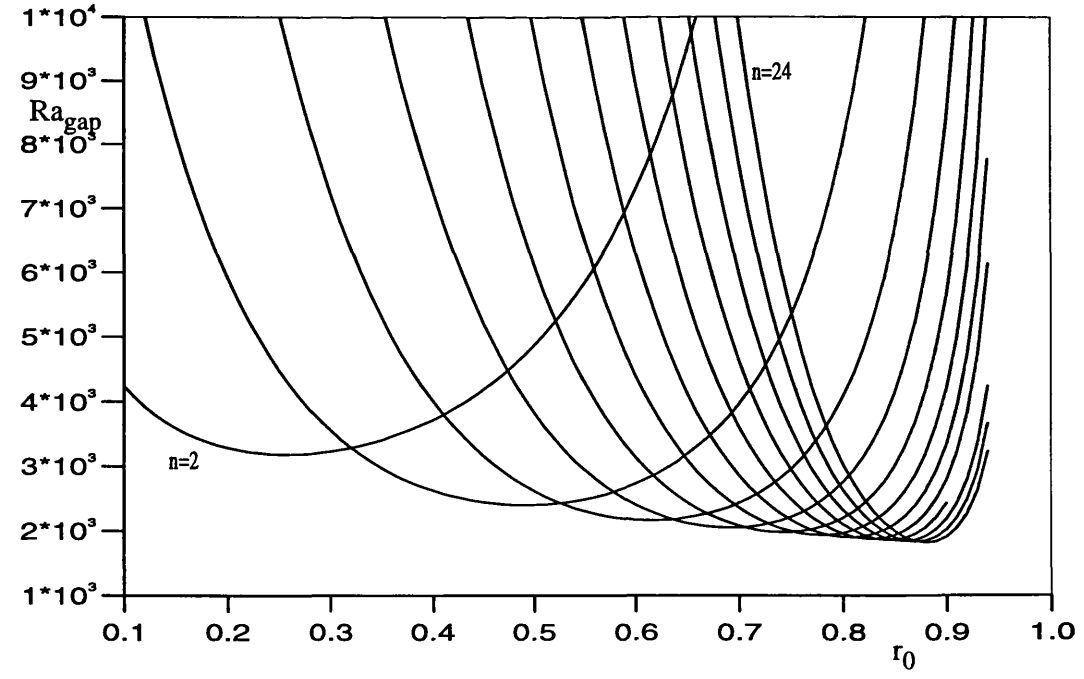

Figure 4.2 Neutral Stability curves based on the gap for n=2,4,6,.....,24 and range of inner radii with Ra/(Re Pr) assumed small.

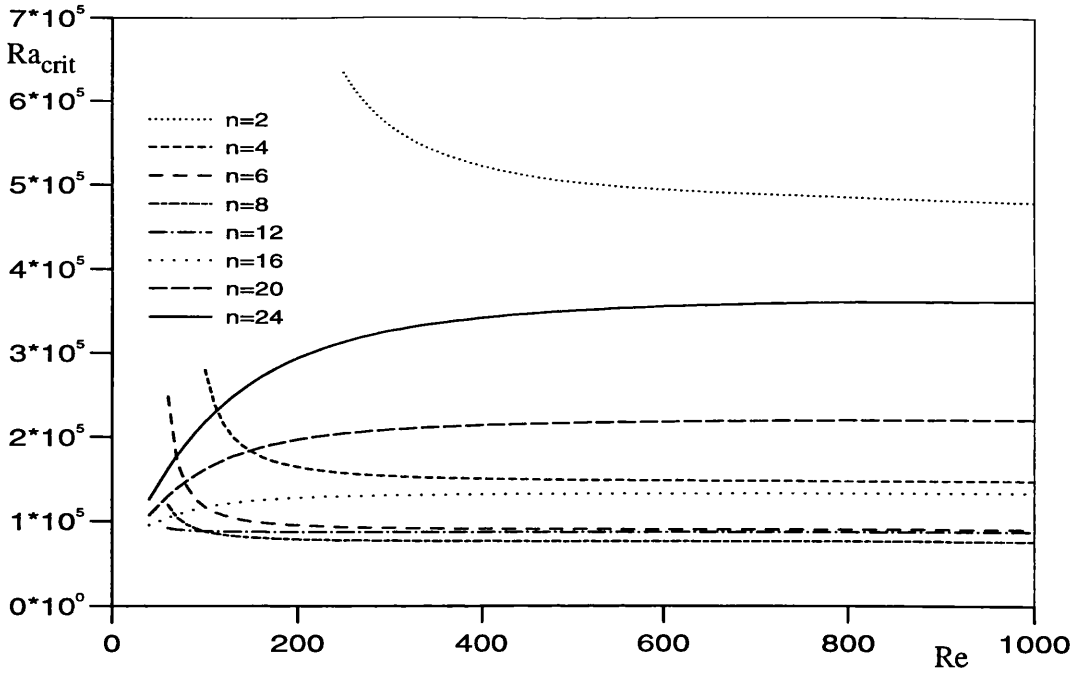

Figure 4.3. Neutral Stability curves for range of Reynolds and wave numbers with r_0=0.7 and buoyancy correction to the Coriolis force terms included.

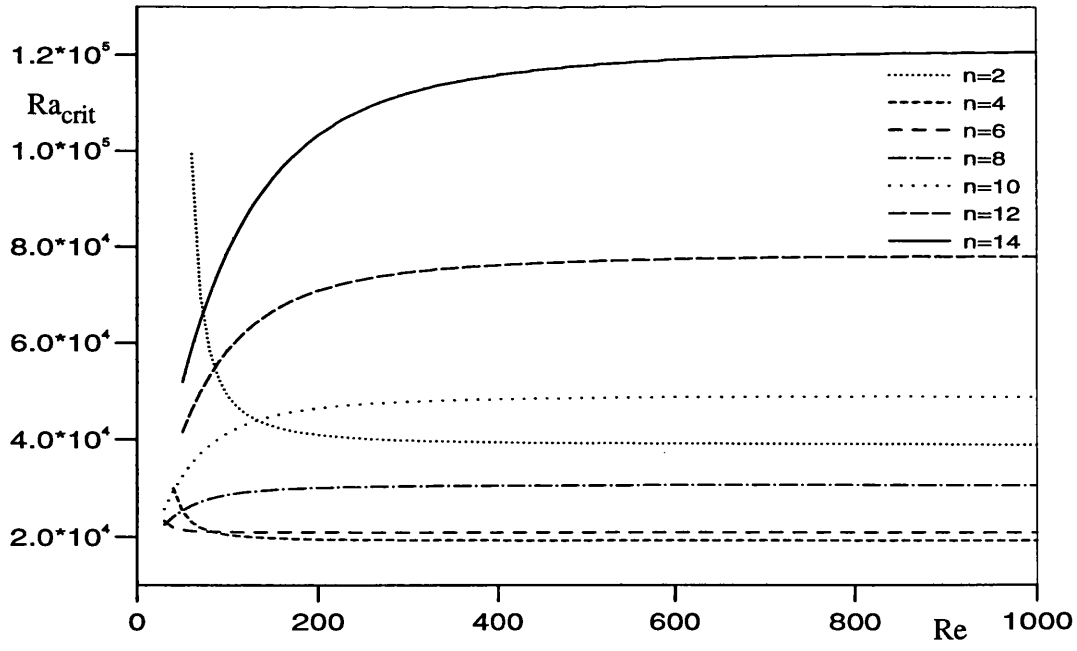

Figure 4.4. Neutral Stability curves for range of Reynolds and wave numbers with r_0=0.5 and buoyancy correction to the Coriolis force terms included.

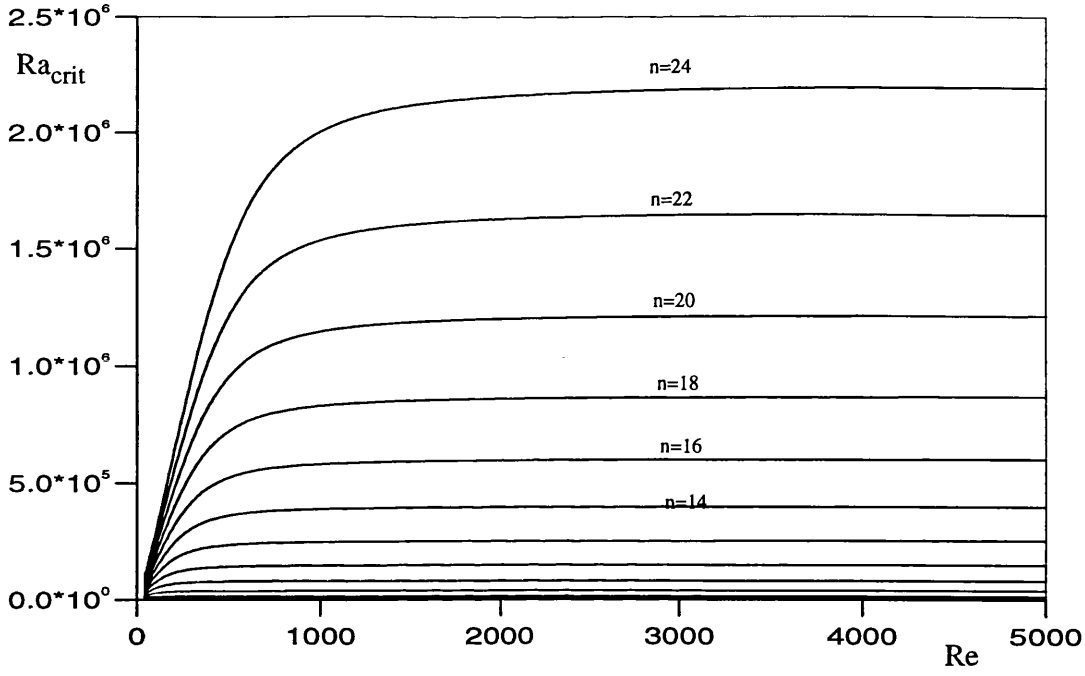

Figure 4.5. Neutral Stability curves for range of Reynolds and n=2,4,6,.....,22,24 with r_0=0.1 and buoyancy correction to the Coriolis force terms included.

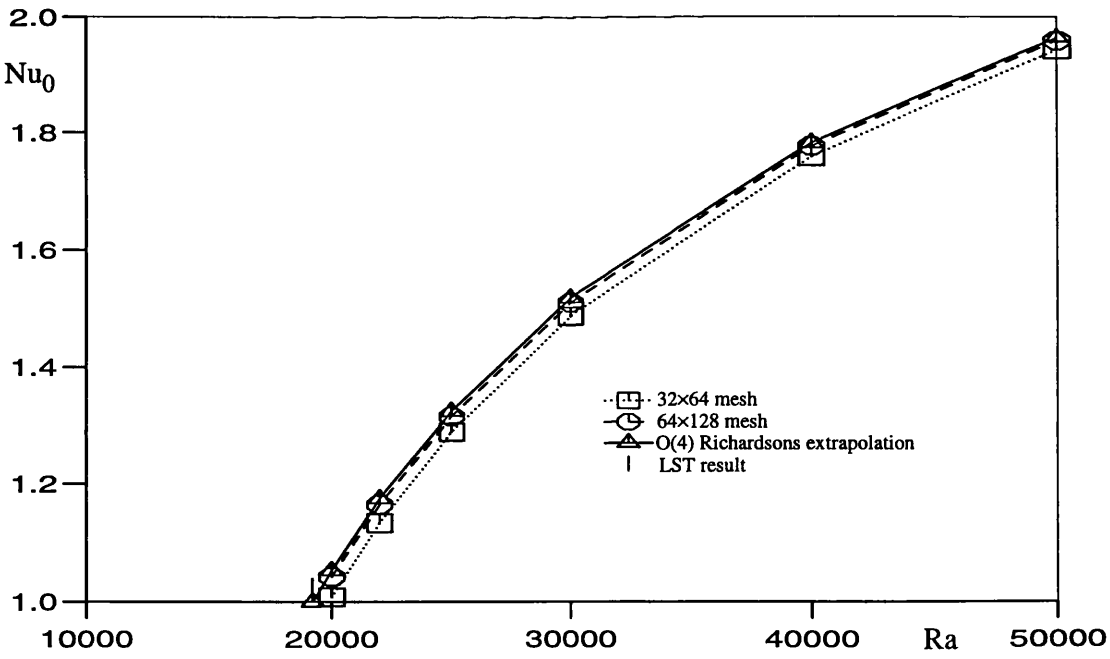

Figure 4.6. Comparison between numerical simulation and LST results for onset of convection for n=4 and r_0=0.5. Ra\(Re Pr) assumed small.

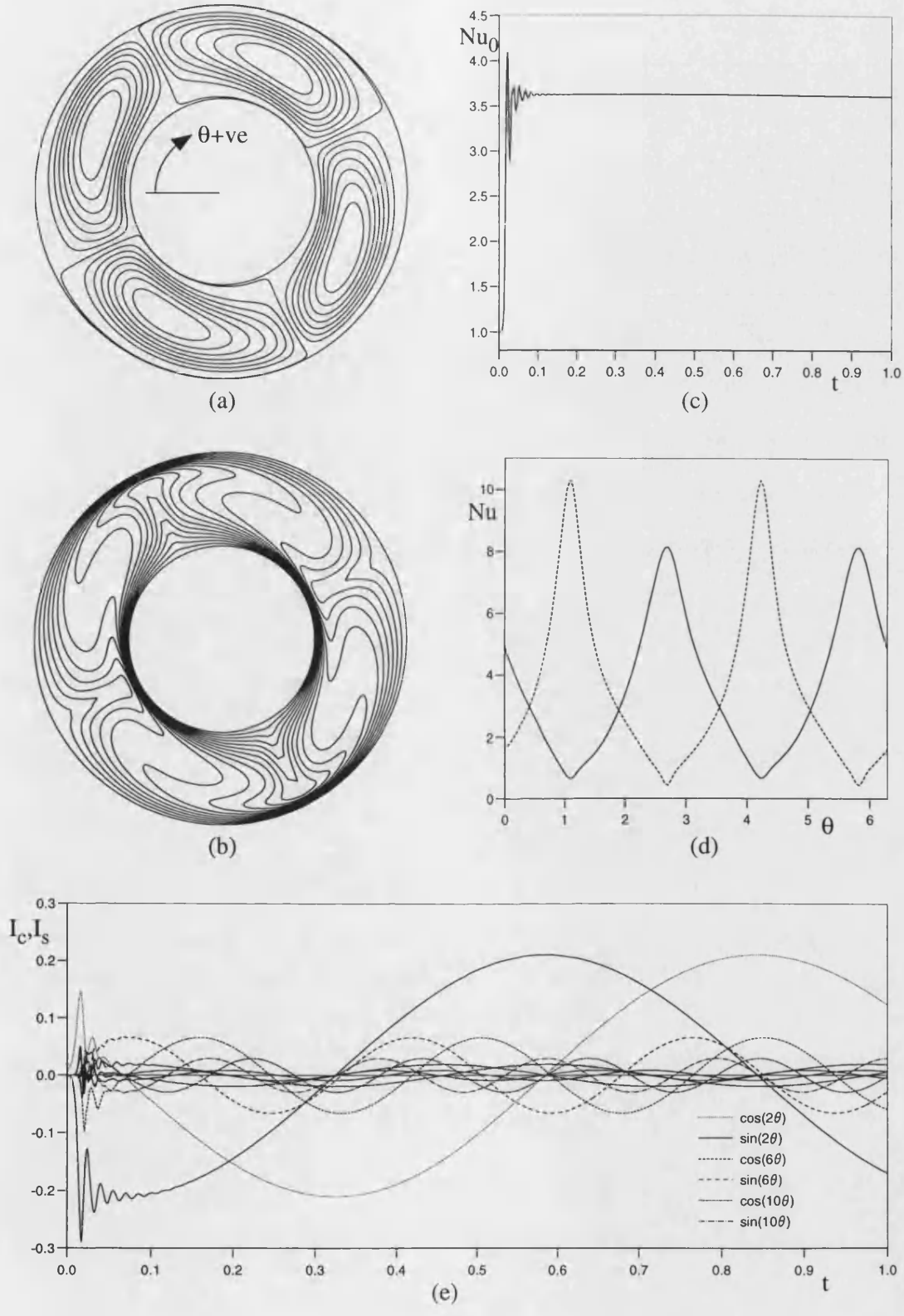

Figure 4.7. Solutions for radial/tangential flow with $Ra=10^6$, $Re=10^3$, $r_0=0.5$ and n=2.
(a) streamlines (b) isotherms
(c) total heat transfer
(d) local heat transfer ——— inner radius - - - - outer radius
(e) Fourier decomposition of the temperature field

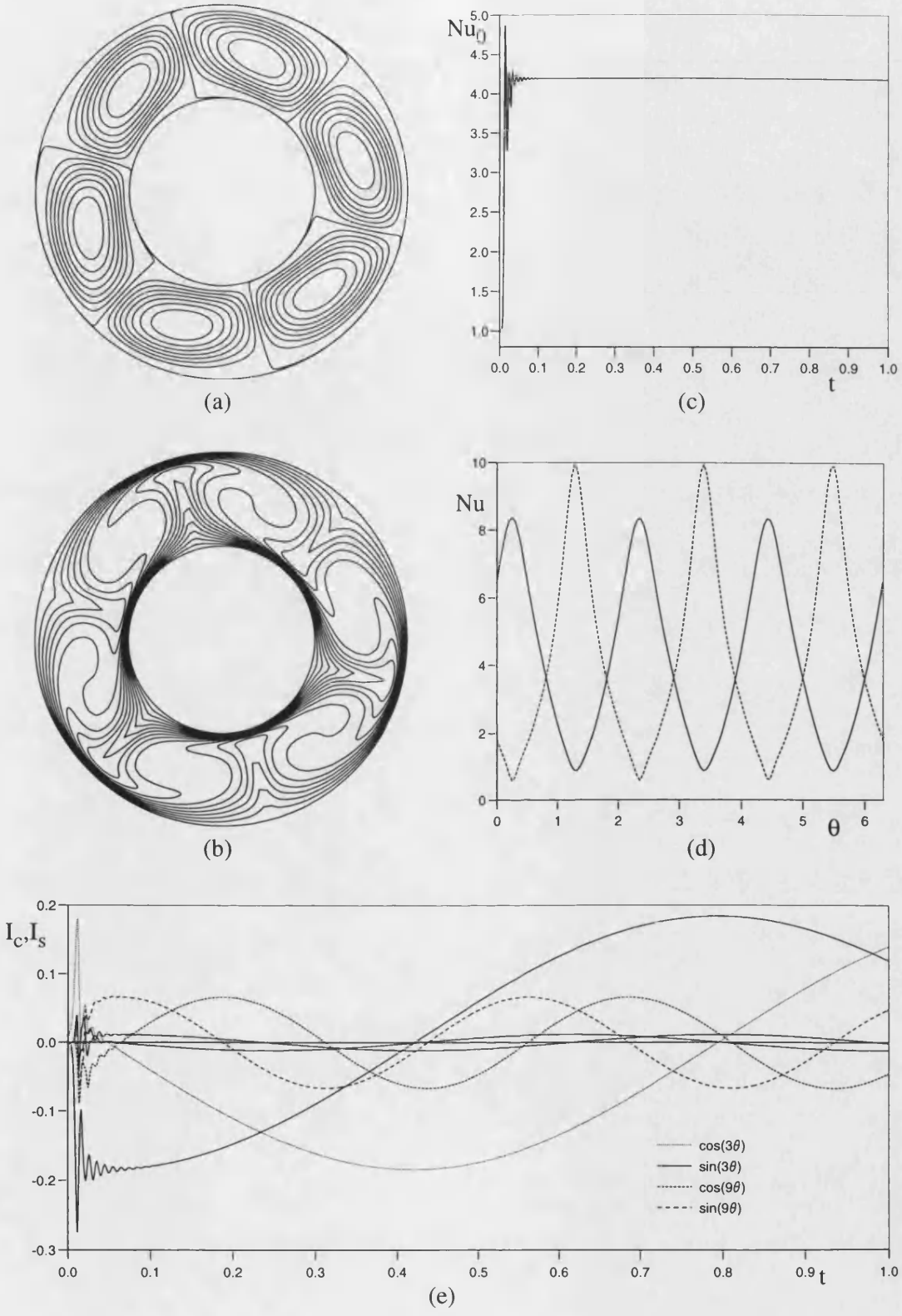

Figure 4.8. Solutions for radial/tangential flow with $Ra=10^6$, $Re=10^3$, $r_0=0.5$ and n=3.
(a) streamlines (b) isotherms
(c) total heat transfer
(d) local heat transfer ——— inner radius - - - - outer radius
(e) Fourier decomposition of the temperature field

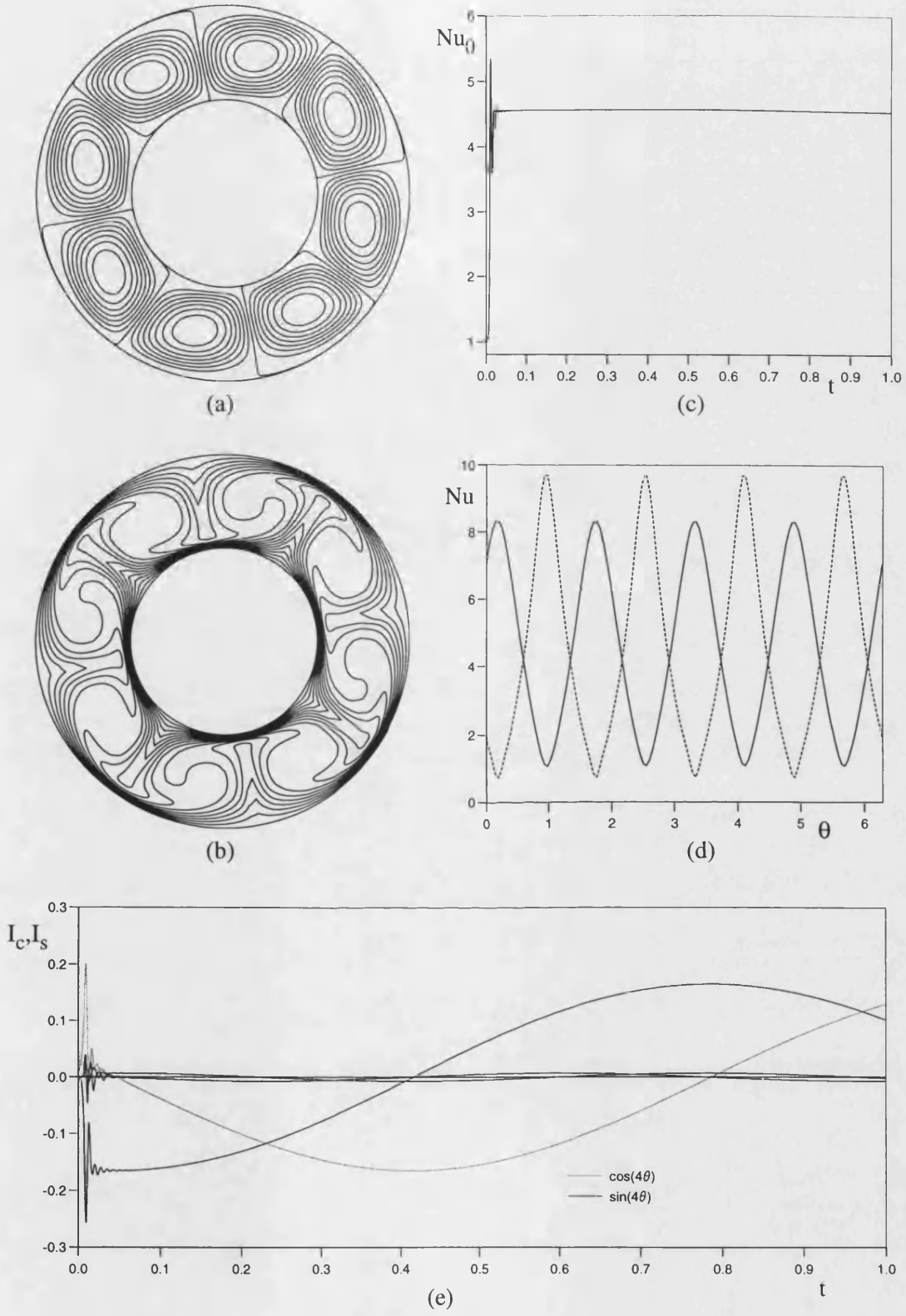

Figure 4.9. Solutions for radial/tangential flow with $Ra=10^6$, $Re=10^3$, $r_0=0.5$ and n=4.
(a) streamlines (b) isotherms
(c) total heat transfer
(d) local heat transfer ——— inner radius - - - - outer radius
(e) Fourier decomposition of the temperature field

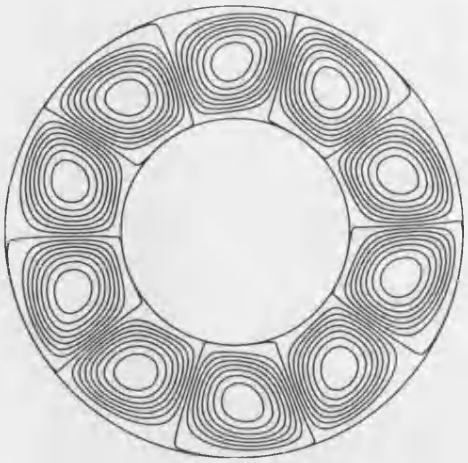

(a)

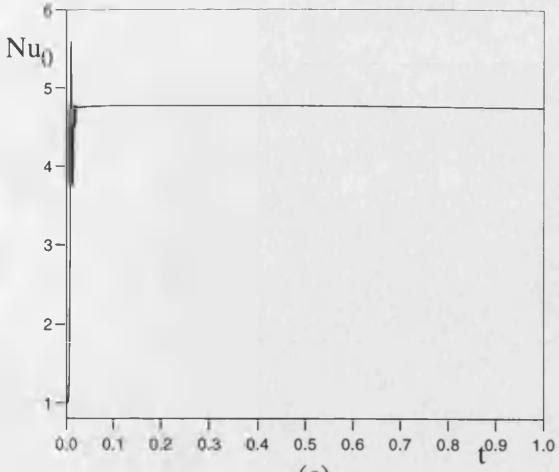

(c)

(b)

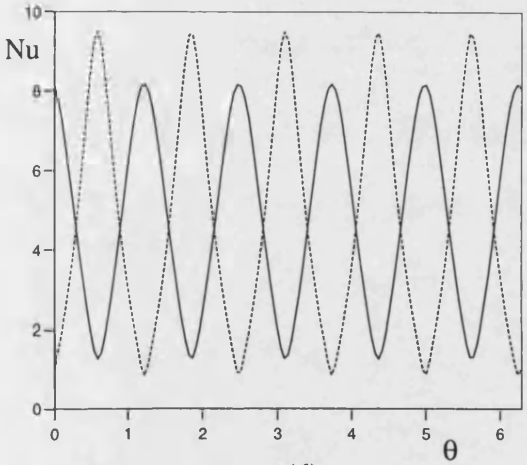

(d)

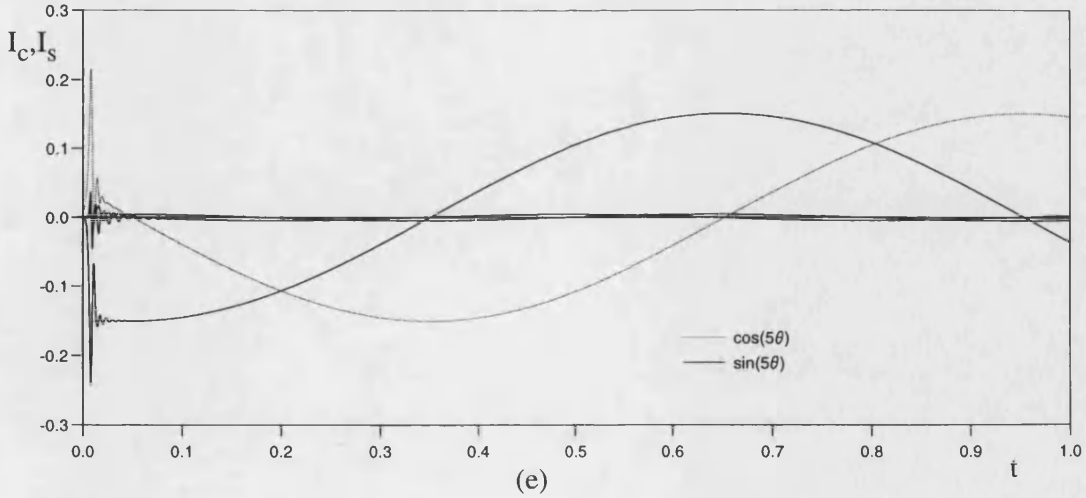

(e)

Figure 4.10. Solutions for radial/tangential flow with $Ra=10^6$, $Re=10^3$, $r_0=0.5$ and n=5.
(a) streamlines (b) isotherms
(c) total heat transfer
(d) local heat transfer ——— inner radius - - - - outer radius
(e) Fourier decomposition of the temperature field

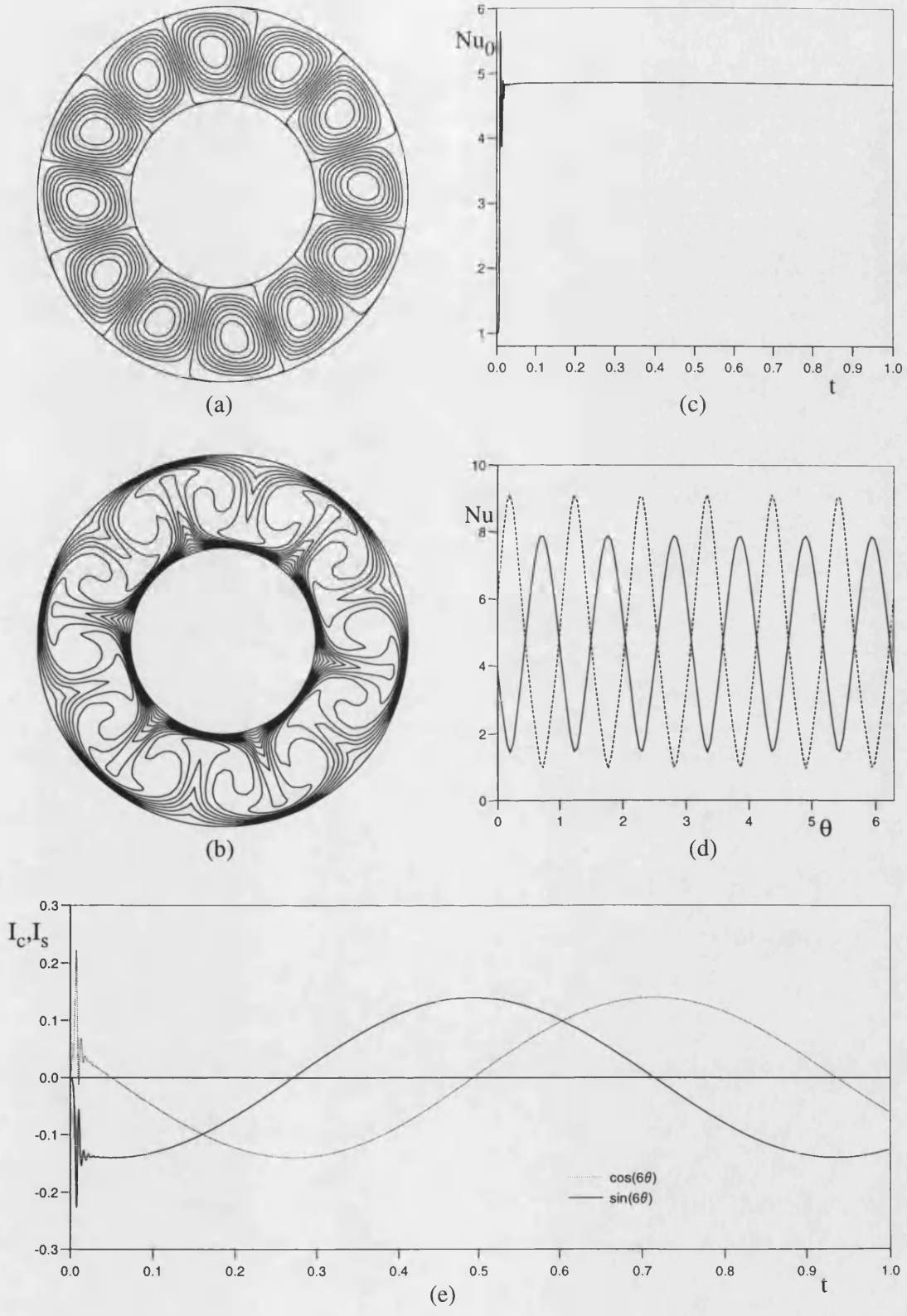

Figure 4.11. Solutions for radial/tangential flow with $Ra=10^6$, $Re=10^3$, $r_0=0.5$ and n=6.
(a) streamlines (b) isotherms
(c) total heat transfer
(d) local heat transfer ——— inner radius - - - - outer radius
(e) Fourier decomposition of the temperature field

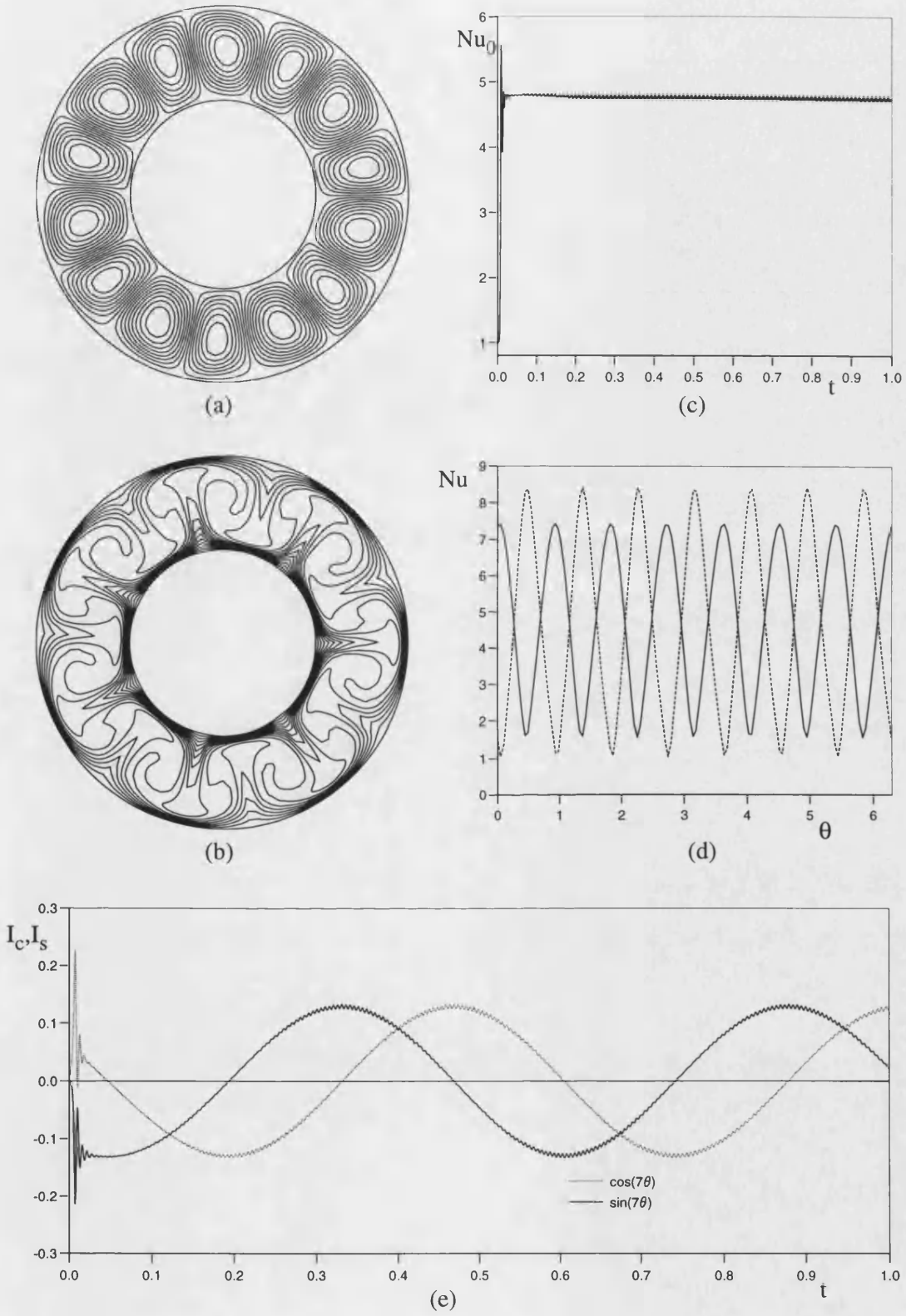

Figure 4.12. Solutions for radial/tangential flow with $Ra=10^6$, $Re=10^3$, $r_0=0.5$ and n=7.
(a) streamlines (b) isotherms
(c) total heat transfer
(d) local heat transfer ——— inner radius - - - - outer radius
(e) Fourier decomposition of the temperature field

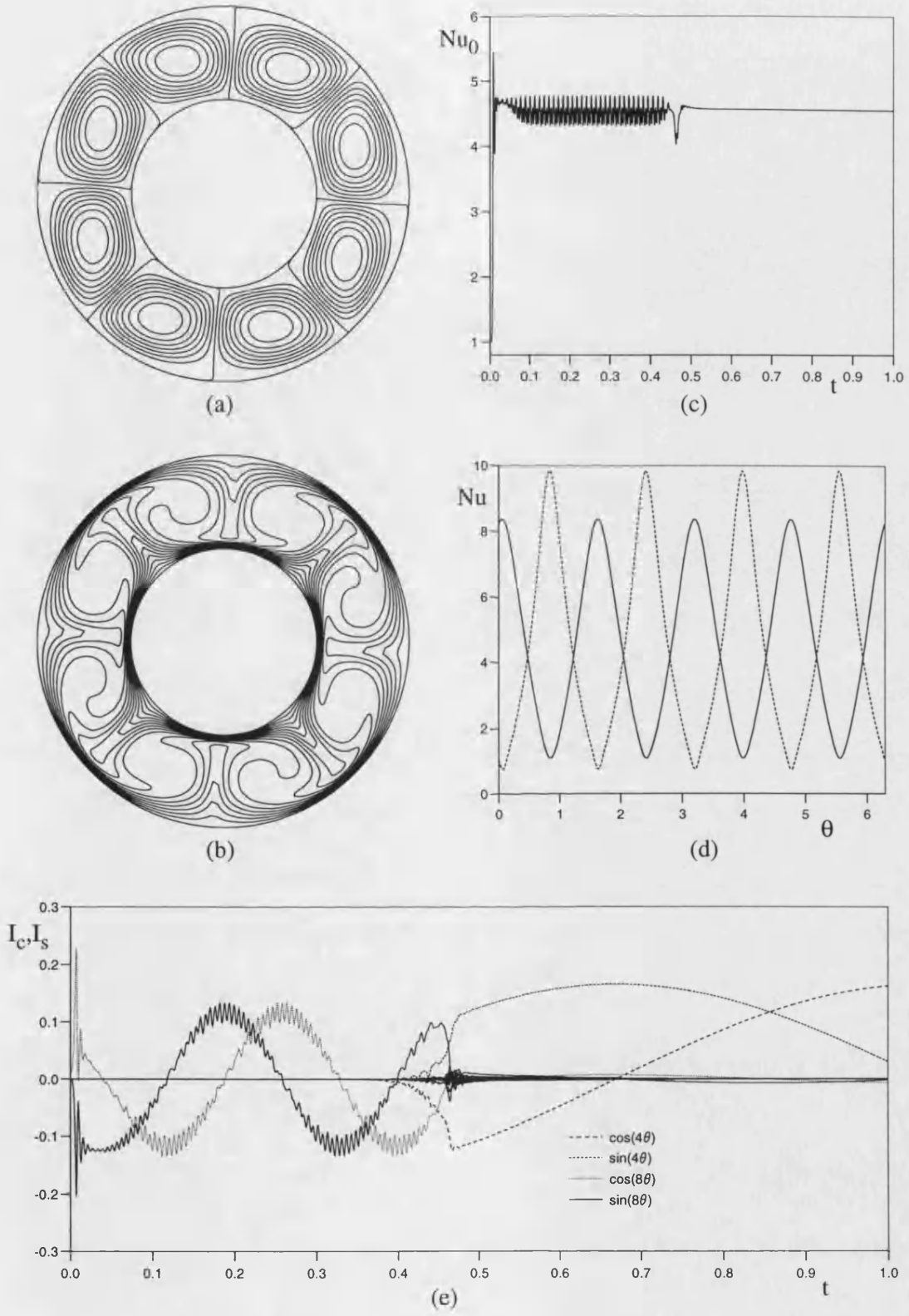

Figure 4.13. Solutions for radial/tangential flow with $Ra=10^6$, $Re=10^3$, $r_0=0.5$ and n=8.
(a) streamlines (b) isotherms
(c) total heat transfer
(d) local heat transfer ——— inner radius- - - - outer radius
(e) Fourier decomposition of the temperature field

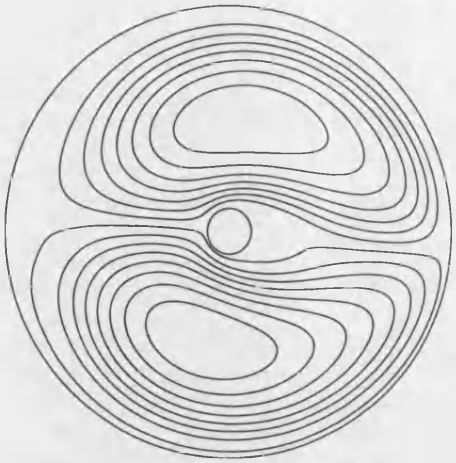

(a)

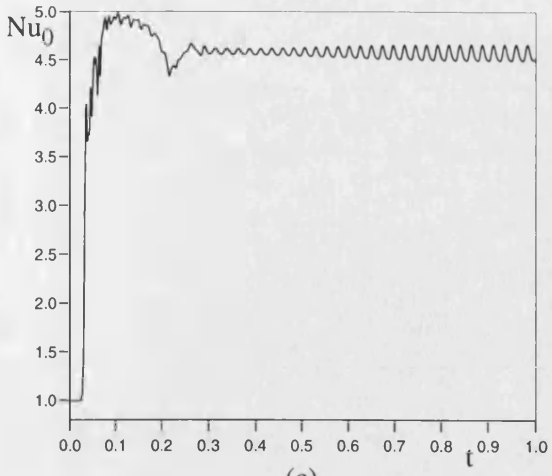

(c)

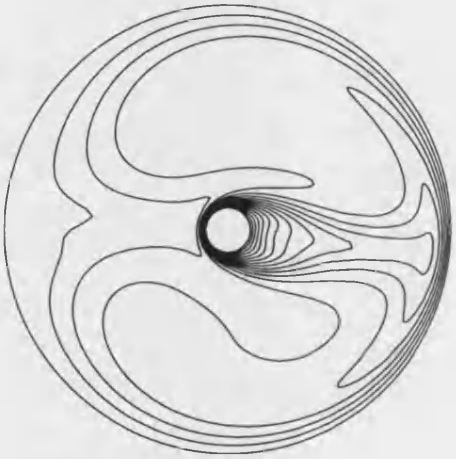

(b)

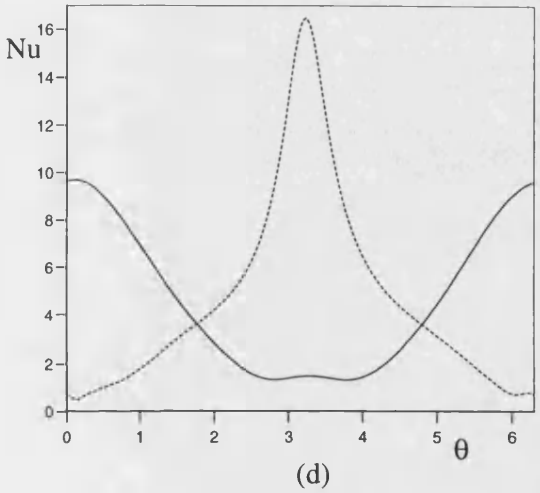

(d)

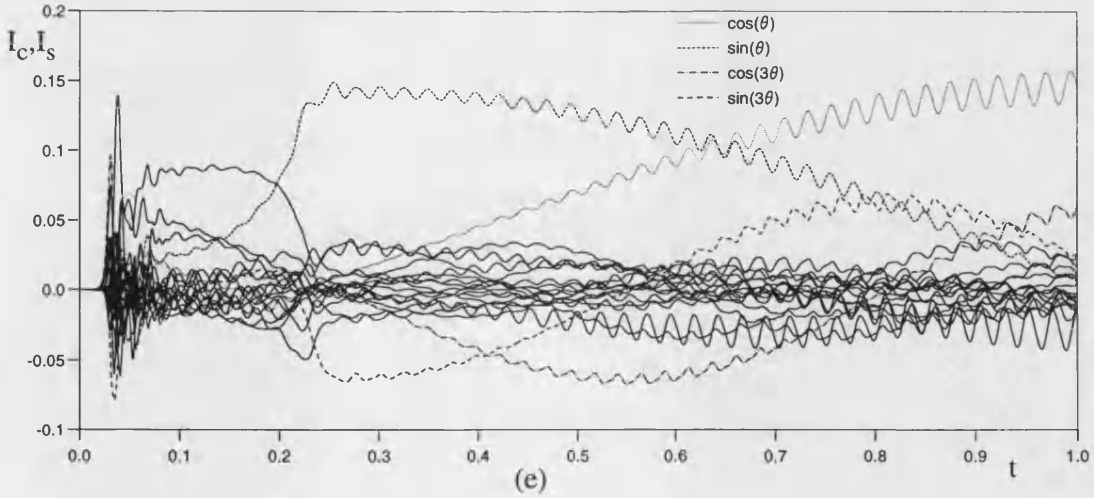

(e)

Figure 4.14. Solutions for radial/tangential flow with Ra=10^6, Re=10^3 and r_0=0.1.
(a) streamlines (b) isotherms
(c) total heat transfer
(d) local heat transfer ——— inner radius - - - - outer radius
(e) Fourier decomposition of the temperature field

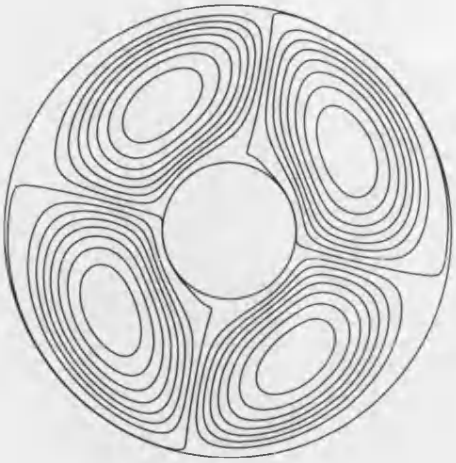

(a)

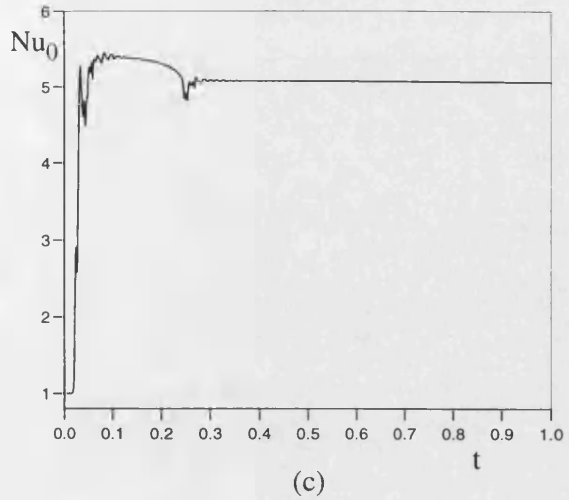

(c)

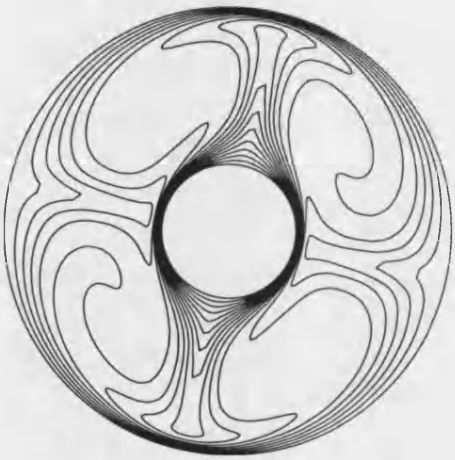

(b)

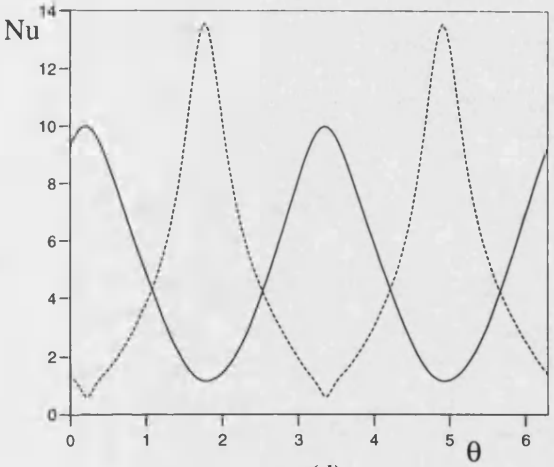

(d)

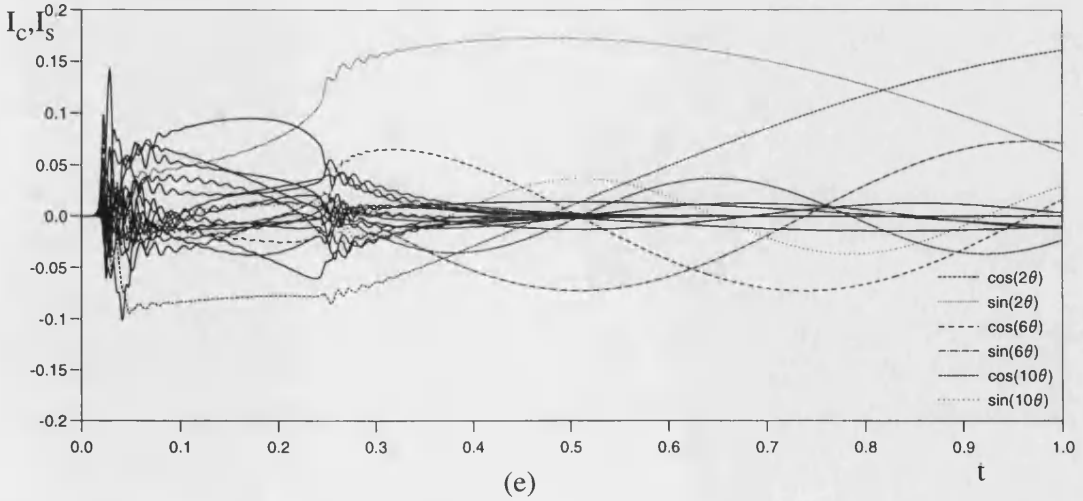

(e)

Figure 4.15. Solutions for radial/tangential flow with $Ra=10^6$, $Re=10^3$ and $r_0=0.3$.
(a) streamlines (b) isotherms
(c) total heat transfer
(d) local heat transfer ——— inner radius - - - - outer radius
(e) Fourier decomposition of the temperature field

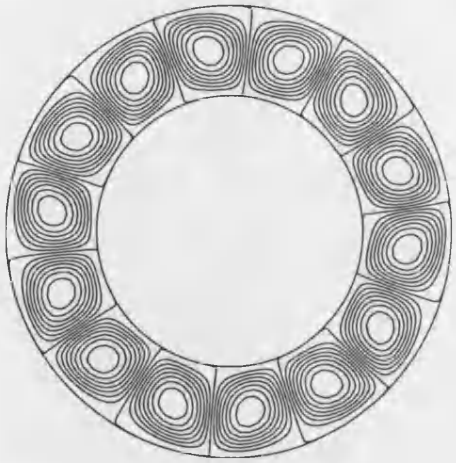

(a)

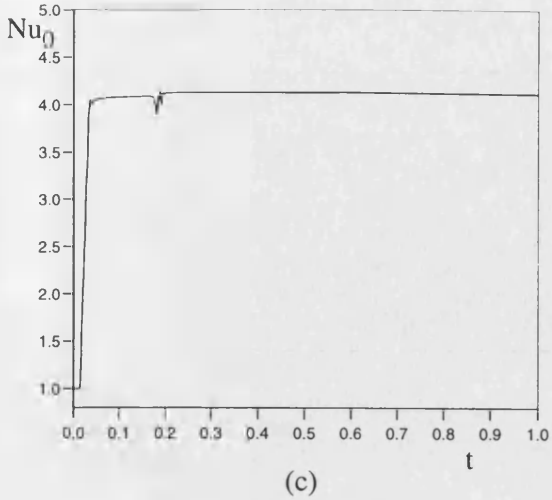

(c)

(b)

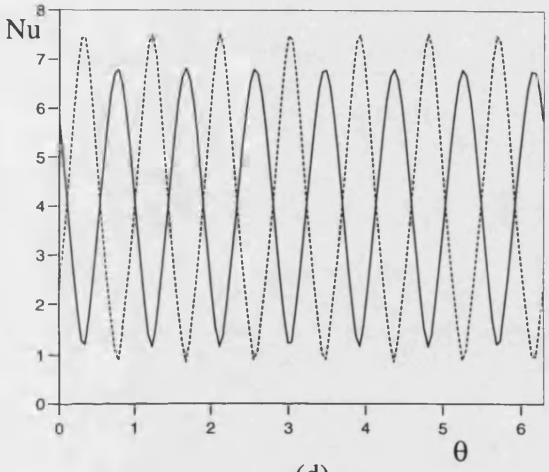

(d)

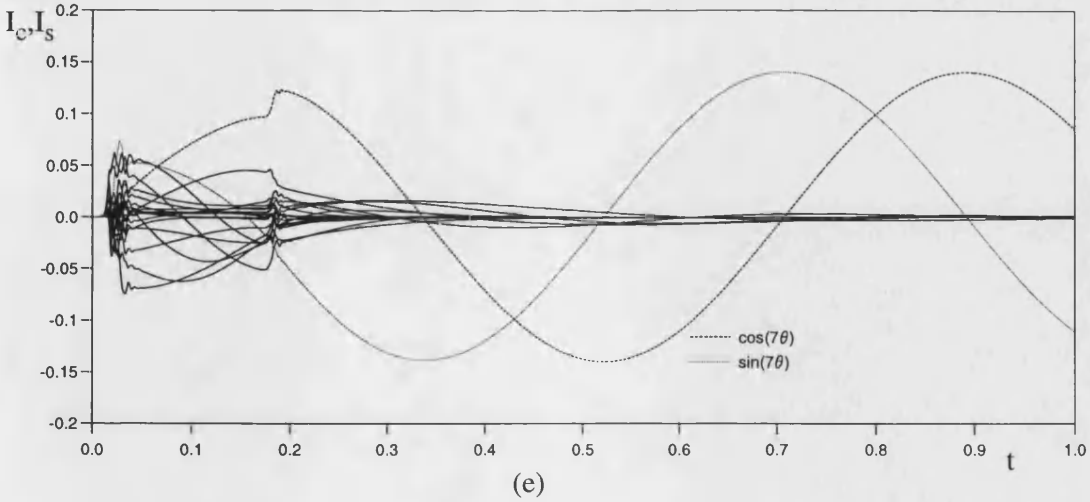

(e)

Figure 4.16. Solutions for radial/tangential flow with $Ra=10^6$, $Re=10^3$ and $r_0=0.6$.
(a) streamlines (b) isotherms
(c) total heat transfer
(d) local heat transfer ——— inner radius - - - - outer radius
(e) Fourier decomposition of the temperature field

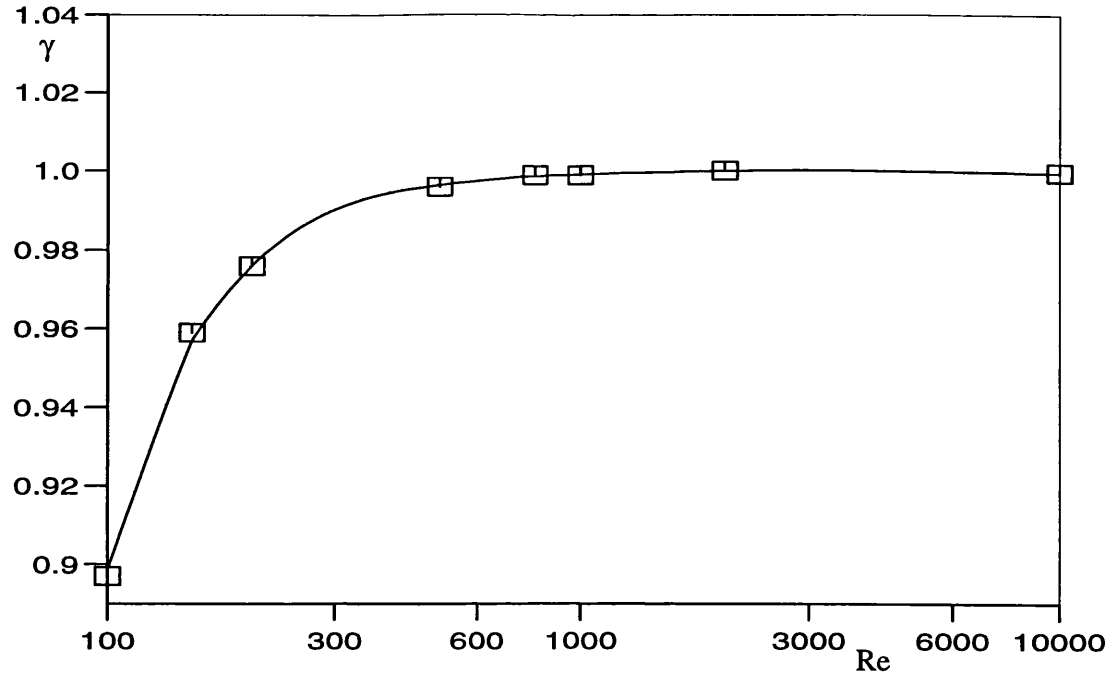

Figure 4.17. Variation of precession of cyclonic and anti–cyclonic pairs with Reynolds number.

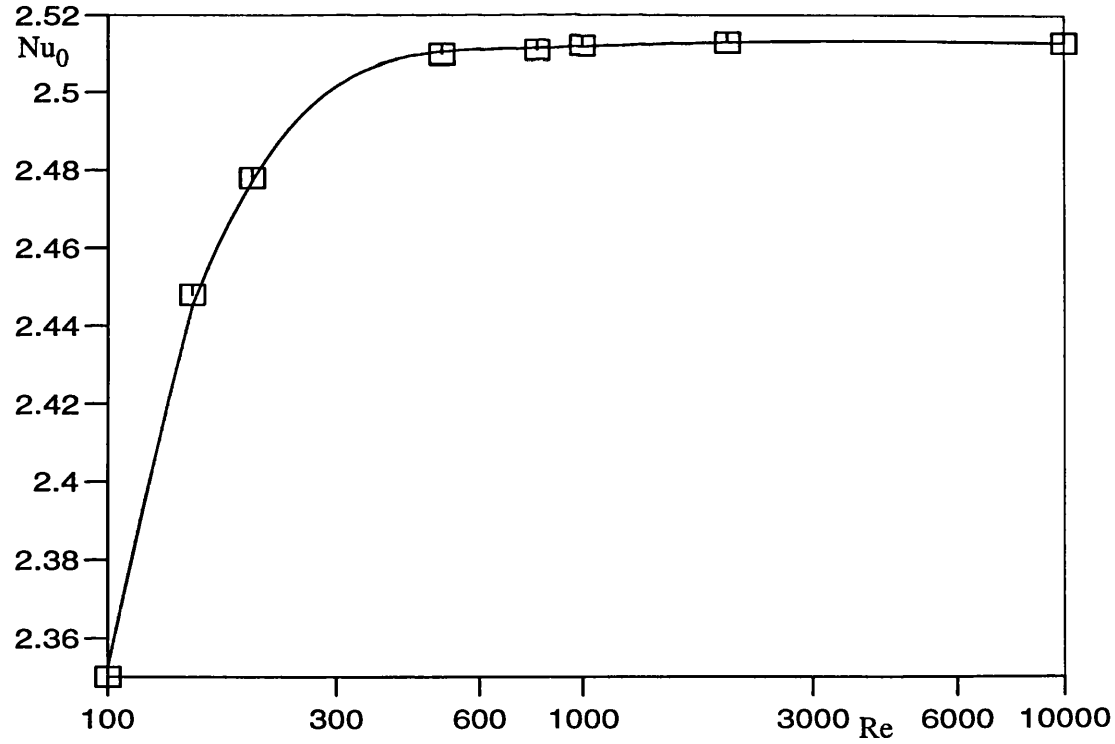

Figure 4.18. Variation of the total heat transfer with Reynolds number.

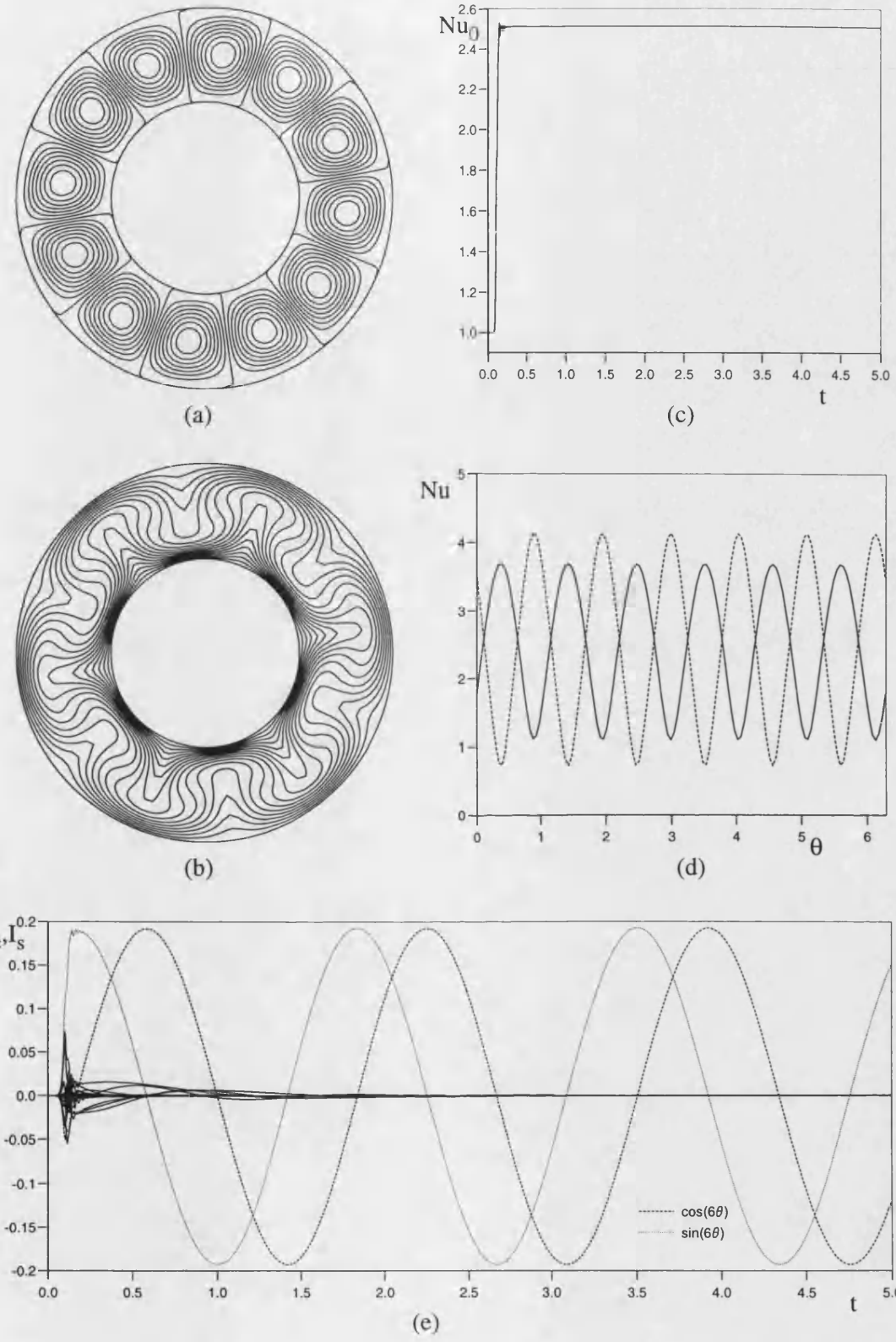

Figure 4.19. Solutions for radial/tangential flow with Ra=10^5, Re=10^3 and r_0=0.5.
(a) streamlines (b) isotherms
(c) total heat transfer
(d) local heat transfer ——— inner radius - - - - outer radius
(e) Fourier decomposition of the temperature field

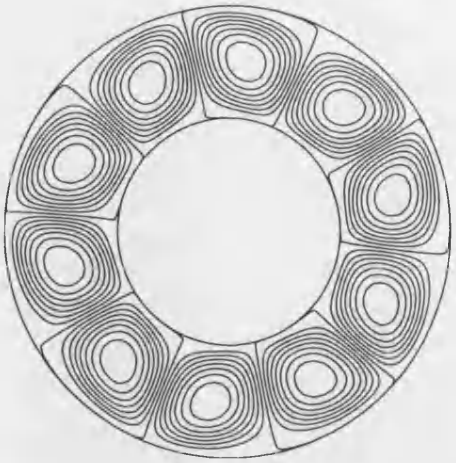

(a)

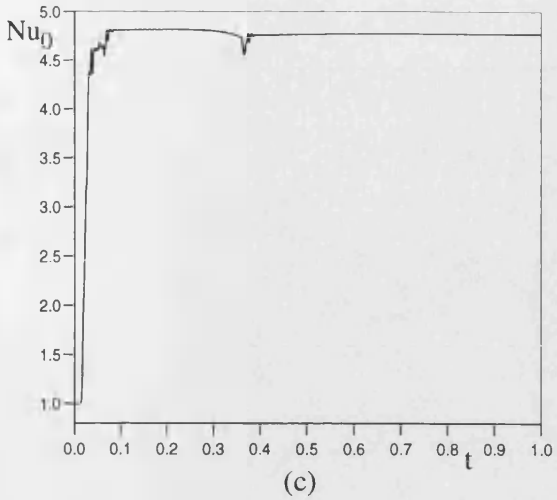

(c)

(b)

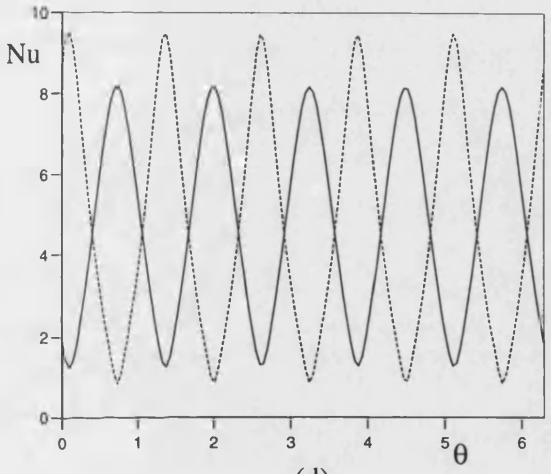

(d)

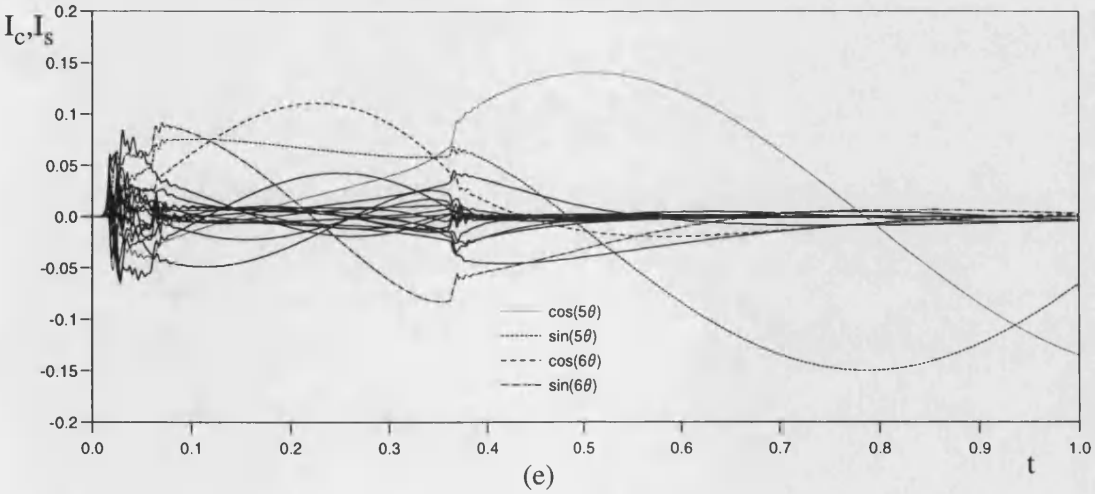

(e)

Figure 4.20. Solutions for radial/tangential flow with $Ra=10^6$, $Re=10^3$ and $r_0=0.5$.
(a) streamlines (b) isotherms
(c) total heat transfer
(d) local heat transfer ——— inner radius - - - - outer radius
(e) Fourier decomposition of the temperature field

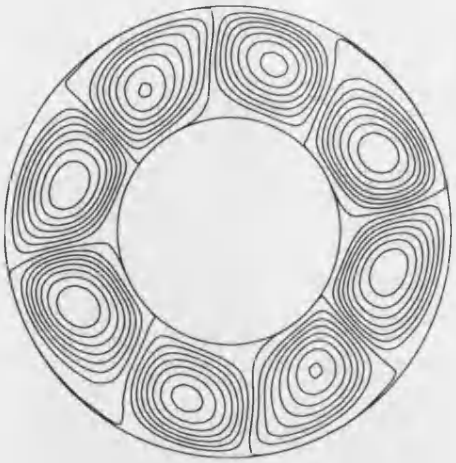

(a)

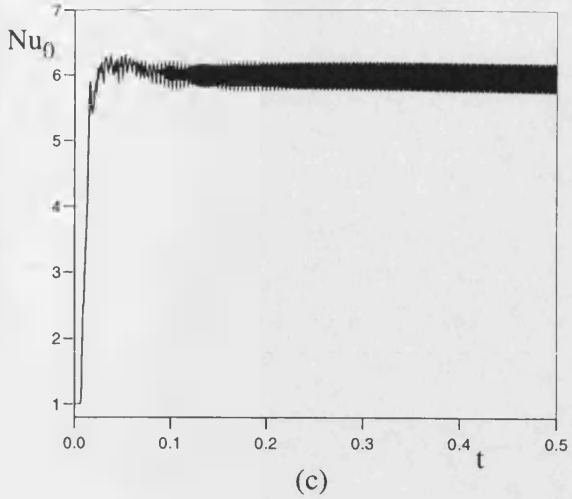

(c)

(b)

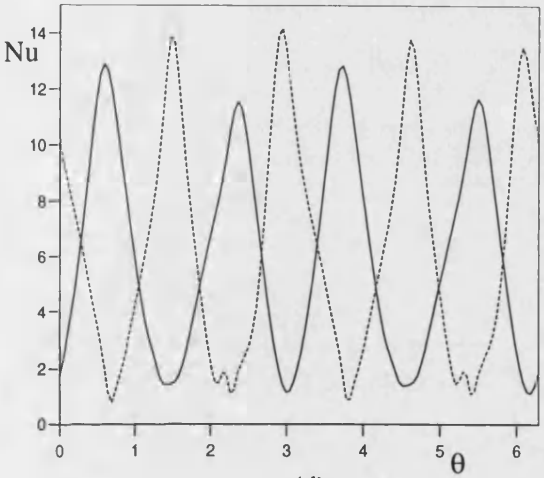

(d)

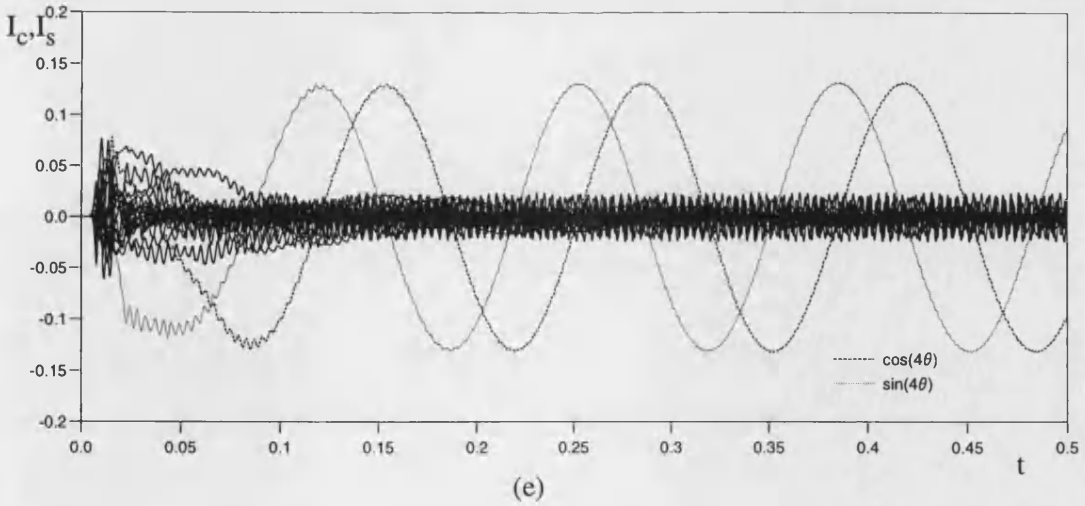

(e)

Figure 4.21. Solutions for radial/tangential flow with $Ra=4\times10^6$, $Re=10^3$ and $r_0=0.5$.
(a) streamlines (b) isotherms
(c) total heat transfer
(d) local heat transfer ——— inner radius - - - - outer radius
(e) Fourier decomposition of the temperature field

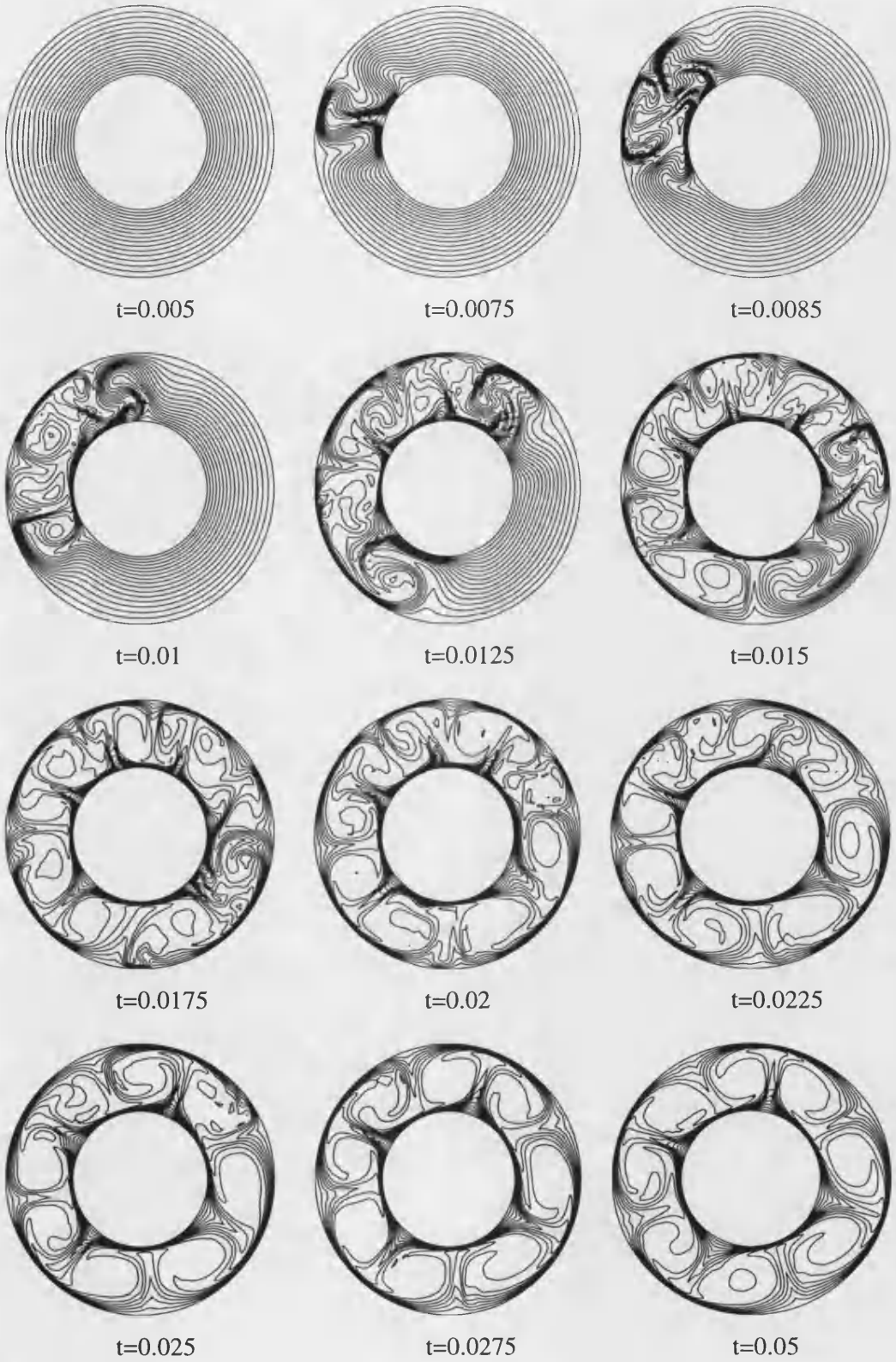

Figure 4.22. Tranisent isotherms at for Ra=4×10^6, Re=10^3 and r_0=0.5.

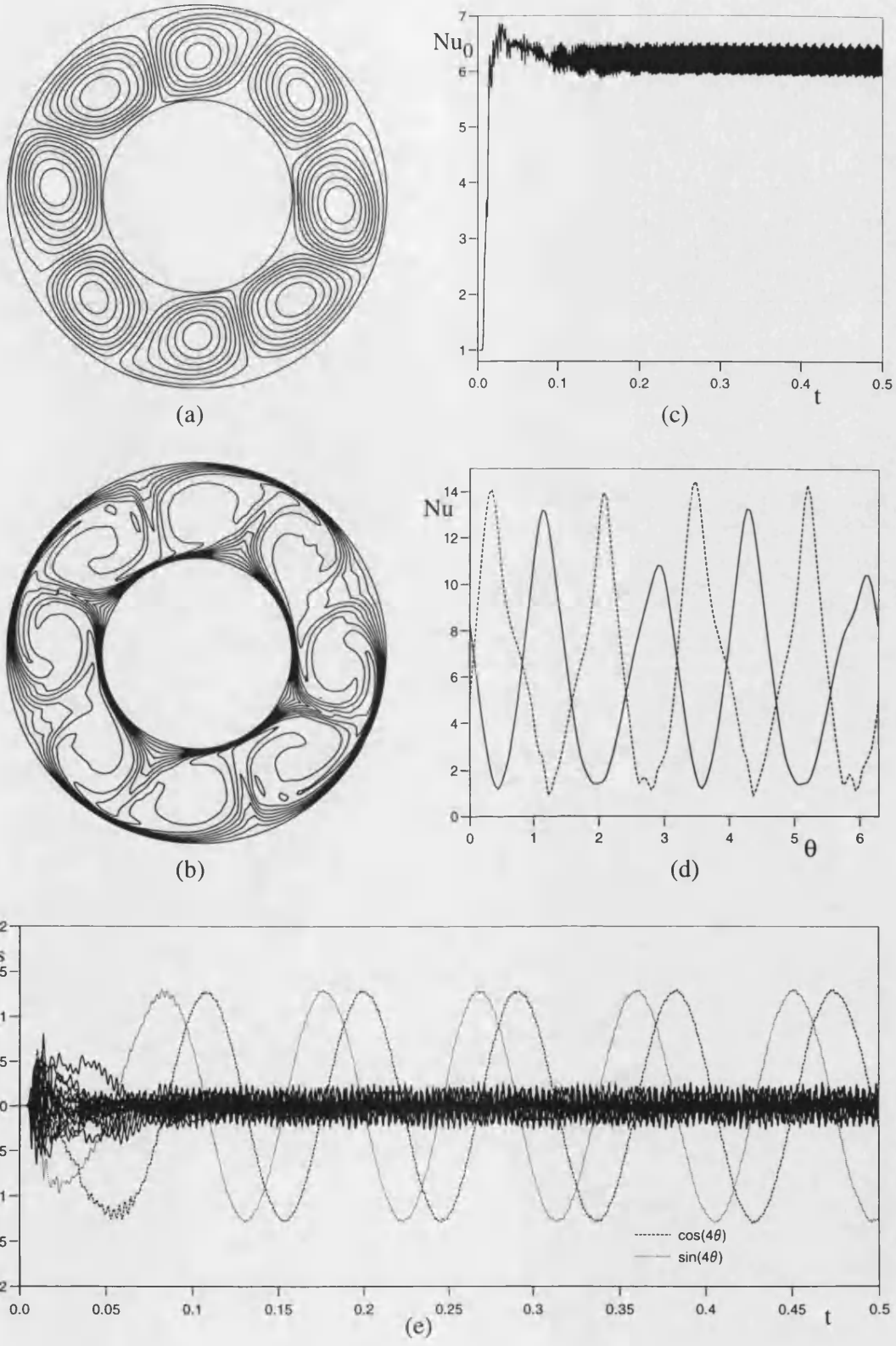

Figure 4.23. Solutions for radial/tangential flow with $Ra=5\times10^6$, $Re=10^3$ and $r_0=0.5$.
(a) streamlines (b) isotherms
(c) total heat transfer
(d) local heat transfer ——— inner radius - - - - outer radius
(e) Fourier decomposition of the temperature field

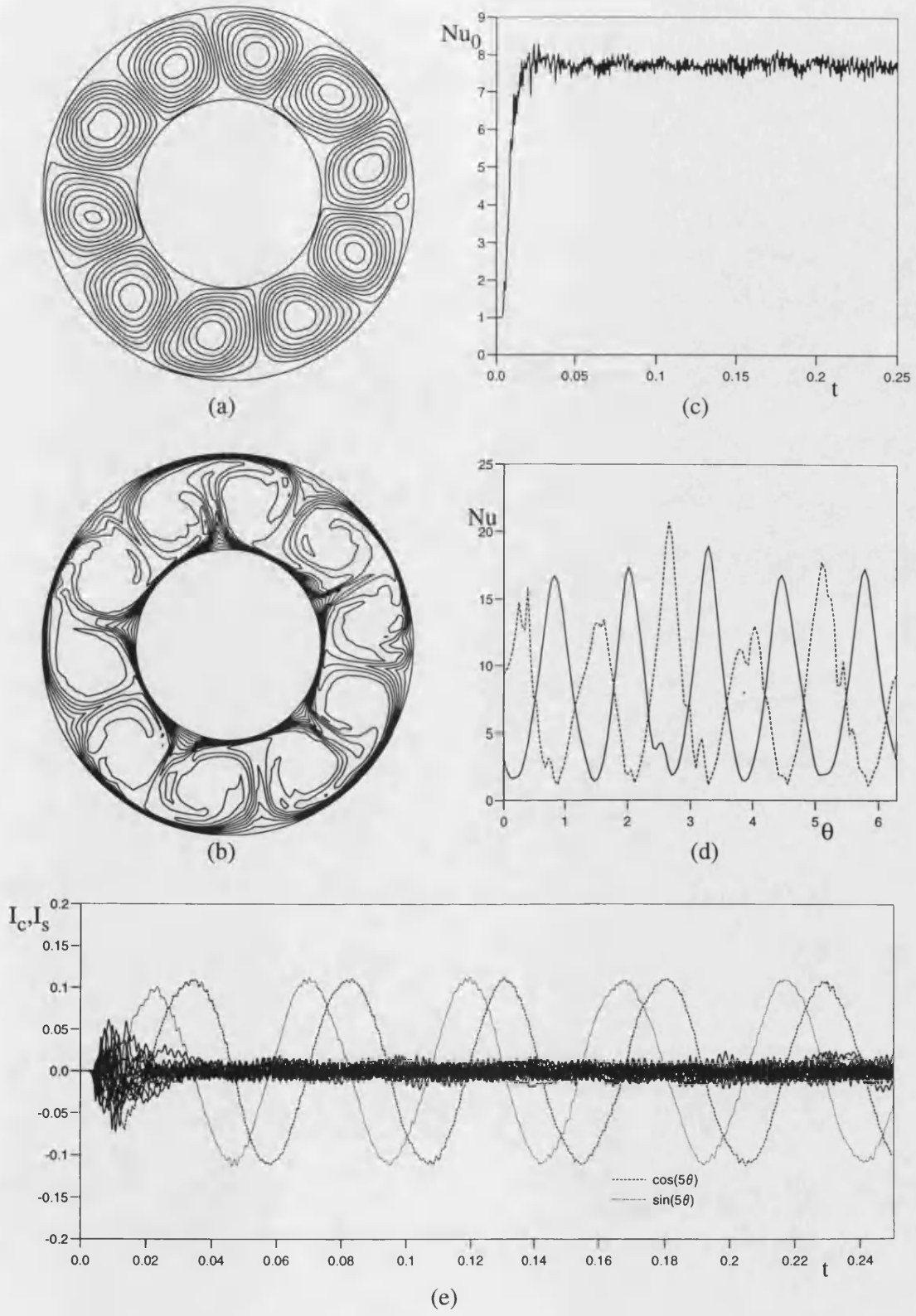

Figure 4.24. Solutions for radial/tangential flow with Ra=10^7, Re=10^3 and r_0=0.5.
(a) streamlines (b) isotherms
(c) total heat transfer
(d) local heat transfer ——— inner radius - - - - outer radius
(e) Fourier decomposition of the temperature field

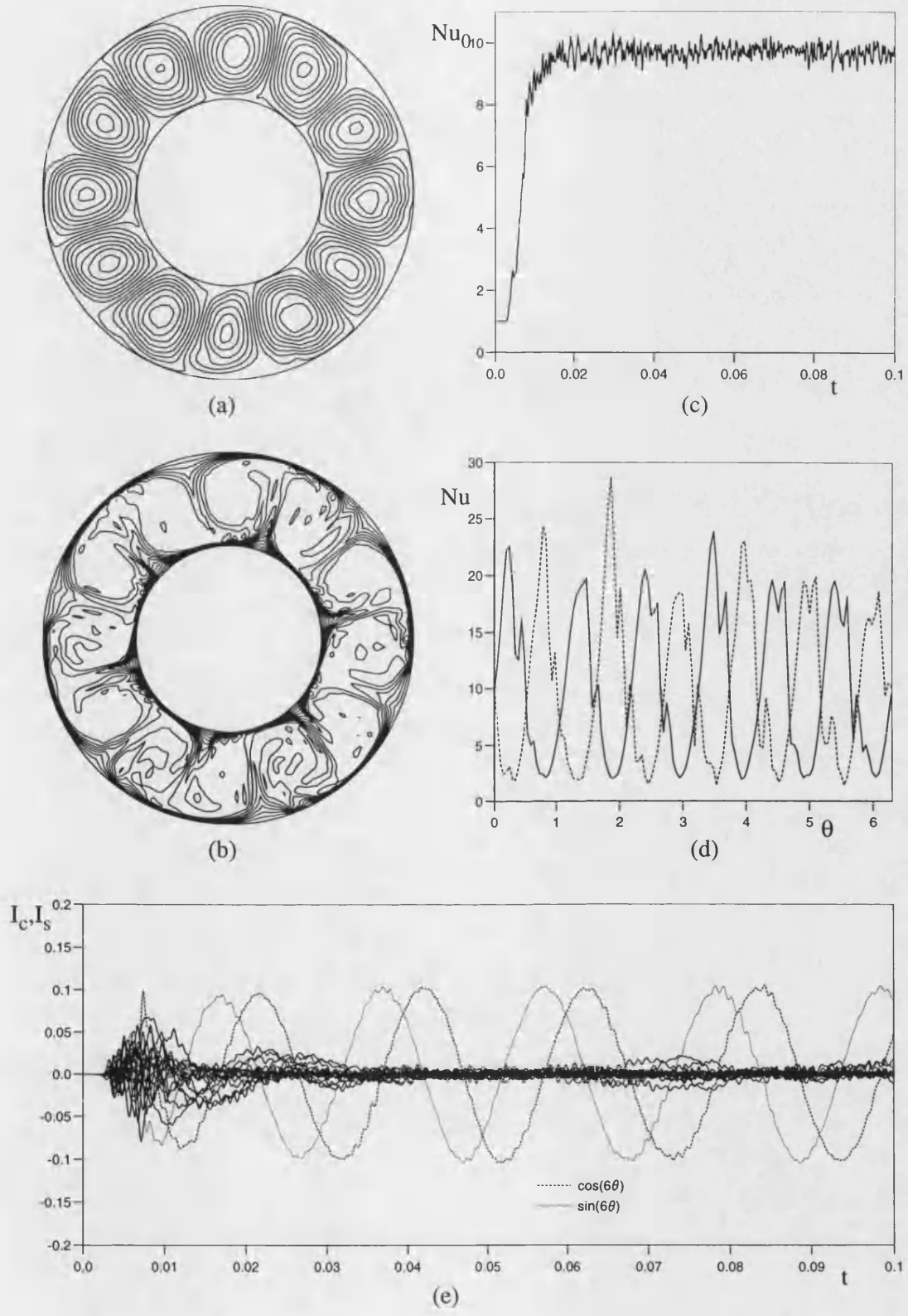

Figure 4.25. Solutions for radial/tangential flow with $Ra=2\times10^7$, $Re=10^3$ and $r_0=0.5$.
(a) streamlines (b) isotherms
(c) total heat transfer
(d) local heat transfer ——— inner radius - - - - outer radius
(e) Fourier decomposition of the temperature field

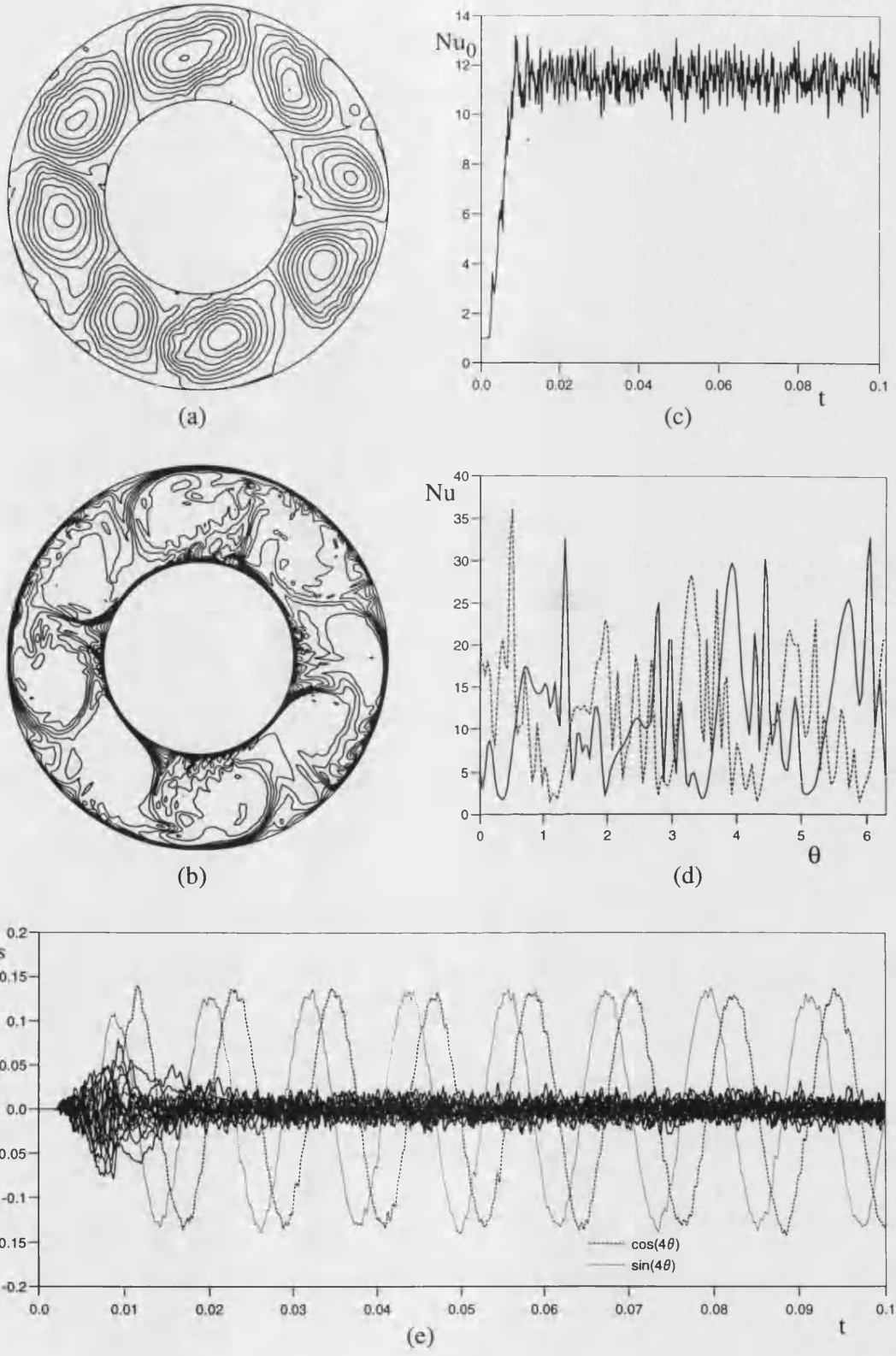

Figure 4.26. Solutions for radial/tangential flow with Ra=5×10^7, Re=10^3 and r_0=0.5.
(a) streamlines (b) isotherms
(c) total heat transfer
(d) local heat transfer ——— inner radius - - - - outer radius
(e) Fourier decomposition of the temperature field

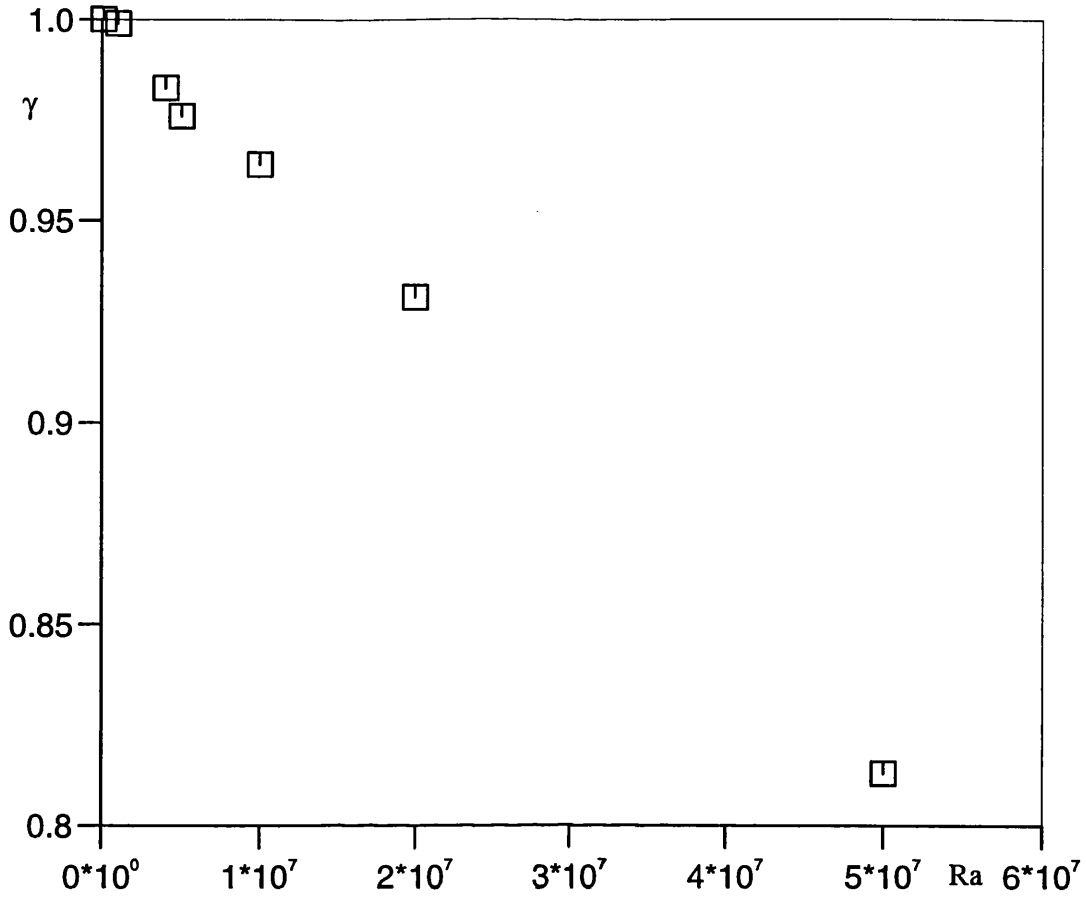

Figure 4.27. Variation of precession of cyclonic and anti–cyclonic pairs with Rayleigh number.

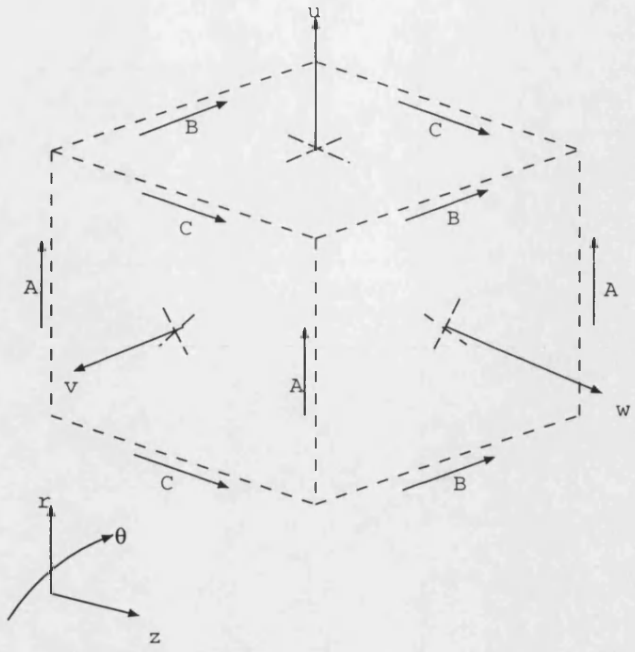

Figure 5.1. Three dimensional staggered grid layout.

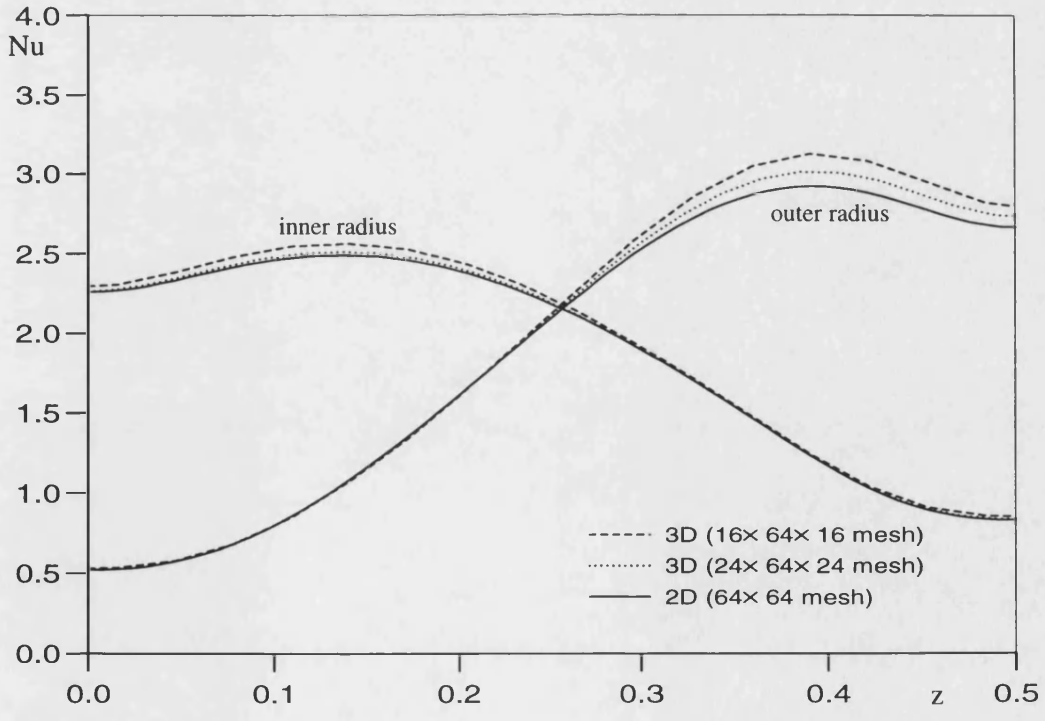

Figure 5.2. Heat transfer comparison for Ra=10^5, Re=100 and r_0=0.5.

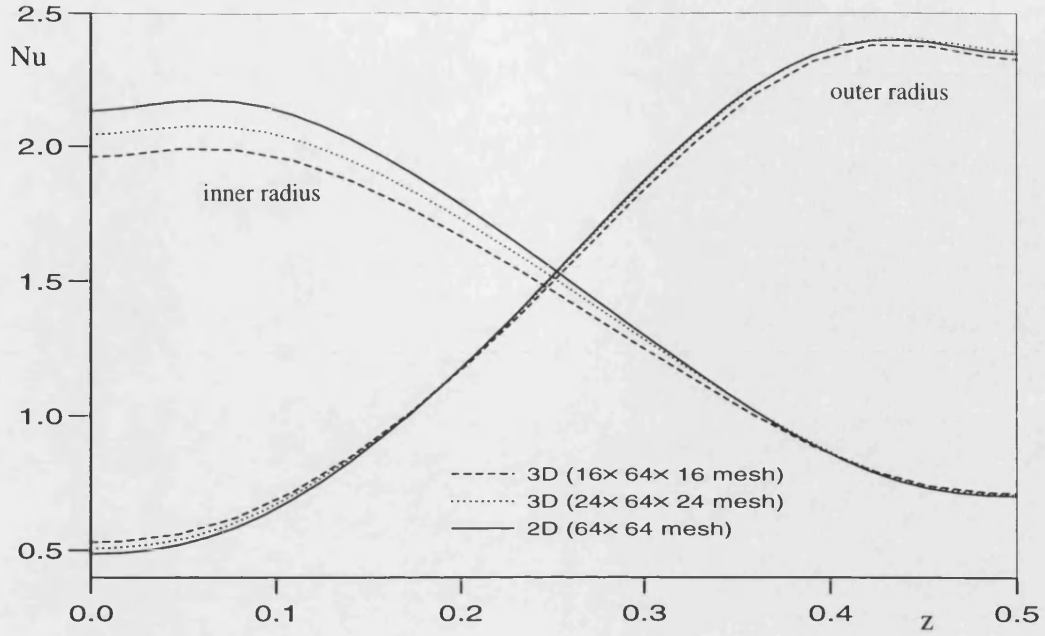

Figure 5.3. Heat transfer comparison for Ra=10^5, Re=200 and r_0=0.5.

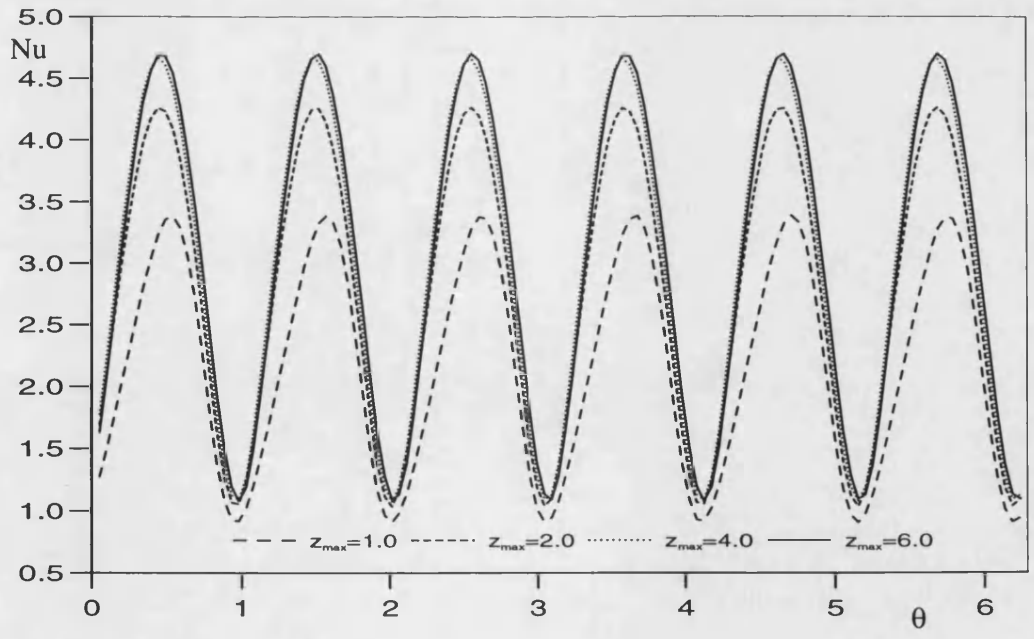

Figure 5.4. Heat transfer at the mid–axial plane on the inner cylindrical hub for Ra=10^5, Re=10^3, r_0=0.5 and various values of z_{max} .

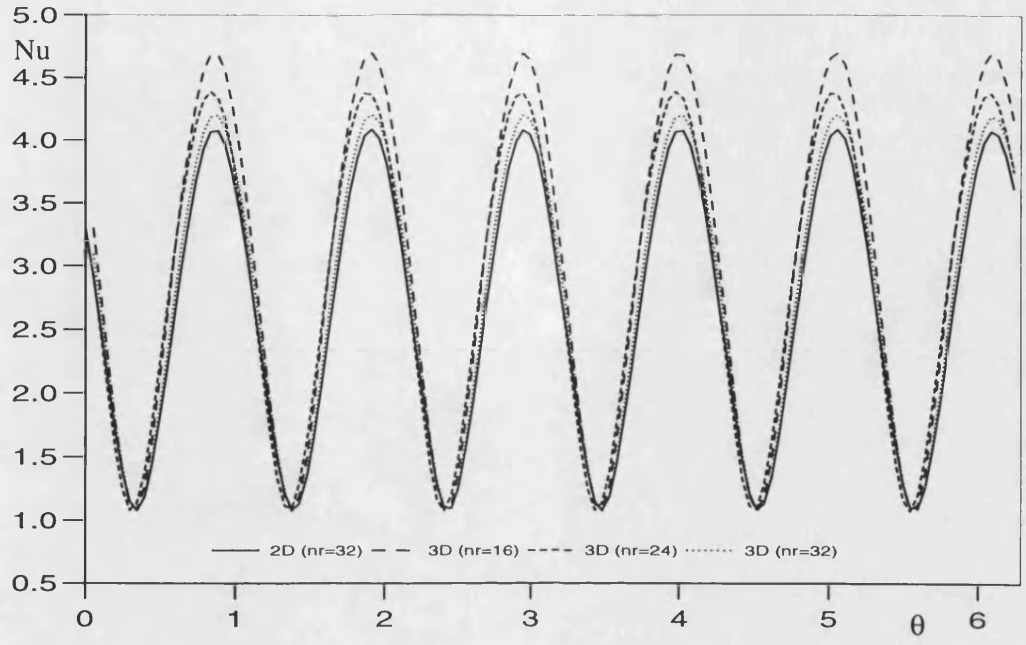

Figure 5.5. Comparison between 3D and 2D computations for heat transfer at the mid–axial plane of the inner cylindrical hub for $Ra=10^5$, $Re=10^3$ and $r_0=0.5$.

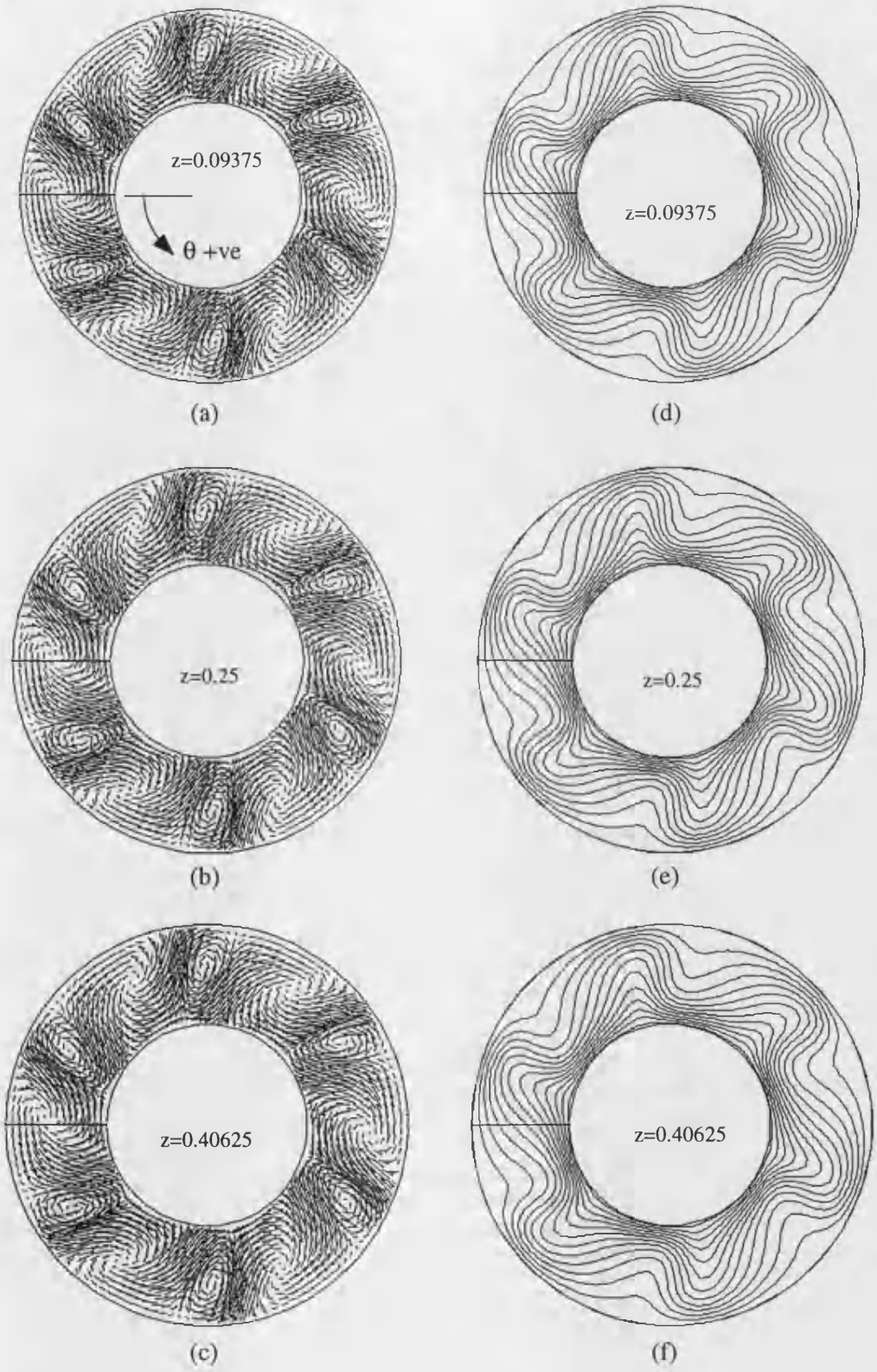

Figure 5.6. Flow vectors and isotherms at various axial locations for Ra=10^5, Re=10^3, r_0=0.5 , z_{max}=0.5 and n=6 initial perturbation.

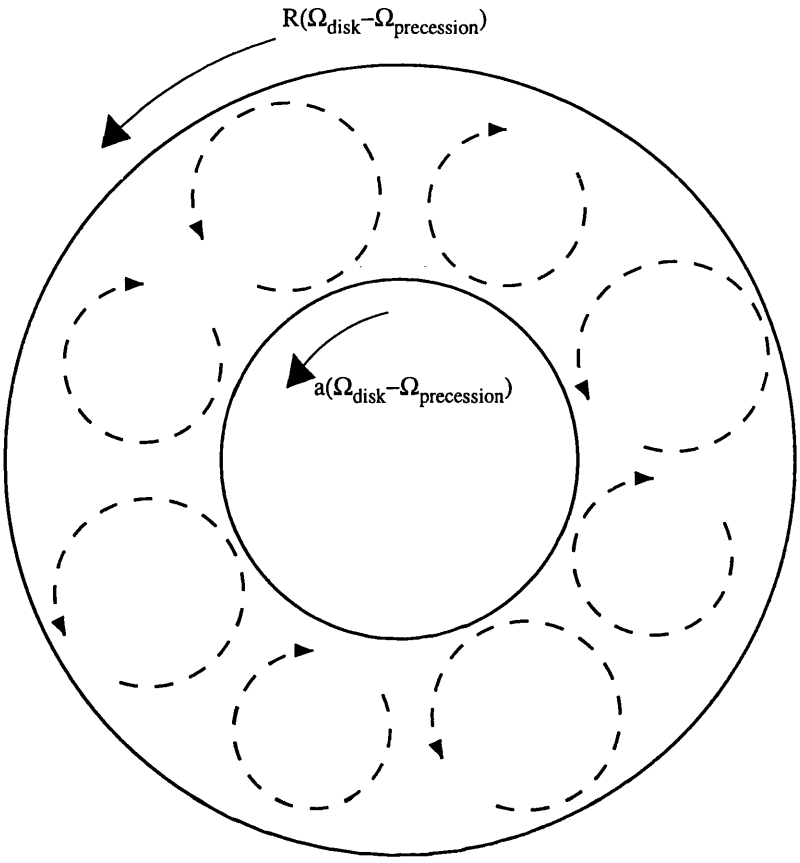

Figure 5.7. Schematic showing inner and outer cylindrical surface velocities relative to a rotating frame fixed to the precessing rolls. (Ω_{disk} is the angular velocity of the rotating surfaces and $\Omega_{precession}$ is the angular velocity of the precessing rolls.)

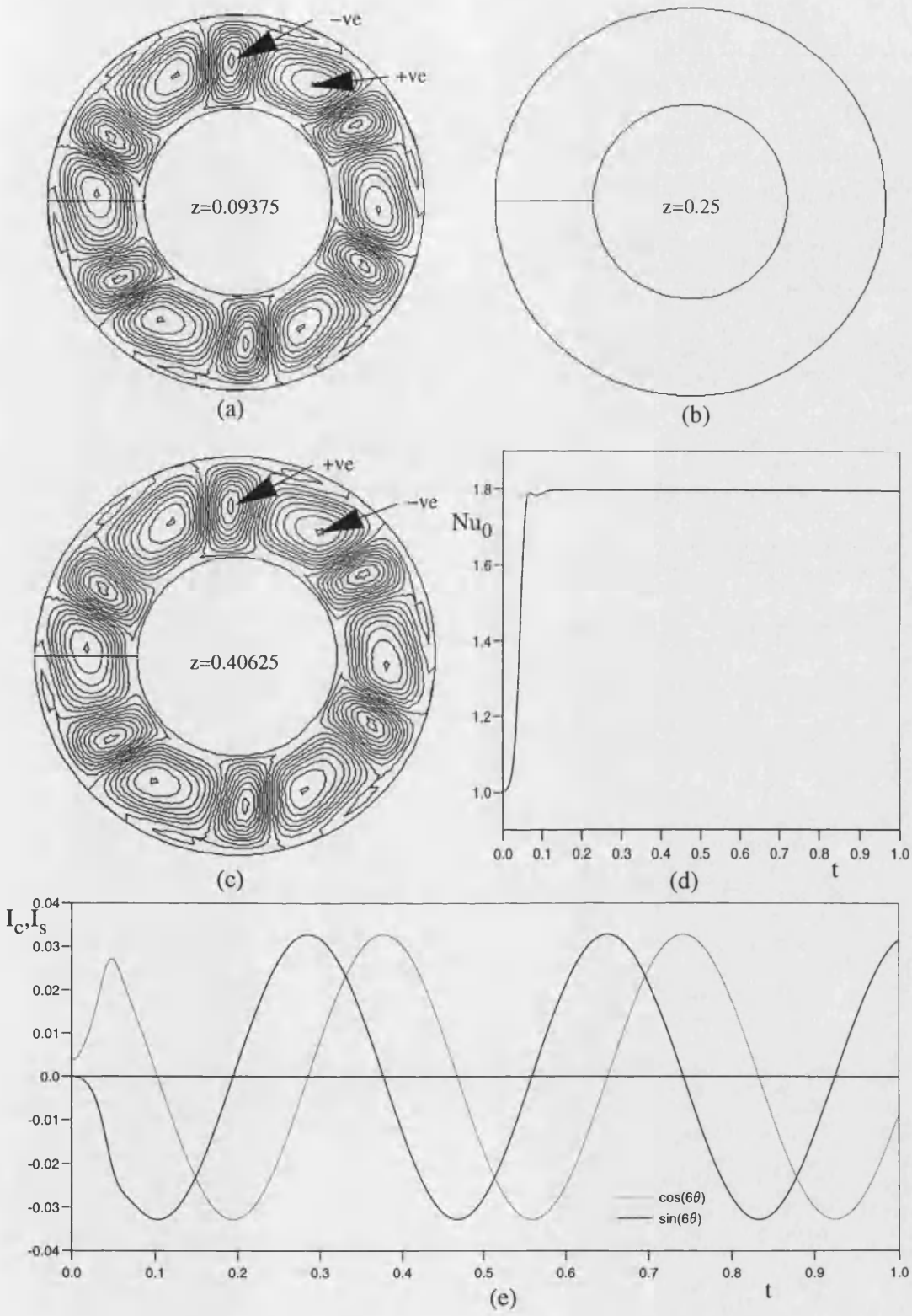

Figure 5.8. Further solutions for 3D flow with $Ra=10^5$, $Re=10^3$, $r_0=0.5$, $z_{max}=0.5$ and n=6 initial perturbation.
(a)–(c) axial velocity iso–lines
(d) total heat transfer
(e) Fourier decomposition of the temperature field

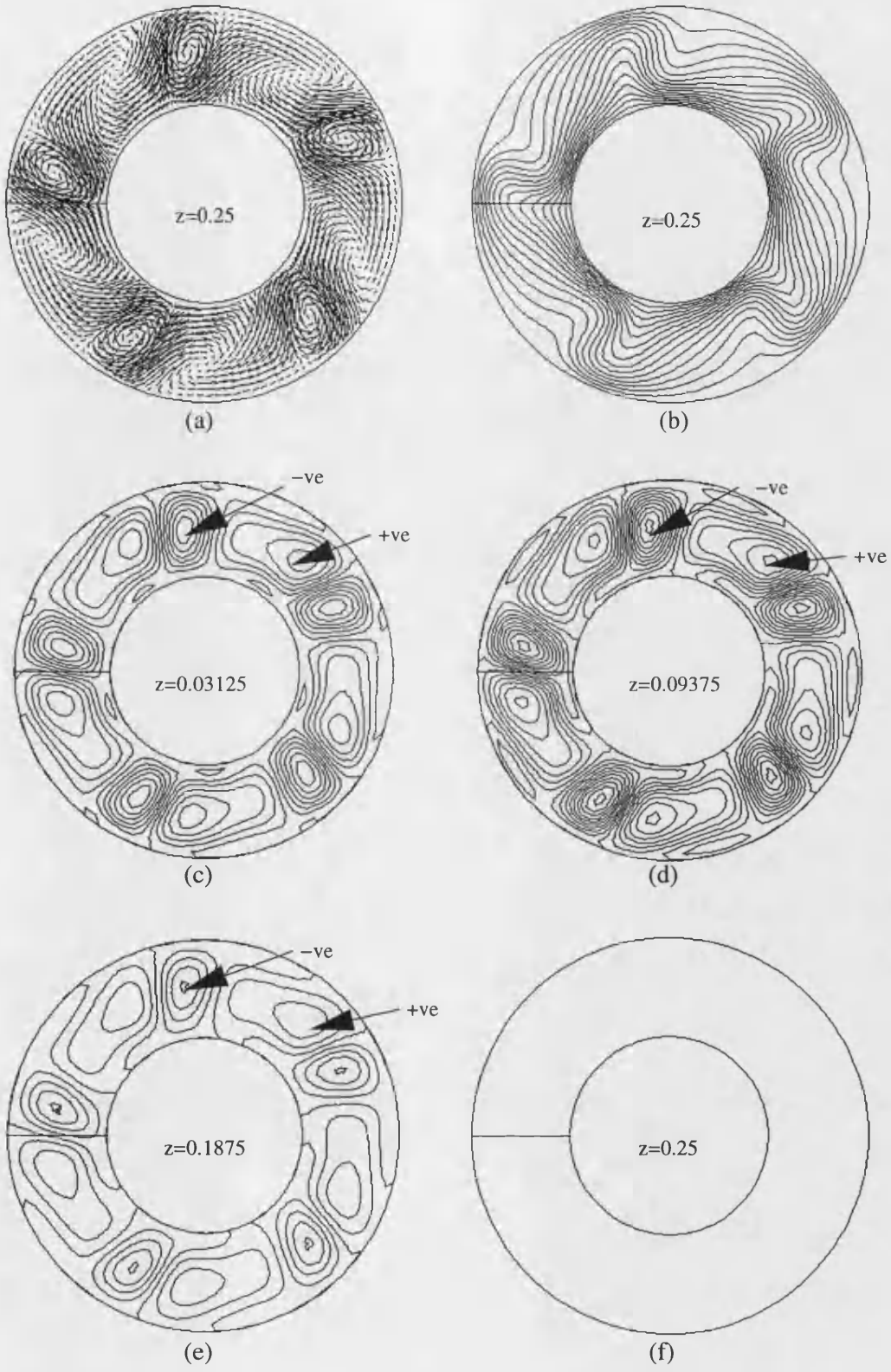

Figure 5.9. Solutions for 3D flow with $Ra=10^5$, $Re=10^3$, $r_0=0.5$, $z_{max}=0.5$ and n=5 initial perturbation.
(a) mid–axial plane flow vectors
(b) mid–axial plane isotherms
(c)–(f) axial velocity iso–lines

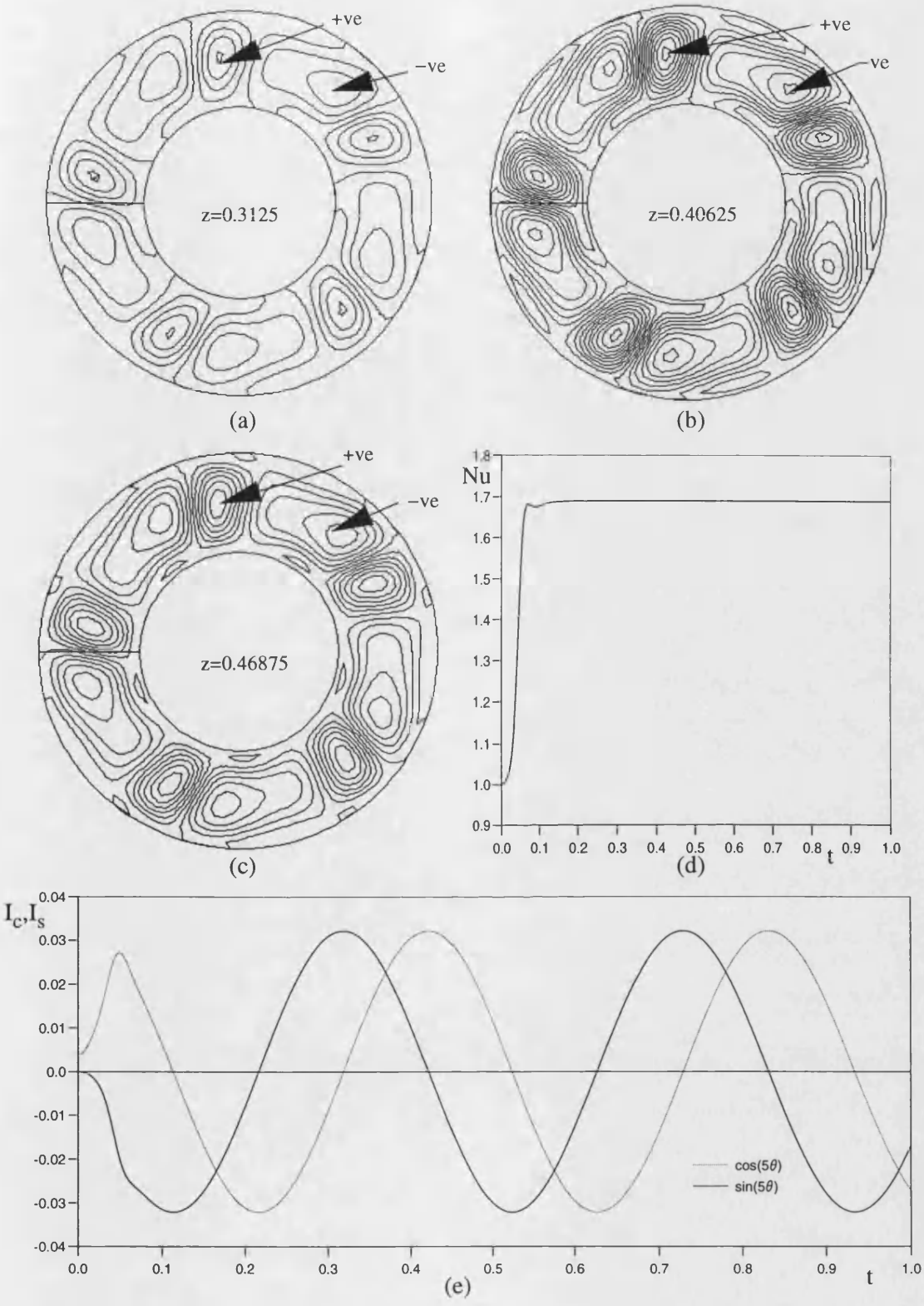

Figure 5.10. Further solutions for 3D flow with $Ra=10^5$, $Re=10^3$, $r_0=0.5$, $z_{max}=0.5$ and n=5 initial perturbation.
(a)–(c) axial velocity iso–lines
(d) total heat transfer
(e) Fourier decomposition of the temperature field

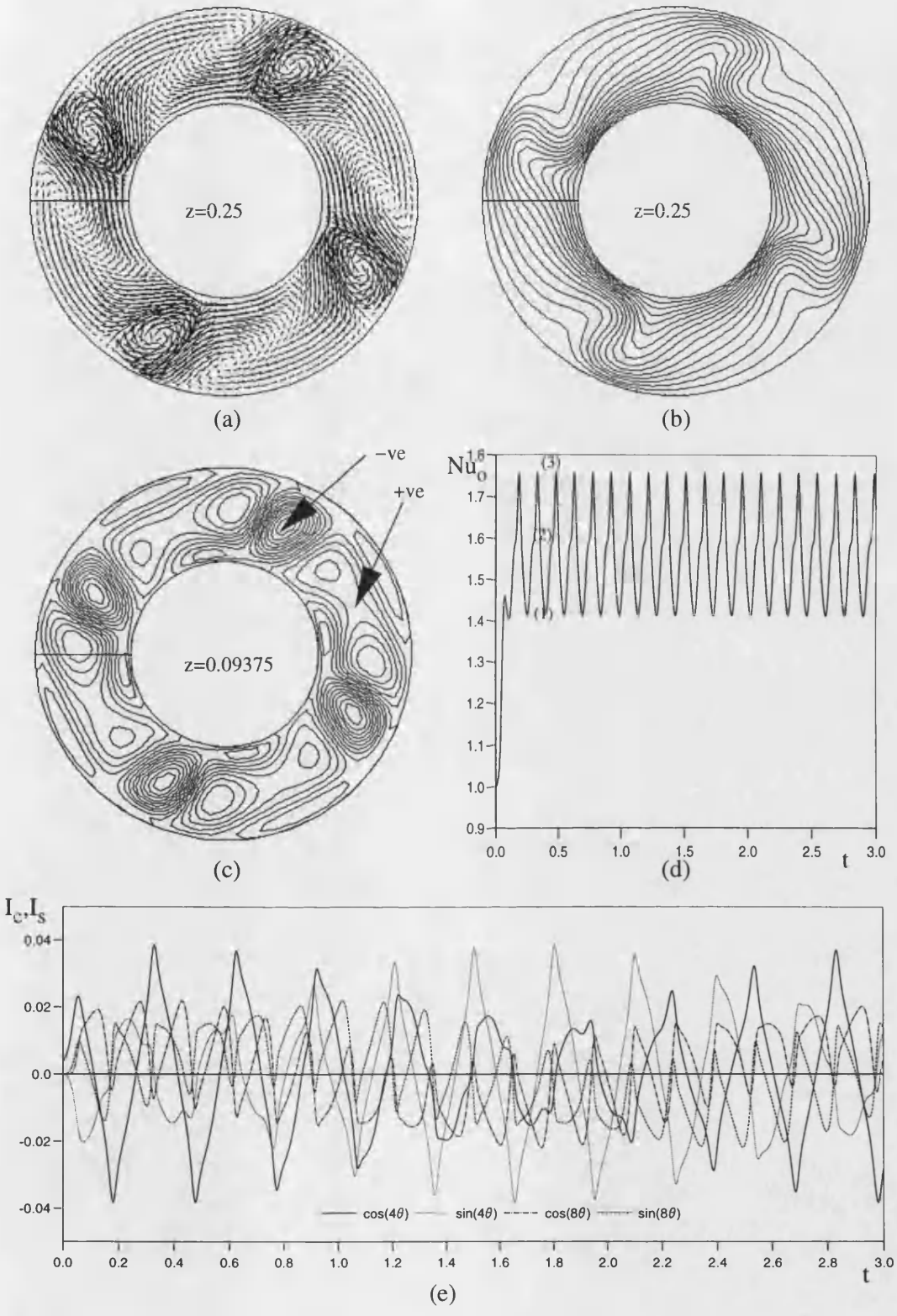

Figure 5.11. Solutions for 3D flow with $Ra=10^5$, $Re=10^3$, $r_0=0.5$, $z_{max}=0.5$ and n=4 initial perturbation.

(a) mid −axial plane flow vectors (b) mid−axial plane isotherms
(c) axial velocity iso−lines (d) total heat transfer
(e) Fourier decomposition of the temperature field

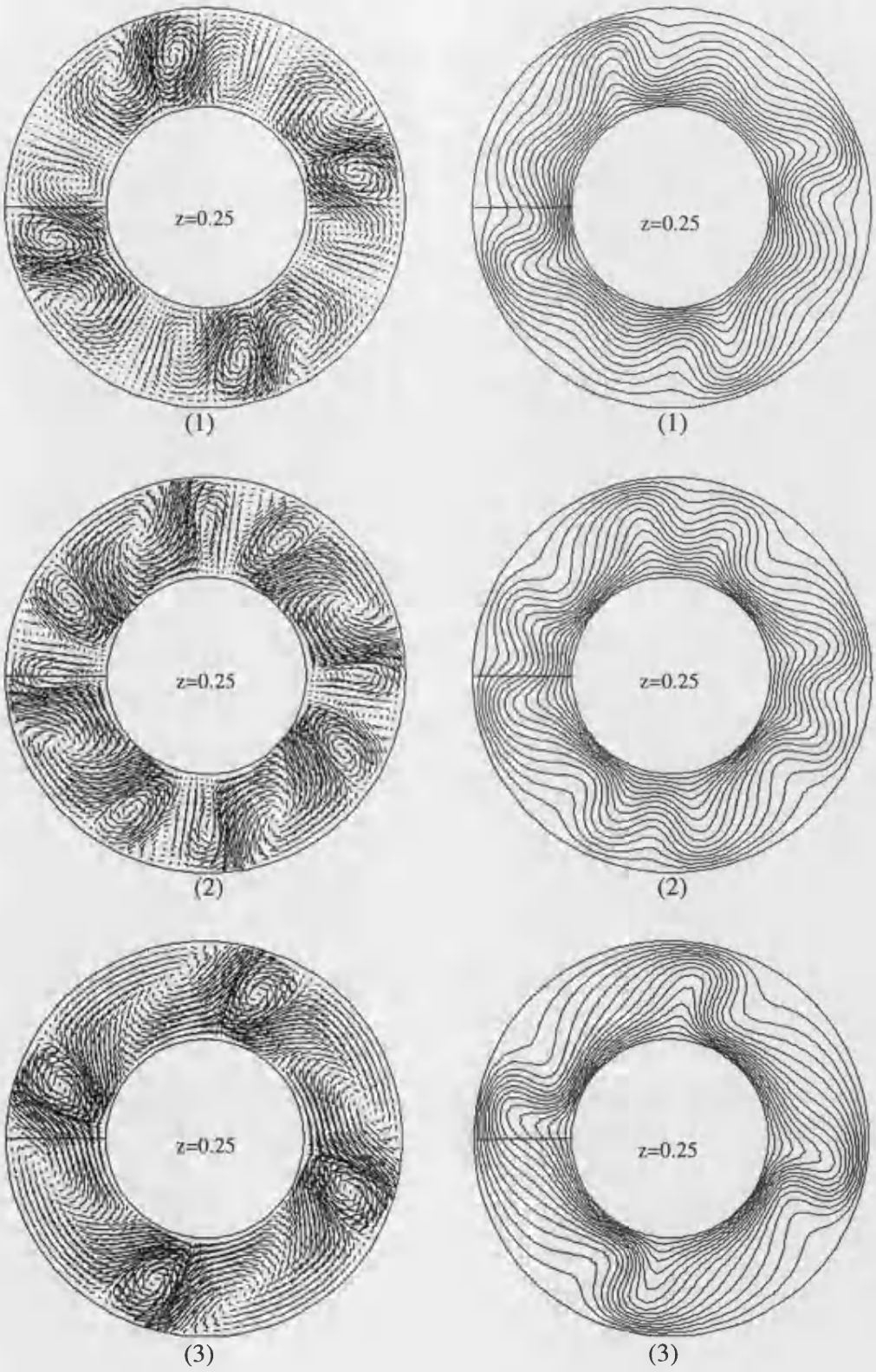

Figure 5.12. Flow vectors and isotherms for 3D flow with $Ra=10^5$, $Re=10^3$, $r_0=0.5$, $z_{max}=0.5$ and n=4 initial perturbation at times;
(1) t=0.40 (2) t=0.45 (3) t=0.48

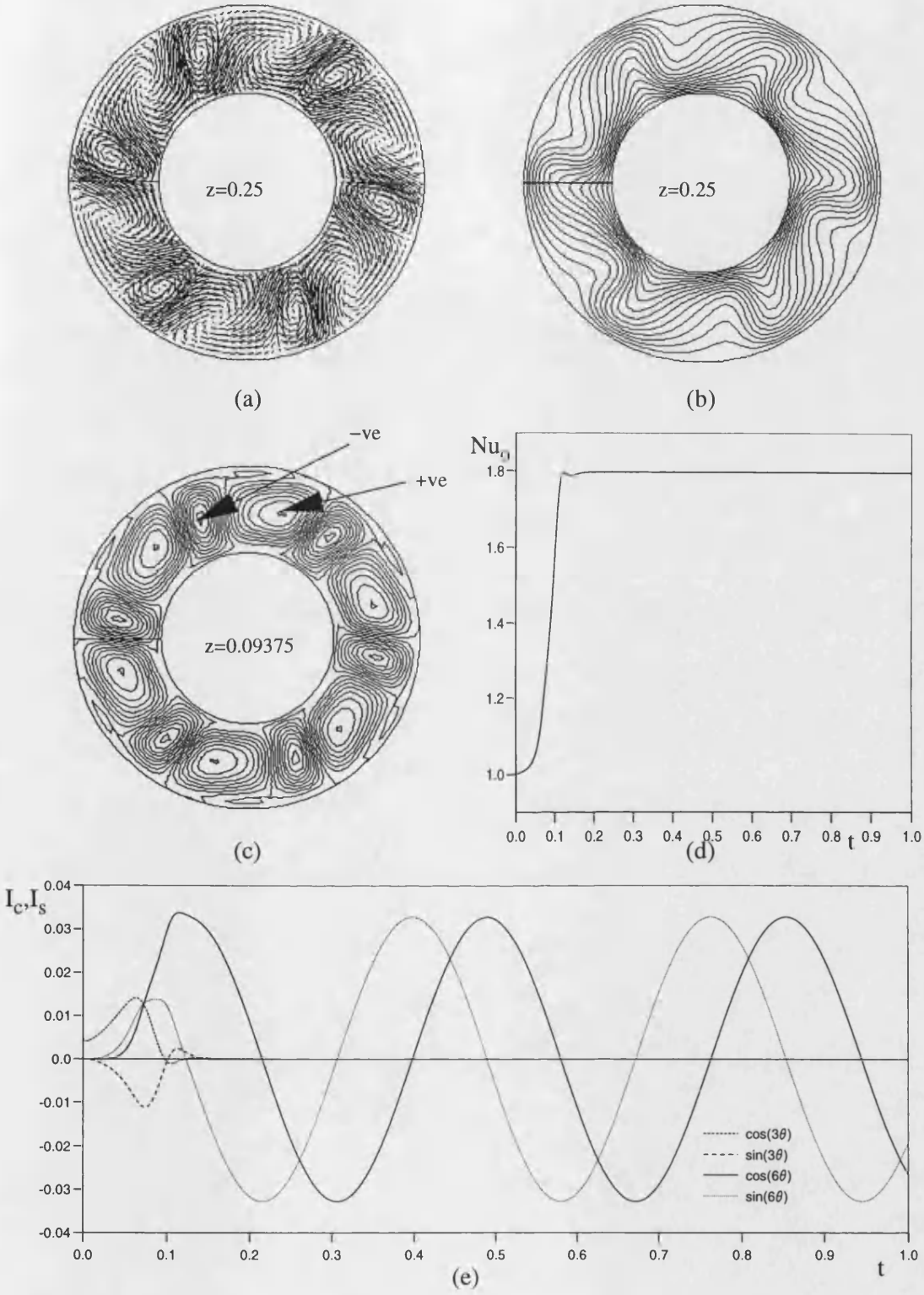

Figure 5.13. Solutions for 3D flow with $Ra=10^5$, $Re=10^3$, $r_0=0.5$, $z_{max}=0.5$ and n=3 initial perturbation.

(a) mid −axial plane flow vectors (b) mid−axial plane isotherms
(c) axial velocity iso−lines (d) total heat transfer
(e) Fourier decomposition of the temperature field

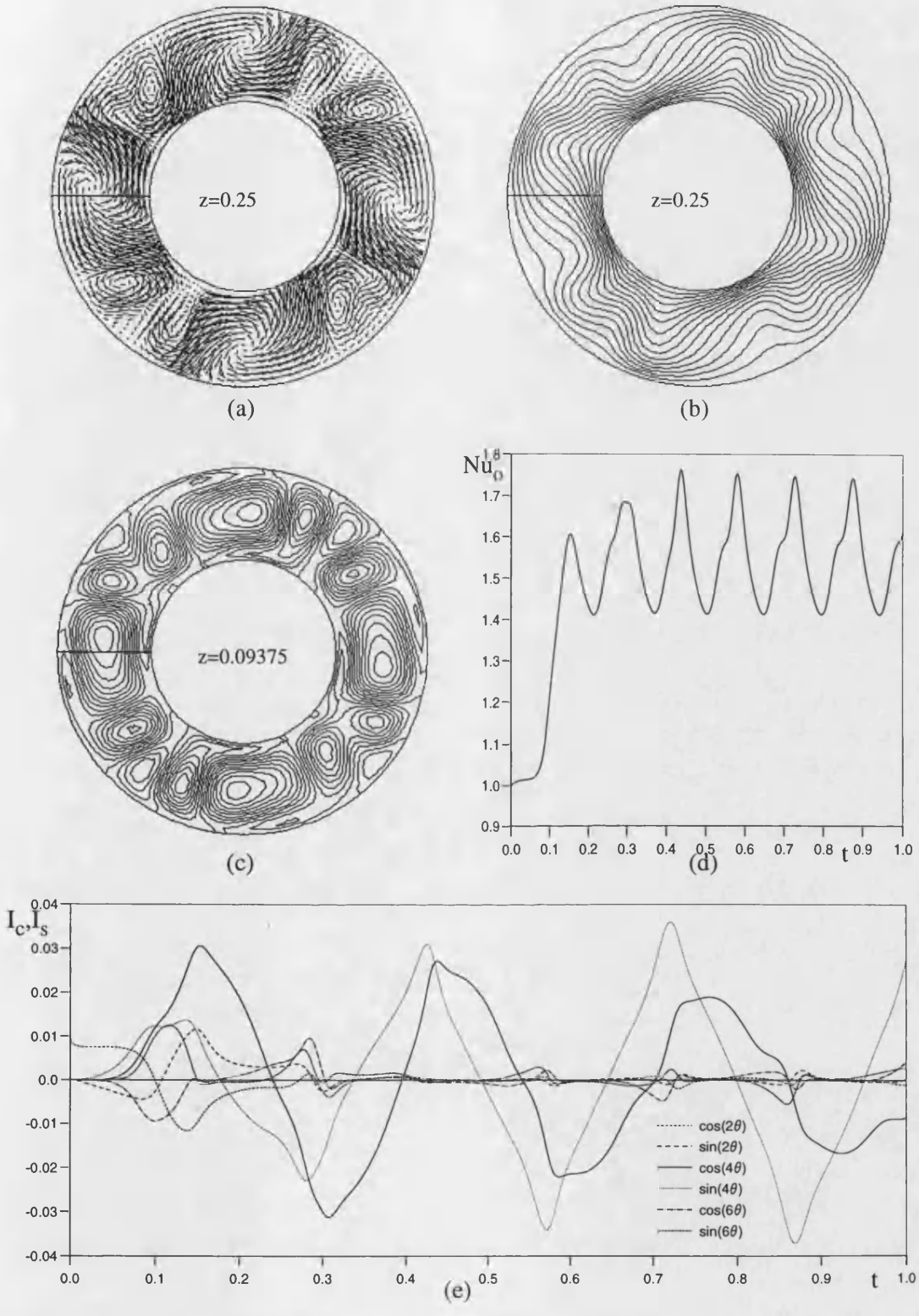

Figure 5.14. Solutions for 3D flow with $Ra=10^5$, $Re=10^3$, $r_0=0.5$, $z_{max}=0.5$ and n=2 initial perturbation.

(a) mid –axial plane flow vectors (b) mid–axial plane isotherms
(c) axial velocity iso–lines (d) total heat transfer
(e) Fourier decomposition of the temperature field

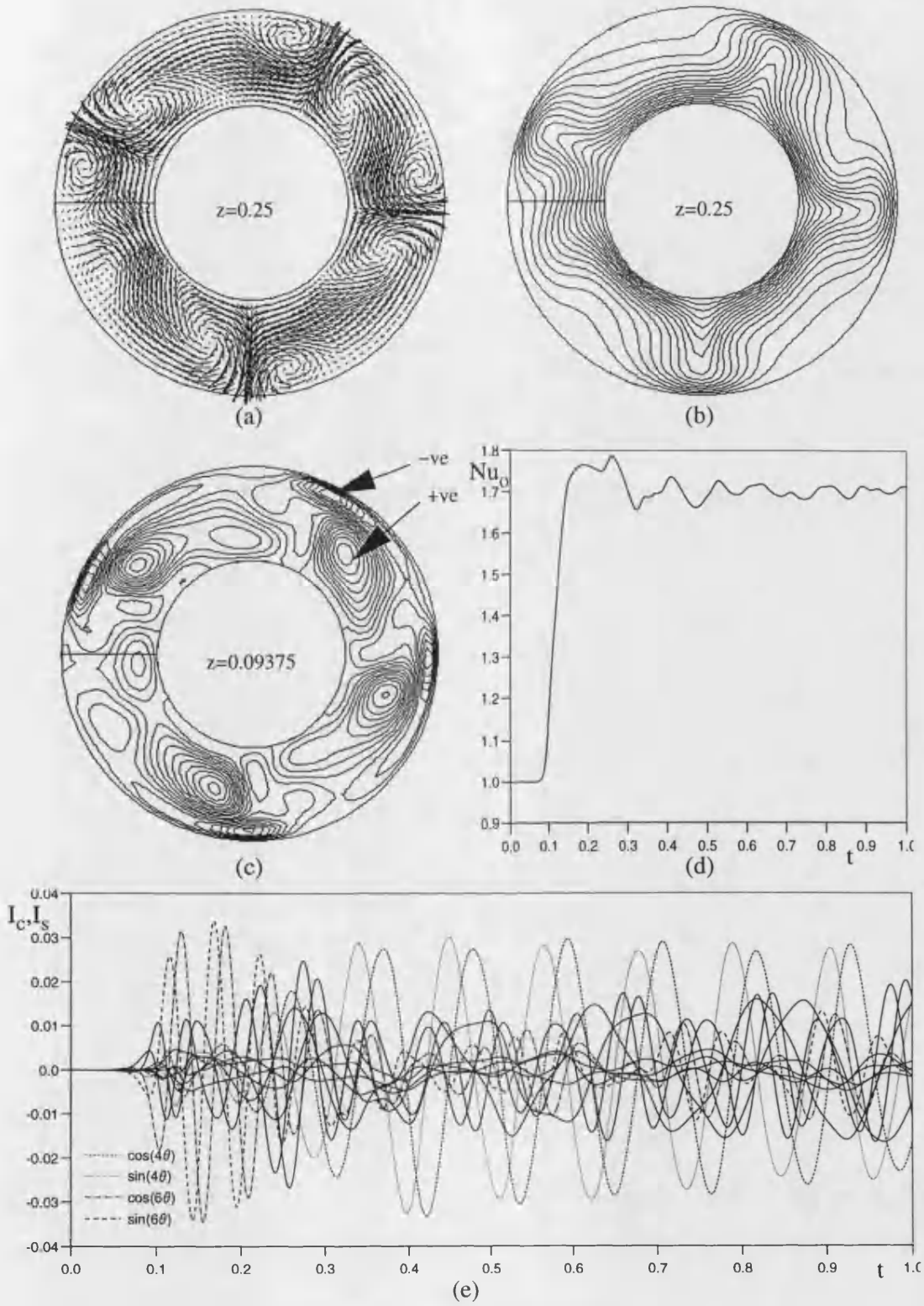

Figure 5.15. Solutions for 3D flow with Ra=10^5, Re=200, r_0=0.5 and z_{max}=0.5.
(a) mid–axial plane flow vectors (b) mid–axial plane isotherms
(c) axial velocity iso–lines (d) total heat transfer
(e) Fourier decomposition of the temperature field

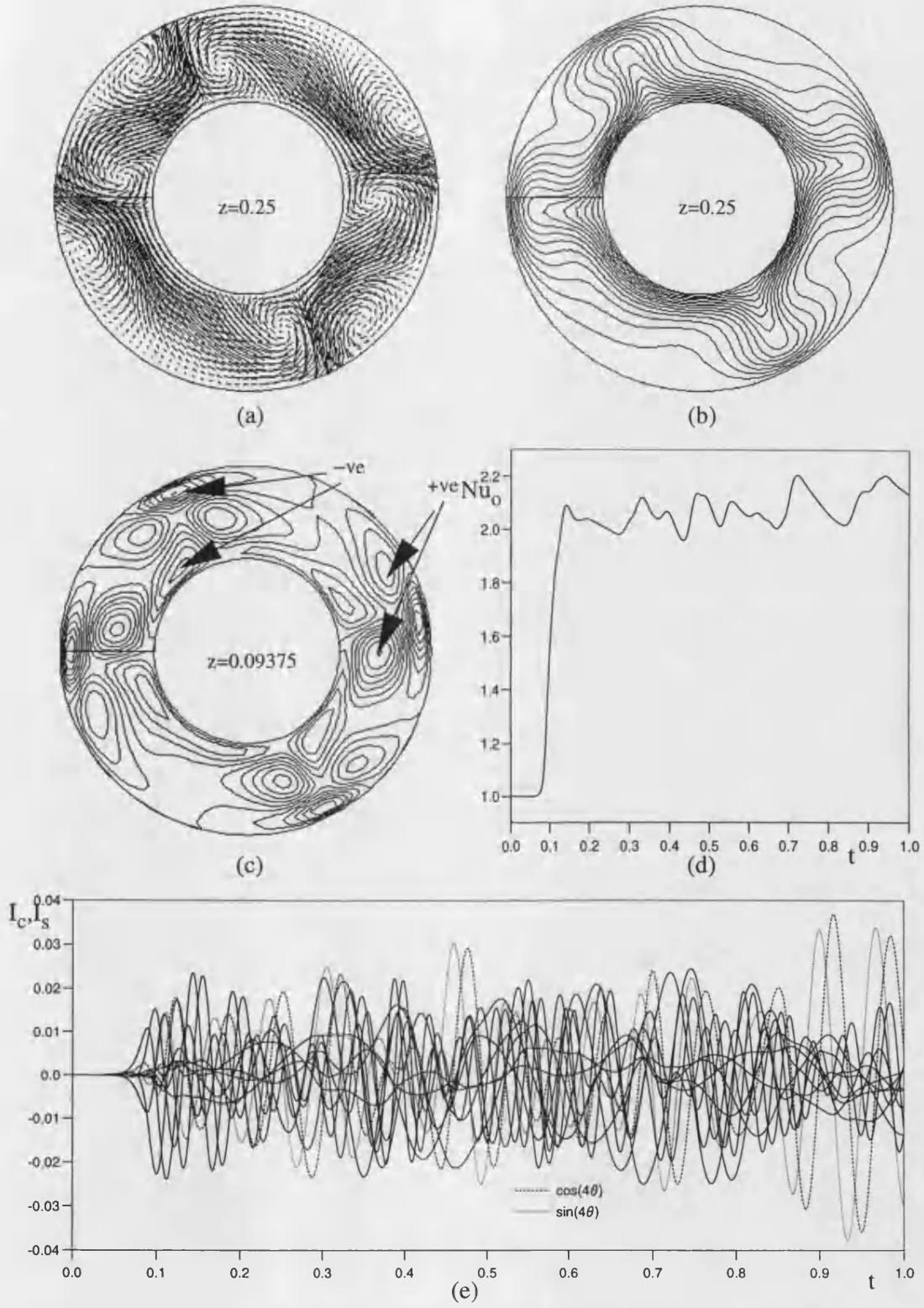

Figure 5.16. Solutions for 3D flow with Ra=10^5, Re=300, r_0=0.5 and z_{max}=0.5.
(a) mid–axial plane flow vectors (b) mid–axial plane isotherms
(c) axial velocity iso–lines (d) total heat transfer
(e) Fourier decomposition of the temperature field

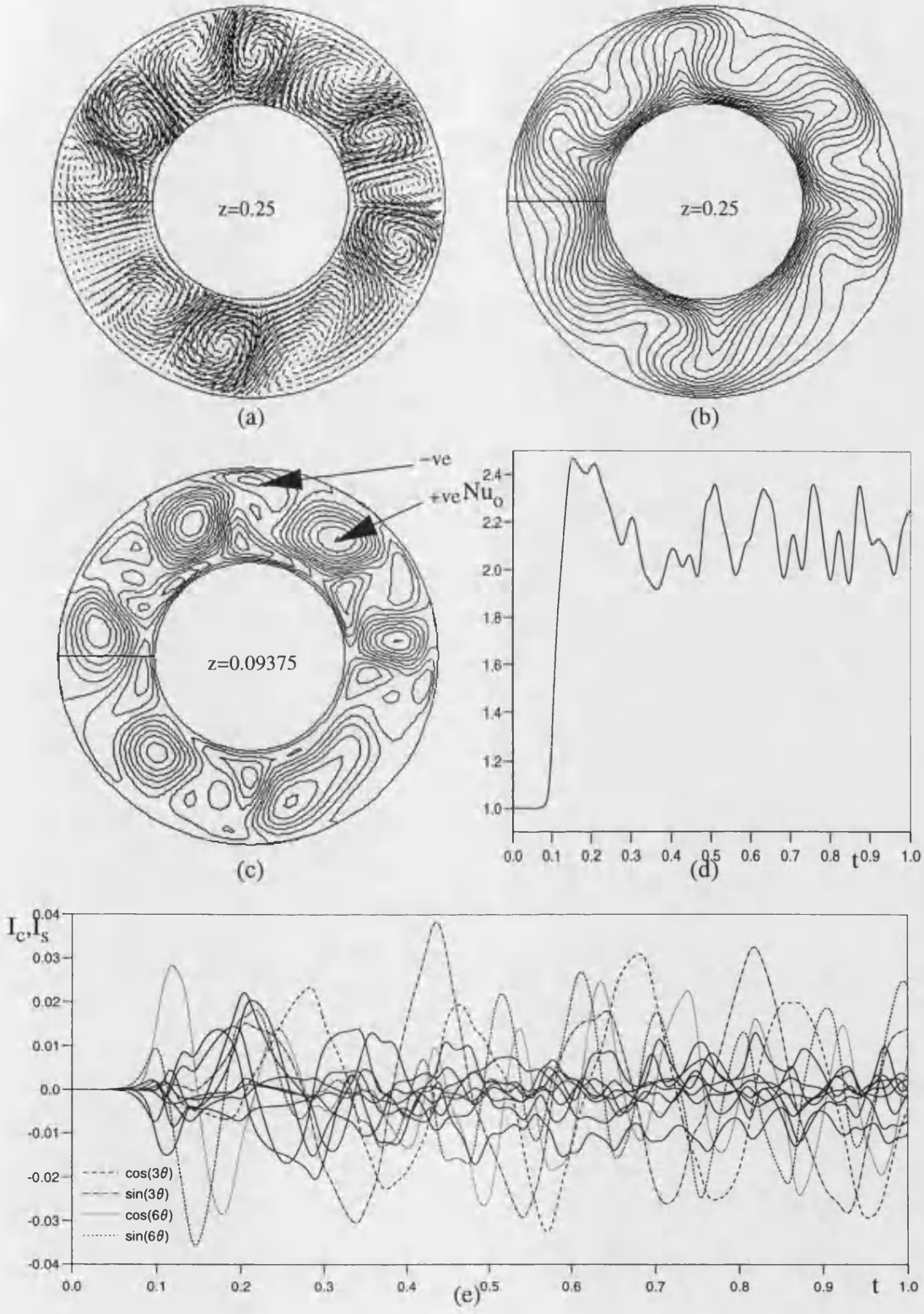

Figure 5.17. Solutions for 3D flow with Ra=10^5, Re=500, r_0=0.5 and z_{max}=0.5.
(a) mid–axial plane flow vectors (b) mid–axial plane isotherms
(c) axial velocity iso–lines (d) total heat transfer
(e) Fourier decomposition of the temperature field

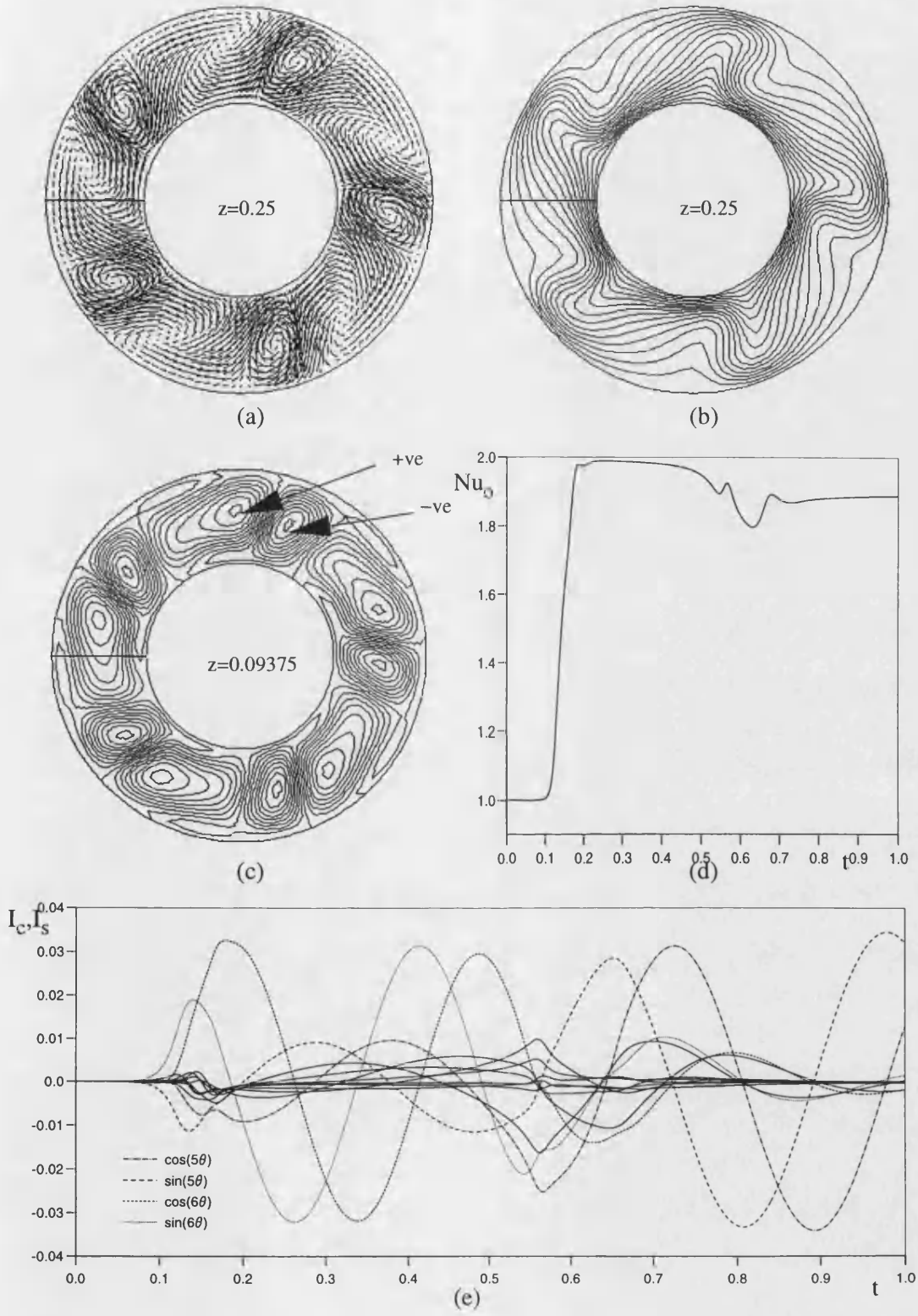

Figure 5.18. Solutions for 3D flow with $Ra=10^5$, $Re=800$, $r_0=0.5$ and $z_{max}=0.5$.
(a) mid–axial plane flow vectors (b) mid–axial plane isotherms
(c) axial velocity iso–lines (d) total heat transfer
(e) Fourier decomposition of the temperature field

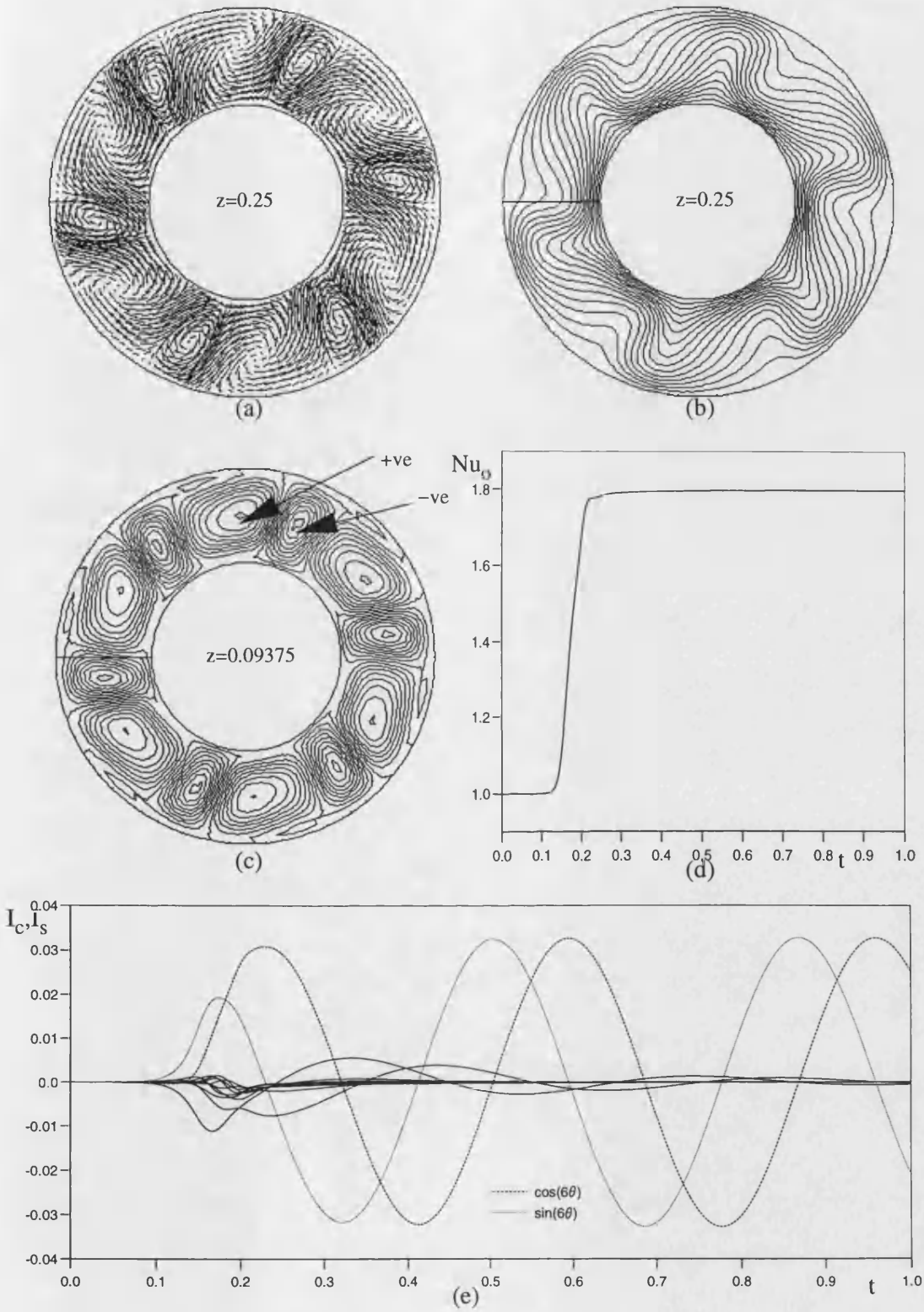

Figure 5.19. Solutions for 3D flow with Ra=10^5, Re=10^3, r_0=0.5 and z_{max}=0.5.
(a) mid–axial plane flow vectors (b) mid–axial plane isotherms
(c) axial velocity iso–lines (d) total heat transfer
(e) Fourier decomposition of the temperature field

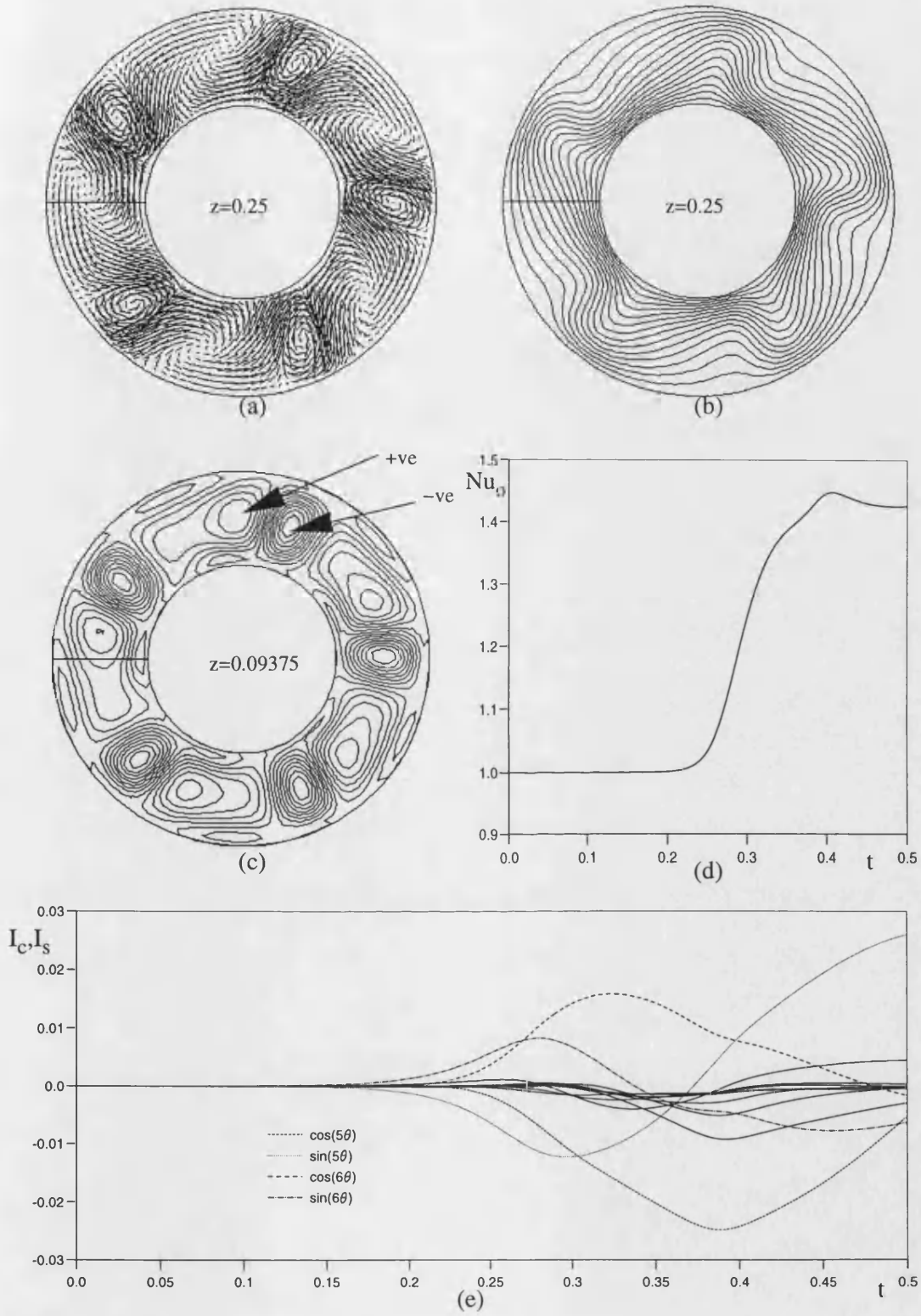

Figure 5.20. Solutions for 3D flow with Ra=10^5, Re=1.5×10^3, r_0=0.5 and z_{max}=0.5.
(a) mid–axial plane flow vectors (b) mid–axial plane isotherms
(c) axial velocity iso–lines (d) total heat transfer
(e) Fourier decomposition of the temperature field

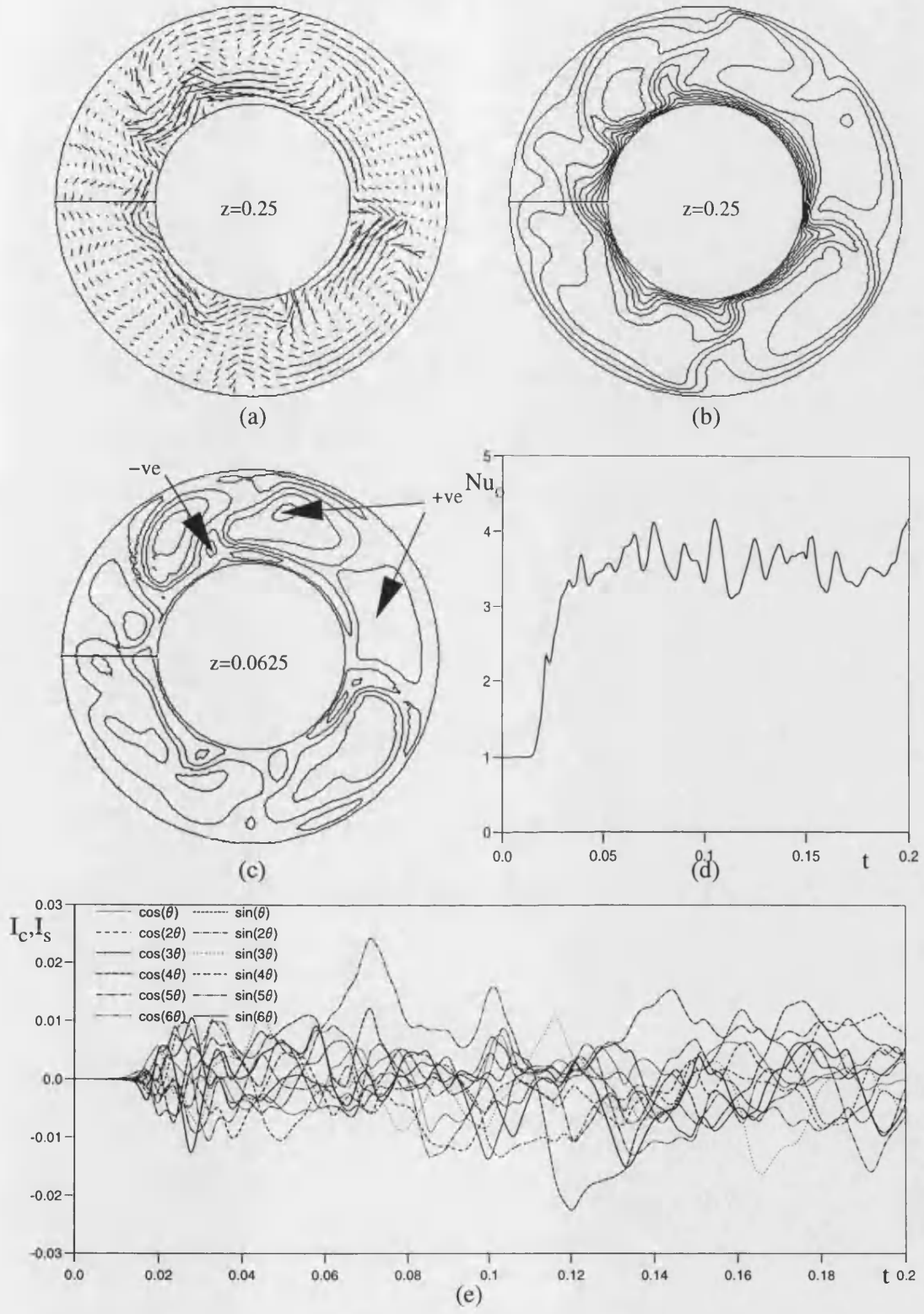

Figure 5.21. Solutions for 3D flow with Ra=10^6, Re=500, r_0=0.5 and z_{max}=0.5.
(a) mid−axial plane flow vectors (b) mid−axial plane isotherms
(c) axial velocity iso−lines (d) total heat transfer
(e) Fourier decomposition of the temperature field

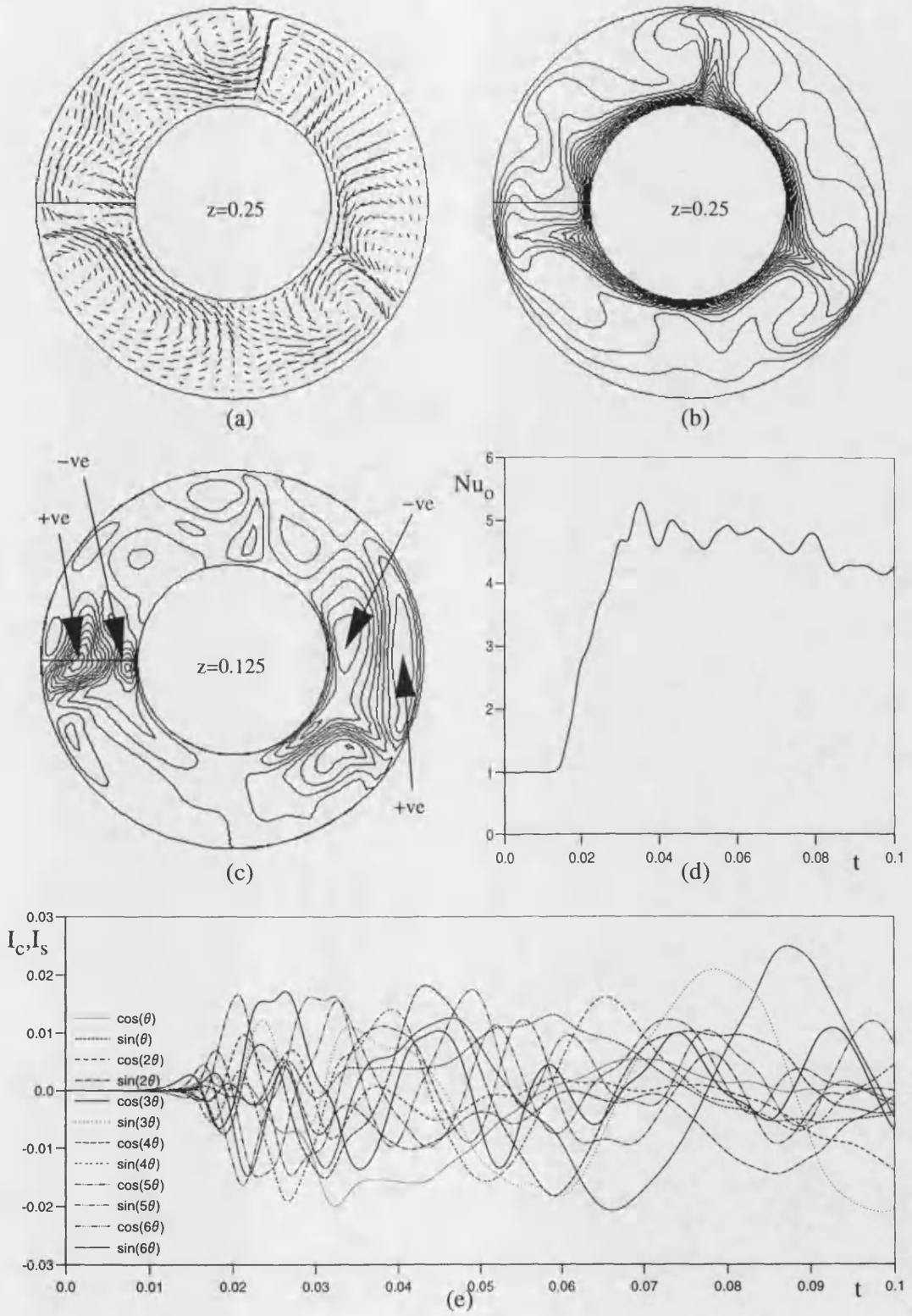

Figure 5.22. Solutions for 3D flow with $Ra=10^6$, $Re=10^3$, $r_0=0.5$ and $z_{max}=0.5$.
(a) mid–axial plane flow vectors (b) mid–axial plane isotherms
(c) axial velocity iso–lines (d) total heat transfer
(e) Fourier decomposition of the temperature field

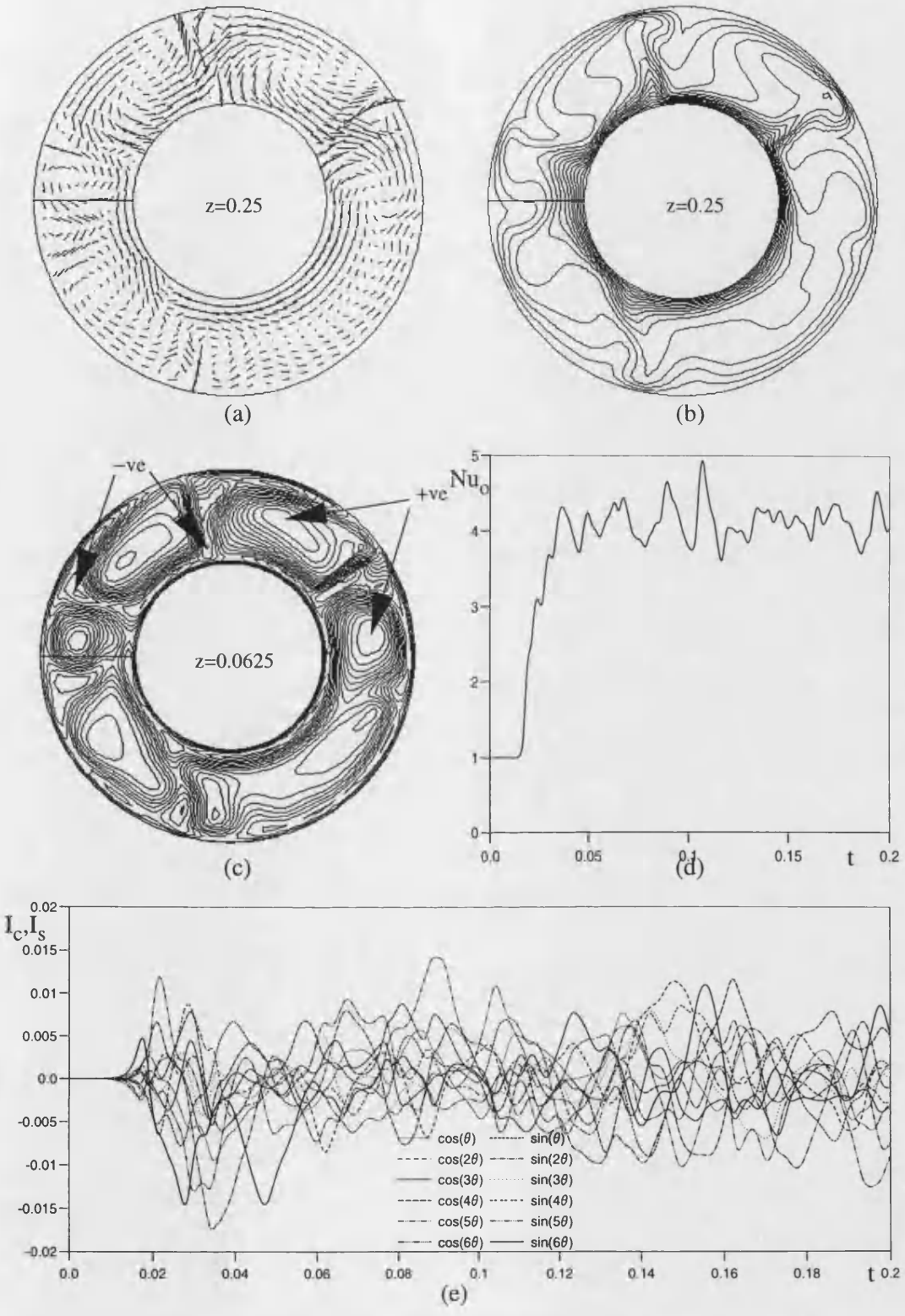

Figure 5.23. Solutions for 3D flow with Ra=10^6, Re=2×10^3, r_0=0.5 and z_{max}=0.5.
(a) mid–axial plane flow vectors (b) mid–axial plane isotherms
(c) axial velocity iso–lines (d) total heat transfer
(e) Fourier decomposition of the temperature field

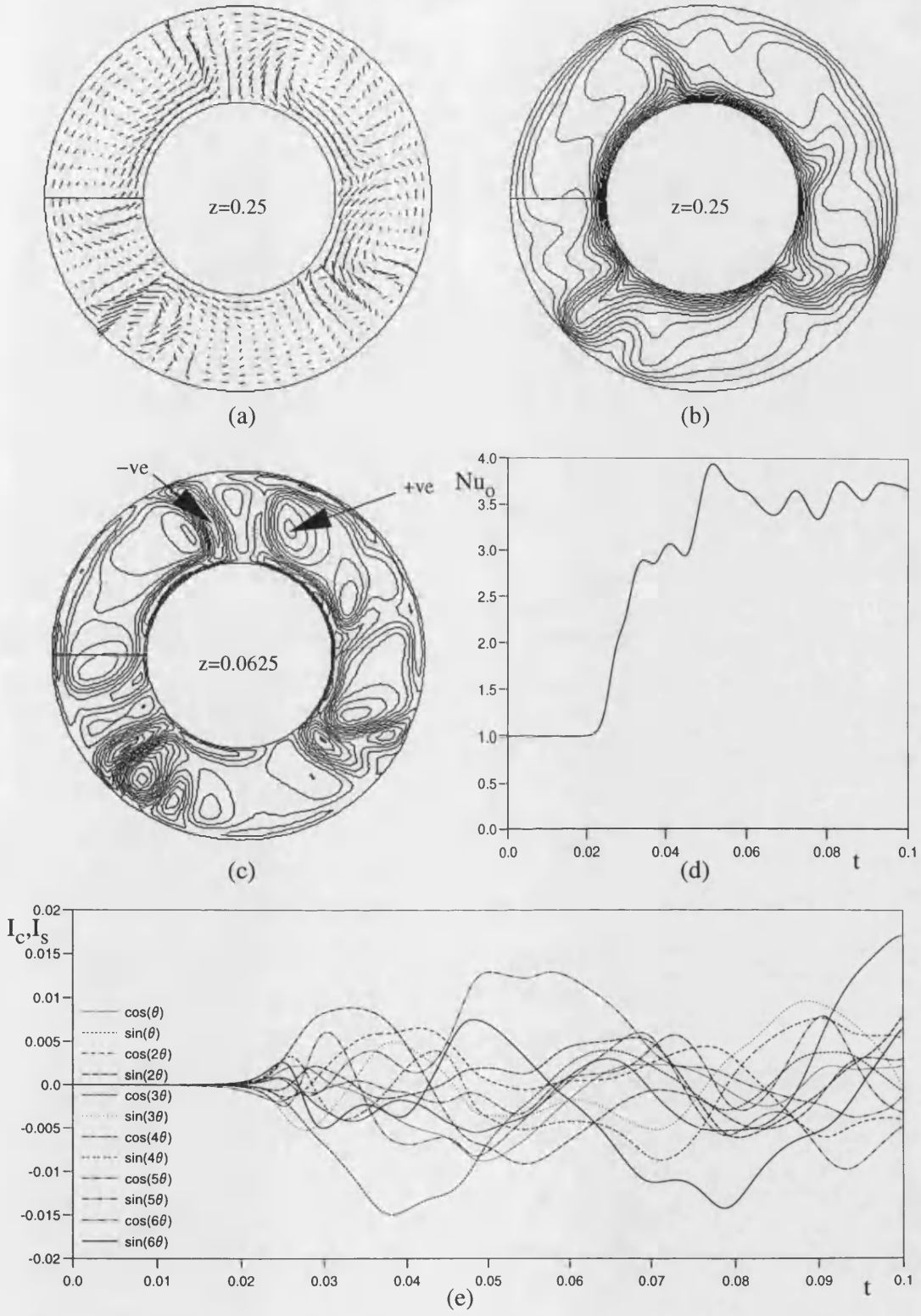

Figure 5.24. Solutions for 3D flow with $Ra=10^6$, $Re=5\times10^3$, $r_0=0.5$ and $z_{max}=0.5$.
(a) mid–axial plane flow vectors (b) mid–axial plane isotherms
(c) axial velocity iso–lines (d) total heat transfer
(e) Fourier decomposition of the temperature field

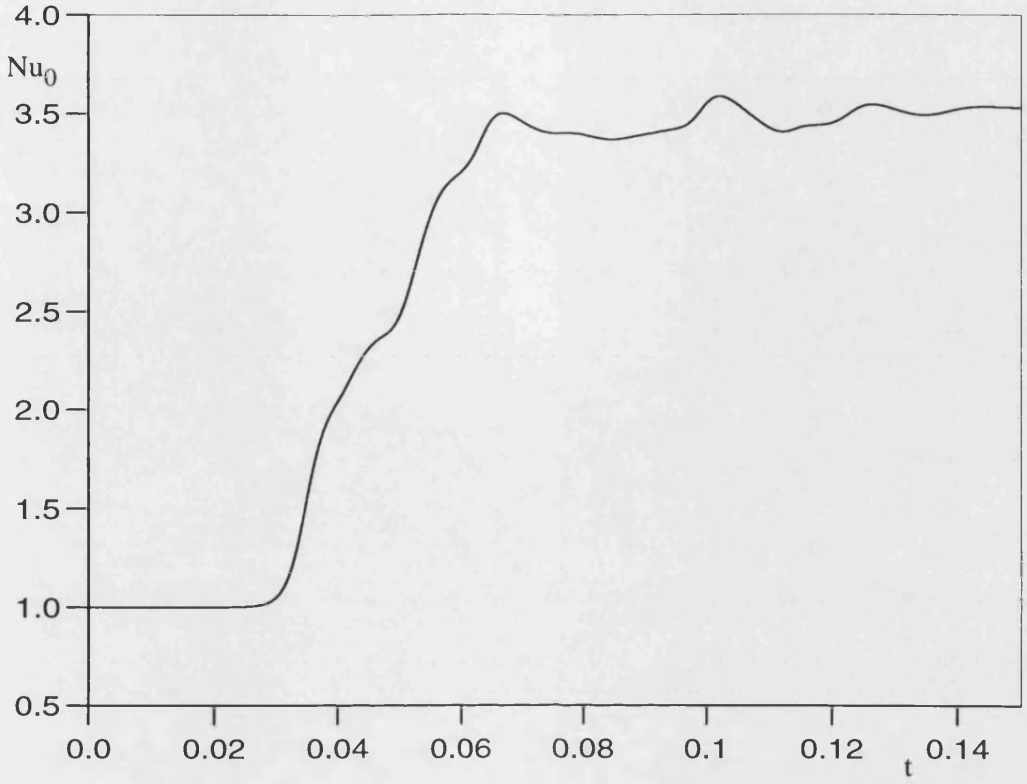

Figure 5.25. Heat transfer with time for Ra=10^6, Re=10^4, r_0=0.5 and z_{max}=0.5.

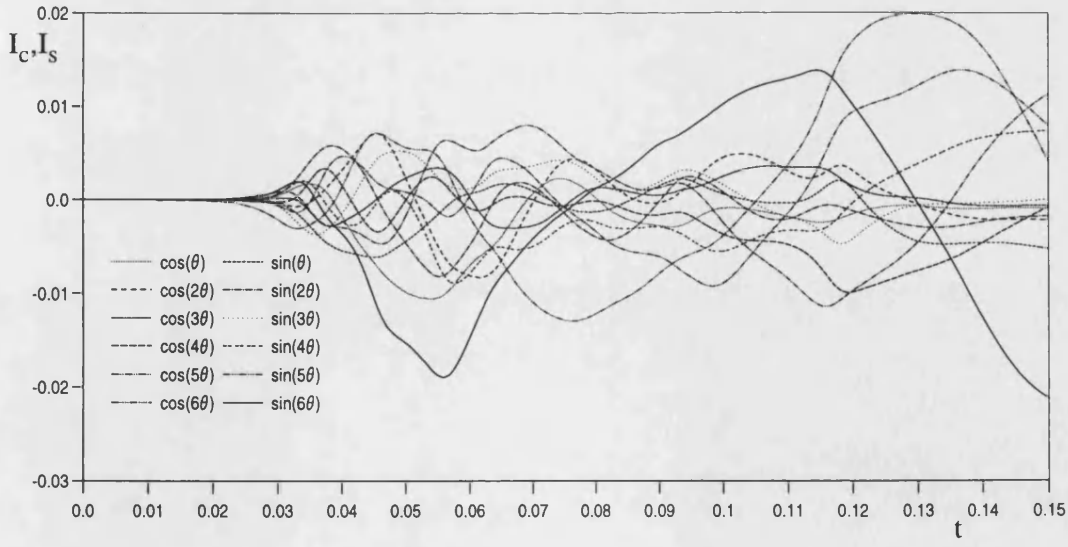

Figure 5.26. Fourier decomposition of the tmperature field for Ra=10^6, Re=10^4, r_0=0.5 and z_{max}=0.5.

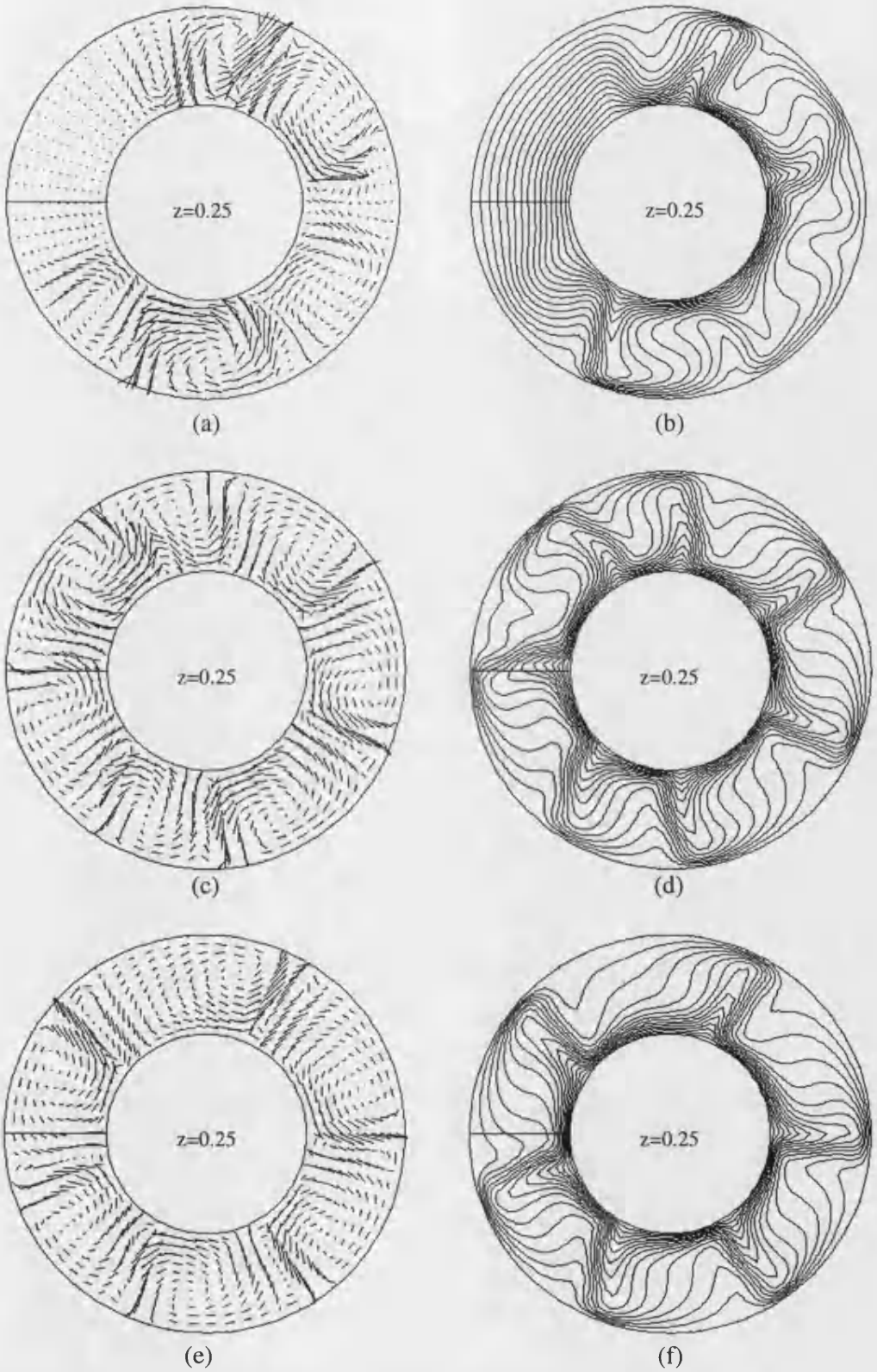

Figure 5.27. Solutions for 3D flow with $Ra=10^6$, $Re=10^4$, $r_0=0.5$ and $z_{max}=0.5$.
(a) ,(b) mid−axial plane flow vectors and isotherms at t=0.05
(c) ,(d) mid−axial plane flow vectors and isotherms at t=0.10
(e) ,(f) mid−axial plane flow vectors and isotherms at t=0.15

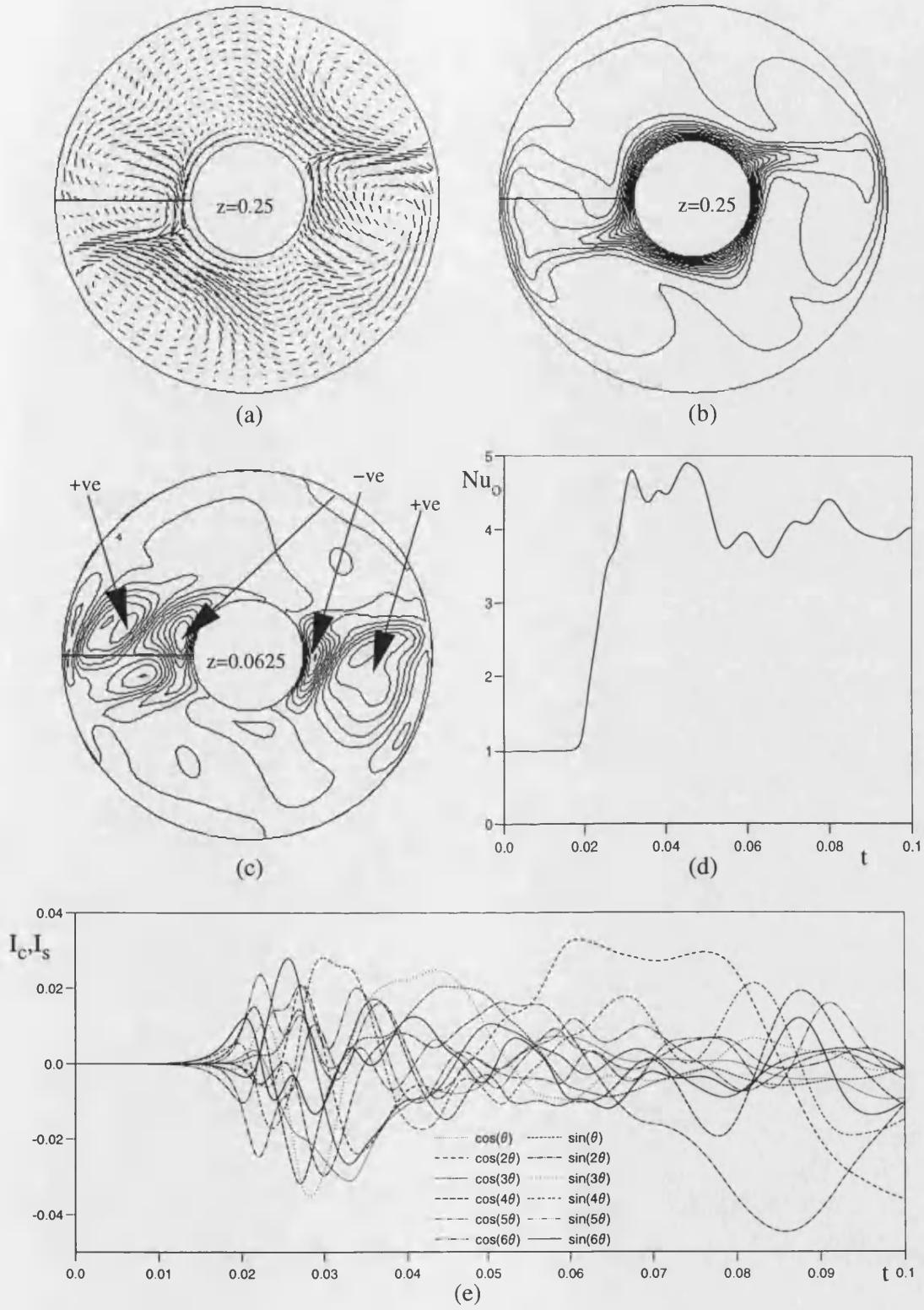

Figure 5.28. Solutions for 3D flow with Ra=10^6, Re=10^3, r_0=0.3 and z_{max}=0.5.
(a) mid–axial plane flow vectors (b) mid–axial plane isotherms
(c) axial velocity iso–lines (d) total heat transfer
(e) Fourier decomposition of the temperature field

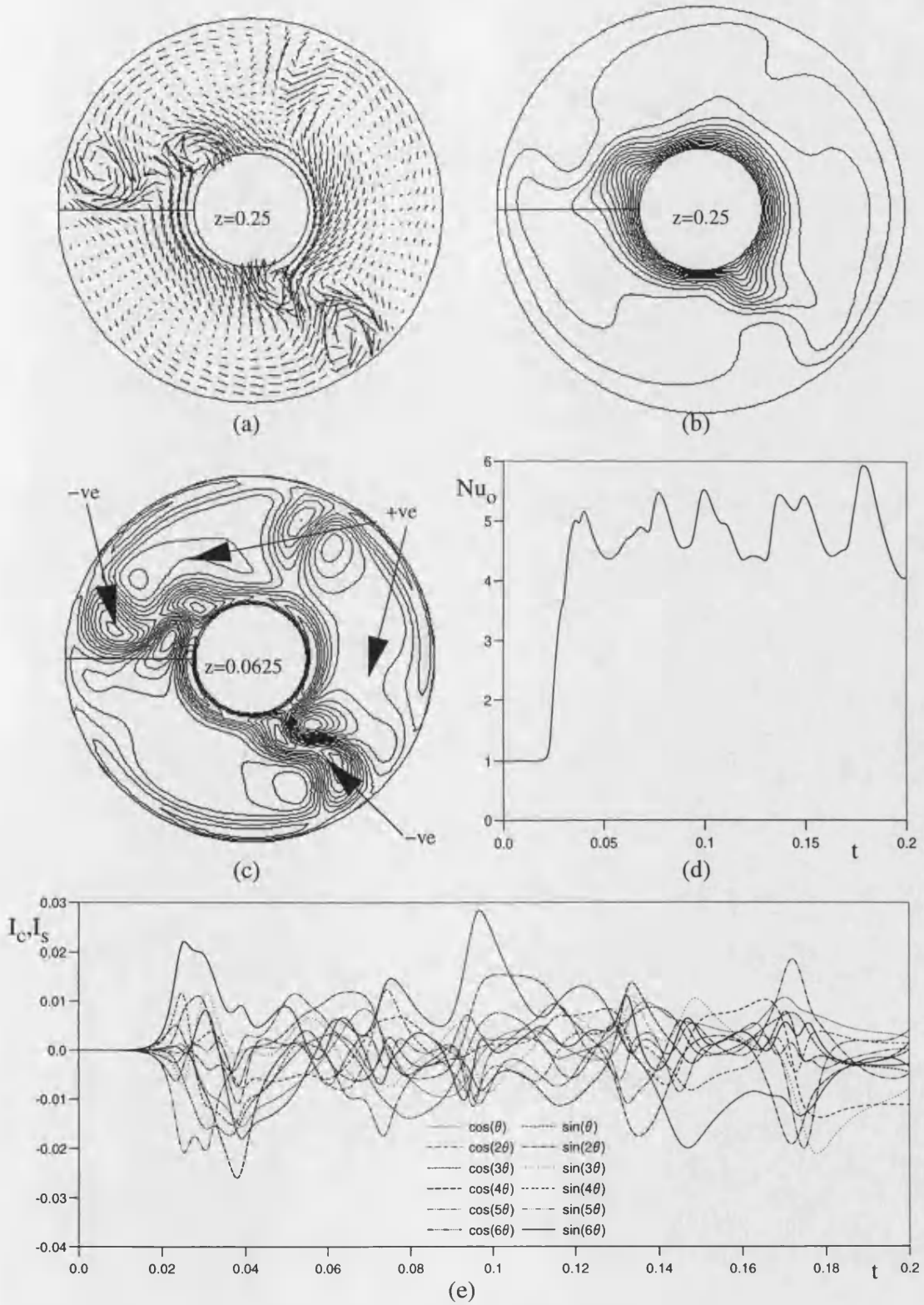

Figure 5.29. Solutions for 3D flow with Ra=10^6, Re=2×10^3, r_0=0.3 and z_{max}=0.5.
(a) mid–axial plane flow vectors (b) mid–axial plane isotherms
(c) axial velocity iso–lines (d) total heat transfer
(e) Fourier decomposition of the temperature field

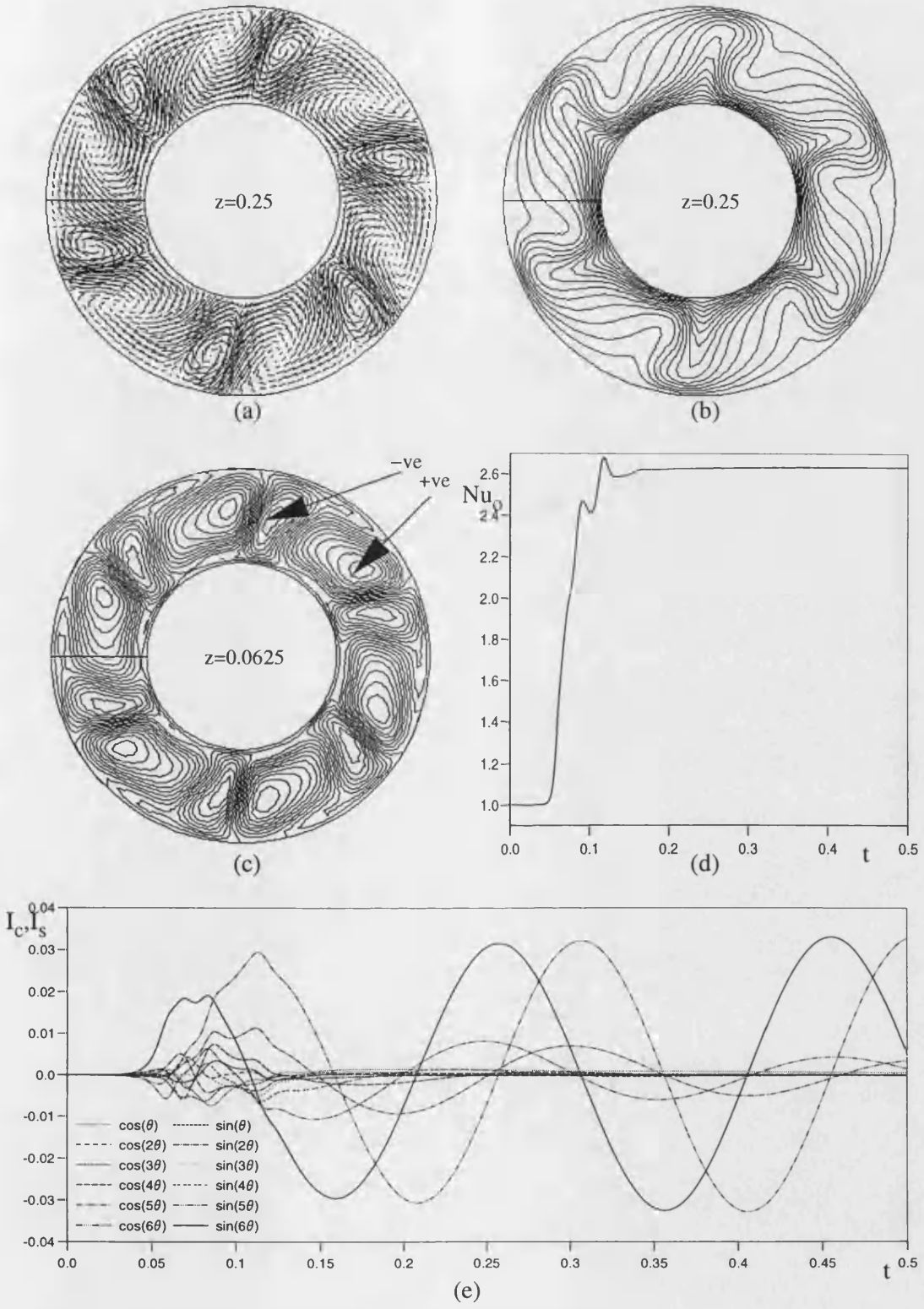

Figure 5.30. Solutions for 3D flow with $Ra=2\times10^5$, $Re=10^3$, $r_0=0.5$ and $z_{max}=0.5$.
(a) mid–axial plane flow vectors (b) mid–axial plane isotherms
(c) axial velocity iso–lines (d) total heat transfer
(e) Fourier decomposition of the temperature field

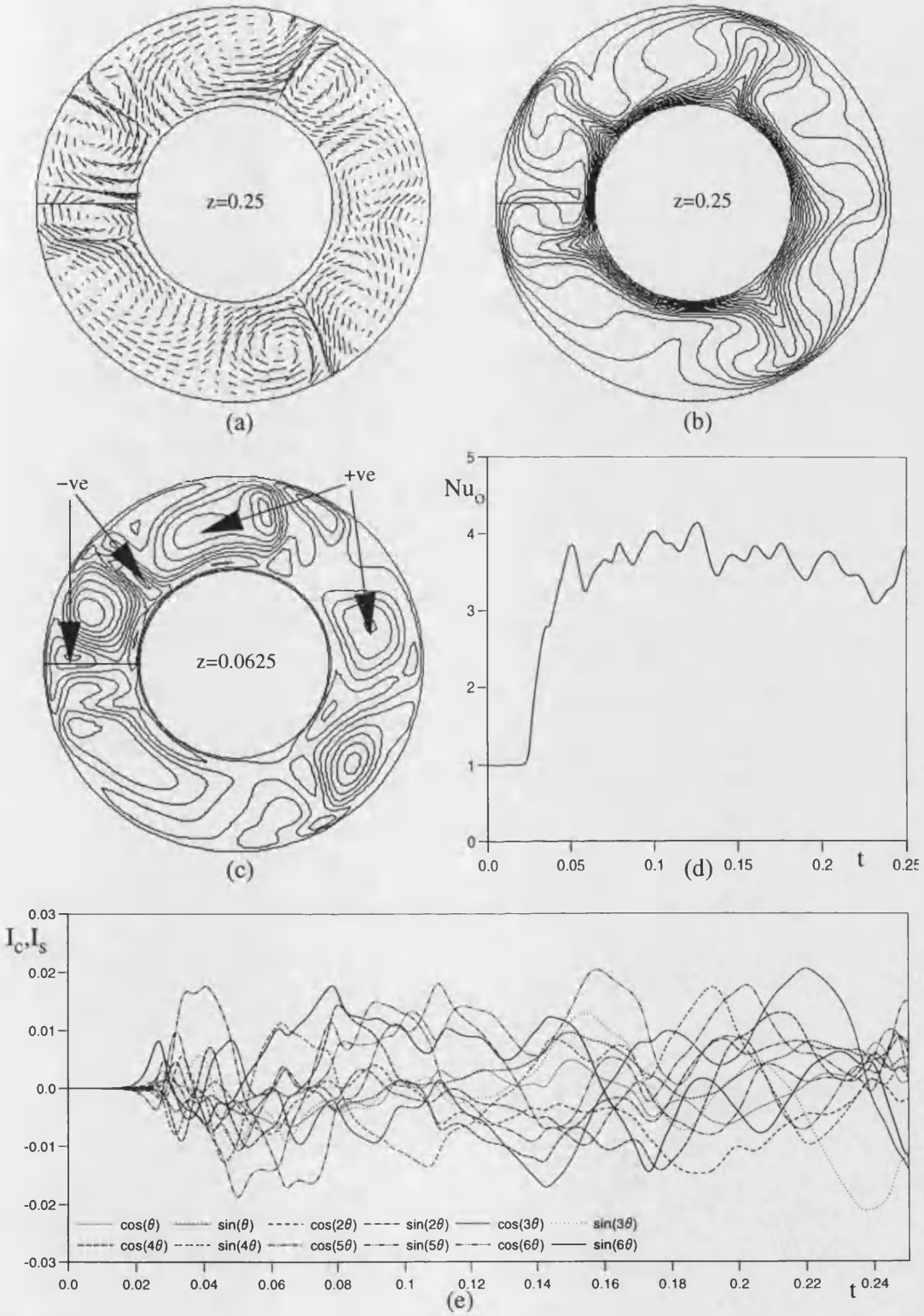

Figure 5.31. Solutions for 3D flow with Ra=5×10^5, Re=10^3, r_0=0.5 and z_{max}=0.5.
(a) mid–axial plane flow vectors (b) mid–axial plane isotherms
(c) axial velocity iso–lines (d) total heat transfer
(e) Fourier decomposition of the temperature field

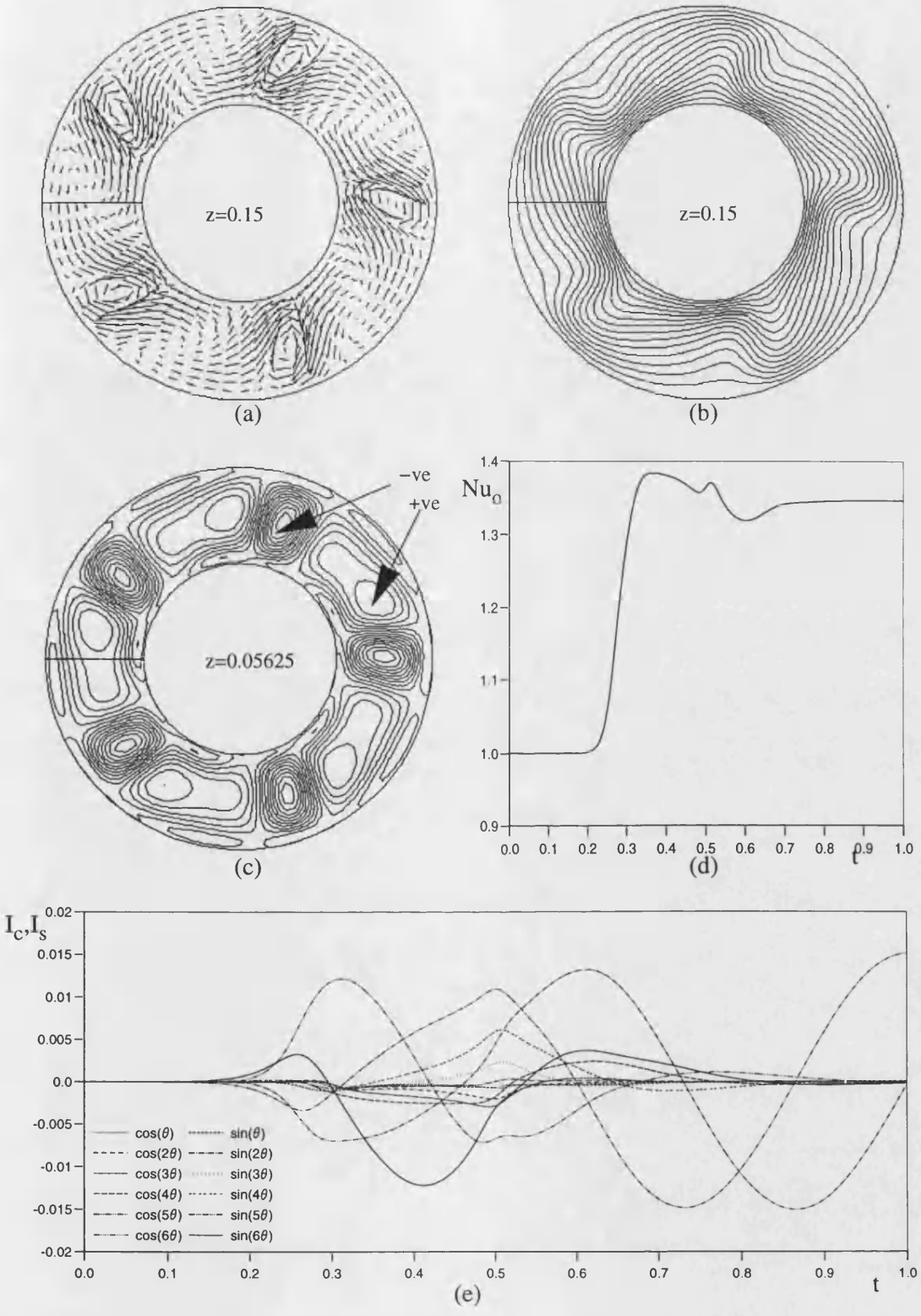

Figure 5.32. Solutions for 3D flow with Ra=10^5, Re=10^3, r_0=0.3 and z_{max}=0.3.
(a) mid−axial plane flow vectors (b) mid−axial plane isotherms
(c) axial velocity iso−lines (d) total heat transfer
(e) Fourier decomposition of the temperature field

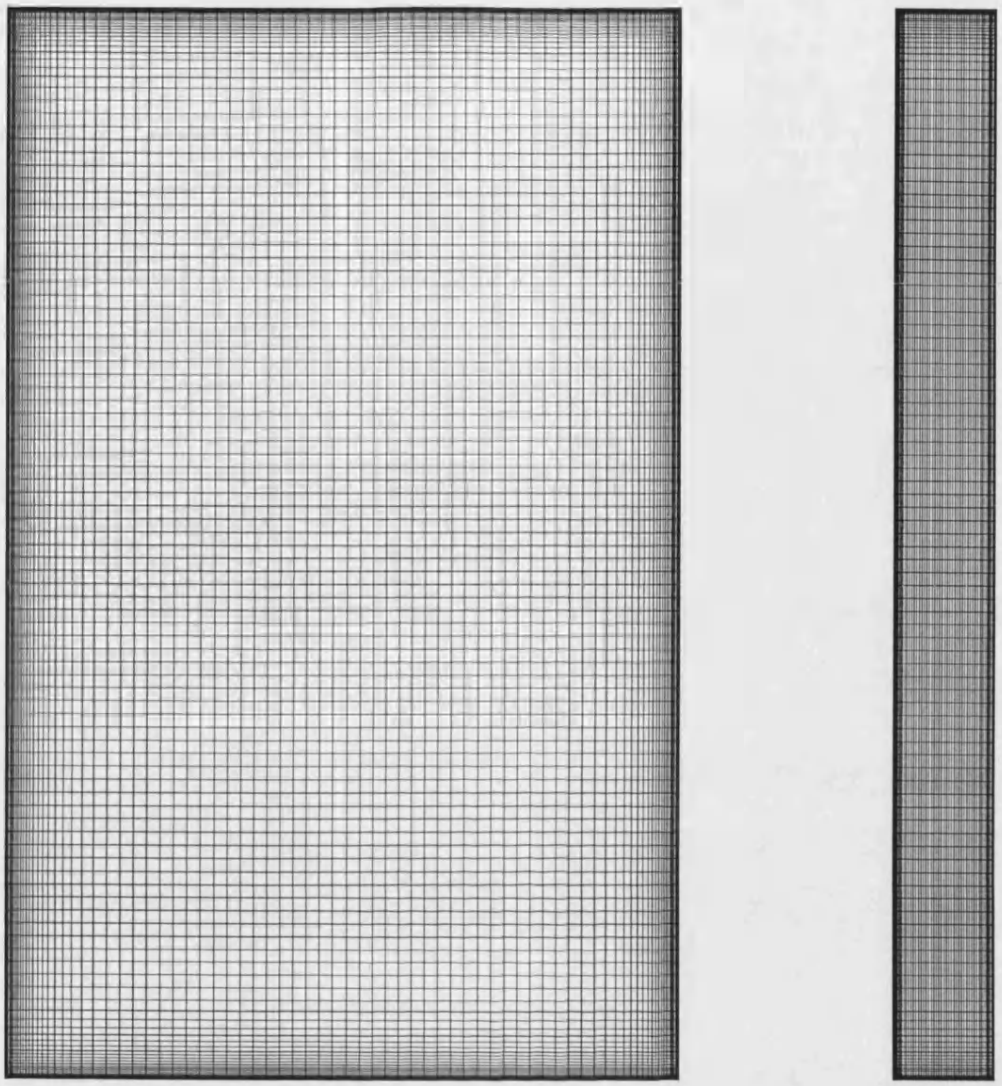

(a) (b)

Figure 6.1. Typical non–uniform grid distributions used for the stationary shroud cases.
(a) 128×96 mesh, r_0=0.5, z_{max}=0.3 and GEF=1.15
(b) 128×64 mesh, r_0=0.5, z_{max}=0.05 and GEF=1.15

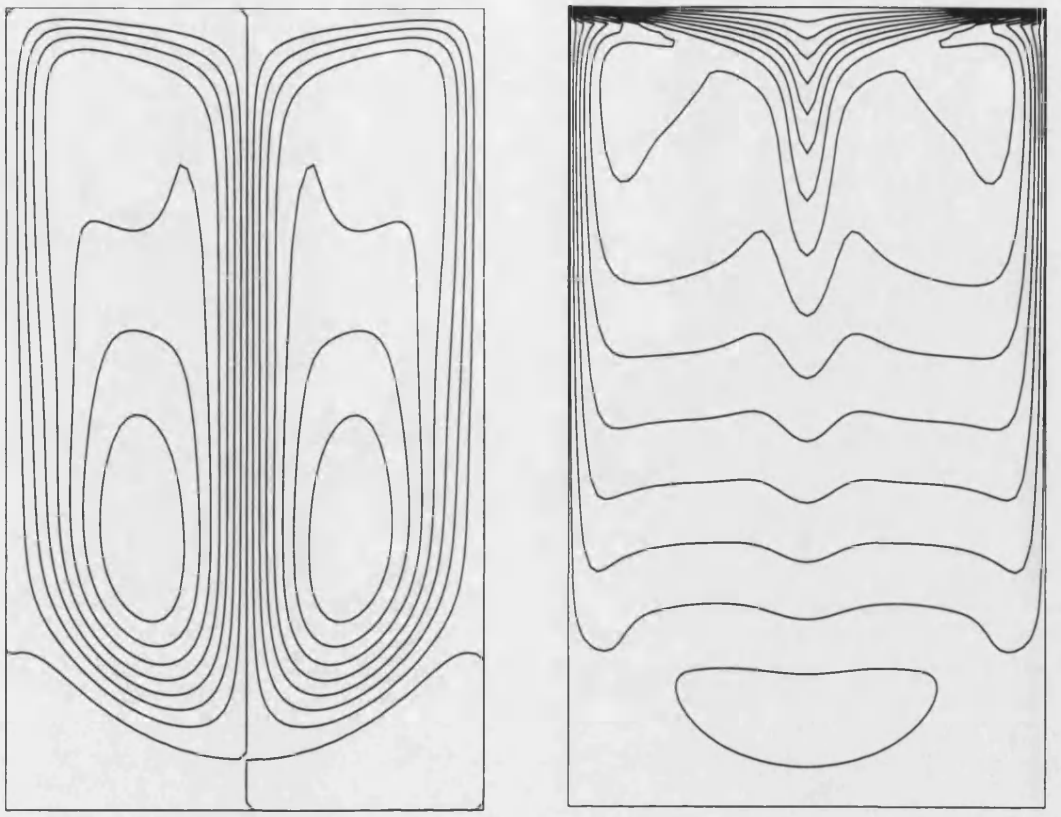

(a) (b)

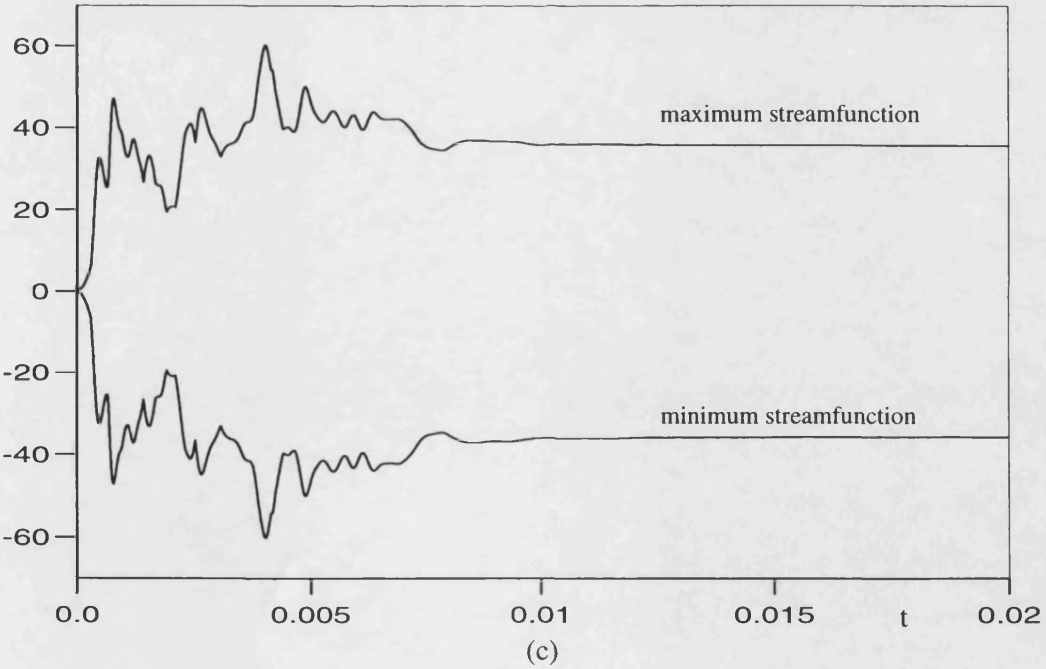

(c)

Figure 6.2. Solutions for Re=10^4, r_0=0.5 and z_{max}=0.3 using uniform grid code and no initial axially varying tangential velocity profile.
(a) end point stream lines
(b) end point tangential velocity iso–lines
(c) maximum/minimum streamfunction

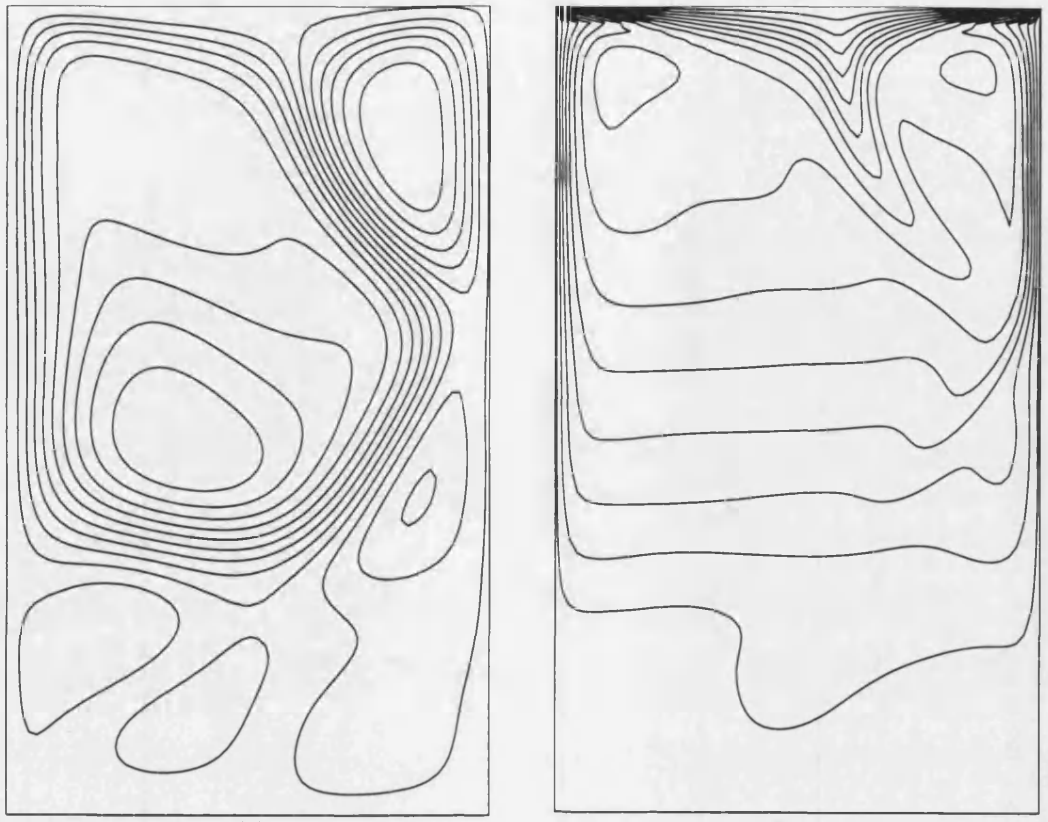

(a) (b)

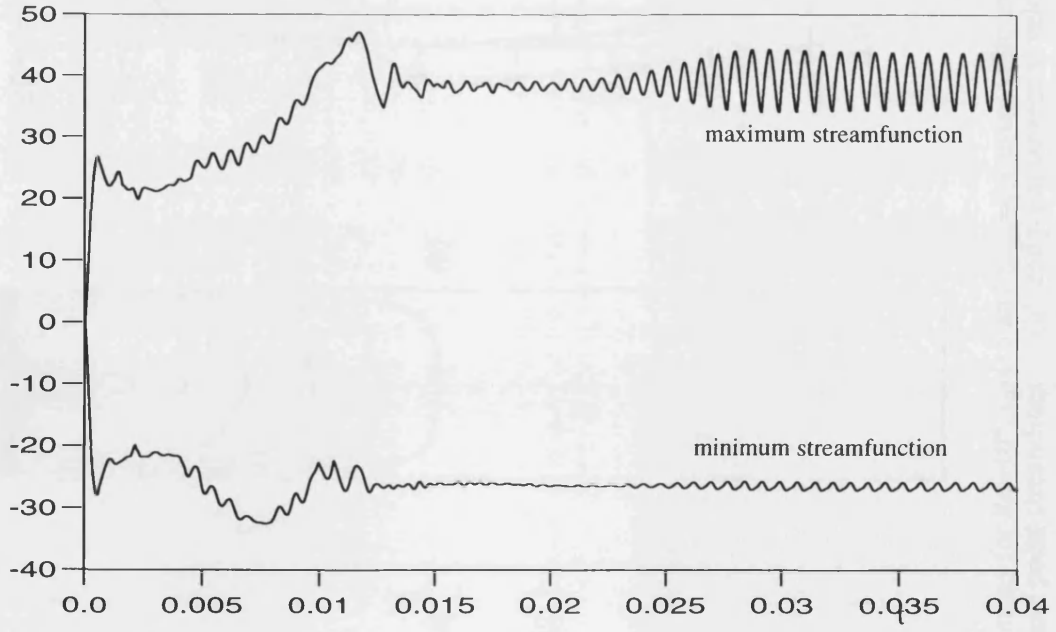

(c)

Figure 6.3. Solutions for Re=10^4, r_0=0.5 and z_{max}=0.3 using uniform grid code and initial axially varying tangential velocity profile.
(a) end point streamlines
(b) end point tangential velocity iso–lines
(c) maximum/minimum streamfunction

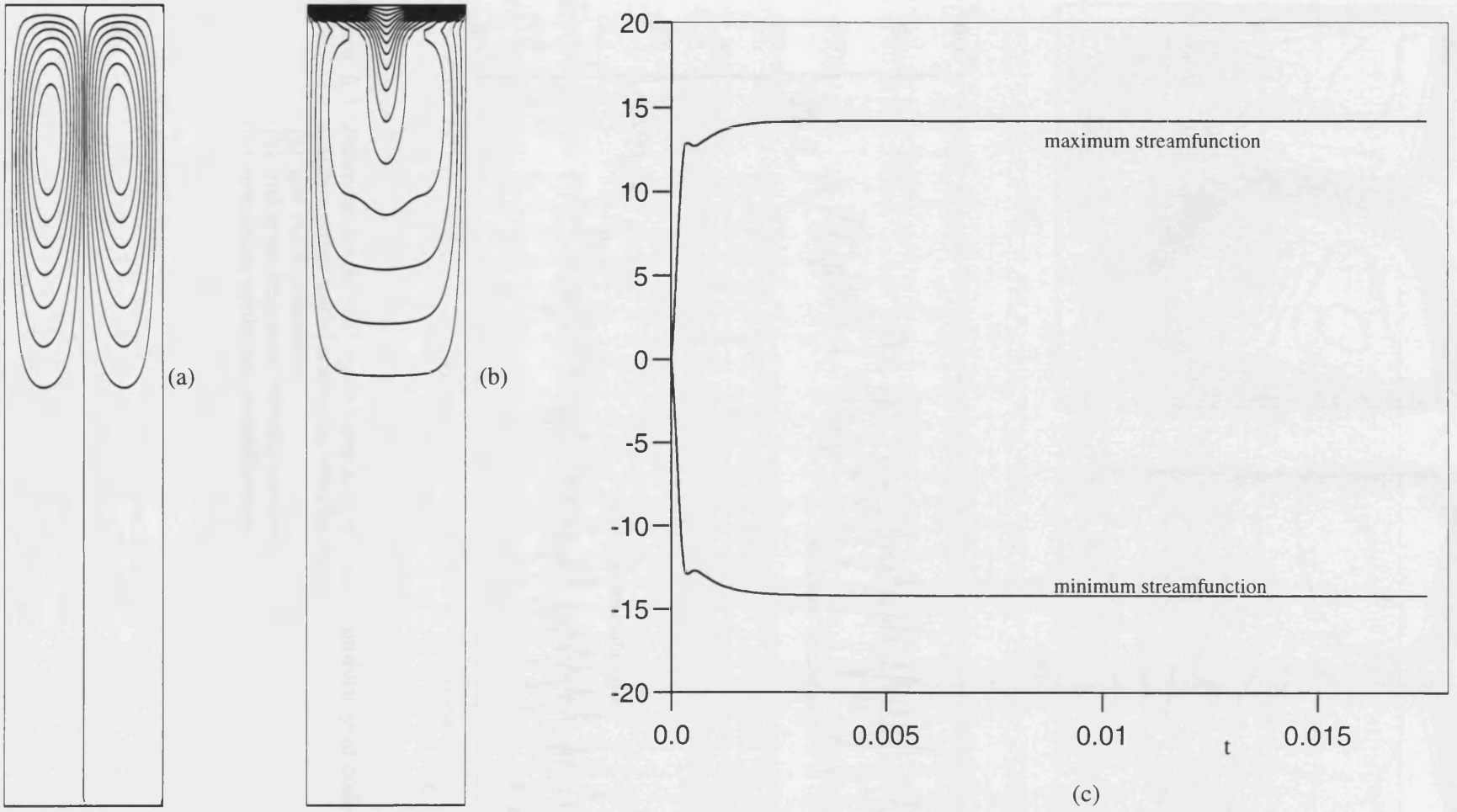

Figure 6.4. Solutions for Re=10^4, r_0=0.5 and z_{max}=0.1 using uniform grid code and axially varying initial tangential velocity profile.
(a) end point streamlines (b) end point tangential velocity iso–lines (c) maximum/minimum streamfunction

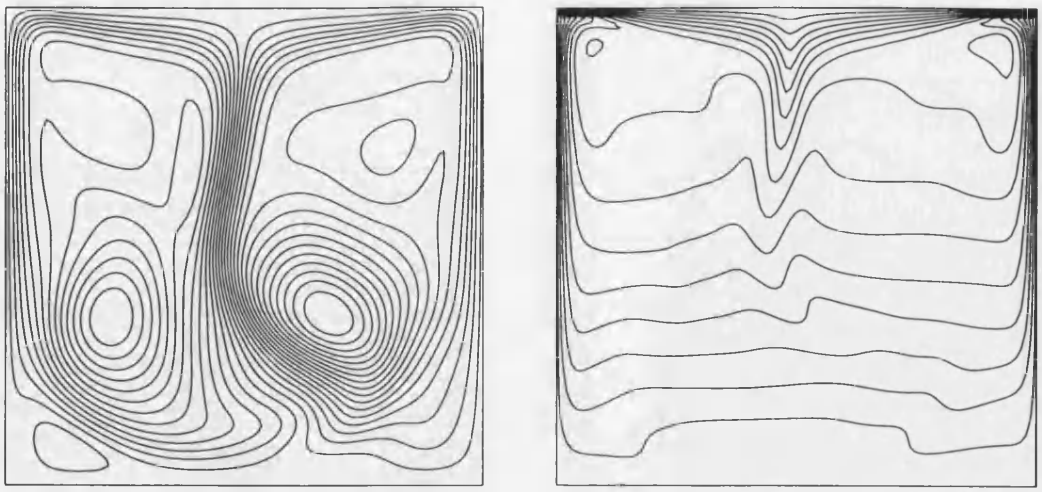

(a) (b)

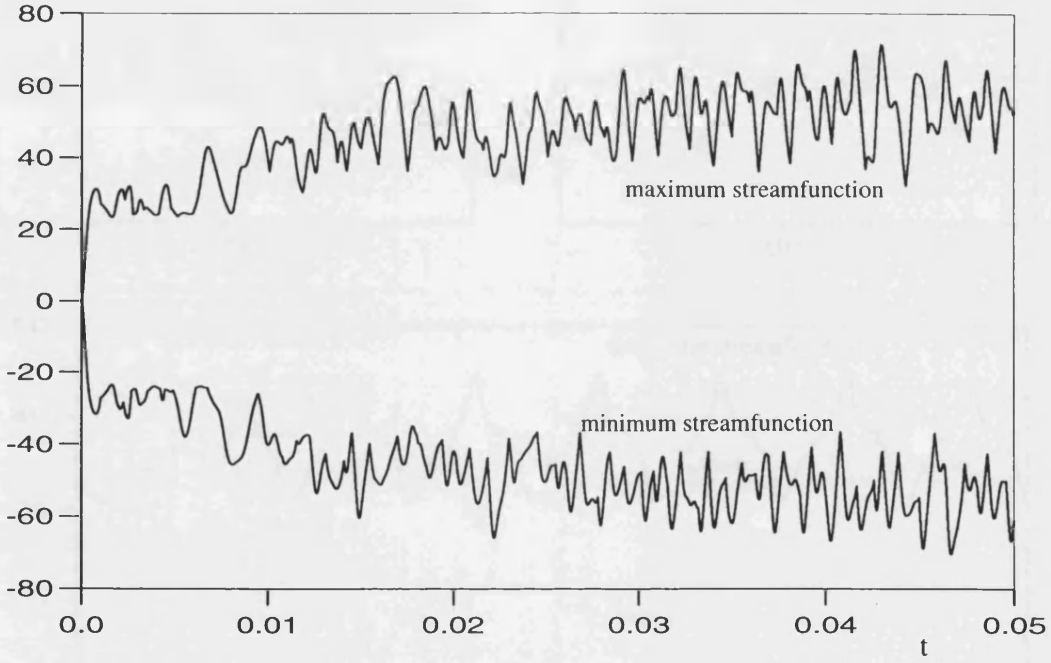

(c)

Figure 6.5. Solutions for Re=10^4, r_0=0.5 and z_{max}=0.5 using uniform grid code and initial axially varying initial tangential velocity profile.
(a) end point streamlines
(b) end point tangential velocity iso–lines
(c) maximum/minimum streamfunction

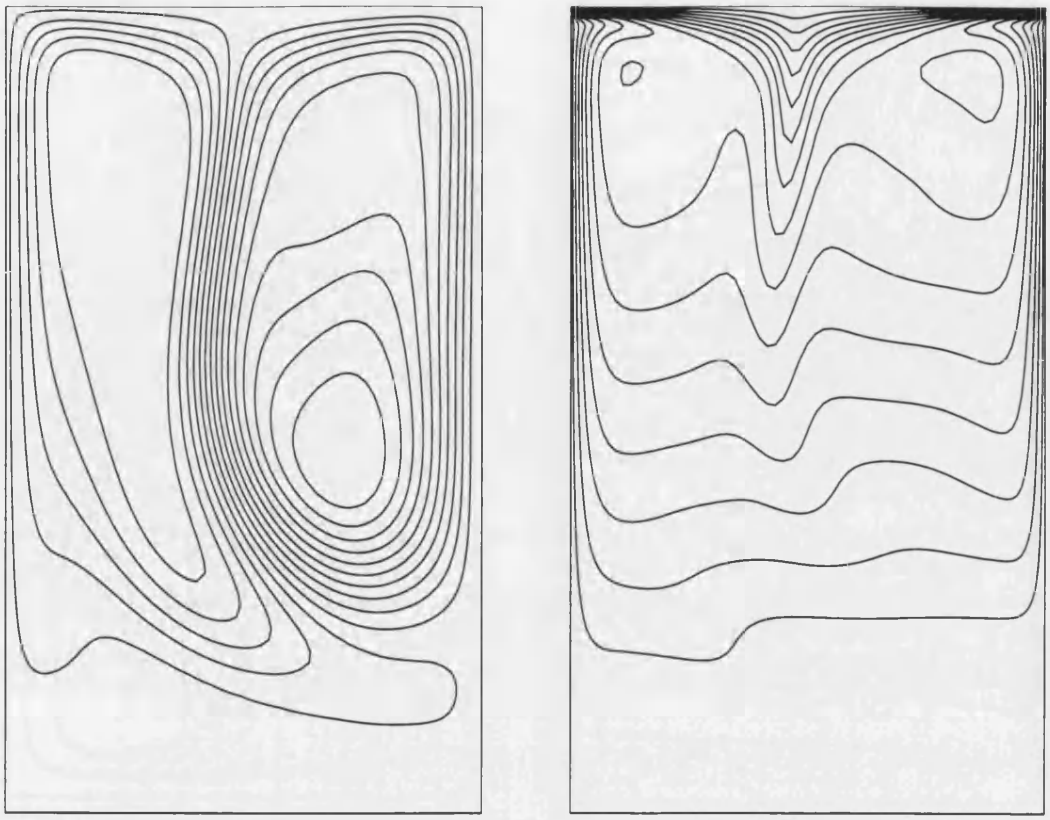

(a) (b)

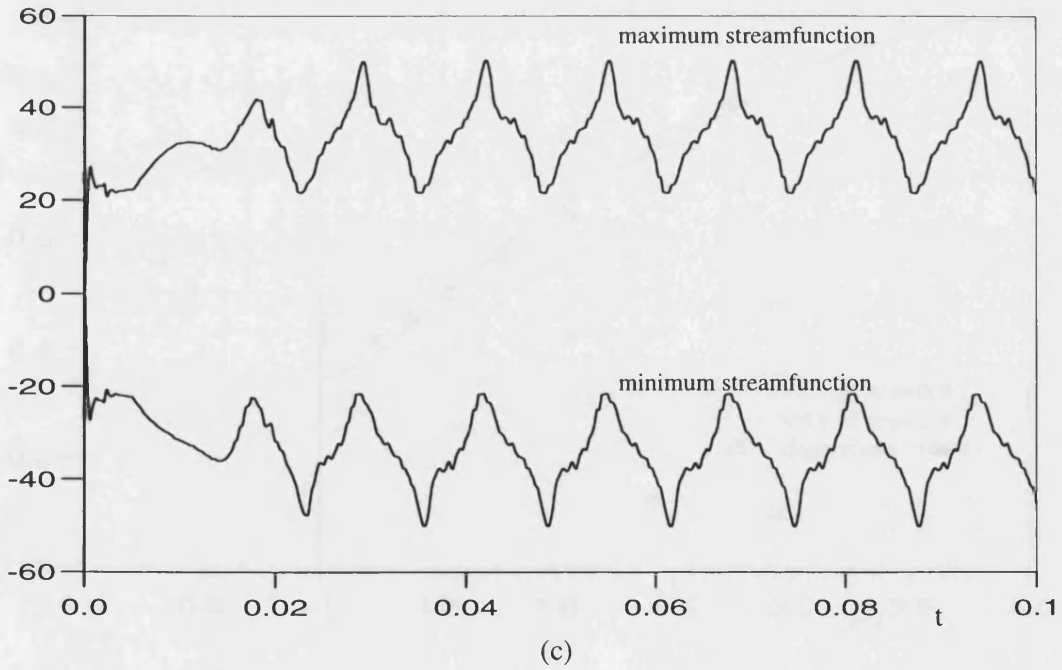

(c)

Figure 6.6. Solutions for Re=10^4, r_0=0.5 and z_{max}=0.3 using non–uniform grid code and initial axially varying tangential velocity profile.
(a) end point streamlines
(b) end point tangential velocity iso–lines
(c) maximum/minimum streamfunction

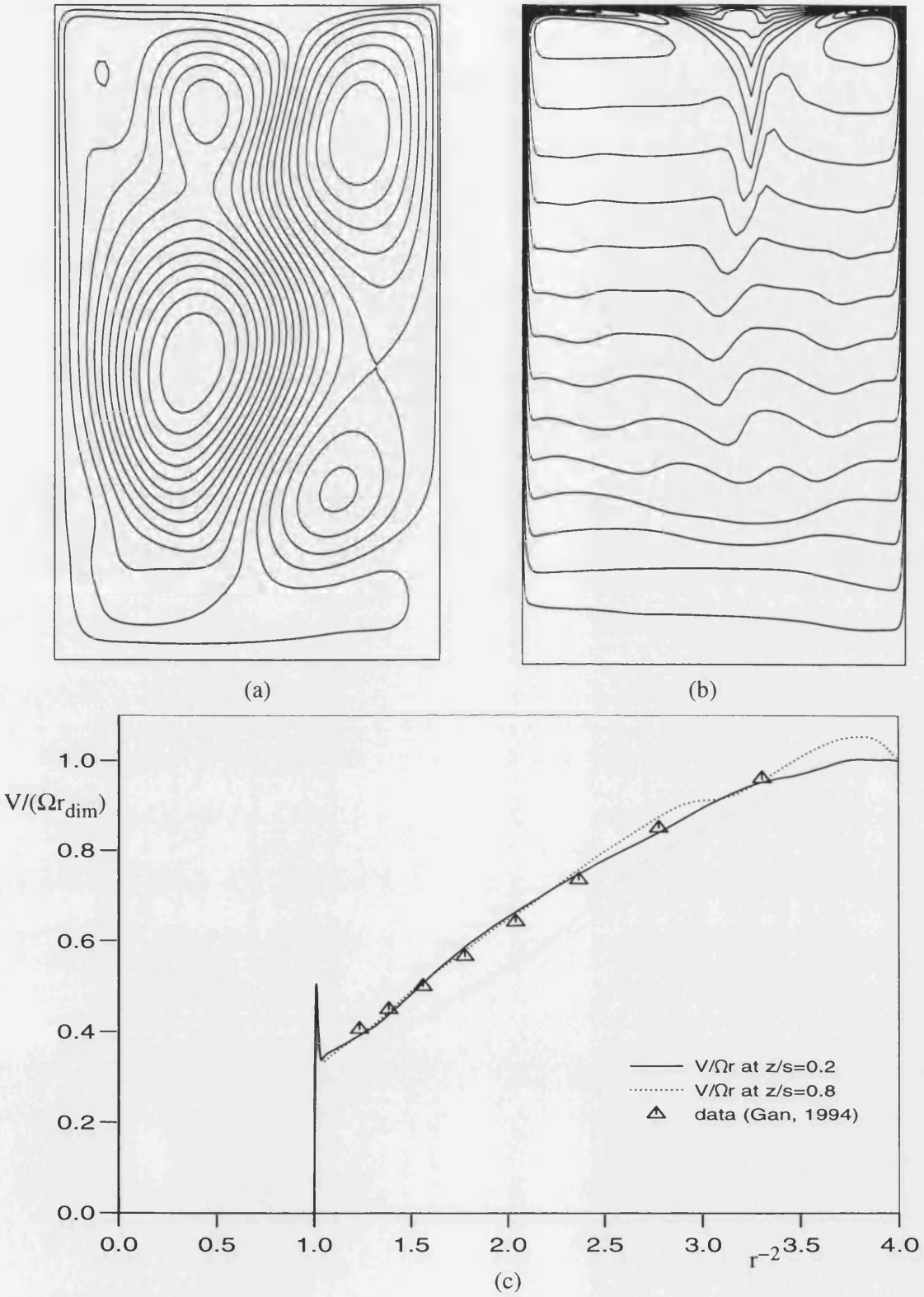

Figure 6.7. Solutions for Re=1.46×10^5, r_0=0.5 and z_{max}=0.3 using non–uniform grid code at non––dimensional time t=0.0025.
(a) streamlines
(b) tangential velocity iso–lines
(c) tangential velocity profile

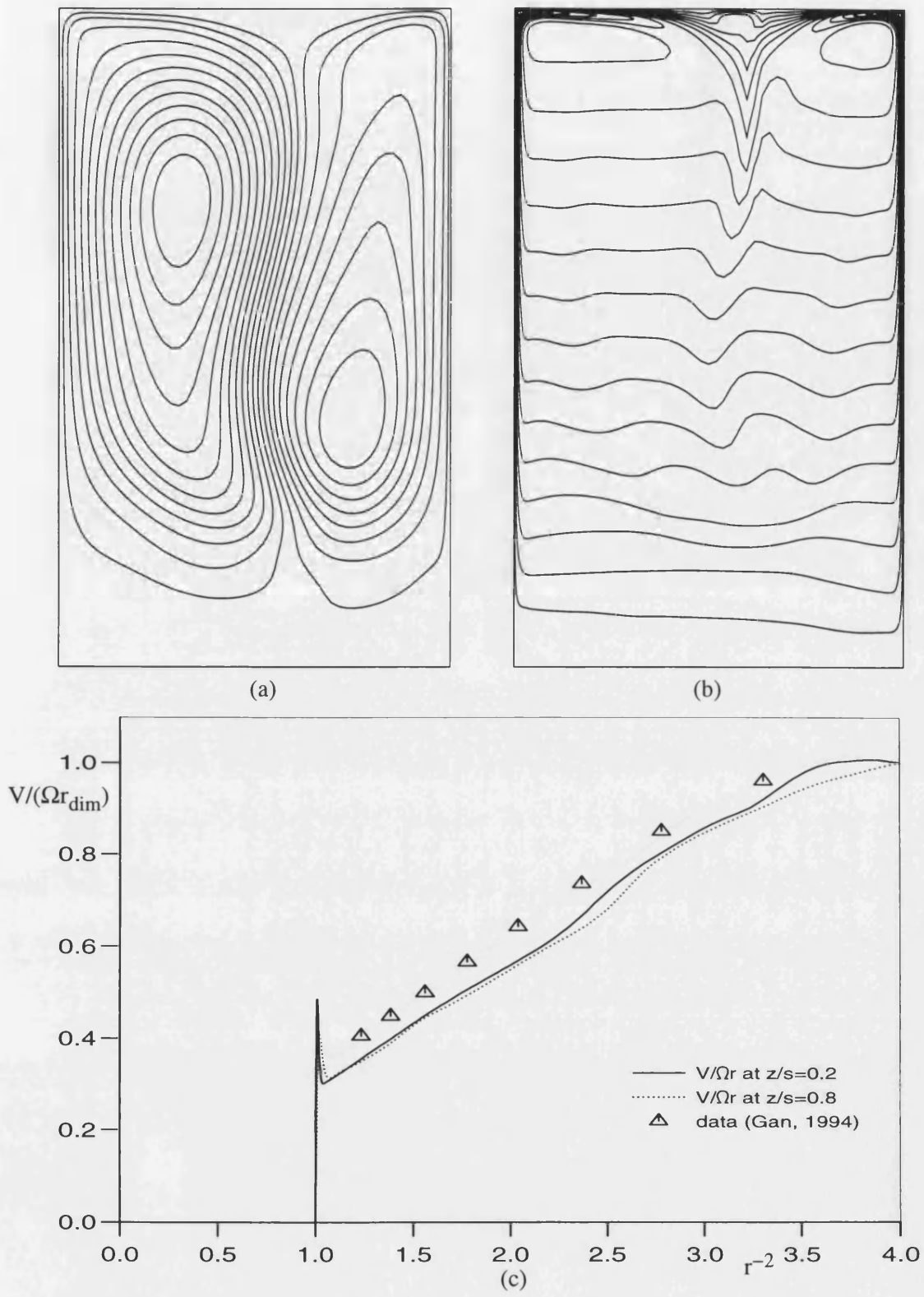

Figure 6.8. Solutions for Re=1.46×10^5, r_0=0.5 and z_{max}=0.3 using non–uniform grid code at non––dimensional time t=0.004.
(a) stream lines
(b) tangential velocity iso–lines
(c) tangential velocity profile

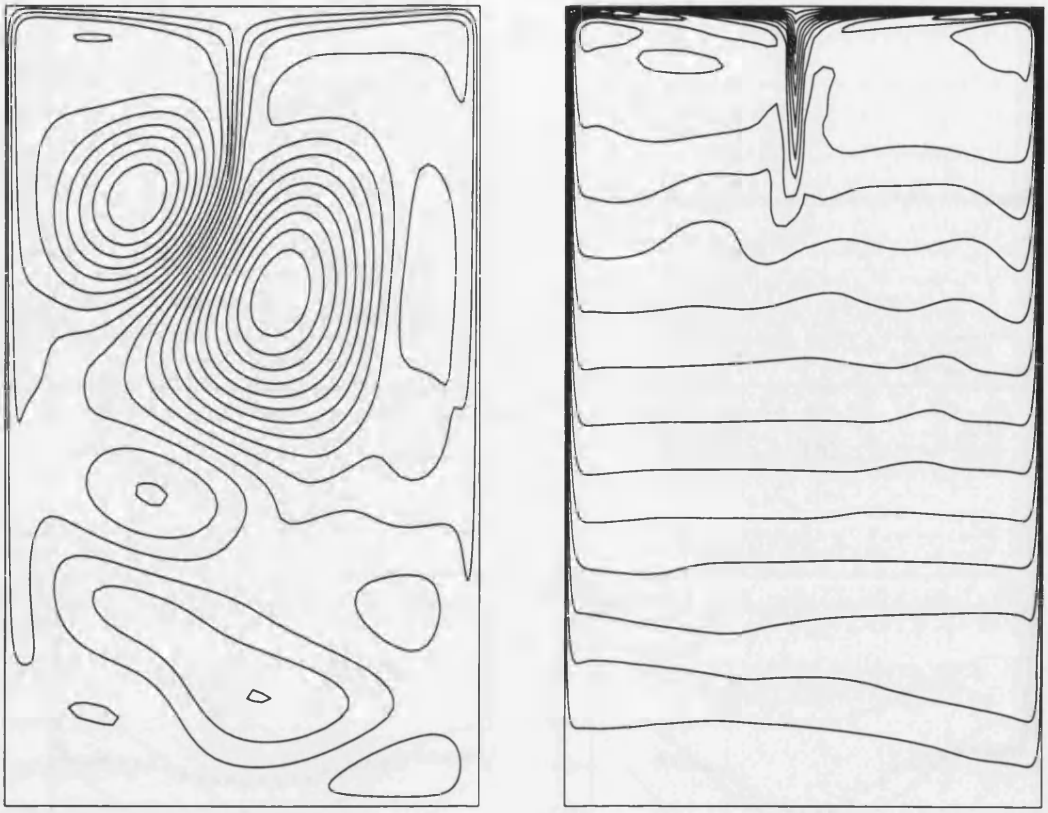

(a) (b)

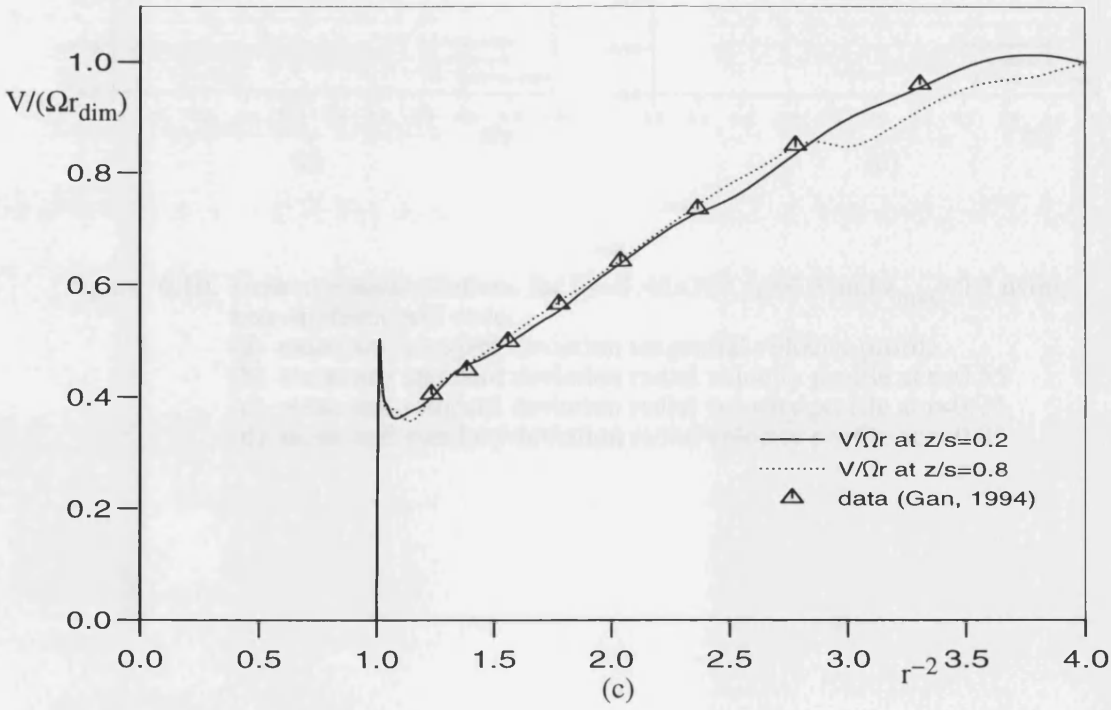

(c)

Figure 6.9 Solutions for $Re=1.46\times10^5$, $r_0=0.5$ and $z_{max}=0.3$ using non–uniform grid code at non––dimensional time t=0.005.
(a) stream lines
(b) tangential velocity iso–lines
(c) tangential velocity profile at z/s=0.2

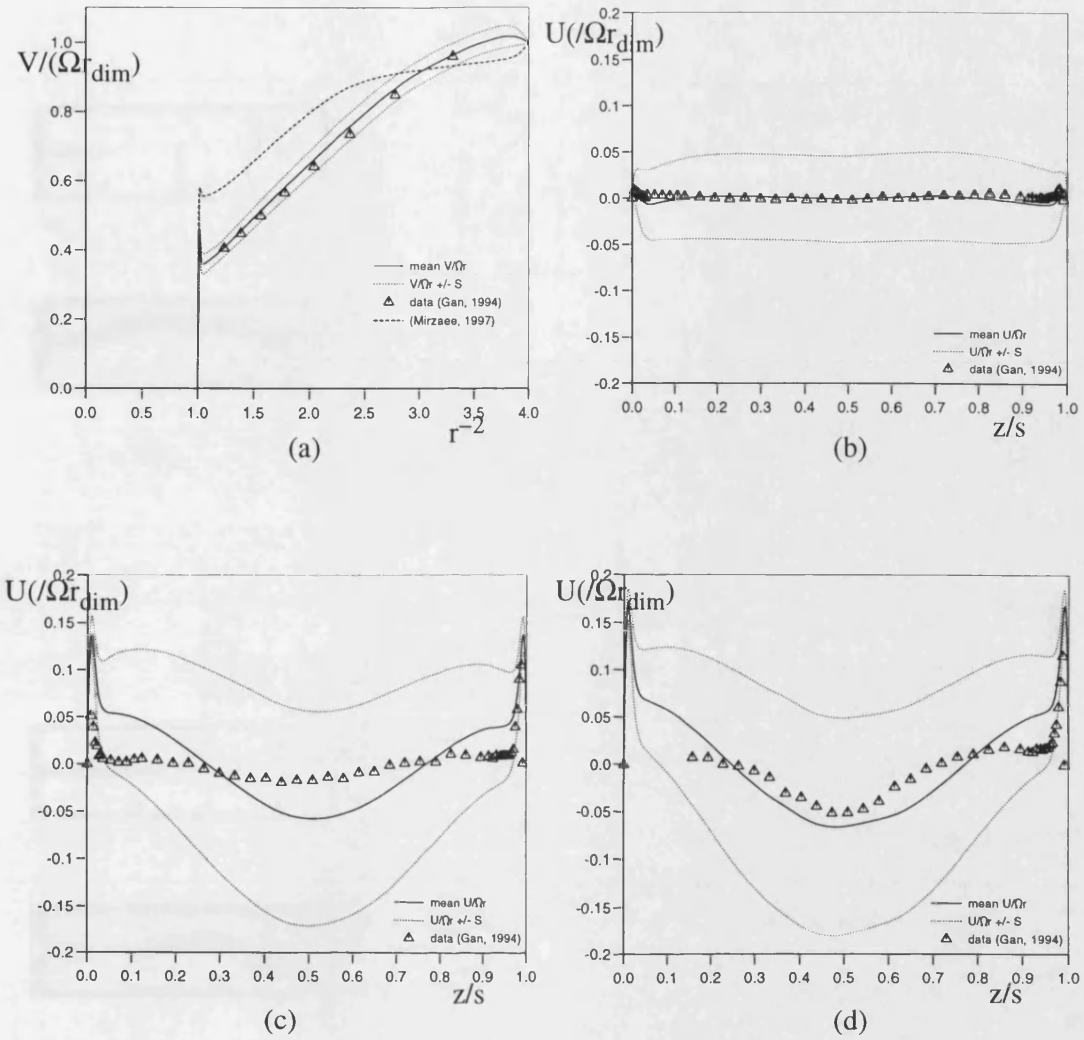

Figure 6.10. Time averaged solutions for Re=1.46×10^5, r_0=0.5 and z_{max}=0.3 using non–uniform grid code.

(a) mean and standard deviation tangential velocity profile
(b) mean and standard deviation radial velocity profile at r=0.55
(c) mean and standard deviation radial velocity profile at r=0.75
(d) mean and standard deviation radial velocity profile at r=0.85

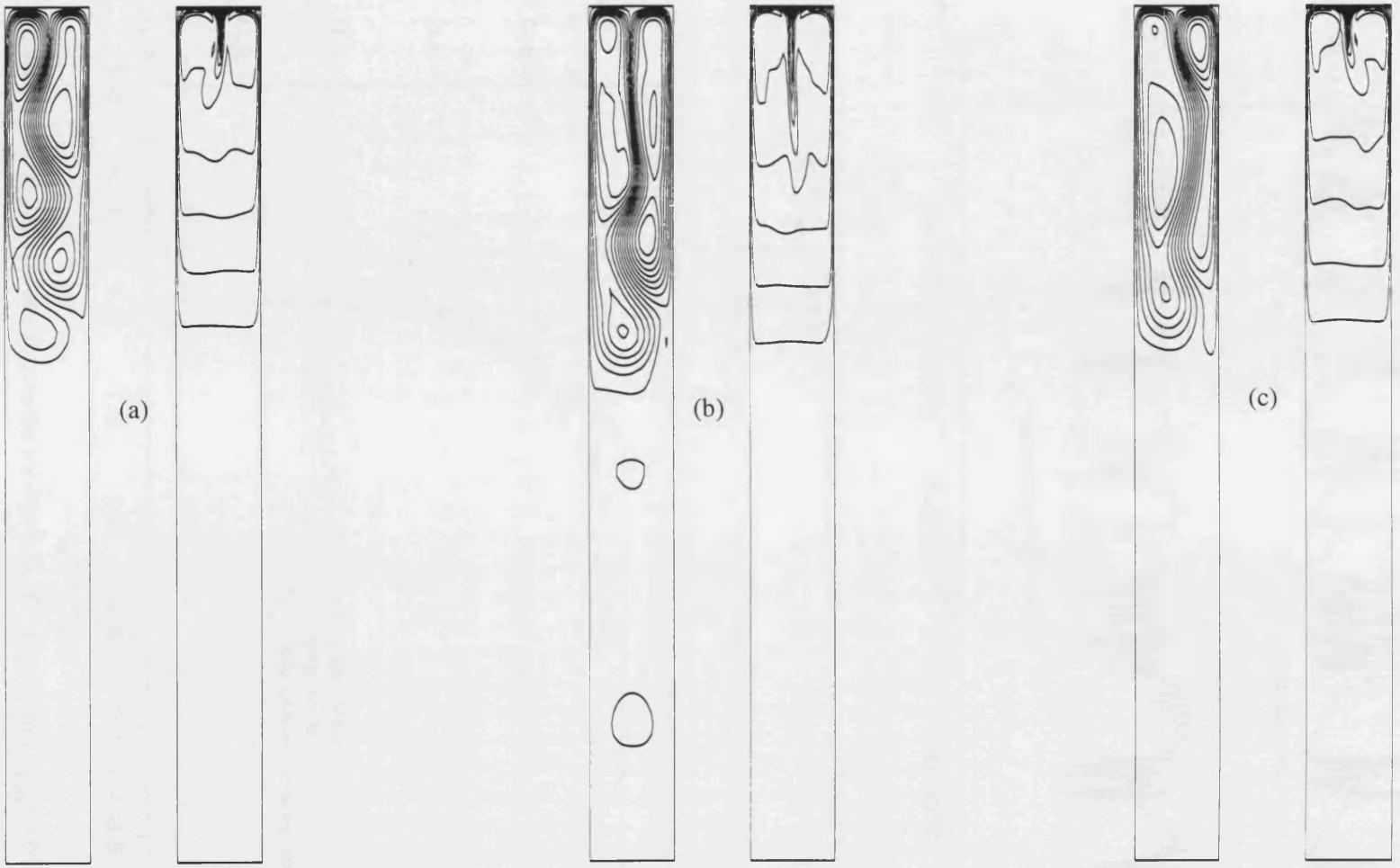

Figure 6.11. Streamlines and tangential velocity iso–lines for $Re=4.5\times10^5$, $r_0=0.5$ and $z_{max}=0.05$ using non–uniform grid code and axially varying initial tangential velocity profile at;
(a) t=0.001 (b) t=0.002 (c) t=0.003

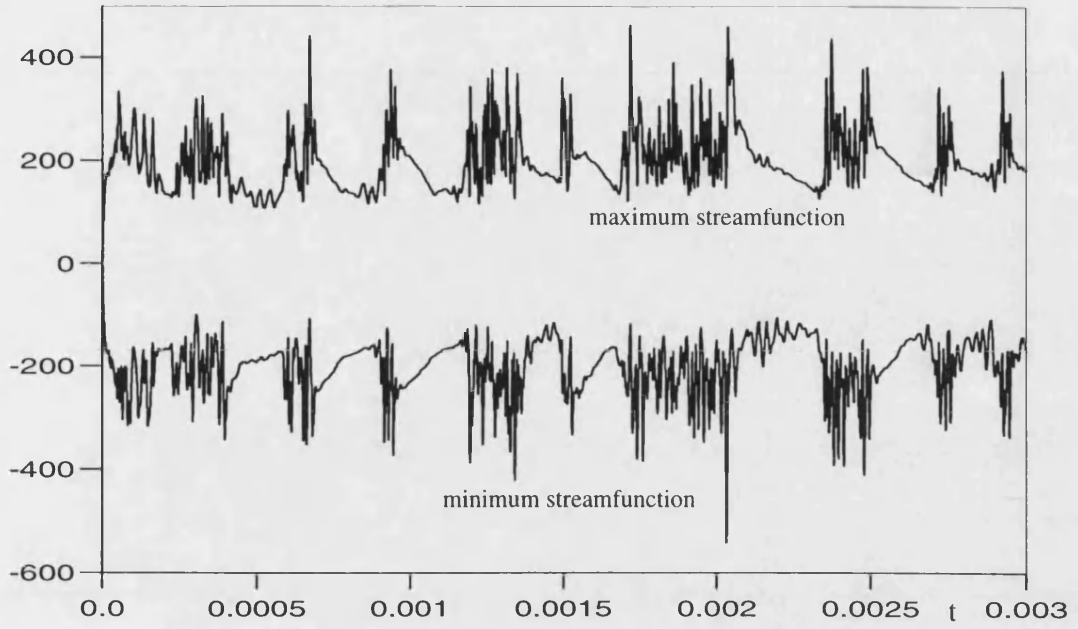

Figure 6.12. Variation in maximum and minimum streamfunction for Re=4.5×10^5, r_0=0.5 and z_{max}=0.05.

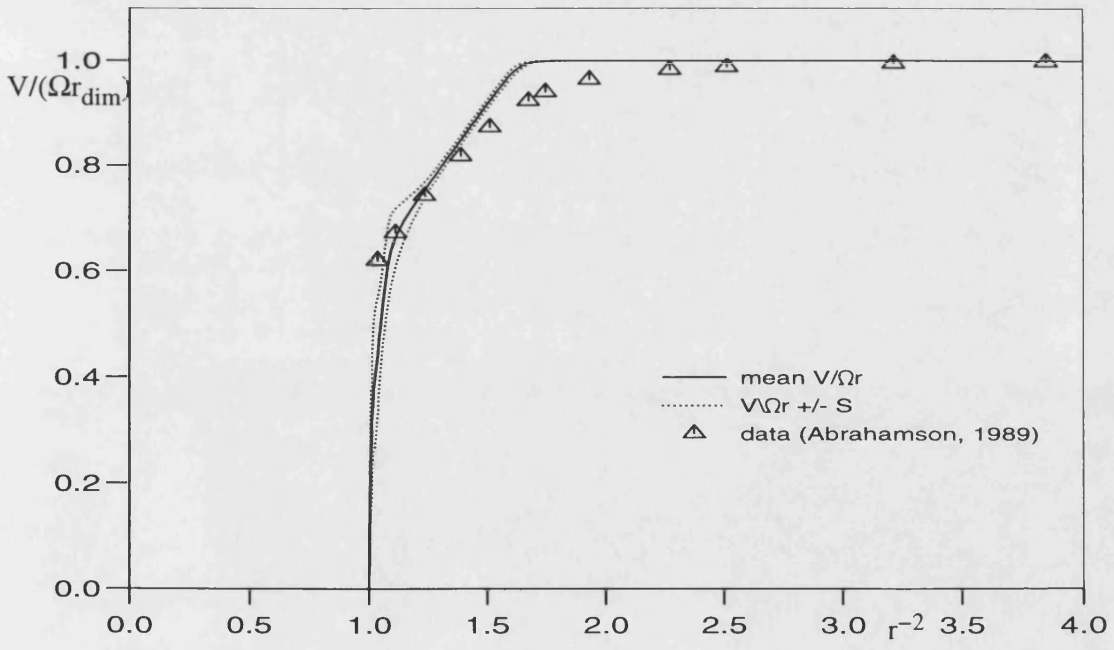

Figure 6.13. Tangential velocity profile for Re=4.5×10^5, r_0=0.5 and z_{max}=0.05.